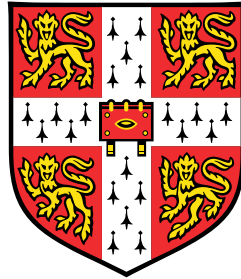


# Dynamic Loading of Structures by High Speed Granular Media



**Ashish Goel**

Department of Engineering  
University of Cambridge

This dissertation is submitted for the degree of  
*Doctor of Philosophy*



# Preface

This dissertation is submitted for the degree of Doctor of Philosophy in the University of Cambridge. The research was carried out during the period from October 2012 to August 2016 in the Department of Engineering, Cambridge, under the supervision of Prof. Vikram Deshpande. The research work was supported by the Office of Naval Research (ONR) and the Defense Advanced Research Projects Agency (DARPA).

I hereby declare that except where specific reference is made to the work of others, the contents of this dissertation are original and have not been submitted in whole or in part for consideration for any other degree or qualification in this, or any other university. This dissertation is my own work and contains nothing which is the outcome of work done in collaboration with others, except as specified in the text. This dissertation contains approximately 52,000 words (including bibliography, footnotes, tables and equations), 112 figures and 1 table, which does not exceed the limits prescribed by the Degree Committee.

Ashish Goel  
June 2018



## Acknowledgements

I am very fortunate to have had this opportunity to do research at the University of Cambridge, particularly under the supervision of Prof. Vikram Deshpande, whose guidance was elemental in completing the work presented in this thesis. My deepest gratitude to him for providing support, direction, challenges and encouragement throughout the research. I specially appreciate the insight that he has provided into all the aspects while keeping a broad perspective. His approach to investigate a problem has greatly improved my aptitude for research. He has always been understanding at professional as well as personal level, helping me through the years of PhD studies. I also want to thank my advisor Prof. Norman Fleck, with whom I have had many fruitful discussions. I am grateful for the financial support provided through Prof. Deshpande and Prof. Fleck, without which I would not have been able to join the PhD program at the University of Cambridge.

My work was greatly supported by the computing and experimental facilities of the CUED Micromechanics group. I admire and thank all the staff for helping with the work and ensuring we never run out of resources to progress with the research. In addition, the department provided me with supervision opportunities, where I loved interacting with other students and gaining deeper subject knowledge. During my four years at the Oatley lab, I have had many great technical discussions with my colleagues and made many friendships, which I would cherish my whole life. Whether meeting at work or socially, they have always made me feel like a family. The ethnic diversity and experiences of my colleagues have provided me with truly enriching time and I am thankful to each of them.

A big thanks to my wife Richa, who has been a foundation on which I have completed my dream of doing a PhD. I am blessed to have her as a companion and would never forget all the sacrifices she has made, which started even before we moved to the UK. Through all the good and difficult times of my PhD, she has always supported me and kept me motivated with her cheerful attitude. I must mention my son Dheer, who was born during third year of my PhD. He has always brought a smile to my face in the most stressful times, and also provided inspiration to persevere, as he learnt from barely being able to move after birth - to turn over - to crawl - to walk - to run around, all within one year. Finally, I want to thank my parents, my sister and my brother, who have always encouraged me with every endeavour I have taken in my life. All my achievements are a result of their support and unwavering faith in my abilities. More importantly, they have instilled a great morale in me, driving me to become a good person.



# Abstract

This thesis analyses the impact of granular aggregates with structures using experiments and numerical simulations. Original contributions include an insight into multiple factors affecting the loading and damage to the structures, along with study of numerical parameters important for realistic prediction of the interaction between the granular media and structures. It extends the current understanding related to such interactions, with an underlying motivation to guide strategies in order to reduce the structural damage. The response of structures impacted by granular media (sand or soil) is of significant research interest for many applications. One of the applications is for landmine explosions which causes ejection of soil from ground and damage to structures impacted by this ejected soil.

Experimentation is done in a laboratory setting where the cylindrical sand slugs are generated at high speed using an impulse provided by a piston. This induces a velocity gradient along the slug, because of which the slug expands during the flight before impacting the target. Deformable as well as rigid flat targets are considered in two orientations relative to the incoming slug: perpendicular (i.e. normal orientation) and inclined at an angle of  $45^\circ$ . The targets are supported by force transducers to capture the loading from the slug. Simulations are performed using a combination of discrete particle and finite element schemes, which enables the analysis of the fully coupled interaction between the flowing granular media and the structure. A contact model involving multiple parameters is used for inter-particle and particle-target contact.

Firstly, a numerical analysis is performed to characterise the temporal evolution of slugs and their impact on monolithic beams constrained at the ends. Out of all the parameters used for inter-particle contact definition in discrete particle method, only the contact stiffness is found to effect the velocity gradient in the slug before it impacts the target. Other factor influencing the gradient is the acceleration provided by the piston. A strong dependence of beam deflection on the stand-off distance is observed due to the velocity gradient in the slugs.

As the second step, the effect of target surface properties on the transmitted momentum is analysed. Experiments are done by applying coatings of different hardness and roughness on the target surface impacted by sand slugs. For normally oriented targets, the transmitted momentum is observed to be insensitive to the change in surface coating. In contrast, for inclined targets, a significant influence of coatings is observed. Additionally, the momentum transmitted to the inclined targets is always less than that for normal targets.

Numerical analysis of this surface effect reveals that assuming the slug particles to be spherical shape in simulations does not capture the particle/target interactions accurately and under-predicts the frictional loading on the target.

Following this, a detailed numerical study is done to understand the effect of the shape of particles in the slug. Simple shaped non-spherical particles are constructed by combining spherical sub-particles. With increasing angularity of particles in the slug, the frictional loading on the target is shown to increase. This results in an increase of momentum transmitted to inclined targets. For normally oriented targets however, the particle shape does not affect the overall transmitted momentum, which is a behaviour similar to that observed when studying the effect of target surface properties. In addition, effect of fracture of particles in the slug is analysed by using beam connections between sub-particles that break during the impact with the target. If the fracture results in increasing particle angularity, the transmitted momentum increases, whereas the situation reverses if fracture results on more spherical shaped particles.

Lastly, a strategy to reduce the loading on the targets is analysed by using sacrificial coating on the target surface. In experiments, this coating is placed on the rigid target surface using a lubricant at their interface. When impacted by the slug, this coating slides on the target surface, resulting in a reduction of frictional loading on the target. If the friction at the coating/target interface vanishes, the transmitted momentum approaches the theoretical minimum value. Simulations are used to first validate the experimental observations and then to extend the concept of sliding coatings using deformable targets. Both the transmitted momentum and deflections depended on the thickness of the target and coating. When a coating is used, the deflections increase due to reduction in target thickness. It is found that the best strategy to reduce the damage to the target is to use least possible thickness of the coating and minimise the friction at the interface between the coating and the target.

The presented work examines many of the factors that affect the loading on the target impacted by granular slugs, in addition to characterising the expansion of slugs before the target impact. The analysed factors include those already known such as target stand-off distance, inclination and unveils others such as target surface properties and granular properties. The numerical analysis discloses important parameters and shows the effect of particle shape, highlighting the shortcomings of widely used spherical particle assumption in the numerical studies. A strategy using a sacrificial coating to reduce damage to the target is also analysed.

# Table of contents

<b>1</b>	<b>Introduction</b>	<b>1</b>
1.1	Motivation . . . . .	1
1.2	Objectives . . . . .	2
1.3	Thesis outline . . . . .	3
1.4	Published work . . . . .	4
<b>2</b>	<b>Literature Review</b>	<b>5</b>
2.1	Introduction . . . . .	5
2.2	Characteristics of landmine blast . . . . .	6
2.3	Effect of depth of burial . . . . .	8
2.4	Effect of stand-off . . . . .	10
2.5	Effect of soil properties . . . . .	11
2.5.1	Water saturation . . . . .	13
2.5.2	Particle shape . . . . .	13
2.5.3	Particle fragmentation . . . . .	16
2.6	Effect of target properties . . . . .	18
2.6.1	Target inclination / V-shaped hulls . . . . .	19
2.6.2	Surface properties . . . . .	24
2.6.3	Collapsible structures . . . . .	26
2.6.4	Sandwich vs monolithic target . . . . .	28
2.7	Reduced scale experiments . . . . .	30
2.8	Numerical modelling methods . . . . .	33
2.8.1	Empirical models . . . . .	33
2.8.2	Continuum models . . . . .	33
2.8.3	Discrete particle method (Discrete Element Method - DEM) . . . . .	37
2.8.4	Modelling non-spherical (angular) particles . . . . .	41
2.9	Mechanical packing of particles . . . . .	43
2.10	Summary and conclusions . . . . .	44

<b>3</b>	<b>Coupled discrete/continuum simulations of the impact of granular slugs with clamped beams: Stand-off effects</b>	<b>47</b>
3.1	Introduction . . . . .	48
3.2	Summary of experimental findings . . . . .	50
3.2.1	Key experimental measurements . . . . .	50
3.3	Numerical simulation methodology . . . . .	51
3.3.1	Discrete particle calculations . . . . .	53
3.3.2	Finite element calculations and coupling to the discrete particle calculations . . . . .	56
3.3.3	Material properties . . . . .	56
3.4	Evolution of the granular slug during free-flight . . . . .	58
3.4.1	Estimation of the particle contact stiffness . . . . .	58
3.4.2	The piston velocity . . . . .	59
3.4.3	The ramp time for piston to acquire its steady-state velocity . . . . .	60
3.4.4	Sensitivity to contact model parameters . . . . .	64
3.5	Impact of granular slug against structures . . . . .	65
3.5.1	Impact against a clamped monolithic beam . . . . .	66
3.5.2	Impact against a rigid stationary target . . . . .	68
3.6	Concluding remarks . . . . .	71
<b>4</b>	<b>Effect of surface properties on momentum transfer to targets impacted by high-velocity sand slugs</b>	<b>73</b>
4.1	Introduction . . . . .	74
4.2	Experimental protocol . . . . .	76
4.2.1	Slug launcher . . . . .	76
4.2.2	Silica sand slugs . . . . .	78
4.2.3	Gas gun to fire projectile . . . . .	79
4.2.4	Target design . . . . .	79
4.2.5	Temporal evolution and characterisation of slugs . . . . .	82
4.2.6	Characterisation of transmitted momentum . . . . .	83
4.3	Measurements for normal impact . . . . .	85
4.4	Measurements for inclined impact . . . . .	86
4.4.1	Effect of surface type . . . . .	88
4.5	Discrete particle simulations and comparisons with measurements . . . . .	92
4.5.1	Simulation methodology . . . . .	92
4.5.2	Generation of the sand slug . . . . .	95
4.5.3	Comparison with measurements . . . . .	97
4.6	Sources of the discrepancy between simulations and measurements . . . . .	100

4.6.1	Role of particle and slug properties . . . . .	100
4.6.2	Effect of rotational inertia . . . . .	102
4.6.3	Discussion on effect of particle shape . . . . .	104
4.7	Concluding remarks . . . . .	105
<b>5</b>	<b>Impact of granular slugs on rigid targets: effect of grain shape and fracture</b>	<b>107</b>
5.1	Introduction . . . . .	108
5.2	Problem description and simulation methodology . . . . .	110
5.2.1	Geometry of the grains . . . . .	111
5.2.2	The particle contact model and coupling to FE simulations . . . . .	113
5.2.3	Construction of granular slugs . . . . .	115
5.2.4	Material parameters . . . . .	117
5.3	Effect of particle shape . . . . .	117
5.3.1	Normal impact on targets . . . . .	117
5.3.2	Impact with inclined targets . . . . .	120
5.4	Effect of particle fragmentation . . . . .	123
5.4.1	Numerical scheme for particle fragmentation . . . . .	123
5.4.2	Summary of numerical results . . . . .	124
5.5	Concluding remarks . . . . .	128
<b>6</b>	<b>Effect of sliding coating on the targets impacted by sand slugs</b>	<b>131</b>
6.1	Introduction . . . . .	132
6.2	Experimental protocol . . . . .	134
6.2.1	Slug launcher . . . . .	134
6.2.2	Silica sand slugs . . . . .	136
6.2.3	Gas gun to fire projectile . . . . .	136
6.2.4	Target design . . . . .	137
6.2.5	Temporal evolution and characterisation of slugs . . . . .	140
6.2.6	Characterisation of transmitted momentum . . . . .	140
6.3	Experimental results . . . . .	142
6.4	Simulation methodology . . . . .	145
6.4.1	Geometry of the granular particles . . . . .	145
6.4.2	The particle contact model and coupling to FE simulations . . . . .	146
6.4.3	Construction of initial granular slugs . . . . .	149
6.4.4	Generation of granular slug . . . . .	149
6.4.5	Calculation of transmitted momentum . . . . .	150

6.4.6	Material parameters . . . . .	151
6.5	Simulation - fixed coating, rigid target . . . . .	152
6.6	Simulation - sliding coating, rigid target . . . . .	152
6.6.1	Sliding coating - no interface friction ( $\mu_s = 0$ ) . . . . .	153
6.6.2	Sliding coating - with interface friction ( $\mu_s \neq 0$ ) . . . . .	155
6.7	Simulation - sliding coating, deformable target . . . . .	157
6.7.1	Inclined impact . . . . .	159
6.7.2	Normal impact . . . . .	162
6.8	Conclusion . . . . .	162
<b>7</b>	<b>Conclusions and future work</b>	<b>167</b>
7.1	Conclusions . . . . .	167
7.1.1	Factors affecting the loading of structure from high speed granular aggregate . . . . .	168
7.1.2	Numerical parameters . . . . .	170
7.1.3	Sliding plate concept for load reduction . . . . .	170
7.2	Future work . . . . .	171
	<b>References</b>	<b>173</b>

# Chapter 1

## Introduction

### 1.1 Motivation

For military applications, there is considerable interest to understand the damage caused to the vehicles and personnel due to landmine explosions. Numerous studies have analysed different aspects of this problem, starting from the detonation of explosive, up to the actual damage inflicted. There is tremendous variation in conditions and many factors across all the stages of this process that affect the damage to the target, making the related studies and methods difficult to standardise. The biggest challenge to better understand this phenomenon is to decouple different aspects. In the past, many strategies have been investigated to help reduce the damage to the vehicle and occupants. These include using V-shaped hull, increasing stand-off distance, using collapsible (energy absorbing) additions and sandwich panels. Ramasamy et al. [103] used field data to confirm that these modifications do help reducing the damage. If the landmine is buried shallow under the ground, the detonation results in rapid expansion and ejection of soil. The primary loading on the target is because of this expanding soil, rather than the blast wave of detonation. The collective behaviour of densely concentrated, high velocity particles is not well established, and impedes the design of protective systems.

This thesis explores the fundamental physics of granular impact on structures using experiments and simulations. Aim is to extend the current understanding related to the mechanics of interaction between high speed granular aggregates and flat targets, studying some of the factors influencing this impact phenomenon and to guide strategies for reducing the loading on the targets. The analyses presented here considers aggregates with typical particle volume fraction of  $\approx 0.25$  when impacting the targets.

The behaviour of impact of aggregate of particles is very different than the single particle impact. For a single particle impact with the target, the rebound direction depends on the incident direction and target loading depends on the coefficient of restitution. However, when an aggregate of particles hits a target, the shape of the flow of particles is similar to

the case of a water jet impacting a target, as shown through the experiments by Cheng et al. [18]. Controlled laboratory experiments have been shown to help better characterise the evolution of granular material after explosion and support building numerical models. Park et al. [95] have shown that slugs of high velocity granular particles can be used to represent ejecta created during a shallow buried explosion. The biggest benefit of using such slugs is getting a well characterised loading.

For the research presented in this thesis, all the experiments were conducted in a laboratory setting with granular slugs similar to those utilised by Park et al. [95]. No explosives were used for the experiments. All the simulations modelling granular aggregates were performed using a discrete particle approach and the interaction with structures was modelled by combining the discrete particle method with finite element method. The two measures used in the thesis to analyse the effect on the target are its deflection and momentum transmitted from the slug.

## 1.2 Objectives

The following lists the main objectives of the research presented in this thesis:

1. Analyse some of the factors affecting the loading of structure from high speed granular aggregates.
2. Study the parameters typically used in the numerical simulations to analyse the flow of granular material before and during the impact with the target.
3. Explore and extend the concept of adding sacrificial sliding plates as a strategy to reduce the target loading.

For the first objective, the factors studied includes those of the target such as stand-off distance, target inclination, target surface properties; and of the properties of particles in the soil such as their shapes and breakage during impact. The dependence on stand-off distance and inclination of the target has been well researched and this thesis adds to the knowledge of fundamental physics behind it. For the dependence on target surface properties, the thesis reveals new phenomenon for the case of target impacted by granular slugs. The dependence on particle shape and their fracture are also original discoveries in this thesis, discussing how properties of the soil affect the loads imposed on structures. It also underlines the shortcomings of widely used spherical shape approximation used for modelling particles.

The second objective aims to pin down the most influential parameters for realistic prediction of results using discrete particle methodology, which is a popular approach to model granular systems. This method is coupled with finite element method in the thesis to show how it can be used to model the complete process of initial impulse, flow

of particles and their interaction with the structure. A novel method is demonstrated to model the non-spherical particles and their fracture.

For the third objective, original contributions are the controlled experiments to confirm the benefits of using the sliding plate concept and the simulations to extend this knowledge to deformable targets.

## 1.3 Thesis outline

This topic of research has been explored by many researchers and various approaches have been used. The relevant literature is reviewed in **Chapter 2**. The chapter discusses overall process of landmine explosion and then delves into the factors affecting the damage to the vehicle. Focus is on the work related to impact of granular aggregates on structures. Research related to various strategies used to reduce the damage to the structure are discussed. The experimental and numerical methodologies used in previous work are also discussed to drive the justification of the approach used for analysis in this thesis.

**Chapter 3** presents a numerical study analysing and extending the experimental observations by Uth et al. [126] for impact of granular slugs against normally oriented deformable beams. The emphasis is on the detailed analysis of temporal evolution of slugs before structural impact and the dependence of structural response on stand-off distance. The numerical parameters critical for realistic prediction of generated slug are established. The influence of stand-off distance is already known and using numerical analysis, the beam deflections for different stand-off distances are benchmarked to give insight into mechanisms and assess the fidelity of numerical approach. This builds the foundation for simulations used in the proceeding chapters.

The properties of the impacted surface can have significant influence on the loads transferred from the impact of granular aggregates. This is studied in **Chapter 4**, where surface properties of rigid stationary targets are varied by applying coatings having different surface hardness and roughness. Experiments and simulations are used to obtain momentum transmitted to the targets with different coatings and it is shown that surface properties affect the frictional loading, which changes the transmitted momentum. In addition to studying the effect of surface properties, it is shown how the orientation of the target and water saturation in slugs make a difference. An intriguing discovery made in this study is that if the particles of the slug are approximated as spheres, the simulations are unable to accurately predict the experimental results.

This need to appropriately parametrise the particle shape in the simulations is explored in **Chapter 5**. This chapter contains a numerical study to analyse the effect of grain shape and fracture on the interaction of slugs with rigid stationary targets. The non-spherical particles are constructed by combining multiple spherical sub-particles. It is shown how the particle shape changes the frictional loading on the target and flow of the granular

aggregate. The fracture of particles during impact also changes the shape of particles, which is shown to influence the target loading.

**Chapter 6** is the final technical chapter where a concept of applying sacrificial coatings on target surface is analysed as a means to reduce the target loading. Experiments as well as simulations are used. The experiments with rigid targets are conducted utilising the setup of experiments in Chapter 4 with the difference being a lubricant gel applied between the coating and the target surface. This allows the coating to slide on the target surface during the impact with the slug, resulting in a change in target loading. Simulations are used to extend this understanding to the deformable targets and also analyse the effect of target inclination.

**Chapter 7** summaries the findings in this thesis and suggests future work.

## 1.4 Published work

- Chapter 3: Published in *Mechanics of Materials*, Volume 116 (2018), Pages 90–103.
- Chapter 4: Published in *International Journal of Impact Engineering*, Volume 103 (2017), Pages 90-106.
- Chapter 5: Accepted for publication in *European Journal of Mechanics/A Solids*, 2018.
- Chapter 6: Manuscript under preparation.

# Chapter 2

## Literature Review

This chapter reviews the literature relevant to the research presented in this thesis, which is to study loading of structures by high speed granular material. Granular loading on structures is of significant interest for many applications. The work in this thesis is motivated by the importance of this topic to shallow-buried landmines, where the damage to the structure is caused by the soil ejected due to the explosion. The broad theme of the research presented in thesis is to investigate the fundamental physics of granular impact on structures and strategies to reduce the damage to the structure. In this chapter, the explosion process is first discussed briefly. The main emphasis while reviewing the literature is given to the work related to dynamic impact of an aggregate of particles on structures, discussing various factors that affect the loading of structure and the strategies used to reduce the damage. The literature relevant to experimental and numerical methodologies is also discussed.

### 2.1 Introduction

A landmine is a device that is placed on or under the ground and explodes by application of pressure. These explosive devices cause damage to the vehicles and/or personnel, and can be used for both attack and defence strategies. There are two broad categories of landmines viz. Anti-vehicle - used to damage vehicles and inflict injury to the occupants, and Anti-personnel - used directly against humans, rather than the vehicles. The damage from landmines is not limited to casualties and injuries from explosion, but it can also close transport routes, obstructing the movement of goods and relief supplies. Ramasamy et al. [103] discussed two approaches to tackle the threat from Anti-vehicle landmines: (i) Removing the mines by deployment of demining teams. This process is both resource and time intensive, with the associated risk of death and injury to the workforce, and (ii) Developing mine resistant vehicles capable of shielding the effects of explosion from the vehicle occupants.

In general during a landmine explosion, the bottom of the vehicle is exposed to the blast. The transfer of momentum from explosives and ejected sand to the vehicle is a very rapid event and usually completes within a few milliseconds, resulting in high loads on the vehicle and causing injuries [85]. The damage to the vehicle depends on various factors including:

- Properties of explosive charge and detonation products.
- Depth of burial of the landmine.
- Properties of soil material surrounding the landmine.
- Stand-off distance: between the top surface of the soil and bottom of the vehicle.
- Properties of the bottom of the vehicle.

To improve the impulsive load resistance of the vehicle underbody structures, various strategies have been proposed, such as (i) replacing the monolithic underbody by sandwich panels [30, 79, 108, 127], (ii) increasing the stand-off distance of the vehicle floor from the ground [30, 11, 56, 98], and (iii) inclining the underbody with respect to the ground by making use of a V-shaped hull design [2, 7, 37, 41]. This chapter reviews the literature on some of the factors listed above that affect the loading on structure and protection strategies, with emphasis on the aspects relevant to the work presented in ensuing technical chapters.

## 2.2 Characteristics of landmine blast

The mechanism of a landmine blast can be divided into various phases [27, 102–104]. These are illustrated in Fig. 2.1 [104] and summarised below:

1. Mine is triggered due to the pressure caused by the vehicle.
2. The explosive in the mine detonates and there is a chemical reaction.
3. Shock wave is created because of detonation of explosives.
4. The gases at high pressure and temperature expand rapidly.
5. After this stage, there may be two mechanisms for inflicting damage, depending on the location of mine relative to the soil top surface:
  - If the landmine is not buried in soil (i.e. laid on the surface) then the blast wave and detonation products damage the vehicle.
  - If the landmine is buried in soil, then the soil is ejected because of the blast wave and this ejected soil contributes to the damage of vehicle.

The shock wave due to detonation interacts with the surrounding soil [8, 124]. When this shock wave reaches the top of the soil surface (i.e. the interface of soil and air), most of it is reflected back into the soil because of the mismatch in acoustic impedance between

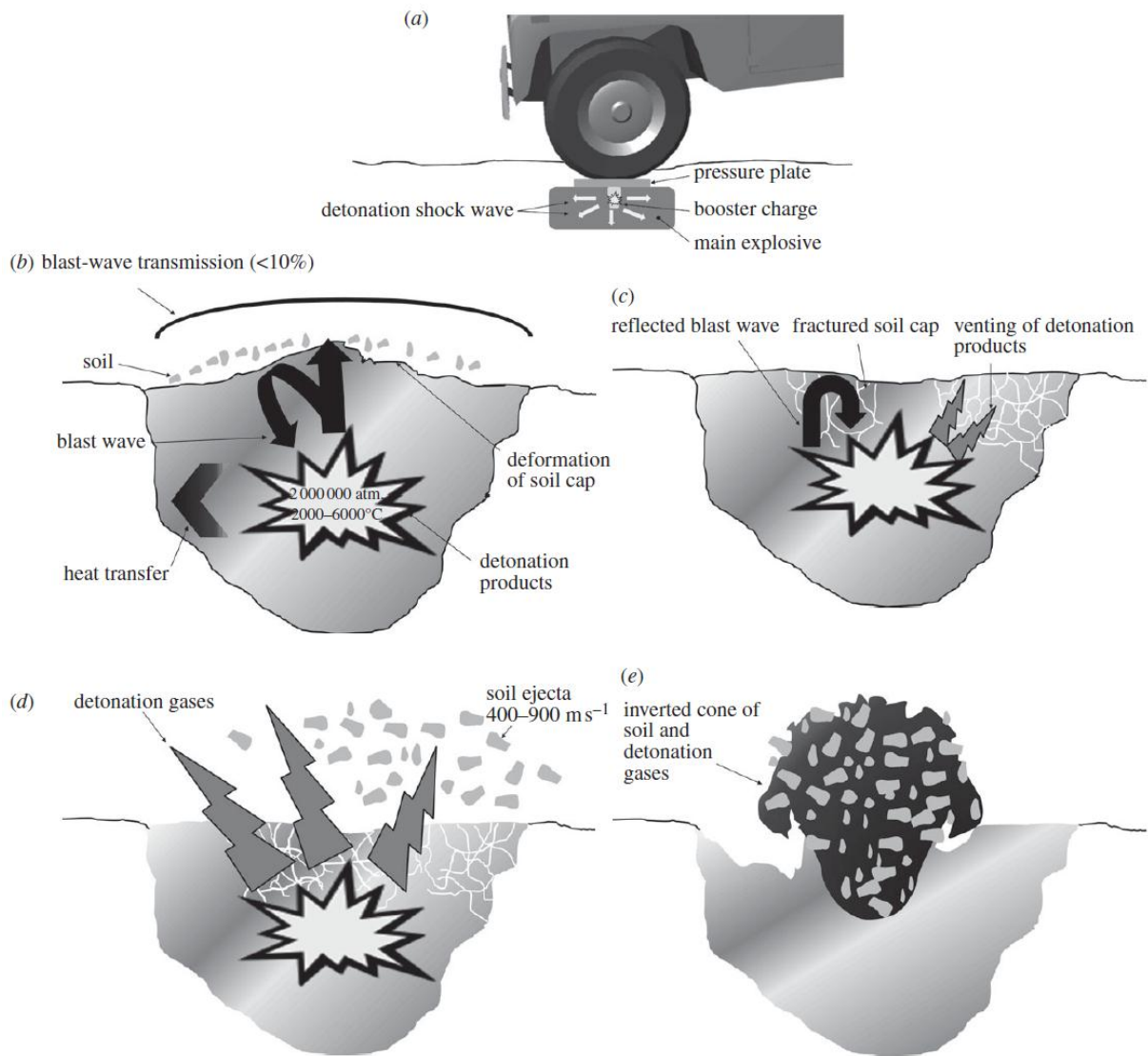


Fig. 2.1 The physics of a mine blast [104]. (a) Mine is triggered by the vehicle and explosive is detonated. (b) Blast wave is partly transmitted and remaining reflected from the soil surface. (c) The soil cap is disturbed and (d) the detonation products exit the soil. This results in the ejection of soil (e) the damage to the vehicle can be potentially because of detonation gases and ejected soil.

the two media [7, 27, 106], with the remaining transmitted into the air. The transmitted shock wave is more relevant if the target is very close to the soil surface such as wheel of the vehicle [42]. However, when the target is located at a distance, most of the loading of the target is because of the impact of the ejected soil [33]. If the landmine is buried too deep, all the energy from the explosives may be absorbed by the surrounding soil, without having any effect on the top surface of the soil and no damage to the vehicle.

## 2.3 Effect of depth of burial

Depth of burial is defined as the vertical distance between the top surface of the soil and location of landmine. The two extreme scenarios are identified [53, 27] as:

- Camouflet scenario: No soil ejection takes place and there is no significant blast wave generated at air/soil interface. This is when the depth of mine burial is large and the energy of detonation products is absorbed by soil compression and deformation.
- Surface detonation: In this case, very little energy is transmitted to the ground and the deformation of nearby structures is mostly because of the detonation products and air shock.

Between these two extremes, there is a broad range of scenarios where most of the available energy from detonation is converted to the kinetic energy of soil, generating an ‘ejecta’. Experimental as well as numerical studies [7, 27, 33, 96, 98, 106] have shown that compared to surface laid explosives, shallow-buried explosives result in higher impulse transmission and larger deflections of the afflicted structure. This increased severity of loading has been attributed to the impact of the granular media that is ejected by the expansion of detonation products.

Bergeron et al. [8] did two series of experiments for shallow-buried landmine explosions with C4 explosives. They used flash x-ray to photograph the motion of soil surface. In Fig. 2.2, the height of the ejected sand is presented as a function of time for the two series of tests performed by Bergeron et al. [8]. For each series, the comparison can be made between the tests with 8 cm and 3 cm depth of burial. It is clear that for a smaller depth of burial, the movement of top of the soil is faster compared to the case with a large depth of burial.

Taylor et al. [117] used laboratory scale explosives buried in saturated sand and examined pressure loading on a flat plate. They found that the impact of soil directly above the charge has an important role in loading. It provides half of the total impulse and acts on a relatively small area of the target, while the remaining of the impulse is because of crater ejecta as crater grows. Zakrisson et al. [138] performed experiments to measure deformation of flat plates and impulse transferred from landmines. They found that the impulse on a flat plate increases with the depth of burial. Through a numerical study of impulse and pressure on a generalised armour structure, Peles et al. [96] found that a buried charge results in higher damage compared to a charge on the surface. They also found that the other parameters such as stand-off, soil type and properties of charge have a significant effect on the load applied to the armour. An effect of depth of burial was also observed by Pickering et al. [98], who did an experimental and numerical investigation of steel plates in case of landmine buried in dry sand. They studied the effect of depth of burial, stand-off distance and mass of explosive and showed that the impulse transferred to the plate increases with the depth of burial. The deflection of the plate reaches maximum

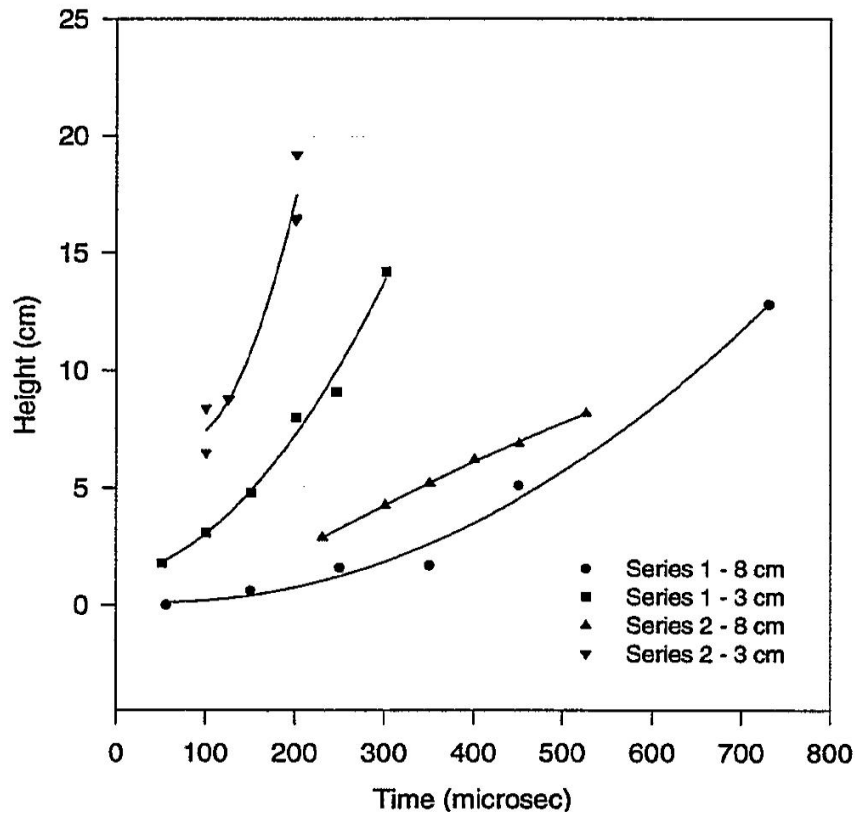


Fig. 2.2 Height of ejected soil for two series of tests, each with two different depth of burials - 3 cm and 8 cm [8].

at a particular depth and then decreases with further increase in depth of burial (Fig. 2.3). This particular depth of burial was found to be independent of the mass of explosive.

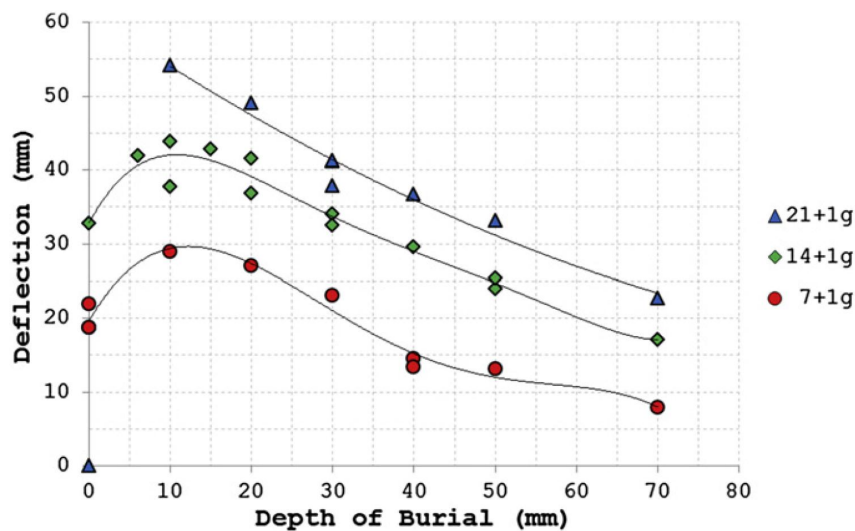


Fig. 2.3 Midpoint deflection vs. depth of burial for 47 mm stand-off distance [98].

Fairlie and Bergeron [33] discussed a methodology for numerical modelling of mine blasts where the explosive can be either placed on the surface or buried under the soil. Fig. 2.4 shows their results for momentum transmitted to the target for a test with buried landmine. The 'blast only' curve shows the momentum transmitted by the mine blast

without an effect from the ejected sand. ‘Fully coupled’ is the result when the effect of ejected sand is included in the calculations. Their observations show that about 38 % of the total transmitted momentum is because of the detonation products and 62 % is caused by the ejected soil. The amount of ejected soil that actually impacts the target depends on factors such as stand-off distance and target size. Genson [42] performed experiments for loading on a target plate from the blast of a buried charge to analyse different loading mechanisms and found that most of the total impulse has a contribution from ejected soil.

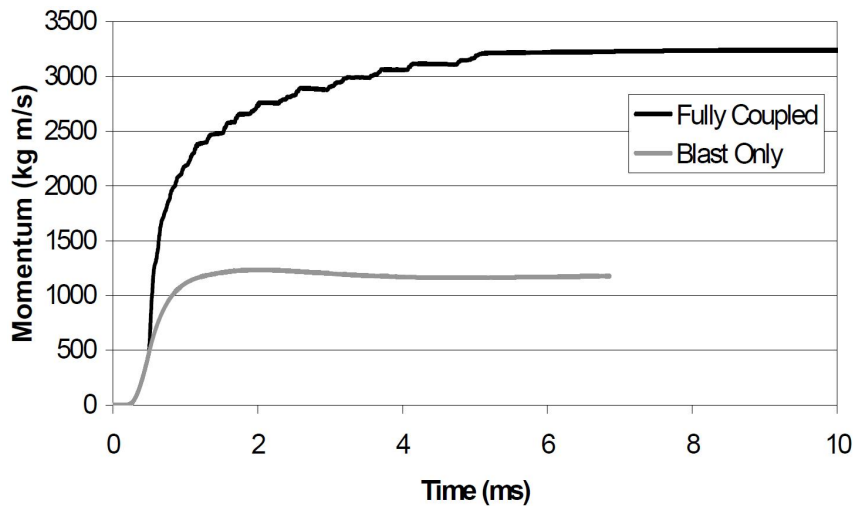


Fig. 2.4 Momentum transmitted to the target from the blast load Fairlie and Bergeron [33].

A numerical study was done by Laine et al. [75] to compute the impulses from landmine detonation for different types of burial and using two different types of soil material namely sand and saturated clay. They found that the incident impulse from the explosion is focussed more above the landmine in case of buried charges than for the mines that are laid on the surface. Pickering et al. [97] also did an experimental investigation of height of burial of the charges on a steel plate, where the height of burial is defined as the distance of explosive from the base of the rigid ground. The material above and below the explosive is the soil material. Fig. 2.5 shows the results from their study where the transferred impulse is shown to decrease with the increase in height of burial (HoB in the figure).

## 2.4 Effect of stand-off

The distance between the explosive and structure is called as the stand-off distance. This distance has a considerable effect on the blast loading of the structure. The intensity of loading on the structure with smaller stand-off distance is higher than those at larger stand-off. In the context of landmines, stand-off is equivalent to ground clearance, defined as the distance between target and soil, and is critical in developing the protection [16]. The effect of stand-off is widely available in literature. Tests conducted by Snyman et al. [113] with large full scale buried charges show that the impulse decreases with increase

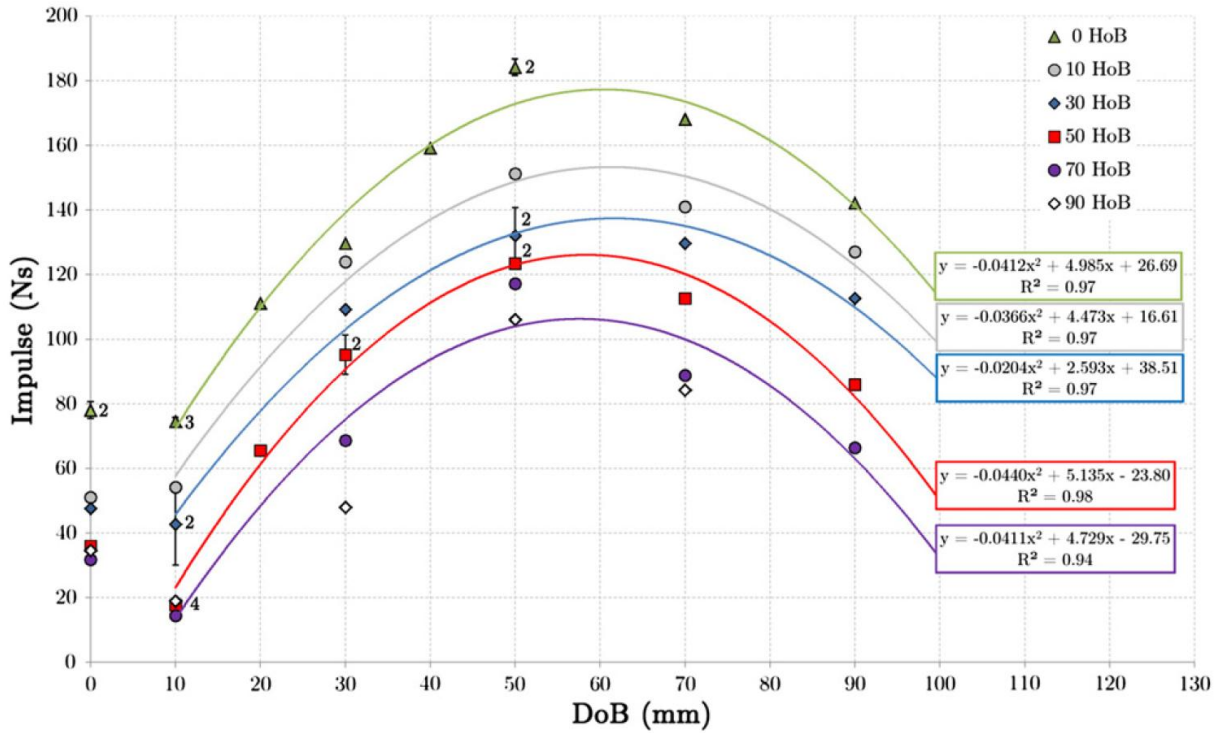


Fig. 2.5 Graph of impulse vs. depth of burial (DoB) for 14+1g PE4 charges at multiple heights of burial (HoB) with a constant stand-off distance (SoD) of 47 mm [97].

in stand-off distance, as depicted in Fig. 2.6 [113]. They also showed the difference due to different amounts of explosives used. Experiments conducted by Taylor et al. [118] and McShane et al. [82] also confirm that if the stand-off is increased, it increases the loading time and reduces the pressure from ejected soil on the targets. A reduction in momentum transferred to the target with increasing stand-off was also shown by Anderson et al. [2]. Rimoli et al. [108] and Dharmasena et al. [30] studied impact from a spherically expanding sand shell and found that damage to the target decreases with increasing stand-off distance (Fig. 2.7). Fourney et al. [38] studied the effect of target size (area of loading) by keeping the stand-off constant. They showed that transmitted momentum increases with an increase in the loaded area and then converges after a sufficiently large area has been achieved. In this thesis, the effect of stand-off is studied in order to obtain a better understanding of the effect observed by Uth et al. [126].

## 2.5 Effect of soil properties

There is extreme variation in the types of soil that can be considered for buried explosions, which makes their characterisation difficult for such applications. Some of the soil properties that can vary include density, particle size, moisture content, presence of organic matter, etc. The approach generally used is to first choose distinct types of soils and then make predictions about other types [13]. However, when changing to the soil type, more than one property may vary, making a structured analysis difficult.

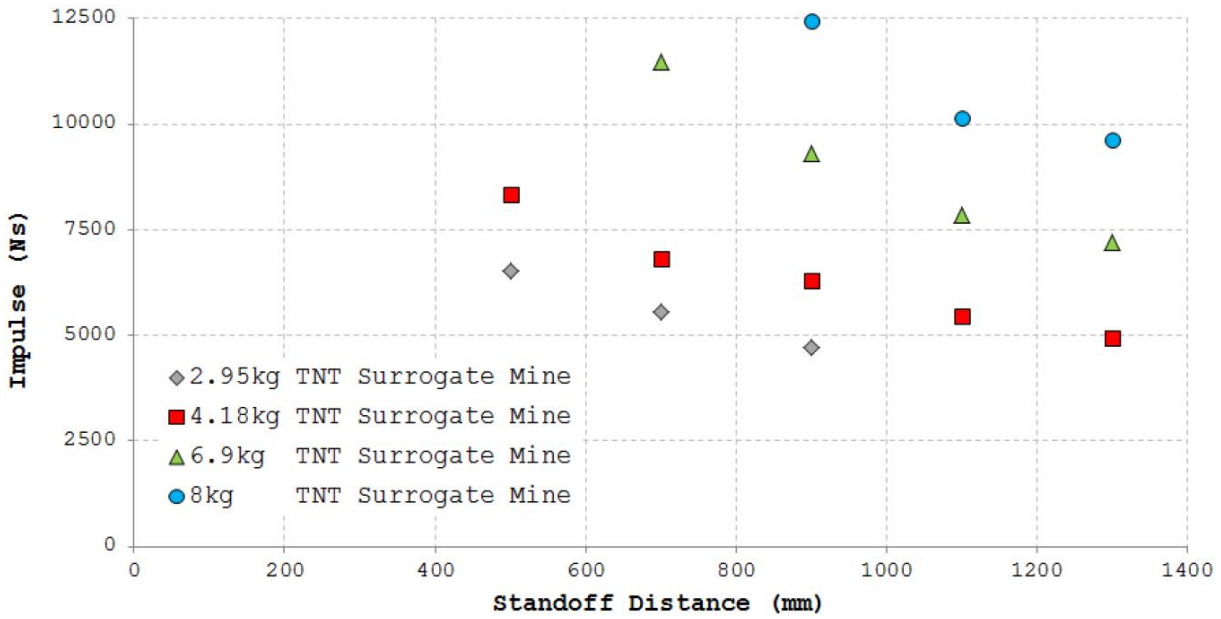


Fig. 2.6 Impulse transfer at different stand-off distances for surrogate mines buried at 50mm depth [113].

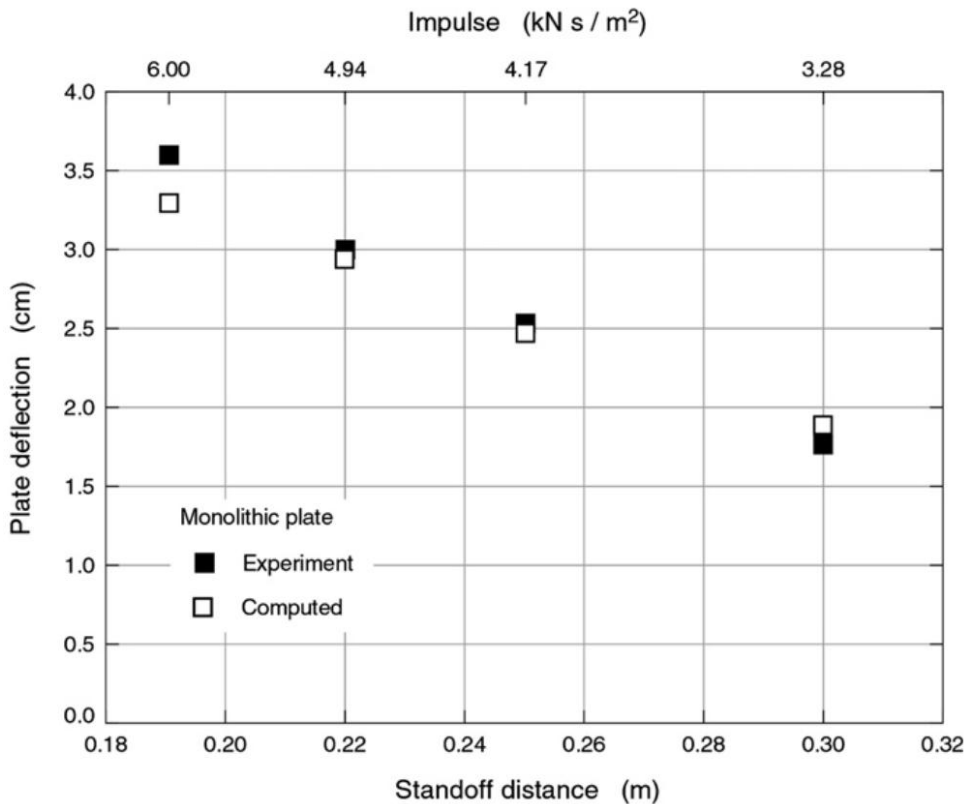


Fig. 2.7 Plate centre displacement (back face) vs. stand-off distance [108].

Through experimental measurements of energy transferred from detonation of explosive buried in two types of soil (prairie and concrete fine aggregate sand), Hlady [56] have shown that there is small difference in energy transferred to the target from these two soil types. The significance of soil type also depends on depth of burial, as demonstrated by Laine et al. [75]. They used two types of soil (sand and saturated clay) and showed that

for the mines laid on the surface, the soil type has little effect on pressure and impulse. However, when the mine is buried, the soil type plays a significant role. Rigby et al. [107] have shown that particle size distributions and soil type (sand versus clay versus gravel) strongly influences the loading imposed on structures. Ehrgott et al. [32] conducted a series of experiments with both surface and shallow buried test charges where they carefully varied the soil type and observed a significant variation in impulse loads as the soil properties were varied. This was attributed to changes in the crater volume and focusing of the ejecta by the surrounding soil bed.

There remains significant uncertainty on how properties of the soil affect the loads imposed on structures by the high velocity granular media. The work in this thesis is related some of the aspects such as water saturation and grain properties (angularity and fragmentation) and the relevant literature is discussed here.

### 2.5.1 Water saturation

One of the most important parameters studied about the soil type for buried explosions is the moisture content. Recent studies [2, 95, 125, 127] have been performed using cohesionless soil (mostly sand) with varying moisture content. These studies suggest that due to the increase in density of soil because of moisture, there is an increase in transmitted impulse to the target. Uth and Deshpande [125] performed controlled laboratory experiments for the impact of sand slugs on monolithic and sandwich beams. They measured the deflection of beams and found that an impact with saturated (wet) sand results in higher deflection of the target (Fig. 2.8). Anderson et al. [2] also found that moisture content is proportional to the momentum transferred to the target.

Fox and Lee [40] studied the influence of sand constitutive model on the blast response of rigid target using quasi-static tests and effective stress theory. They demonstrated that the materials that have lower deviatoric yield strength provided higher momentum loading of the target. For instance, water, which has no strength produced highest loading and dry sand, which has highest strength produced lowest target loading. Grujicic et al. [49] computationally analysed the effect of mine blast on a commercial vehicle structure using the set-up illustrated in Fig. 2.9a. The kinematic response of the vehicle was found to be very sensitive to the water saturation of the sand and a typical response is shown in Fig. 2.9b.

### 2.5.2 Particle shape

Different types of soil can have different particle shapes and this can affect the loading from particles to the structure. It has been shown that particle shape strongly influences the interaction of a single particle with a structure [61, 92, 93]. However, it is not clear how would the particle shape make a difference when a granular aggregate impacts the structure.

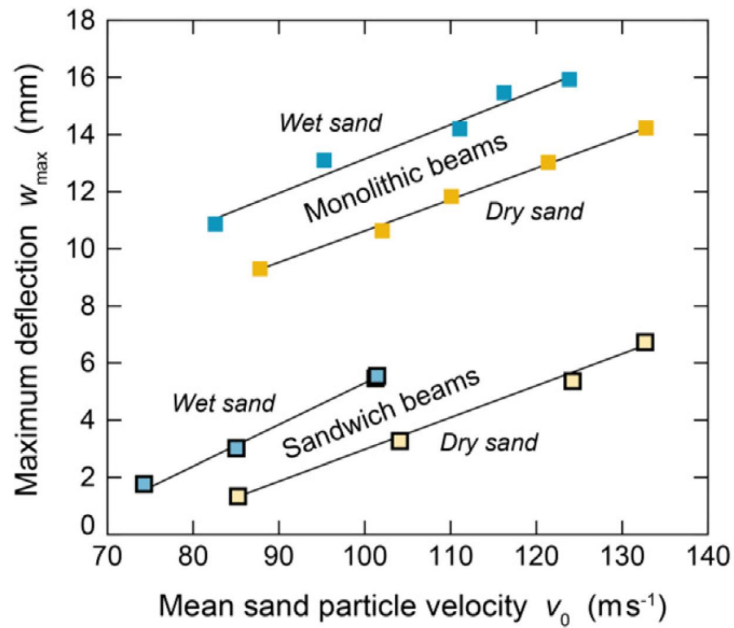


Fig. 2.8 The measured maximum back face deflections at mid-span of the monolithic and sandwich beams impacted by dry and wet sand slugs as a function of mean slug velocity [125].

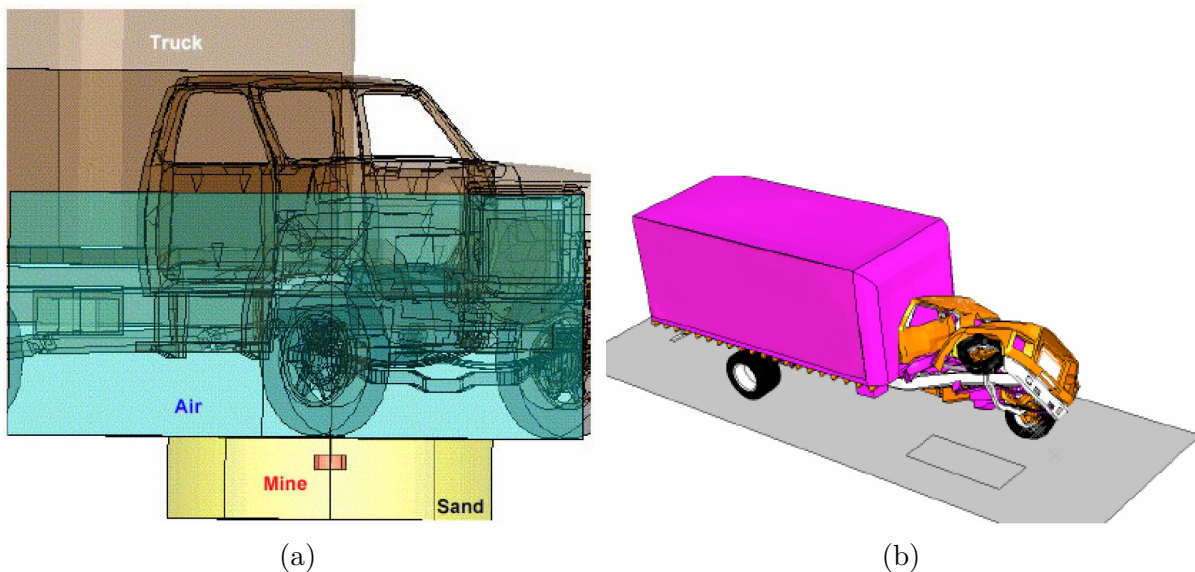


Fig. 2.9 (a) Geometrical model for mine, sand and surrounding air and (b) Truck damage at  $t=0.08$  sec from explosion of 7.5 kg C4 landmine buried 10cm in saturated sand below front right tire [49].

A spherical particle would have a different effect on the target surface as compared to a non-spherical (angular) particle, where a definition of angularity was given by Papini and Spelt [92], shown as  $A$  for a symmetrical particle in Fig. 2.10.

Hutchings [61] performed experiments and calculations for the impact of angular particles on rigid-plastic frictionless surface. He used square plates of hard tool steel, 8.0 mm square and 1.5 mm thick, weighing 0.75 g as angular particles. These plates were accelerated up to velocities 200 m s<sup>-1</sup>. Plates did not suffer permanent deformation

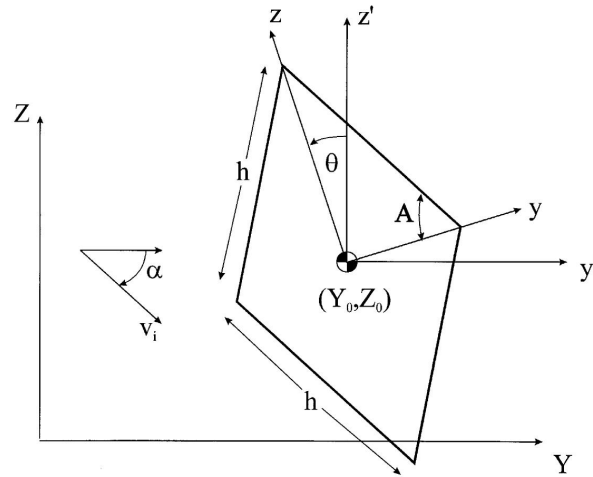


Fig. 2.10 Definition of particle angularity  $A$  [92, 93]

during impact and the target block underwent plastic deformation. The energy lost by the impacting particle, which represents the energy spent in deforming the target or removing metal from the target was found to be between 40 and 80 %. He showed that impact angle and orientation of particle influences the rotation of the particle. This in-turn affects the energy of particle and characteristics of impact crater formed.

Papini and Spelt [92, 93] generalised Hutchings' [61] work for arbitrary shape particles impacting a surface having dynamic hardness and non-zero friction. They developed a numerical model to analyse wear and cratering of rigid-plastic targets by such collisions. They modelled the effect of angle of attack, initial particle orientation and angularity, among other factors that affect the cratering of the target and embedding of the particles in the target. At high angles of attack (more towards normal impact), the particles are likely to get embedded because the particles tend to rotate less and thus less of kinetic energy would be converted to rotational energy. They also showed that more angular particles penetrate deeper than the less angular particles. Fig. 2.11 shows the trajectory of particles after impact for some specific cases. Papini and Dhar [91] performed experiments to further understand the cratering characteristics and particle rebound kinematics for different angularities of particles. Dhar et al. [28] described an apparatus for launching single angular particles of different shapes so that they arrive at the target in a known orientation.

Cho et al. [19] conducted an experimental study on effect of the shape of the particles (Fig. 2.12), packing density, stiffness and strength of natural and crushed sands. They observed that angularity of the particles is responsible for hindered rotation, higher proneness to contact damage, among other factors. This reduced rotational tendency has a significant influence on the loading of the target, as would be discussed in this thesis. Using a continuous Couette shear test, Farhadi and Behringer [34] analysed the effect of particle shape on jamming properties by experiments using disks (quasi-2D particles) of two shapes: Ellipses and circles. They showed that the long-term rheological behaviour

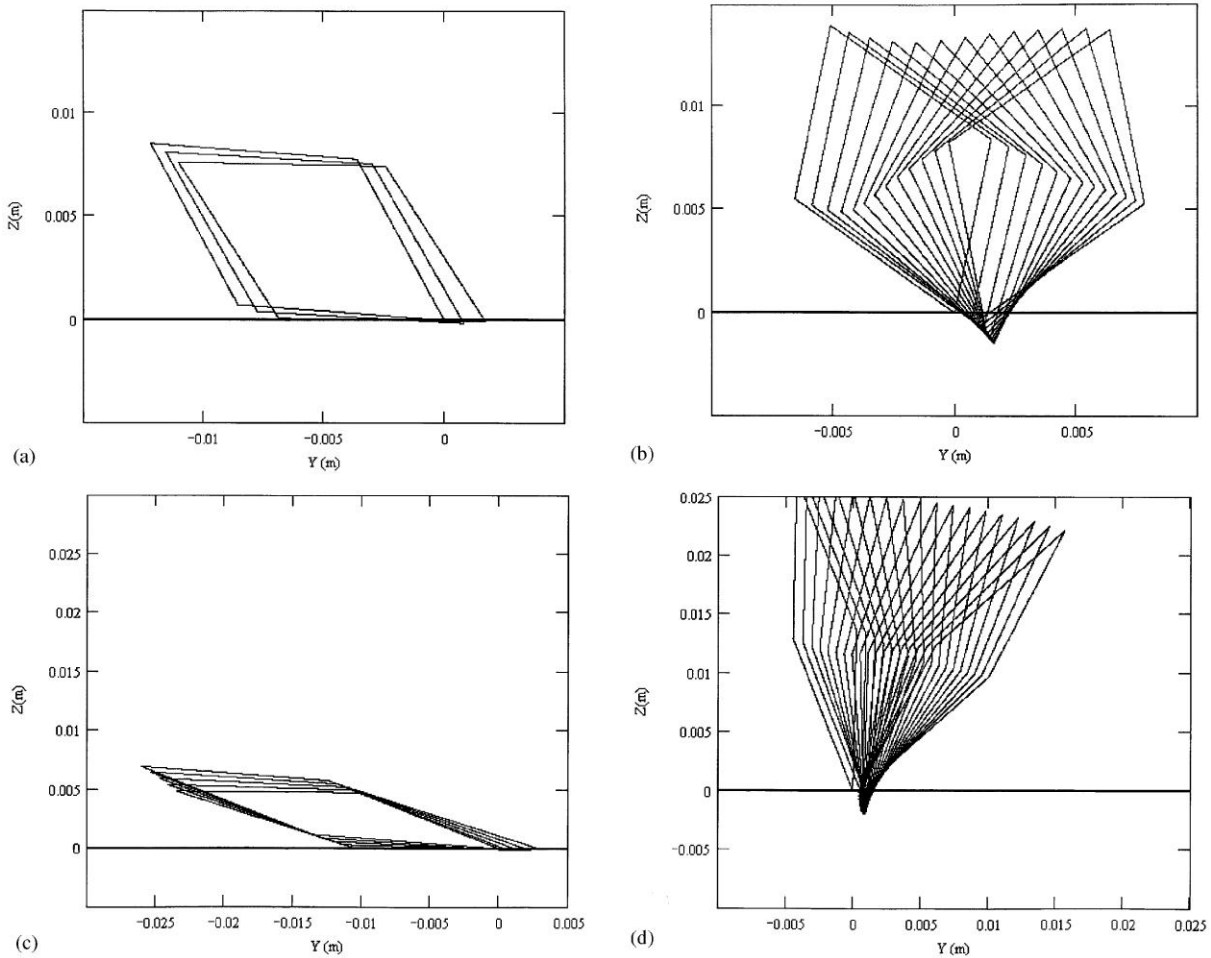


Fig. 2.11 Trajectory of angular particles after impact [93] for different angularity  $A$  and initial orientation  $\theta$  (defined in Fig. 2.10). (a)  $A = 60^\circ$ ,  $\theta = 55^\circ$  (b)  $A = 60^\circ$ ,  $\theta = 20^\circ$  (c)  $A = 80^\circ$ ,  $\theta = 75^\circ$  (d)  $A = 80^\circ$ ,  $\theta = 9^\circ$

depends on particle shape. One of the observations that they make is that the frictional forces are relaxed because of rotation of circular disks. Still, most studies on impact properties of granular media are restricted to spherical particles [46, 68–70, 136].

### 2.5.3 Particle fragmentation

The angularity of grain may not only be because of its initial shape, it can also develop due to fracture during the impact with the structure. Though, many studies are available in literature for the fracture of grains, the effect on the interaction of granular media with structure due to breakage of grains is not well understood. Parab et al. [94] did static and dynamic experiments for failure modes of individual sand particles by applying compressive load at different rates. Behera et al. [5] analysed breaking of two-dimensional circular disc by normal and oblique impact on hard plate using molecular dynamics simulations. They found that the crack pattern are same for normal and oblique impacts and depend on normal component of impact velocity. Using the breakage pattern, fragment mass and

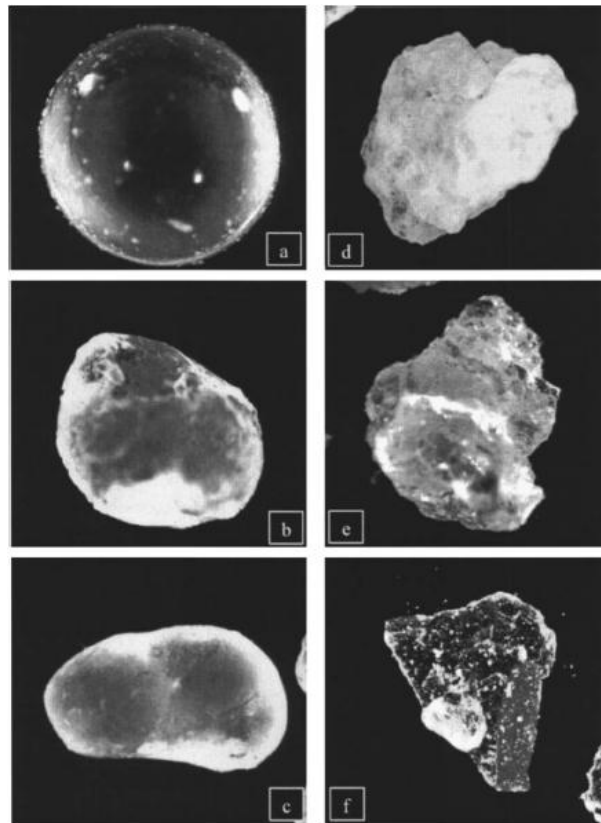


Fig. 2.12 Microphotographs showing various grain shapes used by Cho et al. [19]: (a) glass beads  $D = 0.32$  mm; (b and c) ASTM 20/30 sand  $D = 0.60$  mm; (d) Ticino sand  $D = 0.33$  mm; (e) crushed granite  $D = 0.35$  mm; and (f) fine particle from crushed granite  $D = 0.08$  mm.

velocity, they showed that there exists a critical velocity, below which, a damage cone is formed at the impact site. Over this velocity, particle fragmentation occurs and at very high velocities, the disc completely shatters: See Fig. 2.13.

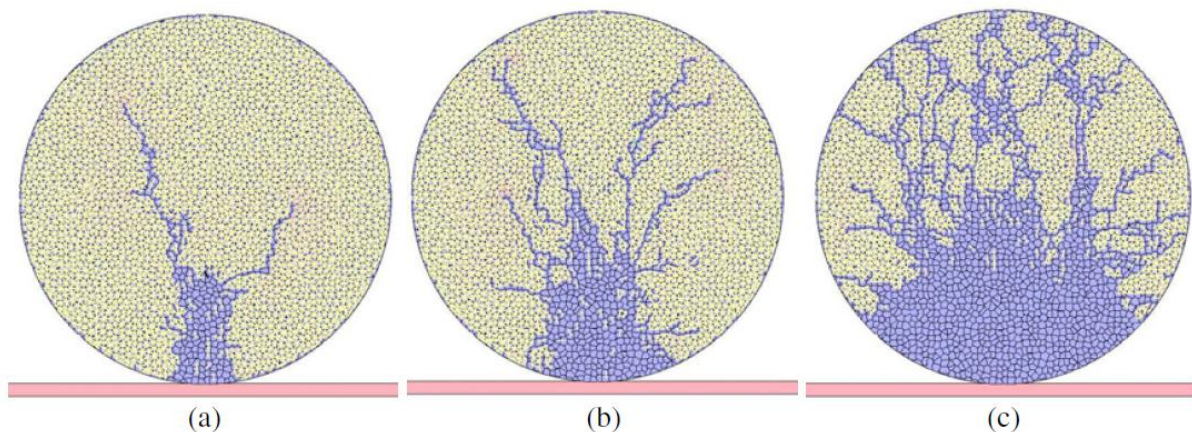


Fig. 2.13 Final reassembled states of the break-up process of a disc of radius 30 cm at different impact velocities dropped on a hard frictionless plate as analysed by Behera et al. [5]. (a)  $v_0 = 100$  cm  $s^{-1}$ . The cone is not fully developed and only a few oblique cracks are present. (b)  $v_0 = 200$  cm  $s^{-1}$ . More oblique cracks develop and travel a greater distance. (c)  $v_0 = 600$  cm  $s^{-1}$ . Both oblique cracks and secondary cracks are present.

Cil and Alshibli [21] used agglomerates of small bonded spherical sub-particles to create a particle. They showed that breakage initiates along the plane connecting two contact points on the particle with adjacent particles. Further, particle failure is effected by boundary conditions and particle interactions. Zheng et al. [139] did a numerical study of breakage behaviour of six different shapes of particle agglomerates because of impact. It is clear from their study that higher impact velocity results in more breakage of particles: Fig. 2.14. They also analysed breakage of coal sample at different impact velocities (Fig. 2.15). At low velocities ( $8 \text{ m s}^{-1}$ ), the coal does not break. At  $12 \text{ m s}^{-1}$ , it is only partly broken and at  $16 \text{ m s}^{-1}$ , it breaks into several fragments. In this thesis, breakage of particles is analysed numerically by constructing them with a combination of spherical sub-particles. It is also shown how particle breakage affects the target loading in case of impact with granular aggregates.

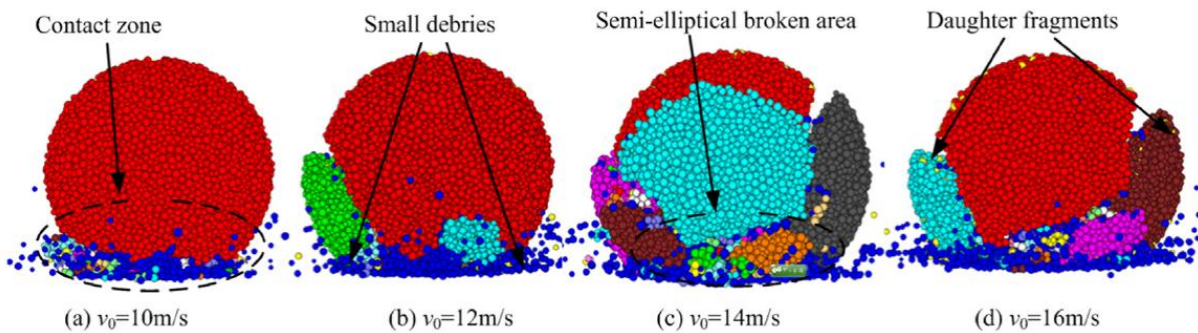


Fig. 2.14 Zheng et al. [139]: Front view of a spherical agglomerate breaking at different impact velocities.



Fig. 2.15 Zheng et al. [139]: Morphology of coal after impact at different impact velocities.

## 2.6 Effect of target properties

Modification of the underbody of the hull is an important strategy to mitigate the effect of landmine explosions. Ramasamy et al. [103] studied the data from 2122 landmine incidents to analyse the benefits of vehicle modifications on injury and casualty of the occupants. They considered a number of modifications to the vehicle and the protection they provide and used the casualty data from mine incidents to examine how the vehicle modifications have reduced fatality and injury from landmine explosions. The modifications included

V-shaped hull, increased ground clearance, widened axles, increasing the weight and using blast deflector. They show that each of these designs can have significant effect on fatality and injury rates from AV (anti-vehicle) land mines. In this section, the literature reviewed is based on some of the modifications.

### 2.6.1 Target inclination / V-shaped hulls

For military application, using a V-shaped vehicle hull is a popular method to mitigate the landmine blast by deflecting the pressure wave and the loads. If the ejecta launched by a buried explosion is brought to rest by a flat rigid target whose surface is perpendicular to the direction of granular impact (Fig. 2.16a), the full normal component of its momentum is transferred to the target and the target is subjected to the stagnation pressure associated with bringing a fluid to rest [27, 95]. The V-shaped hull has two halves that can be considered as targets inclined to the incident wave (Fig. 2.16b). The applied pressure is divided in vertical and horizontal components, where the horizontal component has little effect on the impulse transferred to the vehicle. Hence, by deflecting a part of the incident impulse, the energy transmitted to the target is reduced. There is considerable evidence that V-hull construction significantly enhances the survivability of vehicles subjected to impulsive loading from buried explosions. Some known armoured vehicles with V-shaped hulls include Buffalo MRAP, International MaxxPro MRAP, Casspir and Cougar H. Performance of V-shaped hull against landmines show that simple and easily manufactured modifications can have significant effect on the outcome [103].

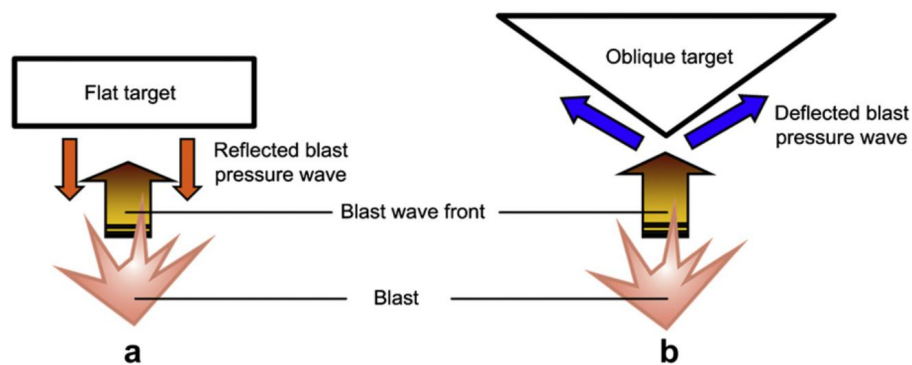


Fig. 2.16 Schematics illustrating assumed blast target interactions [20].

Kleis and Hussainova [70] studied the effect of impact angles using glass and hardened steel spheres impacting against targets of different materials. This angle is defined as the angle between the target surface and the moving particle. So, an angle of  $90^\circ$  is for perpendicular impact. The variation of normalised energy absorbed against impact velocity for different angle of impacts is shown in Fig. 2.17 [70]. The curves 1, 2 and 3 are for impact angles of  $60^\circ$ ,  $45^\circ$  and  $30^\circ$ , respectively. As the impact angle decreases, the target surfaces becomes more aligned to the incident direction of the particle, resulting in a decrease in the energy absorbed. This is because for lower angle of impact, the rebound velocity of the

particle would be lesser, while it slides and rolls on the surface. This definition of angle of impact is similar to the angle of inclination used in this thesis. Additionally, the decrease of momentum transmitted with decreasing inclination is observed in the experiments and simulations presented in this thesis.

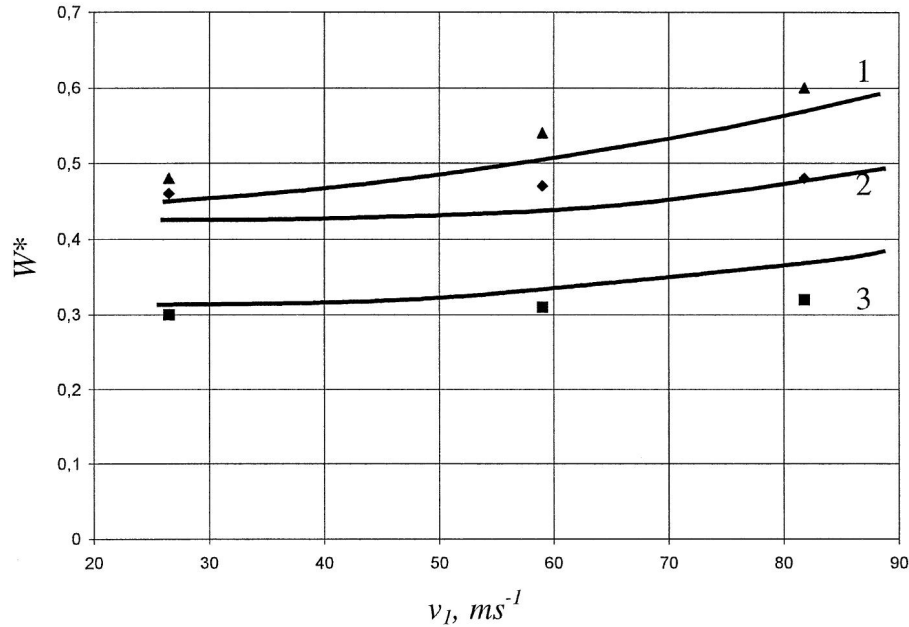


Fig. 2.17 Variation of normalised energy absorbed against impact velocity for steel target [70]. The three curves are for decreasing (1 to 3) impact angles.

Experiments [2, 39, 41, 109] suggest that the momentum transferred from the ejecta into an inclined rigid or V-shaped target is less than that transferred into a normally oriented target. Uth et al. [126] reported detailed laboratory scale measurements of all the components of the momentum transmitted into inclined monolithic and sandwich beams impacted by granular slugs comprising tungsten carbide particles to analyse the effect of inclination and stand-off of beams. High speed images of experiments by Uth et al. [126] with inclined target are shown in Fig. 2.18. These detailed measurements showed that the resultant momentum transmitted into the inclined targets was less than that for the normally oriented counterparts. Benedetti [6] and Follett et al. [37] have reported similar findings for V-hulls made from Aluminium sheets and composite materials, respectively. A numerical investigation of blast effects on vehicular structures done by Gurumurthy [54] also showed that V-shaped hulls provided best performance to reduce the peak head-on impulse. Chung Kim Yuen et al. [20] analysed the deflection of V-shaped plates under localised blast load. They presented experimental and numerical analysis with different included angles, demonstrating that smaller included angle deflect more gas pressure reducing the mid-point deflection of the plate.

Johnson and Basudhar [65] did simulations to compare the effect of different shapes of the underbody (Fig. 2.19) along with the effect from stand-off due to shallow buried landmines. They found that for centre buried loads, V-shaped underbody target performs best in terms of reducing the impulse, compared to other shapes. In a similar study

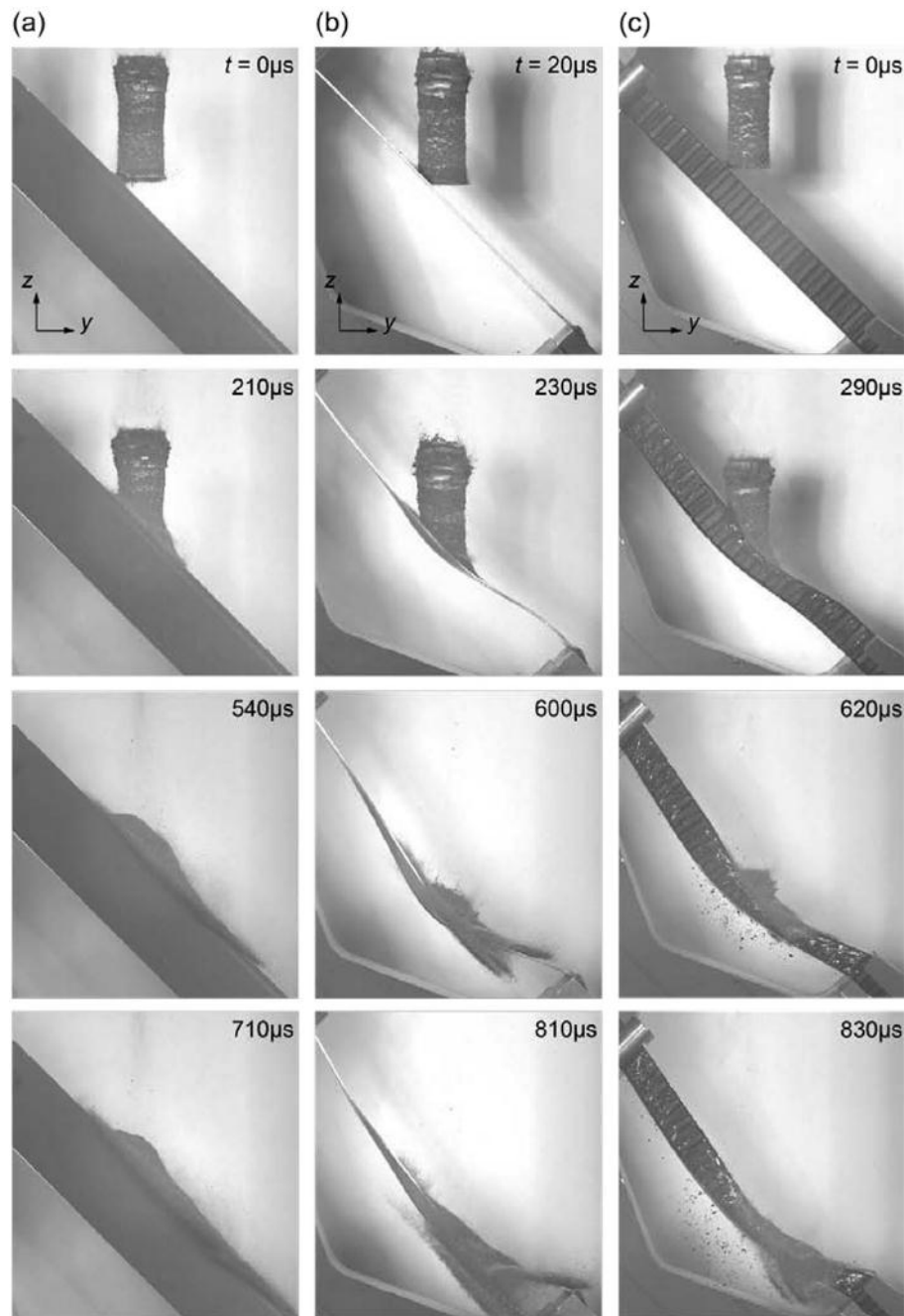


Fig. 2.18 High speed images of impact of granular slug on inclined (a) rigid, (b) monolithic and (c) sandwich beams [126]. Time  $t = 0$  corresponds to the instant that the slug impacts the beam.

using experiments and computations, Fox et al. [41] analysed different geometries (Fig. 2.20) of rigid targets for their response to buried explosions. They found that downward convex targets (a and e) perform better than the other configurations in terms of impulse imparted. Also, the configuration e performs better than a because of smaller included angle. There was no significant difference between the transmitted impulse between the geometries b, c and d.

Tremblay [123] developed an analytical model to study the V-shaped target as a blast deflector. The model was based on empirical equation proposed by Westine et al. [135] to

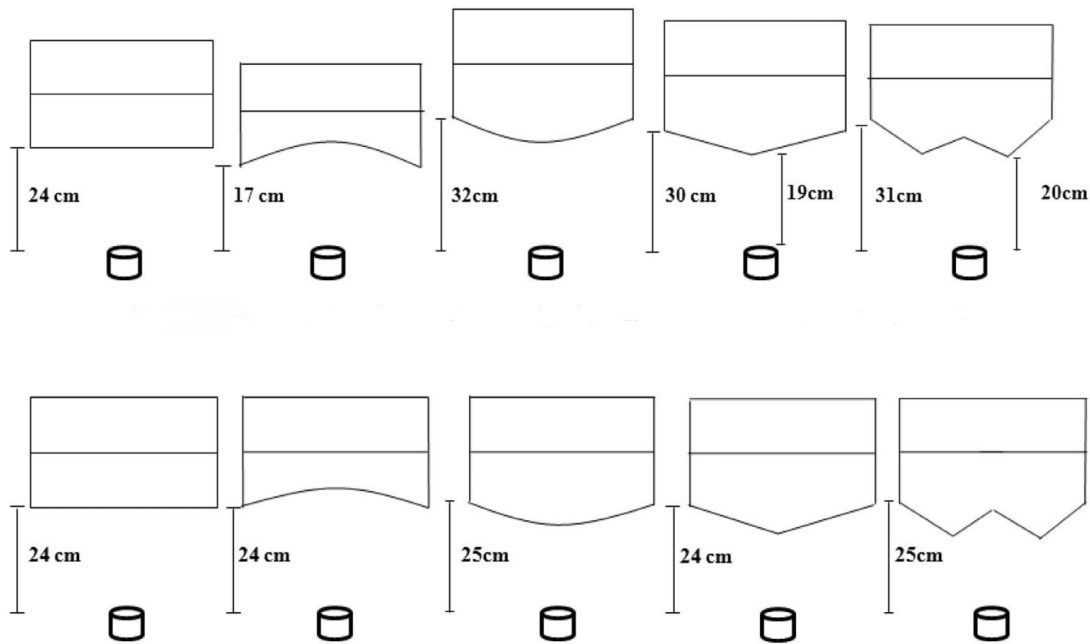


Fig. 2.19 Geometries of the targets analysed for effect from shallow buried landmines [65]. The position of centre of gravity of the targets is vertically aligned.

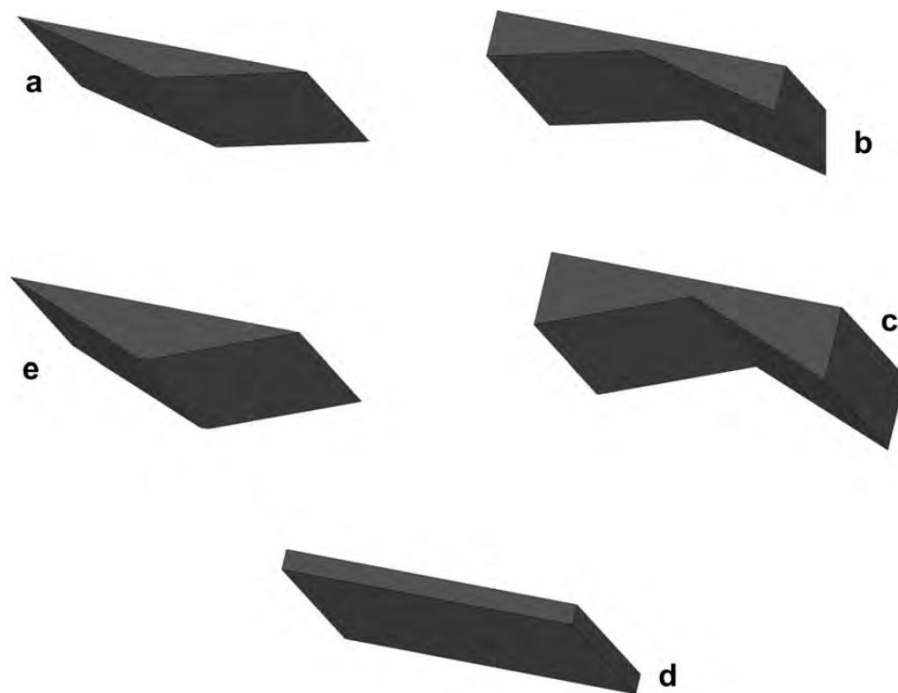


Fig. 2.20 Target plate geometries analysed by Fox et al. [41]: (a)  $13^\circ$  convex down; (b)  $13^\circ$  concave down; (c)  $21^\circ$  concave down; (d) flat; and (e)  $21^\circ$  convex down.

predict the vertical component of the specific impulse for buried charges having a pancake shape. They found that the transmitted impulse increases as the included angle  $\gamma$  is increased as shown in Fig. 2.21.

Anderson et al. [2] performed a series of experiments using flat and V-shaped targets under shallow-buried blast loading. The V-shaped target with  $90^\circ$  is illustrated in Fig. 2.22.

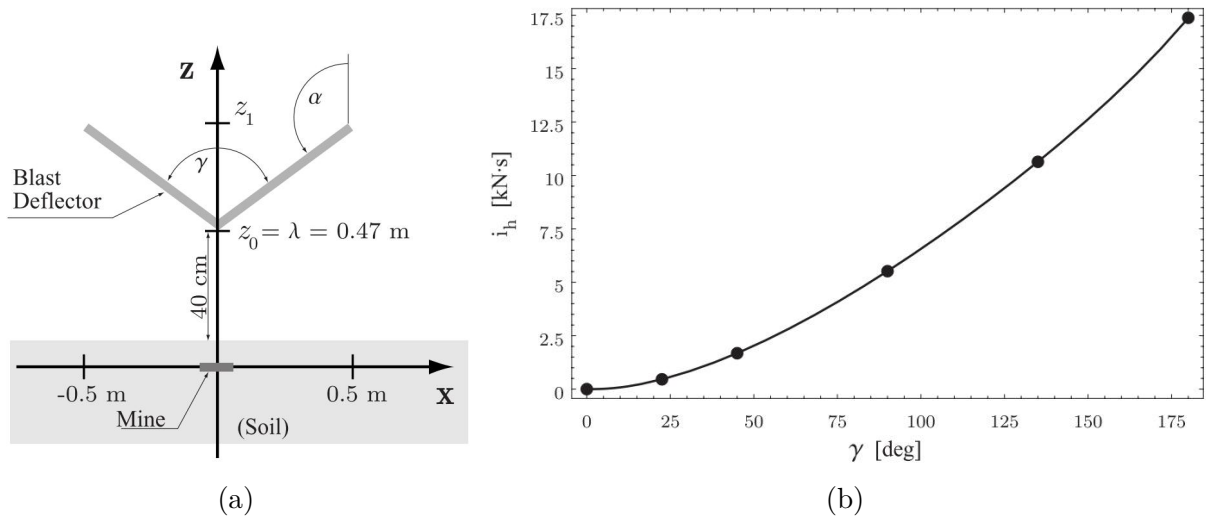


Fig. 2.21 (a) V-shaped blast deflector centred above the mine and (b) Impulse as a function of included angle  $\gamma$  [123].

They also varied the angle of V-shape along with soil moisture and stand-off distance. Their experiments show that V-shaped targets have lesser momentum transferred than the flat bottom. Additionally, the sharper is the V target, the lesser is the momentum transferred. This was attributed to the fact that sand and explosive products not longer stagnate against the plate and can flow along the plate's surface. Because of V-shape, the lower portion of V is closer to the sand surface above the charge. Even then, the performance of V is better.

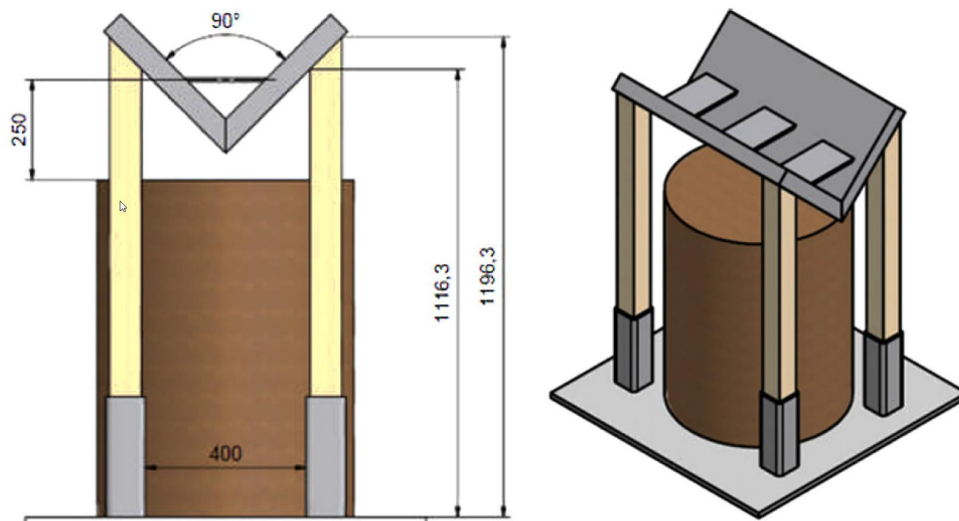


Fig. 2.22 Schematic configuration for the 90° interior angle steel plate experiment performed by Anderson et al. [2]. It has 25 cm stand-off between plate centre of gravity and top of sand (figure dimensions in mm).

An important question considered to analyse the benefit of V-shaped hull design is the included angle of V-shape. It is understood that a more acute angle of V would increase the proportion of deflected blast wave. However, this creates a problem with centre of gravity of the vehicle shifting too high, in order to keep the ground clearance. If the centre

of gravity is brought down, the ground clearance may be reduced, bringing the hull closer to the blast. The real field data from landmine incidents analysed by Ramasamy et al. [103] show that despite the reduction in ground clearance, V-shaped hull (as illustrated in Fig. 2.23) design does provide protection.

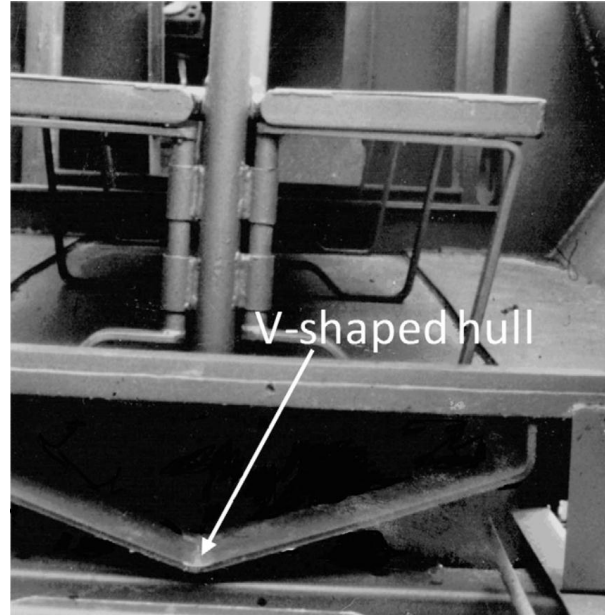


Fig. 2.23 Cross-sectional view of a V-shaped hull, welded on the chassis of commercial truck [103].

### 2.6.2 Surface properties

During the impact of the granular aggregate with the structure, a large fraction of particles impact the target and move along its surface. The amount of frictional loading on the target depends upon properties of the impacted surface and hence the properties of the structure surface play a significant role on the overall loading. In case of a target oriented perpendicular to the incoming granular flow, the symmetry of the impact situation implies that friction does not affect the resultant transmitted momentum. However, friction is expected to influence the momentum transfer when symmetry of the impact geometry is broken. Uth et al. [126] reported measurements of momentum transmitted into inclined monolithic and sandwich beams impacted by granular slugs comprising tungsten carbide particles. They found that the momentum transmitted into the inclined targets was significantly higher than that anticipated from a “water jet” like impact analysis [18, 64] which neglects friction between the granular particles and the target.

A study on particle-target impact was done by Chen and Hutchinson [17] where they analysed the damage because of a foreign object impact on turbine blades. They used spherical particles impacting a thick elastic-plastic target. Their study showed that ricochet velocity of the particle depends heavily on the elasticity of the target. The depth and width of indent are primarily dependent upon the kinetic energy of the particle and yield

strength of the target material as shown in Fig. 2.24 [17]. The indentation also depends upon the rate-dependency of the target material properties.

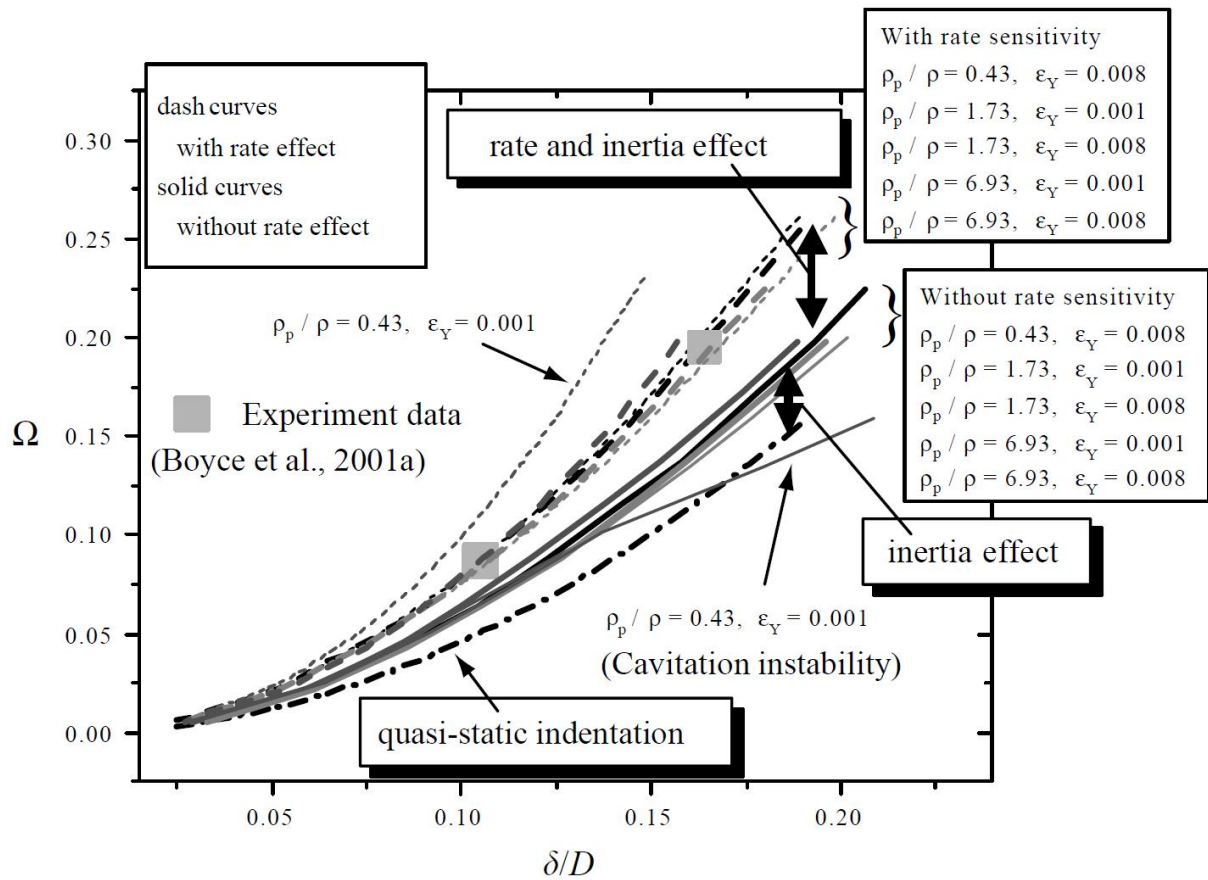


Fig. 2.24 Residual indentation depth  $\delta/D$  as a function of normalised kinetic energy of the particle  $\Omega$  [17].

The effects of friction on the motion of hard spherical particles on an inclined surface was analysed by Kondic [71]. He found that properties of particulate system are influenced by the interaction between particle and target. Even if the collisions are elastic, sliding has a significant influence on the momentum of the particles. Kleis and Hussainova [70] studied the impact of glass and hardened steel spheres against targets of different materials. They analysed the variation of coefficient of restitution with impact velocity, impact angle and target material properties using an energetic impact theory. They showed that the coefficient of restitution decreases with increase in impact velocity (Fig. 2.25). It also decreases if the hardness of the target material is reduced. These observations demonstrate that there is larger plastic deformation of the target if the impact velocity is increased and if hardness of the target is decreased. Hutchings et al. [62] studied the impact of hardened steel spheres against ductile mild steel targets: the contact forces and impact angle  $\alpha$  are shown in Fig. 2.26. They showed that as the impact velocity increases, the volume of the crater formed increases (Fig 2.27a). Also, if the impact angle is increased, the loss of kinetic energy increases (Fig 2.27b).

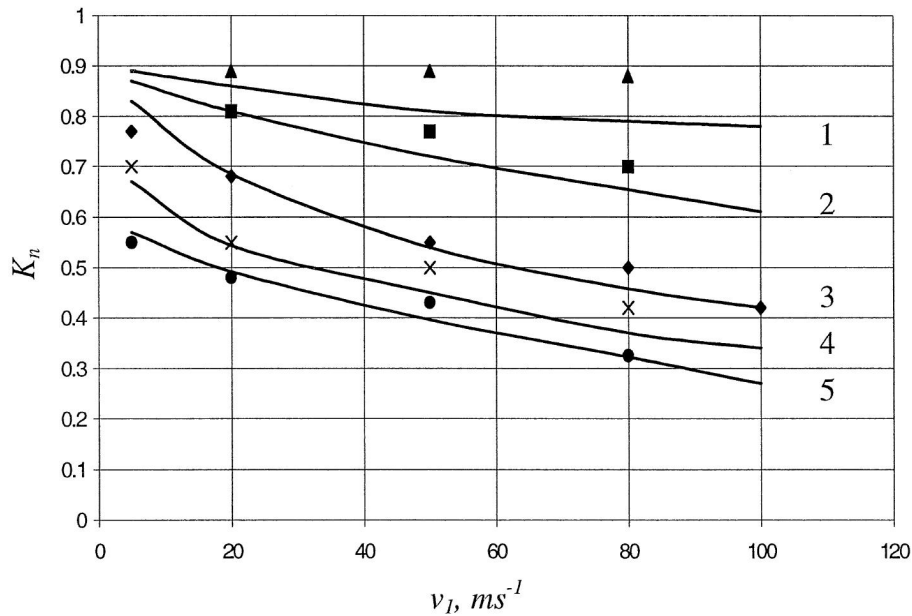


Fig. 2.25 Variation of coefficient of restitution vs. impact velocity for normal impacts [70]. The five different curves are for different target materials with decreasing (1 to 5) Brinell's hardness and dynamic hardness.

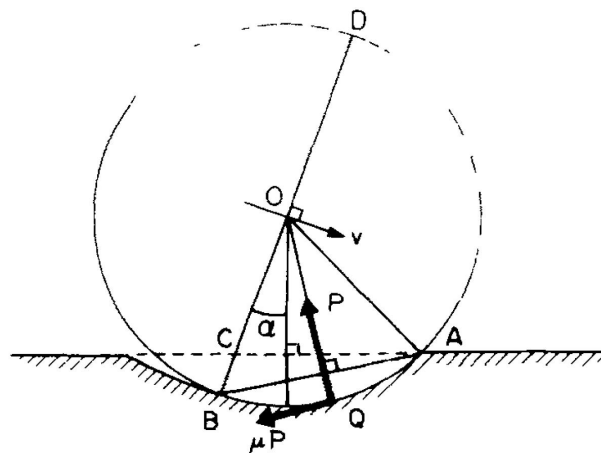
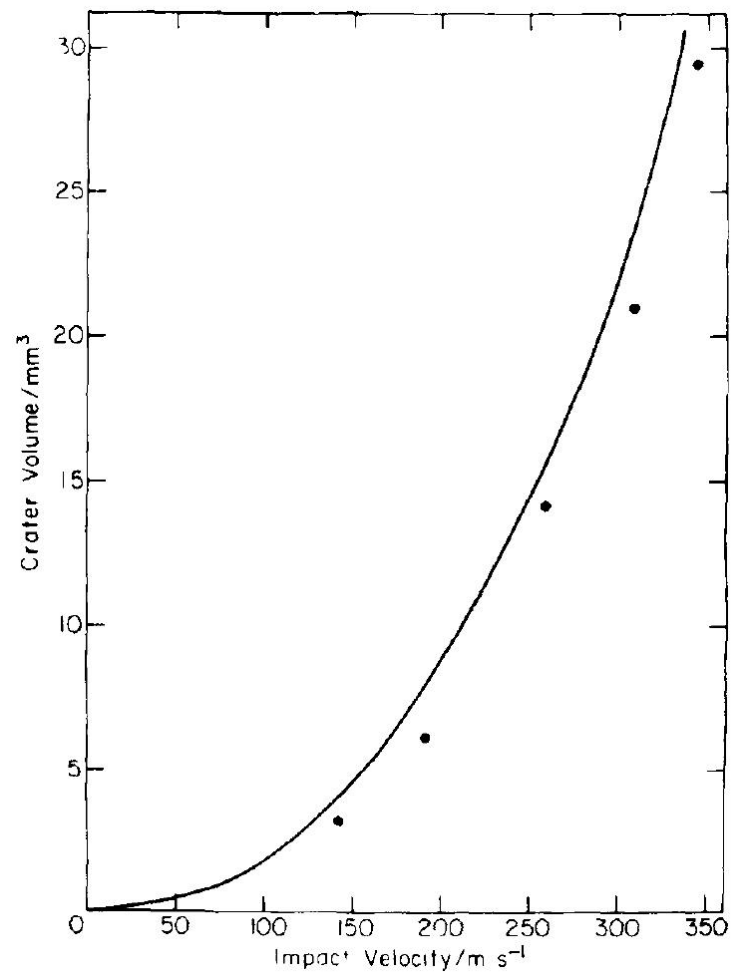


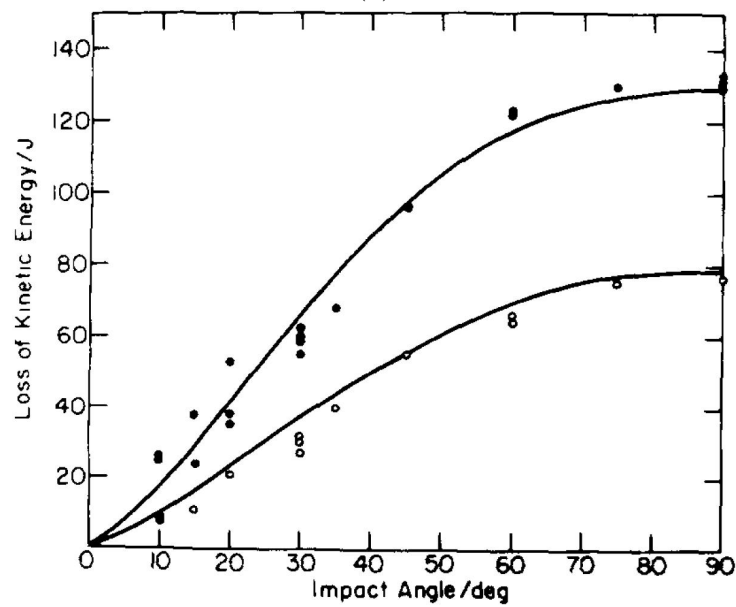
Fig. 2.26 Sketch of a rigid sphere impact ductile target [62].

### 2.6.3 Collapsible structures

A collapsible structure can be used to dissipate the impact energy, interrupt or prolong the momentum transfer. Such systems are known for improving crash-worthiness of the vehicles. Alghamdi [1] reviewed various shapes of collapsible energy absorbers. Snyman [114] performed experiments and simulations for the application of a collapsible region in a target subjected to landmine blast as shown in Fig. 2.28. The part of the target exposed to the explosion is V-shaped, which is attached to the frame using collapsible structure. They found that using the collapsible plate helps in reducing the rate of deceleration of the V-shaped part as compared to the case without collapsible plate, and a reduction of average imparted impulse by 16 % to 18 %.



(a)



(b)

Fig. 2.27 Variation of (a) Crater volume against impact velocities and (b) Loss of kinetic energy against impact angle at impact velocity  $270 \text{ m s}^{-1}$  (upper curve) and  $210 \text{ m s}^{-1}$  (lower curve) [62].

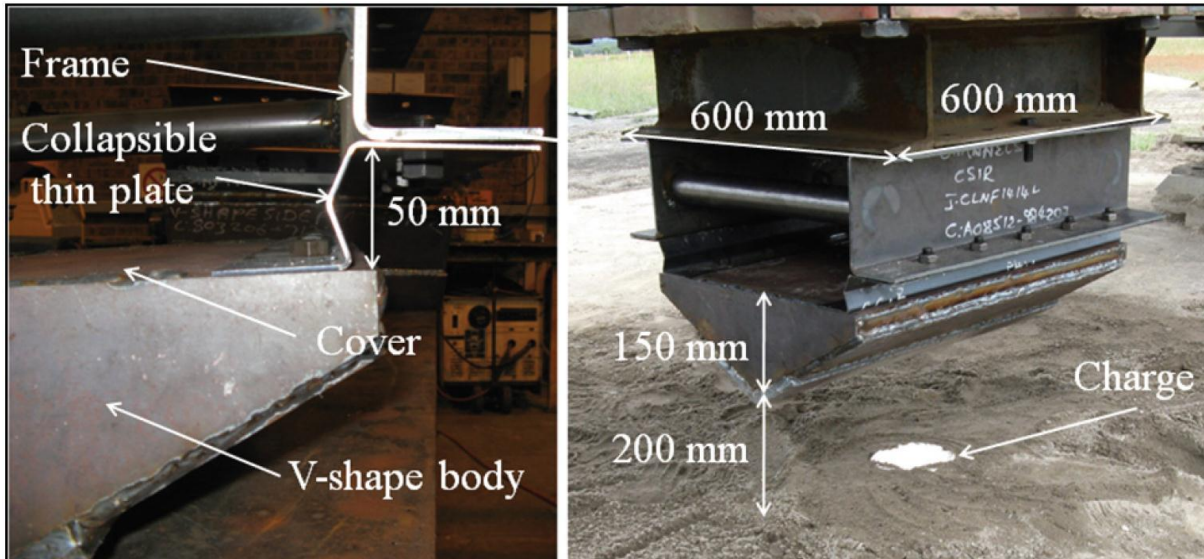


Fig. 2.28 Pictures of the structure used for the impact tests [114]. It consists of a V-shaped part attached to the frame using a collapsible plate.

Cendón et al. [16] numerically analysed different add-ons to the vehicle bottom for impact attenuation. They showed that the distance between the landmine and the add-on protection can be optimized. A large gap causes the strike of the add-on to the original bottom plate, while a small gap causes the damage to the add-on due to large momentum transfer from landmine. Kyner et al. [73] used test facility similar to that utilised by Holloman et al. [58, 57] and implemented additional flat plates on top of rigid target such that the granular ejecta impacted this plate first, rather than the target surface. The interface between this flat plate and target surface was lubricated such that the plate slid off during impact due to frictional loading from granular media and acted as a sacrificial part of the system (Fig. 2.29). Due to low friction between the plate and target, the frictional loading on the target was reduced as compared to the impact of granular media directly on the target. Hence, using sliding sacrificial plates led to substantial reduction in transmitted impulse.

#### 2.6.4 Sandwich vs monolithic target

Many studies have shown that metallic sandwich plates can outperform solid plates in case of water blast [25, 29, 35, 77, 128, 134, 133, 137], where the performance is measured by deflections and reaction forces induced by blast. Deshpande et al. [26] studied the one-dimensional fluid structure interaction (FSI) on sandwich plates using an underwater shock simulator and found that there is a strong FSI effect for loading on sandwich plates by underwater shock load. Fleck and Deshpande [35] showed an improvement of blast resistance by sandwich plates in case of water blast. McShane et al. [83] used a finite element methodology to compare the blast resistance of monolithic and prismatic lattice core sandwich beams against underwater blast. The benefits were confirmed experimentally

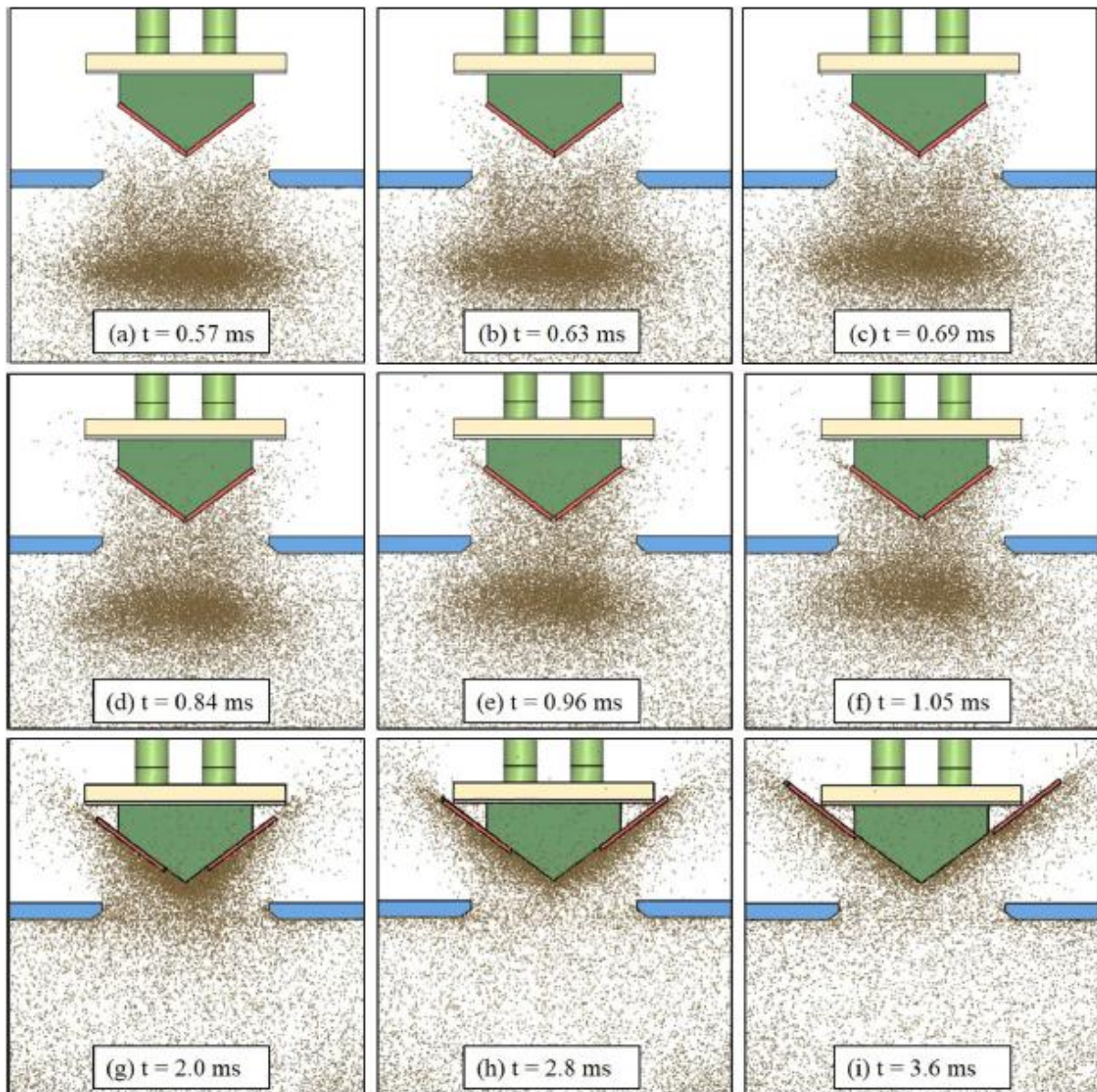


Fig. 2.29 Simulation time sequence of sand impact with the V-shaped target with attached slider plate [73].

by Wadley et al. [128] and Wei et al. [133] showing that sandwich structures with cellular material core has higher resistance to blast loads. Taylor [116] showed that transmitted impulse to the structure is reduced because of FSI effect, while demonstrating that in case of lighter targets, the impulse transmitted is lesser because lighter targets start moving quickly in the direction of incoming momentum of fluid, thus reducing the pressure acting on the surface of the plate.

Numerous studies exist for comparison between monolithic and sandwich panels for blast resistance against granular sprays [11, 57, 58, 108, 125–127]. Pingle et al. [99] have analysed the interaction of spatially uniform granular slugs impacting rigid targets. This rather idealised, but fundamental FSI problem is the “sand-blast” analogue to the classical water propagated shock FSI problem studied by Taylor [116]. Liu et al. [79] extended

the sand column model to investigate the impact of clamped sandwich and monolithic plates. Their numerical results indicate that sandwich panel designs suffer significantly smaller deflections than monolithic plates of identical span and of equal mass per unit area. The performance benefit was due to the higher bending strength of sandwich plates. Dharmasena et al. [30] analysed deformation of sandwich panels and monolithic plates impacted by spherically expanding sand shells using experiments and particle based simulations. For a given stand-off, the deflection of sandwich panels was substantially less than that for monolithic plates (Fig. 2.30). This was again attributed to higher bending strength of sandwich structures.

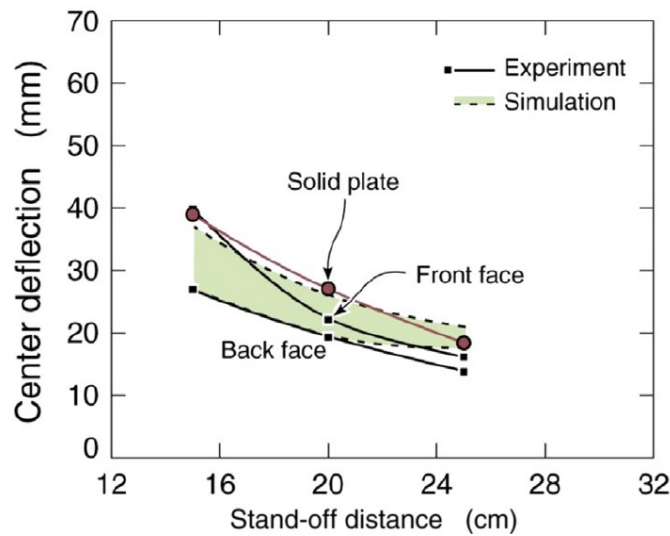


Fig. 2.30 The measured and predicted residual mid-span deflections [30] of monolithic plate and sandwich panel subjected dry sand explosions as a function of stand-off  $S$ . Results are shown for deflections of both the front and rear face of the sandwich panels and the corresponding measurements of the monolithic plates are included.

## 2.7 Reduced scale experiments

Using small-scale tests is cost effective and less time consuming. They can also provide better insight into the physical phenomenon of granular impact as well as the response of structures. Reduced-scale experiments have been increasingly used for studies to understand phenomena associated with dynamic loading of structures by explosively accelerated granular media. For example, Hlady [56] investigated the influence of soil properties using 0.025 kg buried charges with a vertical impulse pendulum and found that the water saturation increased the momentum transmitted to the target plate, but only if a threshold moisture content was exceeded. Taylor et al. [119] and Fourney et al. [38] considered the scalability of buried charge experiments and demonstrated an influence of plate mass. Neuberger et al. [87, 88] examined the deformation of clamped plates loaded by spherical charges either flush buried in dry sand (i.e. zero sand overburden) or in air alone to show that the presence of sand increases the deformation of the target plate.

To generate high velocity sand sprays using expanding explosives, numerous parameters are calibrated. Because of uncertain nature of explosions, discrepancies between experimental observations and numerical predictions are common. The origin of these discrepancies remains unresolved with possible sources of error being: (i) Inability of the simulations to accurately capture the details of the granular spray generated by the loading of the soil due to the expansion of the explosive gas; and/or (ii) Failure of the simulations to correctly capture the interactions between the high velocity granular ejecta and the impacted structure.

The decoupling of these two possible sources of error is problematic in experiments involving detonation of an explosive since (i) typically spherically expanding, optically opaque sand sprays are generated [30, 56, 98] wherein only the outer front is visible and (ii) the explosive gases obscure the view of the impacted structure after the first few milliseconds. Therefore, the only metric available to compare simulations and measurements is the permanent deformations of the structures.

An approach to better control the experimental conditions was developed by Dharmasena et al. [30] and involves explosively accelerating silica glass microspheres that encase a spherical explosive charge. This approach has been utilised by Kyner et al. [74] as it gives repeatable results and therefore is more suitable for detailed numerical modelling. However, the drawback of this approach was that the influence of soil type, including particle shape, upon the impact loading was neglected in the study. McShane et al. [82] developed a laboratory scale experimental technique to mimic the effect of landmine loading, without using explosives. They utilised compressed nitrogen gas beneath the sand layer and analysed the effect of soil saturation and depth of sand layer. Tests performed by Fourney et al. [39] demonstrated that results from small-scale tests may be used to predict the results from full-scale tests, as shown in Fig. 2.31. They did small-scale tests and used its results to predict the results from full-scale tests conducted by U.S. Army Research Laboratory (ARL).

Park et al. [95] developed a technique to generate a high velocity sand slug within a laboratory setting (Fig. 2.32) and without the need for the detonation of an explosive and thereby circumvent the problems associated with explosive detonations. Uth and Deshpande [125] and Uth et al. [126] employed this setup to investigate the dynamic response of monolithic and sandwich structures impacted by such granular slugs. The key feature of these experiments was that the high velocity granular slugs were fully characterised both in terms of their density and spatial distribution of their velocity. Moreover, Uth and Deshpande [125] and Uth et al. [126] reported detailed observations of the dynamic response of the impacted structures visualised using high-speed photography. In this thesis, the experimentation was done using the approach developed by Park et al. [95], as detailed in the subsequent chapters.

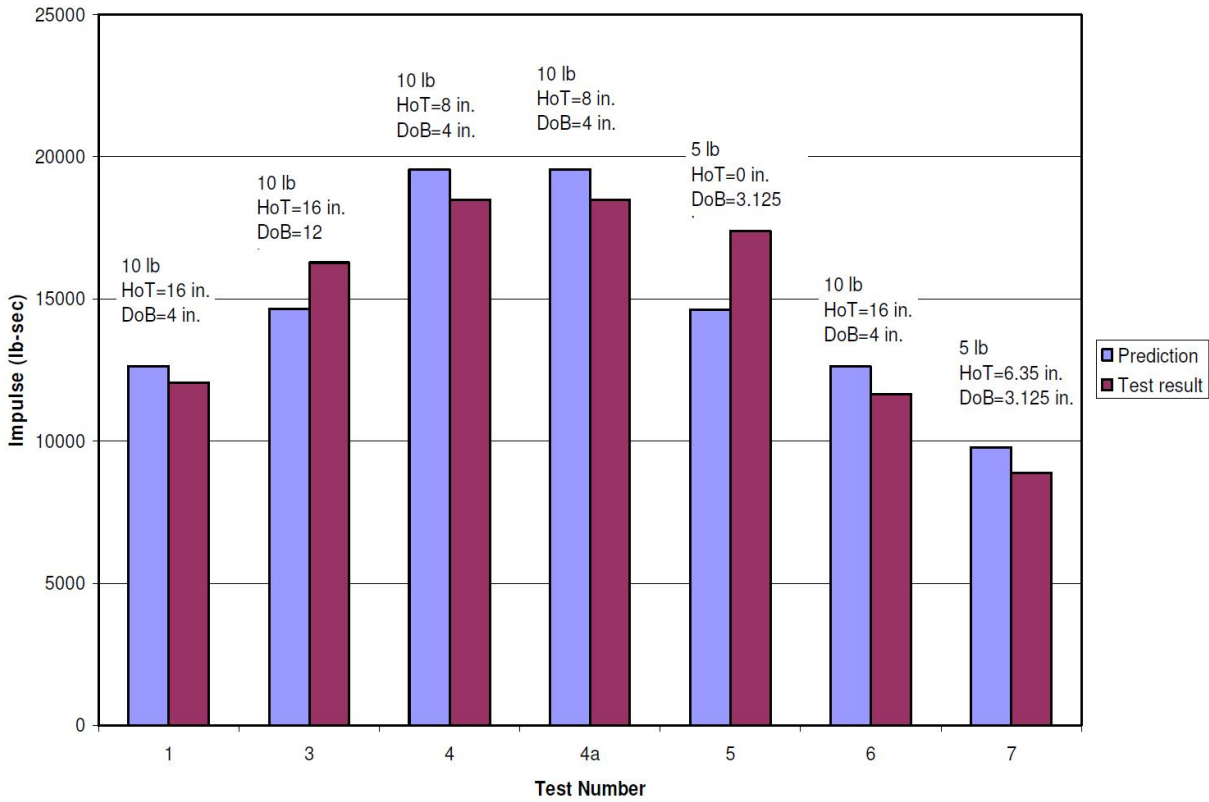


Fig. 2.31 Comparison of impulse predicted by small-scale tests with that predicted by full scale results [39].

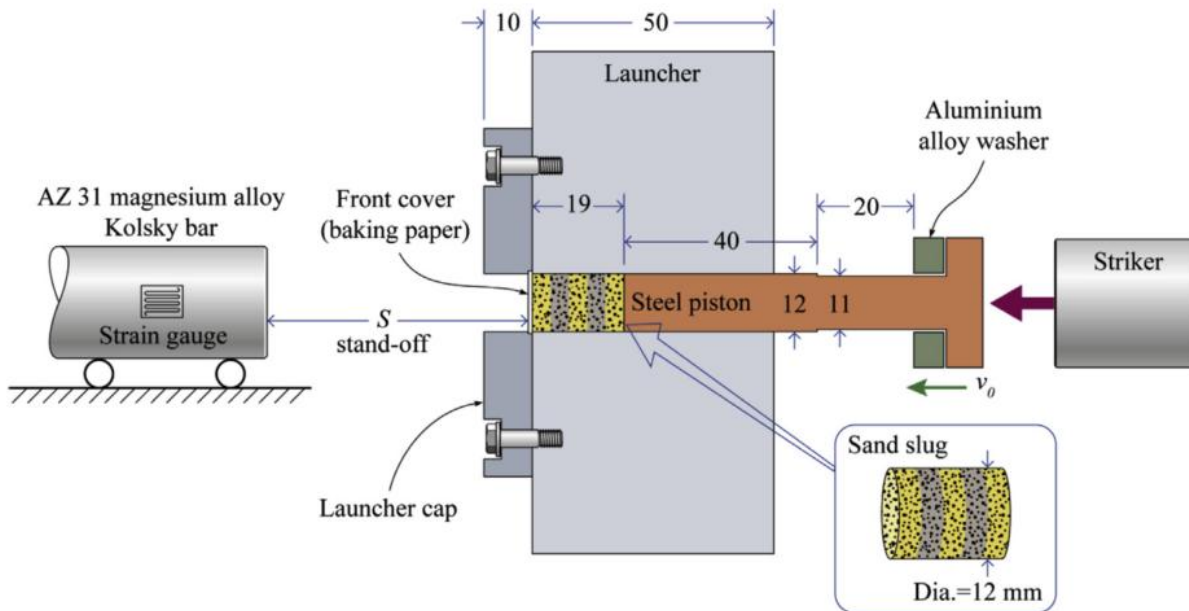


Fig. 2.32 Sketch of the apparatus used to launch the sand slugs [95].

## 2.8 Numerical modelling methods

A number of numerical approaches have been proposed to model the complex dynamic interaction of high velocity granular media with structures. Some of them are discussed here.

### 2.8.1 Empirical models

Empirical relations to quantify the deformations of plates subjected to buried explosions have been proposed [88, 135] based on experimental tests [8, 13, 132]. Westine et al. [135] developed an empirical model to numerically predict the loads generated by blasts from buried explosives. They did experiments and then developed empirical model for the response of floor plate from shallow-buried landmine explosions. Tremblay [123] used the model of Westine et al. [135] to analyse the effect of target inclination. Morris [84] further extended the model by Westine et al. [135] and developed a structural design code including the effect of target inclination. These studies using empirical models show that the impulse depends on the stand-off, depth of burial and horizontal distance from the centre of landmine. Empirical models are limited to conditions they are derived from and tend to give unrealistic results when used under different loading conditions or when interacting with different kind of structures such as sandwich panels [49, 84].

### 2.8.2 Continuum models

#### Porous-material compaction model and three-phase soil model

A porous-material/compaction model was demonstrated by Laine and Sandvik [76] using the porous equation of state obtained from tri-axial compression tests with isotropic consolidation. Additionally, Wang et al. [130] and Wang and Lu [131] demonstrated a three phase soil model by modifying Drucker and Prager model [31]. It was developed for simulating stress wave propagation through soils in case of blast loading. They modelled soil as three-phase mass including solid particles, water and air. The conceptual model of soil under shock loading is illustrated in Fig. 2.33a, which is then detailed as illustrated in Fig. 2.33b. The parts A,B and C correspond to the deformation of solid particles, water and air. D is defined as the friction between solid particles and E is the bond linkage between the particles. The load is taken up by the branches  $a$ ,  $b$  and  $c$  where  $a$  is the friction force between particles,  $b$  is the force taken by water and air, and  $c$  is the force in the bond between the solid particles.



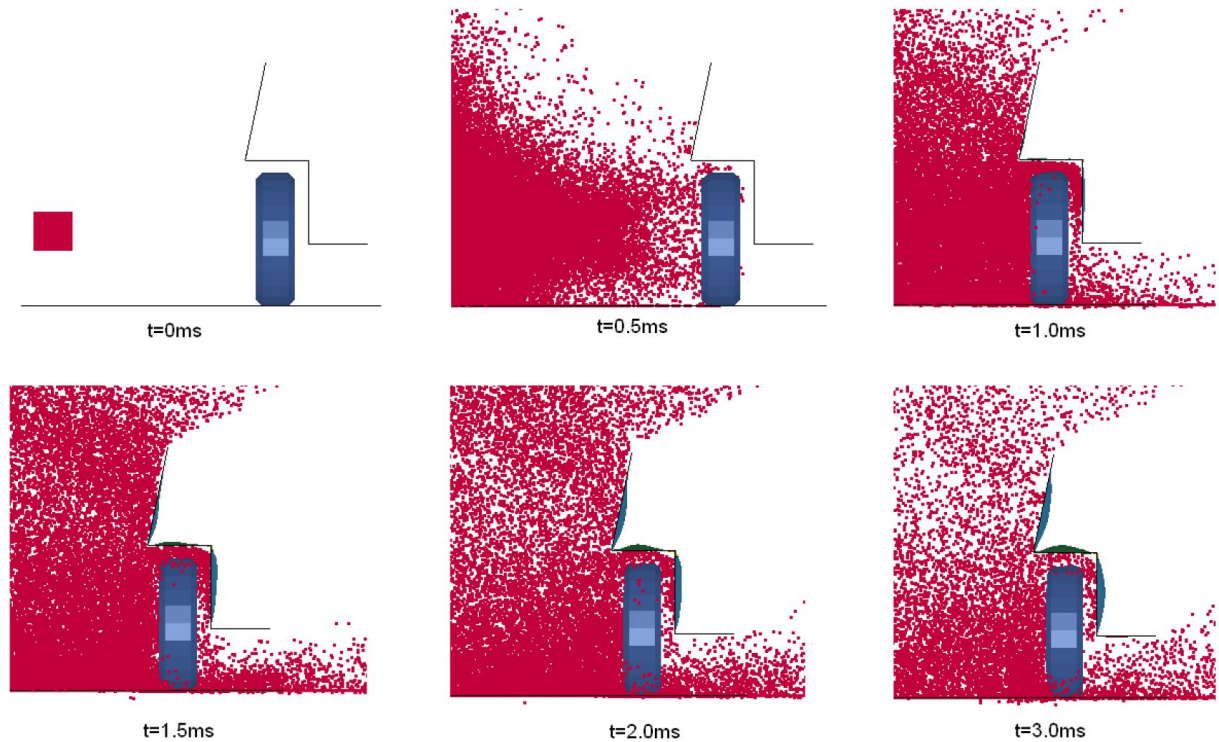


Fig. 2.34 Analysis of near-field blast using smoothed particle hydrodynamics (SPH) technique [122].

by landmine blast. The soil constitutive relationship needs to be defined for different phases such as initial compressive shock loading, spallation, propagation through air and structural impact. Hence, the accuracy depends upon the availability of constitutive models. For this, empirical three-phase models [130], or porous-material/compaction model [76] have been used previously.

There are numerous characteristics of soil that can affect the loading on the impacted structure. These include void ratio, saturation, material properties of particles, size of particles, etc. [130]. Grujicic et al. [48, 52] have developed constitutive models by including the effect of moisture and compared with the data from tests by Bergeron and Tremblay [7]. The deformation of sand material using this model is illustrated in Figure 2.35. Grujicic et al. [47, 50, 52] used CEL method to analyse the impulsive loading from the buried landmine for different depths of burial in water-saturated sand. Wang et al. [130] also used this method to simulate landmine explosions. The predictions of blast impulse and plate deformation was compared with the measurements from Bergeron and Tremblay [7] and Foedinger [36].

Modifying the constitutive model of Bagnold [3], Deshpande et al. [27] developed an alternative approach to model dynamic response of soils over entire range of states. They combined two formulations to cover both the regimes. One regime is where the particles are dispersed and they are assumed to collide with each other and surroundings. This regime is modelled using soft particle model, first utilized by Cundall and Strack [24]. The other regime is for higher packing densities where the contacts can be assumed semi-permanent.

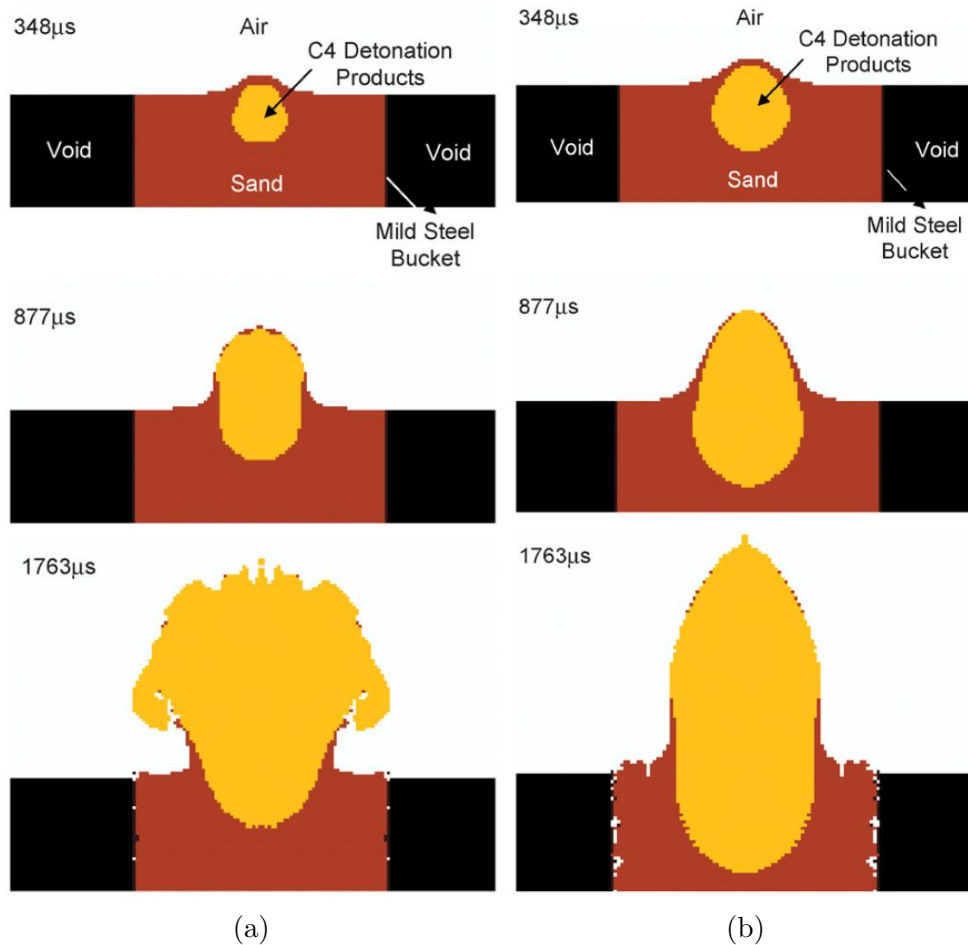


Fig. 2.35 Temporal evolution of material deformation during landmine explosion [52]. (a) Dry sand, (b) Fully saturated sand.

This regime is modelled using Drucker-Prager models [31] and implemented in a CEL framework. Borvik et al. [10] analysed the blast loading of structures using uncoupled and fully-coupled Eulerian-Lagrangian simulations, demonstrating a reduction in pressure due to flexibility of the structure. Rimoli et al. [108] used a decoupled method to analyse the impact of wet sand on sandwich structure. They used a constitutive model [27] to determine the pressure profile on the plate, which was then applied to find deformation using finite element approach. The problem with this approach is it fails to capture the fluid-structure interaction effects, i.e. dynamic interaction of deforming structure and soil.

Most of these continuum models are more appropriate for modelling initial phase of explosion when the packing density of soil is sufficiently high. During this phase, the particle-particle contacts are semi-permanent. However, at later stages when the particle density becomes low, the results from such models may deviate [27, 129, 130]. Also, it is difficult to accurately represent the response of materials in blast event using the currently available material models [48]. The issue is because the deformations are large and rapid.

### 2.8.3 Discrete particle method (Discrete Element Method - DEM)

Discrete element method (DEM) is widely used tool for numerical modelling of granular material. The approach considers particles as discrete elements and the force acts between them only during active contact and collisions. It is also known as soft particle model and was first used for soils by Cundall and Strack [24]. The benefit of DEM is that particles are allowed to undergo large displacements and rotations, which makes it a popular method to simulate particles in numerous applications. Because of the explicit integration used in DEM approach, time step of integration is an important parameter. Too large a time step leads to large overlap and missed contacts between fast moving particles. This may cause unrealistic forces applied to the particles. If the time step is too small, the solution may become computationally expensive. Coupling of DEM with continuum simulations provides a promising method of simulating the response of structures impacted by high-velocity granular media and it has been used in this thesis. Following are the advantages of using this approach:

- There is no need of estimating the constitutive model of the aggregate. The behaviour evolves with the contact between the particles.
- Since the particles are modelled as discrete, the numerical roadblocks (such as contact errors and computational time) associated with solving continuum models are reduced.

Norouzi et al. [89] used DEM to model non-spherical particles for analysing granular flow in rotating drums and found that DEM produces satisfactory results when compared with experiments for average surface velocity and average circulation time. DEM was used by Zheng et al. [139] to simulate breakage of particle agglomerates because of impact. They used uniaxial compressive experiments and single coal rock test to obtain parameters for numerical model. 6 different shapes of agglomerates were used. To construct the agglomerate, rigid discrete spheres were used as primary particles connected by parallel bonds, which were used to transmit forces and moments. Cil and Alshibli [21] used DEM to model breaking of particles using agglomerates with spherical sub-particles, where the bonding was done using bonded particle model (BPM). They showed that breakage initiates along the plane connecting two contact points on the particle with adjacent particles. Borvik et al. [9] utilised DEM to study the penetration of bullets in constrained granular media. Huang et al. [60] used DEM to study the flow of granular jets against target and compared with the experimental data from Cheng et al. [18]. They have also discussed the importance of time step, and other parameters of the DEM model.

The forces between the particles are transferred using the contact model. An impact model between particle and large target surface was developed by Brach [12] from the principles of momentum and impulse. They used the coefficient of restitution and friction to understand the energy loss. Numerous contact models have been developed [63, 72, 105] to be used for DEM. A soft-particle contact model was introduced by Cundall and Strack

[24] and extended to large scale simulations by Campbell and Brennen [15] and Campbell [14].

For the research presented in this thesis, soil is treated as an aggregate of particles modelled using DEM technique. This DEM model is coupled with finite element simulations to model the interaction of particles with the structure. The overall behaviour is governed by using the contact law among the particles and between particles and contacting structure, as demonstrated by Pingle et al. [99]. They showed that this method is quite strong in capturing the interactions between disperse particles and the structure when investigating the response of a rigid target (fixed - Fig. 2.36a and movable - Fig.2.36b) impacted by column of particles. Two dimensional calculations were performed where the particles were modelled as circular discs. They also studied the influence of various numerical parameters in the discrete particle model and found that pressure on the target because of the particle column is independent of coefficient of restitution for particle impact and friction coefficient between the particles but strongly dependent on relative density of particles in the aggregate. The pressure on a stationary target was found to scale as  $\rho\rho_s v_0^2$  where  $\rho$  is the relative density of the aggregate,  $\rho_s$  is the density of solid particles and  $v_0$  is the velocity of particles. The elastic stiffness between the particle controls the deformation of aggregate of particles. An important finding was that the collision between aggregate of particles and target is inelastic with effective coefficient of restitution between 0 and 0.35. This implies that the momentum transmitted to the target can be up to 35 % higher than the incoming momentum. For a movable target, the transmitted momentum was dependent upon ratio of areal mass of the sand column and the target. If lateral spreading is allowed, as shown in Fig. 2.37, then majority of the particles attain a velocity along the target surface after impact and there is very little reflection. Hence the transmitted momentum is equal to the incoming momentum. They also looked at the foam analogy of sand slug (where the impact of the particles is modelled using an equivalent foam projectile) and apply that for impact on the beams.

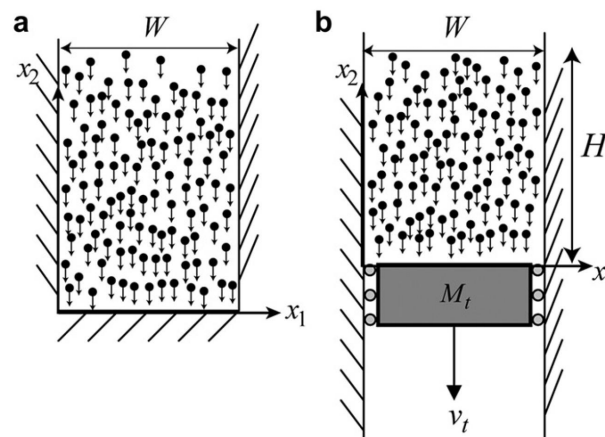


Fig. 2.36 Sketch of the problem analysed by Pingle et al. [99] with lateral constraint. (a) consists of rigid stationary target and a semi-infinite column and (b) has a rigid movable target and a granular column of finite height.

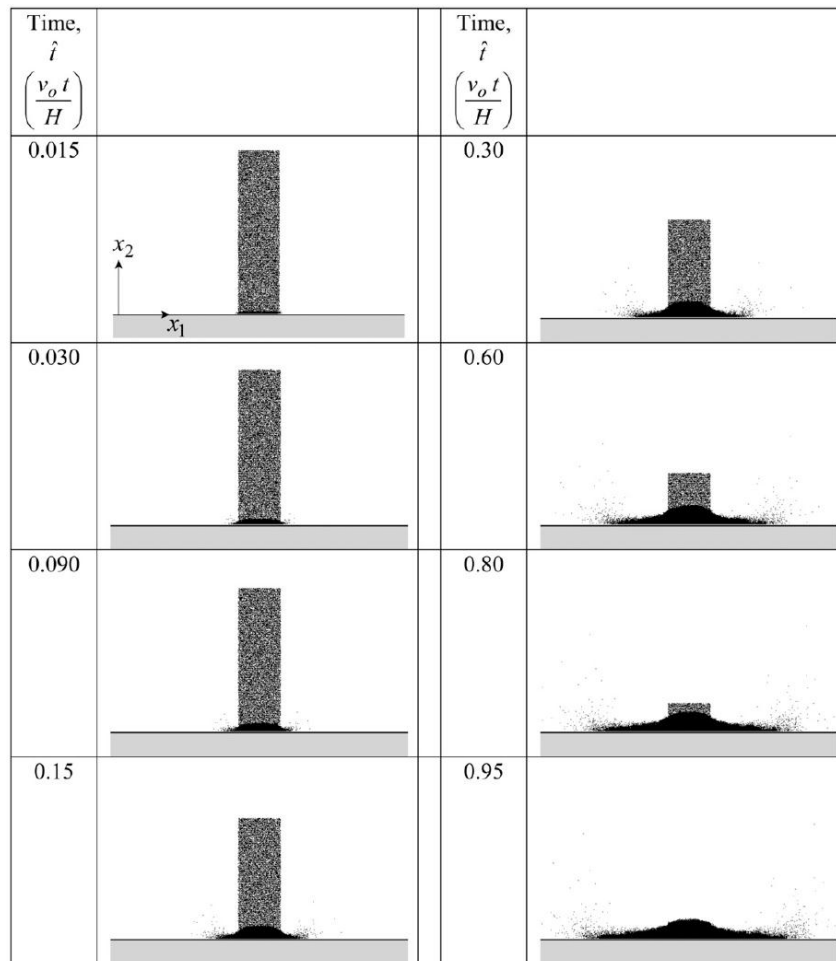


Fig. 2.37 Snapshots showing impact of unconstrained sand column on stationary target [99].

Liu et al. [79] used the discrete particle technique to study the response of clamped beams and plates impacted by a column of particles. The snapshots of monolithic beam deformation at different times using this technique is shown in Fig. 2.38. They demonstrated that loading due to sand is primarily inertial with little fluid-structure interaction effects. This implies that the momentum transferred to the structure was approximately equal to the momentum of incoming sand slug. They found that deflection of the target is mainly affected by the momentum of the incoming sand slug and the loading time, as depicted in Fig. 2.39. Additionally, they demonstrated that sandwich beams outperform monolithic beams with equal areal mass. This performance enhancement was attributed to the higher bending strength of the sandwich beam to that of monolithic beam. Liu et al. [80] further used this technique to understand the compression of plates supported by foam and impacted by high velocity soil.

The discrete particle approach is also used in Corpuscular method [90] to model the expansion of soil particles due to detonation of explosive. In this method, Maxwell's kinetic molecular theory is used to model the detonation products and they transfer the energy to soil particles using collisions. This method was implemented by Borvik et al. [11], and

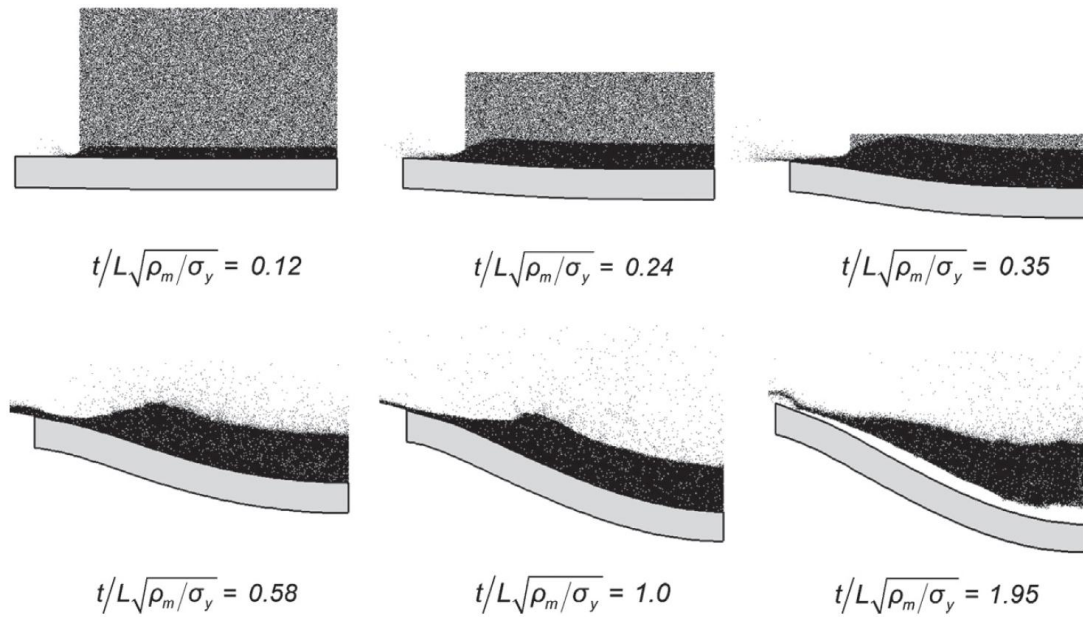


Fig. 2.38 Deformation of monolithic beam impacted by sand slug at selected times [79].

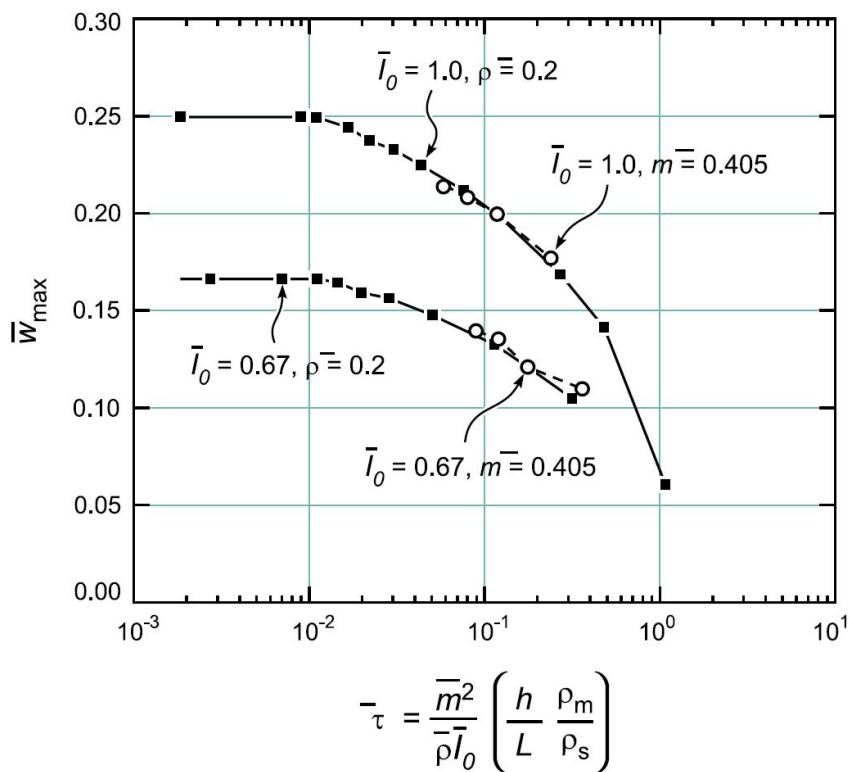


Fig. 2.39 Predictions of the normalised maximum deflection of the monolithic beams as a function of normalised loading time [79]. The results are presented for two cases of normalised incoming momentum of the slug.

coupled with finite element method to model the response of monolithic plates impacted by spherically expanding detonation products (air shock and sand), as depicted in Fig. 2.40. Recently, this method was used by Wadley et al. [127] and Holloman et al. [58] to analyse blast events. Wadley et al. [127] used DEM to understand the deformation and

fracture of sandwich panels loaded impulsively by spherically expanding sand shell under blast load. In Fig. 2.41, they show how the impulse vary with stand-off distance.

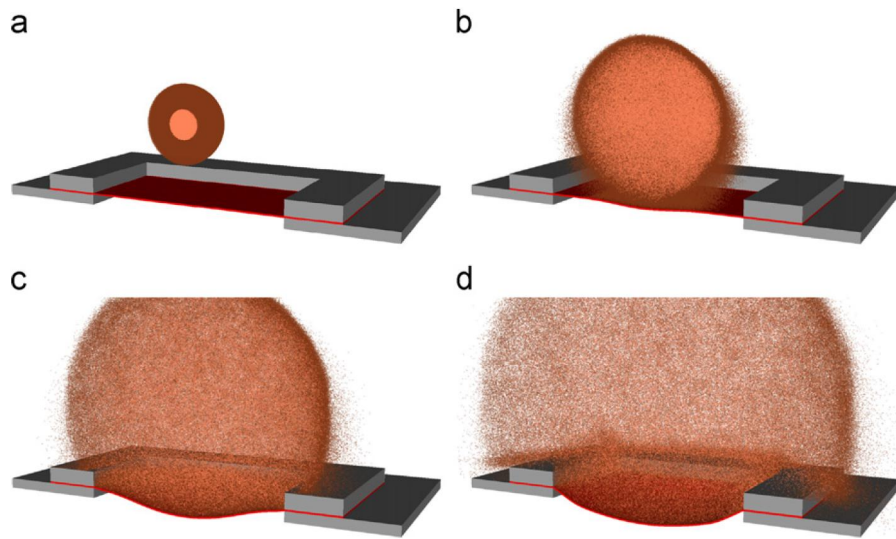


Fig. 2.40 Deformation of plate after impact of C-4 and saturated wet sand at stand-off distance of 150mm [11]. (a)  $t=0 \mu\text{s}$ , (b)  $t=200 \mu\text{s}$ , (c)  $t=400 \mu\text{s}$ , (d)  $t=800 \mu\text{s}$ .

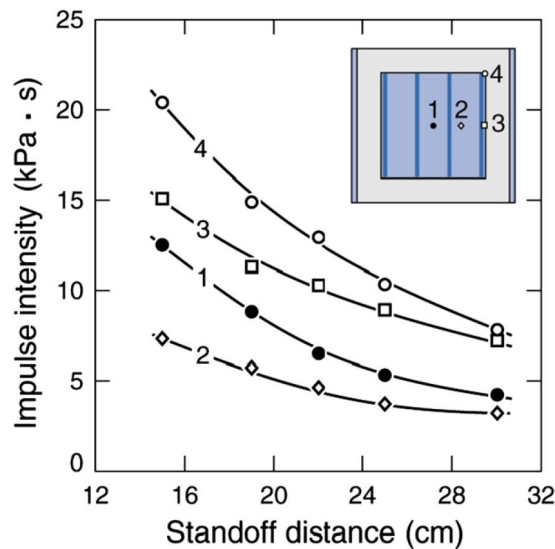


Fig. 2.41 Impulse intensity at different plate locations vs stand-off distance [127].

The earlier mentioned work by Pingle et al. [99] and Liu et al. [79, 80] concentrated on the interaction of granular material with the structure. In this thesis, emphasis is also given to the phase when the ejecta expands before impacting the structure.

#### 2.8.4 Modelling non-spherical (angular) particles

The studies using discrete particle methods typically utilise spheres to represent granular particles, whereas in reality, the soil particles are non-spherical. When interacting with structure, spherical particles can have drastically different motion and effect compared

to spherical particles, as discussed in Section 2.5.2. For instance, non-spherical particles would have higher propensity to slide rather than roll on the target surface, resulting in increased frictional interactions. In this section, some numerical methodologies used to simulate angular particles are discussed.

Norouzi et al. [89] performed simulations of spherical and non-spherical particles to analyse the flow of particles in rotating drums. They investigated the velocity profile and circulation time because of rolling and cascading of the particles in the drum. To model non-spherical shapes, they use a combination of multiple spheres glued to each other as shown in Fig. 2.42. The benefit of using this technique is that since the surface of particles are still spherical, the contact force equations [14, 15, 24] used for sphere are applicable here. They found that particle shape has an influence on mean circulation time as well as transition of the flow from rolling to cascading regime. Coetzee [23] also used clumping of spheres to represent a non-spherical particle as shown in Fig. 2.43 to perform shear calculation of crushed rock particles.

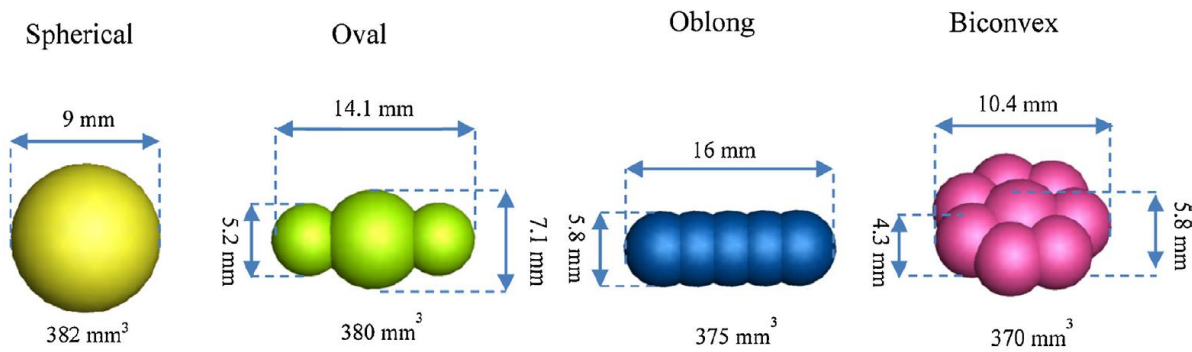


Fig. 2.42 Different shapes of particles used in simulations [89]

A new technique for modelling non-spherical particles was presented by Hopkins [59] using non-convex polyhedral grain shapes for discrete element modelling. Polyhedral grains were first dilated and then a contact algorithm was used. By using this method, Hopkins demonstrated that non-spherical particles can be modelled without employing the usual approach of using a cluster of spheres. He showed how sharp, non-convex granular material can be modelled without very high level of complexity in the code.

For the granular impact studies, discrete particle simulations using spherical particles have been implemented in various ways. For example, Liu et al. [79] and Dharmasena et al. [30] allow for three rotational and three translational degrees of freedom for the particles while the approaches of Borvik et al. [11], Kyner et al. [73] and Holloman et al. [58, 57] restrict rotational motion of the spheres, even though tangential frictional forces that result in torques on the particles are included in the analyses. Since all these studies were restricted to spherical particles, they were unable to investigate the effect of particle angularity on the dynamic flow and impact of granular media. In this thesis, the particle angularity is analysed using simple shapes through a combination of spherical sub-particles combined using rigid connections joining their centres.

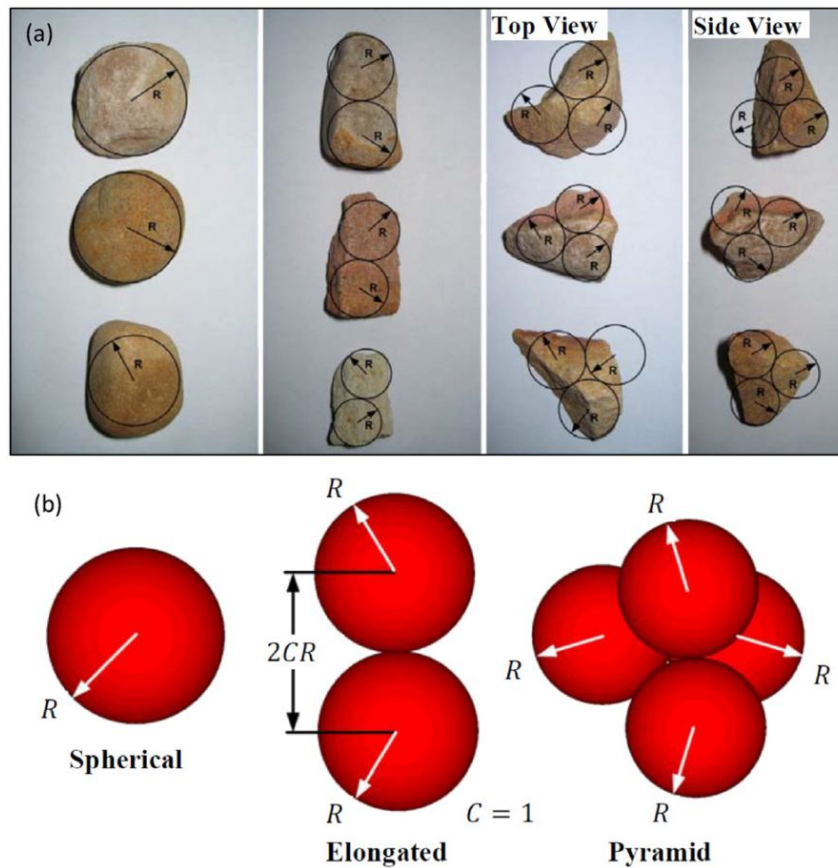


Fig. 2.43 (a) The rock particles and (b) the manual clump representation [23]

## 2.9 Mechanical packing of particles

Since the presented research is based on discrete particle method, it is important to have the particles present at the required spatial locations in order to start the calculations. Many other applications in research require packing of rigid particles. Packing density (or volume fraction) is defined as the ratio of actual weight of the particles inserted in a container by the weight of the same solid material with the volume of the container. This is the same as the ratio of the volume of all spherical particles to the total volume of the container where the particles are poured.

McGeary [81] did an experimental study of particle packing. He found out that if spheres of same size were used, then they pack at a density of about 62.5 % in square or cylindrical containers. The studies were generally done using a vibrating container. As mentioned by Torquato et al. [121], there are various computer algorithms to generate higher random packing densities. They introduce the term jammed state (i.e. it is not possible to translate a particle while positioning all other particles) that can be used to generate random packing of the particles. Recently, Shi and Zhang [111] presented a numerical method for loose packing of spherical particles. They studied the effect of particle size distribution on the packing structure. They showed that higher packing

density can be obtained using bimodal size distribution. In this thesis, a random number generator is used to assess the position of the particle to be inserted.

## 2.10 Summary and conclusions

The field of blast protection of vehicles against landmines is widely studied and many aspects have been looked into. There is considerable amount of literature discussing various factors that affect the loading of structure from a landmine. The biggest challenge to study these effects is the tremendous variation in conditions and the coupling of different physics. In this chapter, the literature related to some of the factors including depth of burial of explosive, soil properties, stand-off distance and target properties have been discussed. In the past, many strategies have been investigated to help reduce the damage to the vehicle and occupants. These include using V-shaped hull, increasing stand-off distance, using collapsible (energy absorbing) additions and sandwich panels.

Studies have shown that if the explosive is buried into the soil, then the damage to the vehicle is higher compared to the scenario of surface-laid explosive. This is because the process of underground explosion causes the soil layer to expand and eject at high speed, which inflicts on the bottom of the vehicle, causing high energy transfer. The primary loading on the target is because of the expanding soil, rather than the blast wave of detonation. Hence, this chapter mainly reviews the literature related to impact of granular aggregates on structures. The main conclusions from this chapter can be summarised in the following points:

1. The distance between the top of the soil and the target (stand-off distance) has a considerable effect on the blast loading of the structure. The intensity of loading on the structure with smaller stand-off distance is higher than those at larger stand-off. In this thesis, the effect of stand-off is looked upon briefly, with a purpose of validating the numerical methods against experimental observations.

2. Soil type plays a significant role on target loading in case of a buried mine, whereas it has very little effect if the mine is laid on surface. One of the most important parameters studied about the soil type for buried explosions is the moisture content, which increases the density of soil and hence the target loading. In addition, different types of soil can have different grain shapes and this can affect the loading on the structure. Most of the numerical studies related to this field utilise spherical particles. A spherical particle has been shown to have higher tendency to roll than slide on the surface, affecting the frictional loading. This phenomenon can have a significance when a granular aggregate impacts the target, and this is not well understood. Grain angularity can also develop because of fragmentation during the impact with the structure. Again, the effect of this phenomenon is not well understood in the context of impact of granular aggregates.

**3.** There can be many modifications to the target that can help reduce the damage. One of the most popular is a V-shaped bottom which deflects the momentum from soil to the sides of the vehicle. This is equivalent to combining two inclined targets impacted by soil ejecta. By inclining the target relative to the incoming granular material, the applied impulse is divided into vertical and horizontal components, where the damage is mostly done by the vertical component. Hence, the transmitted momentum is reduced. An important consideration in V-shaped hull design is the included angle of V-shape. More acute angle improves the protection, but it also reduces the stand-off (the lower portion of V is closer to the sand surface above the charge) and changes the centre of gravity, which can have negative effect on blast protection. Numerous studies exist for comparison between monolithic and sandwich panels for blast resistance against granular sprays. The sandwich panels were found to perform better due to their higher bending strength.

**4.** During impact of granular aggregate with the structure, a large fraction of particles impact the target and move along its surface. The amount of frictional loading on the structure depends upon properties of the impacted surface and hence the properties of the target surface play a significant role on the loading.

**5.** There are many approaches used for numerical modelling for this application. Major focus of the previous work have been to develop constitutive models for soil that can be implemented in Eulerian framework, which is then coupled with Lagrangian finite element (FE) method to investigate the response of the structure. Large scattering of grains make this method difficult and inaccurate to apply in such scenarios. Discrete element method (DEM) is alternative and widely used tool for numerical modelling of granular material. The main benefit of DEM is that particles are allowed to undergo large displacements and rotations. The discrete particle approach may not accurately represent the complexity of soil material, but it does provide a method to understand the physics behind soil-structure interaction. Previous studies have concentrated on the interaction of granular media with the structure, but the phase when ejecta expands before impacting the structure is not well understood.

The reviewed literature and above discussion highlights certain gaps with the overall knowledge in this field. In the ensuing technical chapters, these gaps are addressed, while also adding clarity to some of the existing knowledge. The broad topics of technical work are:

- Calibration and better understanding of numerical parameters to predict the evolution of soil ejecta and its interaction with the structure in a fully-coupled manner.
- The effect of target properties such as surface roughness, stand-off and inclination.
- The effect of soil properties such as grain angularity and fragmentation, and methodologies for their numerical analysis.
- Analysis of the existing strategy for reducing the impact by using collapsible/sacrificial components.



# Chapter 3

## Coupled discrete/continuum simulations of the impact of granular slugs with clamped beams: Stand-off effects

### Abstract

Coupled discrete particle/continuum simulations of the normal (zero obliquity) impact of granular slugs against the centre of deformable, end-clamped beams are reported. The simulations analyse the experiments of Uth et al. [126] enabling a detailed interpretation of their observations of temporal evolution of granular slug and a strong stand-off distance dependence of the structural response. The high velocity granular slugs were generated by the pushing action of a piston and develop a spatial velocity gradient due to elastic energy stored during the loading phase by the piston. The velocity gradient within the “stretching” slug is a strong function of the inter-particle contact stiffness and the time the piston takes to ramp up to its final velocity. Other inter-particle contact properties such as damping and friction are shown to have negligible effect on the evolution of the granular slug. The velocity gradients result in a slug density that decreases with increasing stand-off distance, and therefore the pressure imposed by the slug on the beams is reduced with increasing stand-off. This results in the stand-off dependence of the beam’s deflection observed by Uth et al. [126]. The coupled simulations capture both the permanent deflections of the beams and their dynamic deformation modes with a high degree of fidelity. These simulations shed new light on the stand-off effect observed during the loading of structures by shallow-buried explosions.

### 3.1 Introduction

Much attention has been devoted to the dynamic response of above-ground structures subjected to blast loading from a shallow-buried explosion [2]. Experimental as well as numerical studies have shown that compared to surface laid explosives, shallow-buried explosives result in higher impulse transmission and larger deflections of the afflicted structure [27, 96, 98]. This increased severity of loading has been attributed to the impact of the granular media that is ejected by the expansion of detonation products in shallow-buried explosives [7, 33, 106] compared to explosions in air.

A number of experimental studies have proposed empirical relations to quantify the deformations of plates subjected to buried explosions; see for example Westine et al. [135] and Neuberger et al. [88]. Based on such empirical relations, Morris [84] proposed a design-for-survivability code for structures subjected to such impulsive loading events. A parallel effort has sought to numerically simulate the deformations of structures subjected to the complex loadings created by such explosions. For example, Rimoli et al. [108] used a soil model [27] to deduce the impulse applied to structures by explosively driven spherical sand, and then simulated the ensuing (uncoupled) deformation of aluminium monolithic and sandwich plates using finite element calculations. Grujicic et al. [48, 52, 51] and Wang et al. [130] have presented coupled Eulerian/Lagrangian simulations of landmine explosions and attempted to compare their predictions with blast impulse and plate deformation measurements from Bergeron and Tremblay [7] and Foedinger [36].

More recently, coupled discrete particle/continuum simulations have been used to investigate the response of structures impacted by high velocity granular media. For example, Borvik et al. [11] followed by Dharmasena et al. [30], and Holloman et al. [58, 57] used this approach to simulate the response of a variety of monolithic and sandwich structures loaded by high velocity sand sprays generated by buried explosions. Various calibrated parameters are used to produce the high velocity sand spray generated by the expanding explosive and the measurements of the response of the structure impacted by this spray are compared against the predictions. In all cases, discrepancies exist between measurements and predictions. One issue arises from the ill-defined foundation upon which a buried explosive rests. With the use of concentric soil shells surrounding suspended explosive charges, Wadley et al. [127] has overcome this issue, discrepancies still remain. The origin of these discrepancies remains unresolved with possible sources of error being:

1. Inability of the simulations to accurately capture the details of the granular spray generated by the loading of the soil due to the expansion of the explosive gas; and/or
2. Failure of the simulations to correctly capture the interactions between the high velocity granular ejecta and the impacted structure.

The decoupling of these two possible sources of error is problematic in experiments involving detonation of an explosive since (i) typically spherically expanding, optically

opaque sand sprays are generated [56, 98, 30] wherein only the outer front is visible and (ii) the explosive gases obscure the view of the impacted structure after the first few milliseconds. Therefore, the only metric available to compare simulations and measurements is the permanent deformations of the structures. This metric is an integrated (and therefore very coarse) measure of the fidelity of the simulations and makes it difficult to determine the precise sources of any discrepancies.

In order to address this deficiency, Park et al. [95] developed a technique to generate a high velocity sand slug within a laboratory setting and without the need for the detonation of an explosive. Uth and Deshpande [125] and Uth et al. [126] employed this setup to investigate the dynamic response of monolithic and sandwich structures impacted by such granular slugs. The key feature of these experiments was that the high velocity granular slugs were fully characterised both in terms of their density and spatial distribution of their velocity. Moreover, Uth and Deshpande [125] and Uth et al. [126] reported detailed observations of the dynamic response of the impacted structures visualised using high-speed photography.

Pingle et al. [99] have analysed the interaction of spatially uniform granular slugs impacting rigid targets. This rather idealised, but fundamental fluid-structure interaction (FSI) problem is the “sand-blast” analogue to the classical water propagated shock FSI problem studied by Taylor [116]. Liu et al. [79] extended the sand column model to investigate the impact of clamped sandwich and monolithic plates. Their numerical results indicate that some edge clamped sandwich panel designs suffer significantly smaller deflections than monolithic plates of identical span and of equal mass per unit area. The performance benefit was due to the higher bending strength of sandwich plates. This contrasts with water-blast of sandwich structures, where significant benefits accrue from fluid-structure interaction effects [25, 29, 128, 134]. The loading of structures by a slug of high velocity granular particles not only provides physical insight into the interaction of granular media with structures, but is also directly representative of the ejecta created during a shallow-buried explosion as shown in the experiments reported by Holloman et al. [58, 57] and Park et al. [95]. Thus, the impact of high velocity granular slugs against a test structure is of considerable theoretical and experimental interest.

Uth et al. [126] reported experimental observations for the zero obliquity (normal) impact of granular slugs comprising tungsten carbide particles against clamped beams. These measurements provide extensive data that show the dependence of the dynamic response of the beams to not only the velocity of the slug but also the stand-off distance between the launch position of the slug and the location of the beam. While this data presented clear trends, a lack of numerical simulations precluded elucidation of the physical mechanisms at play in the experiments. In this study we report detailed numerical simulations of the experiments of Uth et al. [126]. Comparisons with the experiments are used to (i) provide a detailed test of the fidelity of the coupled discrete particle/continuum simulation methodology and (ii) provide mechanistic explanations for

the temporal evolution of the granular slugs and the ensuing stand-off dependence of the beam's dynamic response observed in the experiments.

## 3.2 Summary of experimental findings

Uth et al. [126] presented an experimental investigation of the response of monolithic beams impacted normally and centrally by slugs of Tungsten Carbide (WC) particles. Here we analyse the data from Uth et al. [126] to test the fidelity of the coupled discrete particle/continuum numerical models<sup>1</sup>. It is thus instructive to first briefly describe the experimental setup and the key findings.

Cylindrical slugs of mass 22.7g (diameter  $D_0 = 12.7$  mm and resting length  $L_0 = 20$  mm), comprising WC particles with a diameter range of 45-150  $\mu\text{m}$  were impacted against monolithic clamped AISI 304 stainless steel beams. A sketch of the experimental setup is included in Fig. 3.1 and comprises four main components (from right to left): (i) a gas gun to fire a solid projectile, which then accelerates the piston of (ii) a slug launcher apparatus based upon that developed by Park et al. [95]; (iii) a WC slug that initially rests inside the cylindrical cavity of the launcher; and (iv) the beams clamped to a support rig. The projectile fired from the gas gun impacts the piston which in turn pushes the granular slug within the cylindrical cavity towards the clamped beam. The impact velocity of the projectile sets the speed with which the slug impacts the beam centre at normal incidence angle.

Clamped 304 stainless steel beams of span  $L_b = 100$  mm, width 21.3 mm and thickness 0.69 mm were used in the experiments of Uth et al. [126]. High-speed photography was employed in the experiments to visualise both the granular slug in free-flight and the subsequent impact of the slug against the beam as well as the ensuing deformations.

### 3.2.1 Key experimental measurements

Uth et al. [126] presented their data in terms of the projectile impact velocity  $V$  and the average velocity of the granular slug. However, for the purposes of the numerical calculations presented here it is more convenient to present the results in terms of piston velocity  $v_p$ : details of the method employed to determine  $v_p$  from the measurements are presented in Section 3.4.2.

The evolution of the granular slug ejected by a piston velocity  $v_p = 83.5$  m s<sup>-1</sup> as visualised by high-speed photography is shown in Fig. 3.2a. Images at four instants in time are shown with time  $t_s = 0$  chosen arbitrarily for the first snapshot corresponded to

---

<sup>1</sup>We emphasise that while the data from the study of Uth et al. [126] used here was gathered in the original investigation, we reanalyzed some of their data (especially the high-speed photographs) in order to extract some additional information (e.g. the velocity of the piston) required for the numerical calculations.

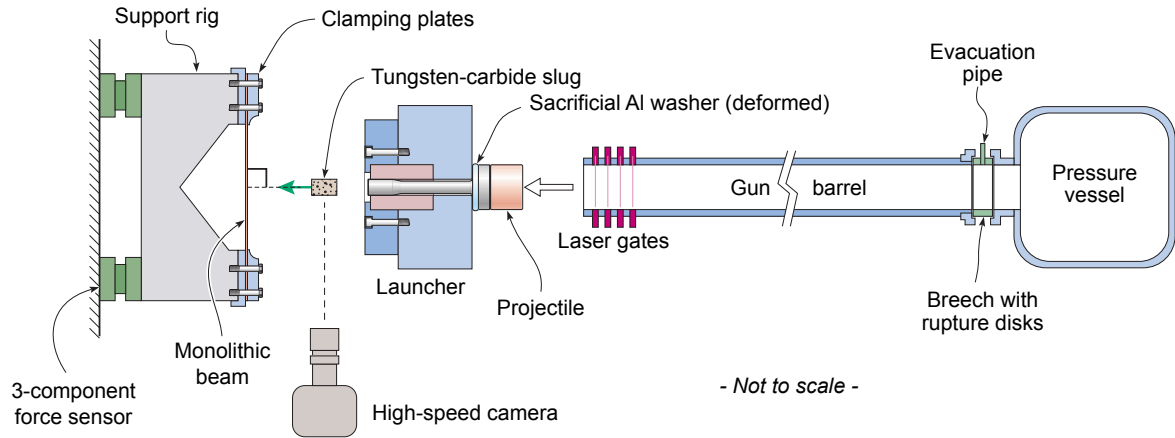


Fig. 3.1 Sketch of the experimental setup used in the experimental investigation of Uth et al. [126] to investigate the impact of granular slugs comprising WC particles against clamped beams.

the time at which the distance  $s$  travelled by the slug was  $s = 51$  mm. The travel distance  $s$  is defined in Fig. 3.2b, which shows the launcher section of the apparatus:  $s$  is equal to the distance travelled by the leading edge of the granular slug from its resting position within the launcher. The images clearly show that while the slug remains approximately cylindrical with an invariant diameter, it lengthens with increasing  $s$ . This is emphasised in Fig. 3.2c where the evolution of the slug length  $L_s$  ( $L_s = L_0$  at  $s=0$ ) is shown as a function of  $s$  for two piston velocities.

High-speed photographs of the impact of the granular slug against the clamped beam located at a stand-off  $S = 65$  mm are shown in Fig. 3.3a for  $v_p = 69.5$  m s<sup>-1</sup>. Here the stand-off  $S$  is defined in Fig. 3.4 and is equal to the distance between the leading end of the resting granular slug within the launcher and the front face of the beam. Upon impact, a plastic travelling hinge emanates from the impact site and travels to the supports. Simultaneously, the slug compacts and flows against the beam as it deforms (Fig. 3.3a). The permanent deflections  $w_p$  of the beam at mid-span (i.e. residual deflection at time  $t \rightarrow \infty$  after impact) are plotted in Fig. 3.5 as a function of  $v_p$  for two values of the stand-off  $S$ : the deflections increase with increasing  $v_p$  and decreasing  $S$ . These are the primary observations that we aim to model and thereby provide a more physical understanding of the mechanisms involved in interaction of high velocity granular media with deformable structures.

### 3.3 Numerical simulation methodology

The deformation of the beams resulting from impact of the WC particles was modelled using a coupled discrete particle/Lagrangian finite element simulation scheme. In this approach, the WC particles were modelled as discrete spherical particles using the GRANULAR

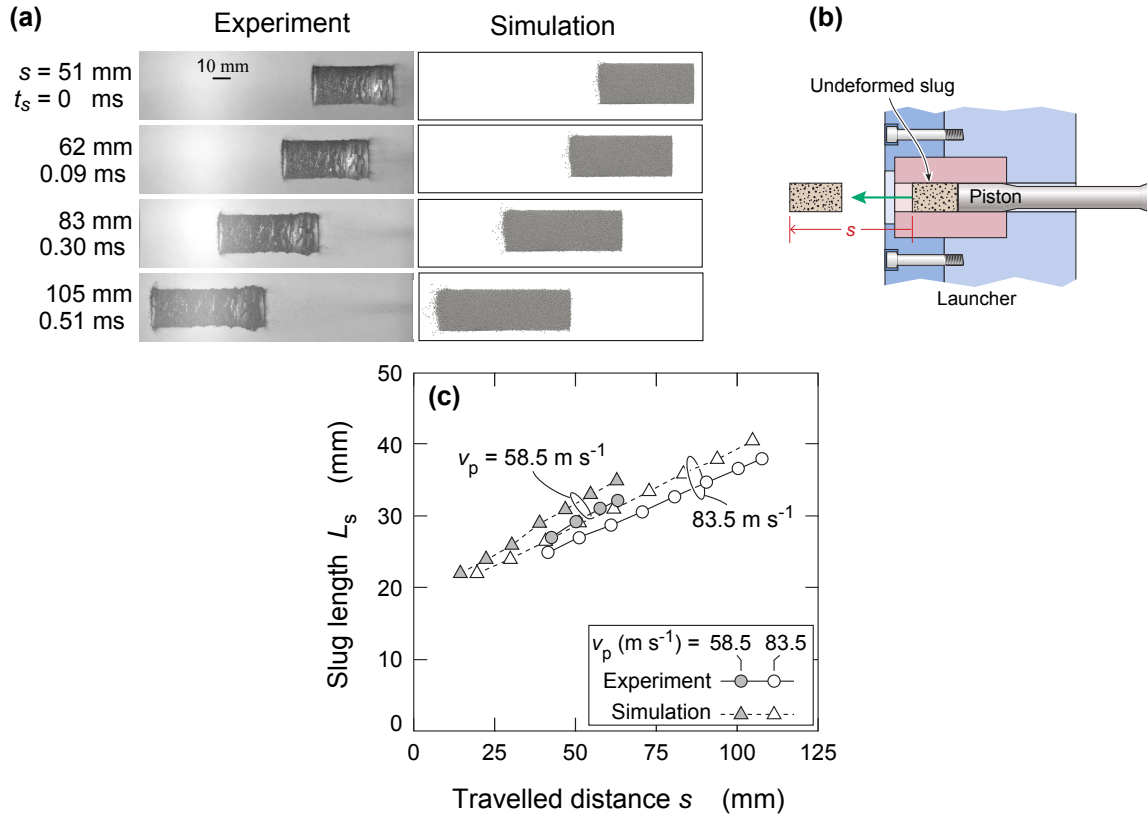


Fig. 3.2 (a) Snapshots from the observations of Uth et al. [126] and corresponding simulations showing the evolution of the granular slug generated (by piston velocity  $v_p = 83.5 \text{ m s}^{-1}$ ) at four selected values of the distance travelled  $s$ . The distance  $s$  is defined in (b) while time  $t_s=0$  is chosen arbitrarily for the first snapshot. (c) The corresponding measurements and predictions of the variation of the slug length  $L_s$  with  $s$  for two selected values of  $v_p$ .

package in the multi-purpose molecular dynamics code LAMMPS<sup>2</sup> while the beams were modelled within the Lagrangian commercial finite element package Abaqus<sup>3</sup>. These two modelling schemes were coupled using the multi-physics coupling code interface (MpCCI<sup>4</sup>) as described below. The modelling scheme therefore consisted of four steps: (i) the discrete particle approach to model the WC particles; (ii) generation of the high velocity slug due to the pushing of the slug out of the launcher by the piston; (iii) an FE scheme to model the beam; (iv) an MpCCI interface for coupling between the discrete particle and FE schemes. Effects of gravity and air drag<sup>5</sup> were neglected in the simulations.

<sup>2</sup><http://lammmps.sandia.gov/>

<sup>3</sup><http://www.3ds.com/>

<sup>4</sup><http://www.mpcci.de/>

<sup>5</sup>At the relatively low velocities considered here, we are in a Stokes drag regime where the reduction in the velocity of the particles over the millisecond time frames considered are negligible

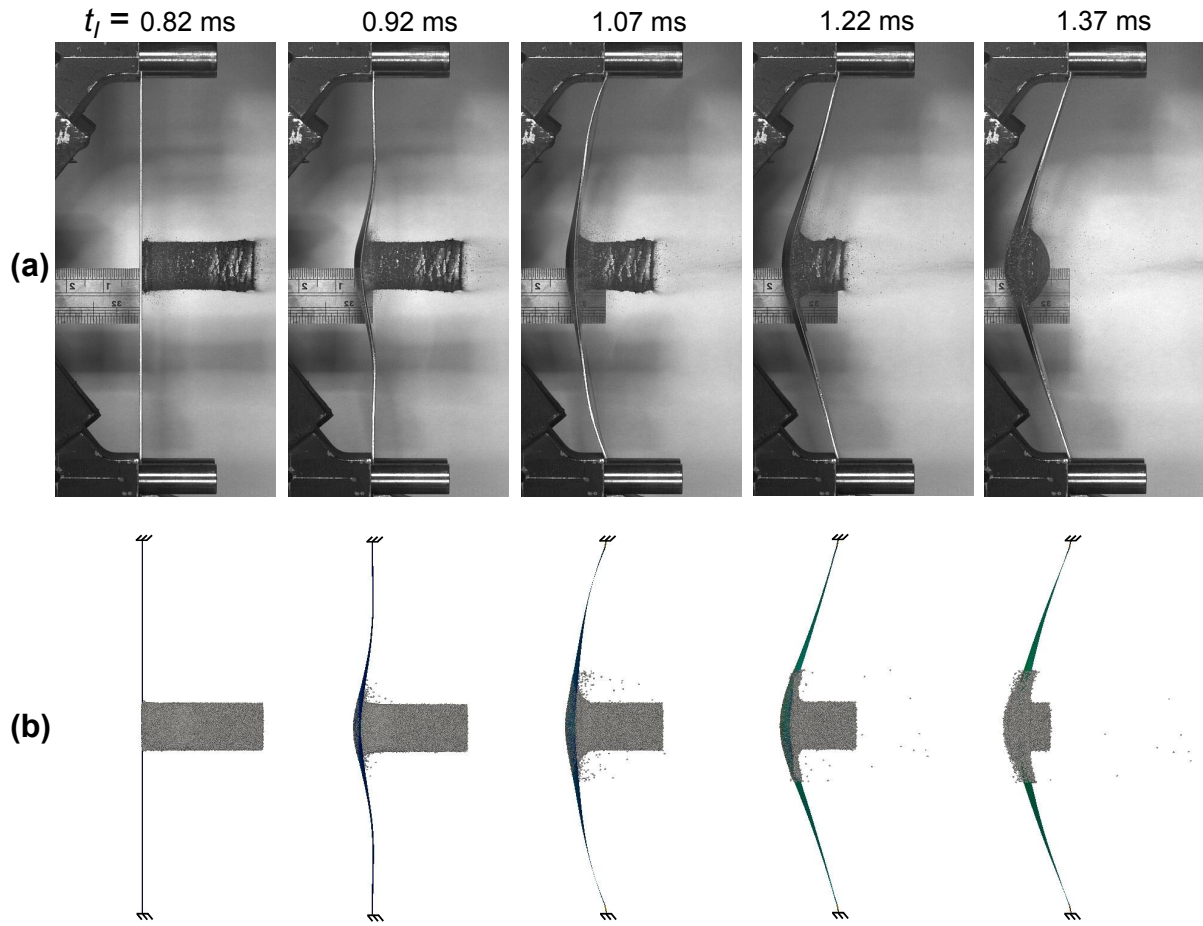


Fig. 3.3 (a) High-speed photographs showing a side view a granular slug generated by a piston at  $v_p = 69.5 \text{ m s}^{-1}$  impacting the clamped beam at a stand-off  $S = 65 \text{ mm}$  [126]. Photographs are shown at 5 selected values of time  $t_I$ , where  $t_I = 0$  corresponds to the instant the projectile impacts the piston. (b) The corresponding predictions using the coupled discrete/continuum simulations are also included.

### 3.3.1 Discrete particle calculations

The discrete particle calculations were done using the GRANULAR package in the multi-purpose molecular dynamics code LAMMPS [100]. Three dimensional simulations were performed using mono-sized spherical particles of diameter  $D$  and mass  $m_p$ . The granular package in LAMMPS is based on soft-particle contact model (Fig. 3.6), introduced by Cundall and Strack [24] and extended to large scale simulations by Campbell and Brennen [15] and Campbell [14]. The contact law comprises:

1. Linear spring with spring constant  $K_n$  and linear dashpot with damping constant  $\gamma_n$  connected in parallel, governing the contact in the direction connecting the particle centres.
2. Linear spring of constant  $K_s$  and Coulomb friction coefficient  $\mu$  connected in series, governing the tangential contact.

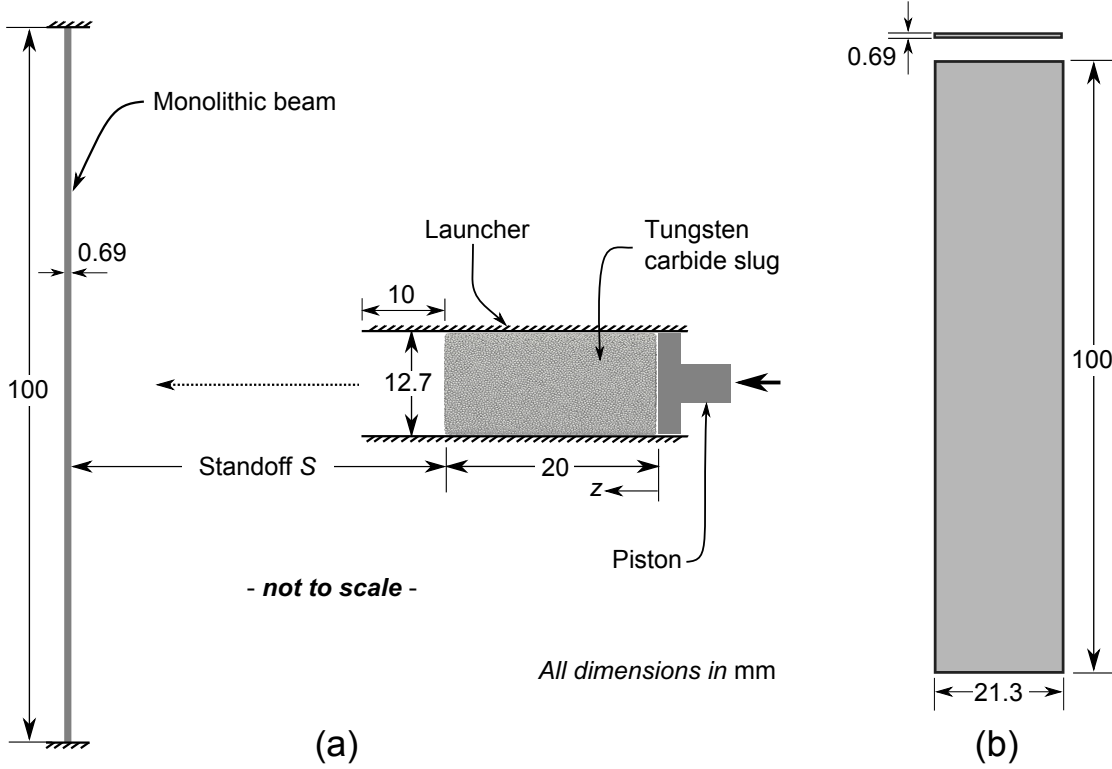


Fig. 3.4 (a) A side view sketch showing the setup used in the numerical simulations of the experiments of Uth et al. [126] and (b) plan view of the beam to show the span and width. All critical dimensions of the launcher, granular slug and beam are marked along with the definition of the stand-off  $S$ . The sketch is not shown to scale.

With  $r$  as the separation of the particle centres, and the interpenetration given by  $\delta_n = r - D$ , the normal force during active contact ( $\delta_n < 0$ ) is given by

$$F_n = K_n \delta_n + m_{\text{eff}} \gamma_n \dot{\delta}_n \quad (3.1)$$

where  $m_{\text{eff}}$  is the effective or reduced mass of the two contacting bodies. We take  $m_{\text{eff}} = m_p/2$  for impacts between particles, and  $m_{\text{eff}} = m_p$  for impacts between a particle and the beam.

The tangential force  $F_s$  only exists during active contact, and opposes sliding. It is limited in magnitude to  $|F_s| < \mu|F_n|$  as follows. Define  $\dot{\delta}_s$  as the tangential displacement rate between the contacting particles. Then,  $F_s$  is given by an “elastic-plastic” relation with stiffness  $K_s$ , i.e.

$$\dot{F}_s = \left\{ \begin{array}{ll} K_s \dot{\delta}_s & \text{if } |F_s| < \mu|F_n| \text{ or } F_s \dot{\delta}_s < 0 \\ 0 & \text{otherwise} \end{array} \right\} \quad (3.2)$$

The value of damping constant  $\gamma_n$  dictates the loss of energy during normal collision and is directly related to the coefficient of restitution  $e$  according to

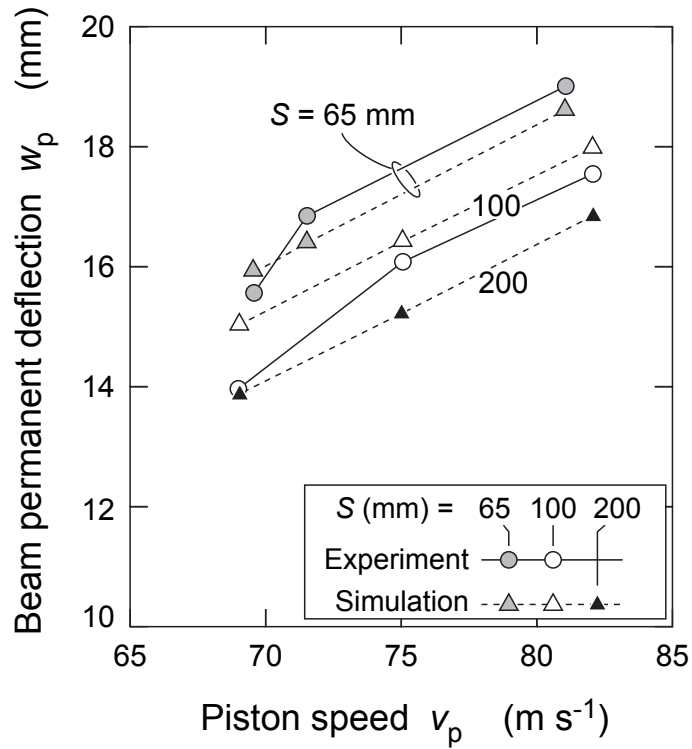


Fig. 3.5 Comparison between measurements and predictions of the permanent deflection of the mid-span of the beam as function of the piston velocity  $v_p$ . The results are shown for the two values of stand-off  $S = 65$  mm and 110 mm investigated by Uth et al. [126]. In addition predictions for  $S = 200$  mm are also included.

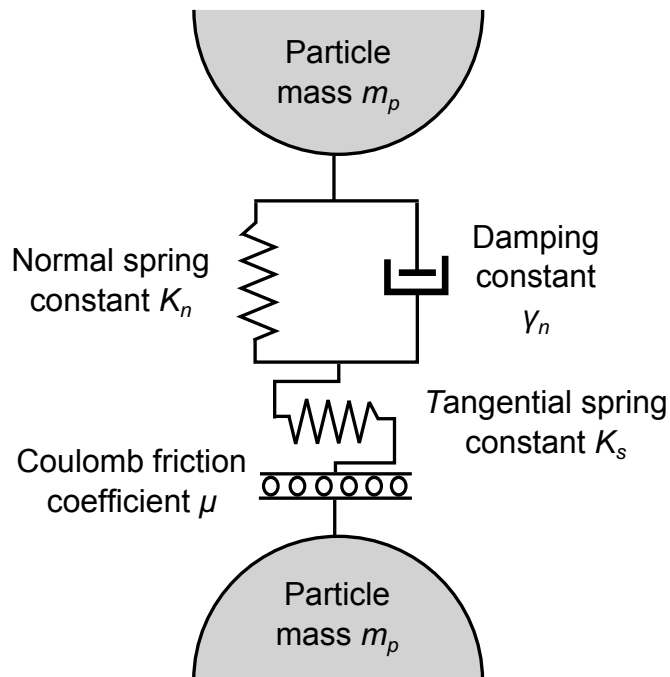


Fig. 3.6 Sketch of the inter-particle contact model between spherical particles of diameter  $D$  used to simulate the WC particles in the granular slug.

$$e = \exp \left[ - \frac{\pi}{\left( \frac{8K_n}{\gamma_n^2 m_p} - 1 \right)^{1/2}} \right] \quad (3.3)$$

The collision time  $t_e$  for individual binary collisions is given as as

$$t_e = -2 \frac{\ln(e)}{\gamma_n} \quad (3.4)$$

and thus in the limit of plastic collisions with  $e \rightarrow 0$ , the contact time  $t_e \rightarrow \infty$ .

Newton equations for both the translational and rotational motions of the particles were integrated using a Verlet time-integration scheme (i.e. Newmark-Beta with  $\beta = 0.5$ ). The time-step for integration was taken to be less than  $t_e/10$  in order to ensure accurate integration of the contact Eqs. 3.1 and 3.2.

### 3.3.2 Finite element calculations and coupling to the discrete particle calculations

The beams were modelled using three-node triangular elements (S3 in Abaqus notation). Clamped boundary conditions, with vanishing displacements were prescribed at the clamped ends (Fig. 3.4). The coupling between the LAMMPS discrete particle and the Abaqus finite element calculations was carried out via the MpCCI Code adapter API as follows. At any time  $t$ , suppose that a proportion of the particles are in contact with the plate. Consider one such particle. The displacement  $\delta_n$  is defined as  $\delta_n = r - D/2$ , where  $r$  is the distance between particle centre and contact point on the beam. The rate  $\dot{\delta}_n$  is the relative approach velocity of the particle and the point of contact on the beam surface, and likewise  $\dot{\delta}_s$  is the tangential velocity. The normal and tangential contact forces are calculated using Eqs. 3.1 and 3.2. These forces were then added as nodal forces to the appropriate elements of the Abaqus finite element calculations to complete the coupling between the discrete and finite element calculations.

### 3.3.3 Material properties

The beams were made from 304 stainless steel sheets which were modelled as J2-flow theory rate dependent solid of density  $\rho = 7900 \text{ kg m}^{-3}$ , Young's modulus  $E = 210 \text{ GPa}$  and Poisson's ratio  $\nu = 0.3$ . Uth et al. [126] reported the quasi-static tensile stress versus strain curve for the 304 stainless steel they employed in their study measured at an applied plastic strain rate  $\dot{\varepsilon}^p = 10^{-4} \text{ s}^{-1}$ . However, for the impact simulations we need to include strain rate sensitivity of the material, i.e. the strength  $\sigma_d(\varepsilon^p, \dot{\varepsilon}^p)$  as a function of both the plastic strain  $\varepsilon^p$  and strain rate  $\dot{\varepsilon}^p$ . Here we estimate  $\sigma_d$  as

$$\sigma_d(\varepsilon^p, \dot{\varepsilon}^p) = R(\dot{\varepsilon}^p)\sigma_0(\varepsilon^p) \quad (3.5)$$

where  $\sigma_0(\varepsilon^p)$  is the measured quasi-static stress versus strain curve and  $R(\dot{\varepsilon}^p)$  the strength enhancement at high strain rate. This strain rate enhancement factor was not reported by Uth et al. [126] so here we take  $R(\dot{\varepsilon}^p)$  from the measurements of Lichtenfeld et al. [78] who reported high strain rate experiments on stainless steel. The uniaxial tensile true stress versus equivalent plastic strain curves estimated using this procedure are plotted in Fig. 3.7 at selected values of the plastic strain-rate  $\dot{\varepsilon}^p$ . We emphasise here that Lichtenfeld et al. [78] reported measurements up to a maximum plastic strain-rate of  $400 \text{ s}^{-1}$ . However, strain rates on the order of  $2000 \text{ s}^{-1}$  were attained within the beam in the experiments. Thus, we linearly extrapolated  $R(\dot{\varepsilon}^p)$  from the Lichtenfeld et al. [78] measurements and included data in Abaqus simulations for strain rates  $10^{-4} \text{ s}^{-1} \leq \dot{\varepsilon}^p \leq 10^4 \text{ s}^{-1}$ .

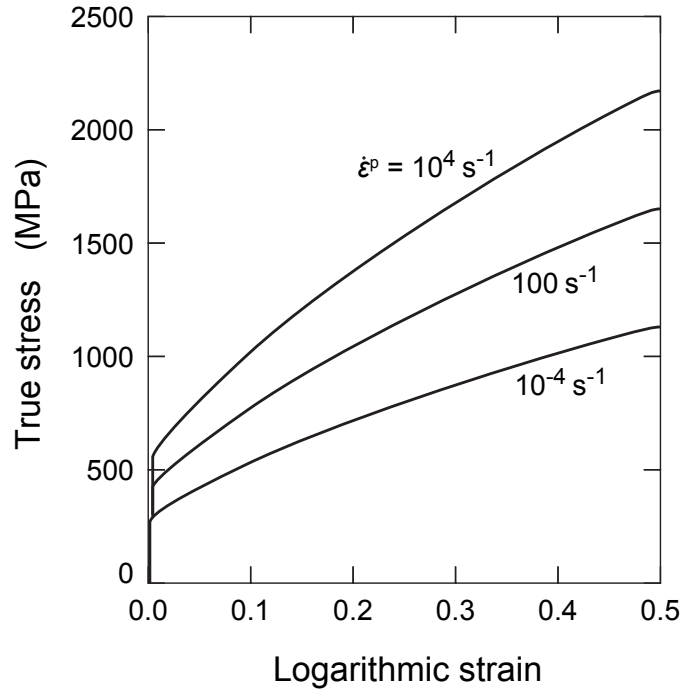


Fig. 3.7 The uniaxial true stress versus logarithmic strain curves of the AISI 304 stainless steel used to manufacture the test beams. The data for the quasi-static response measured at a strain rate  $\dot{\varepsilon}^p = 10^{-4} \text{ s}^{-1}$  is from Uth et al. [126] while the high strain rate behaviour is calculated by scaling this data using  $R(\dot{\varepsilon}^p)$  inferred from the measurements by Lichtenfeld et al. [78]; see Eq. 3.5.

The granular slug was modelled as comprising spherical particles of diameter  $D = 300 \text{ }\mu\text{m}$  made from a solid of density  $15630 \text{ kg m}^{-3}$  (equal to that of WC). Recall that the particles in experiments had sizes in the range  $45 \text{ }\mu\text{m}$  to  $150 \text{ }\mu\text{m}$ . However, in the simulations we chose a uniform particle size of  $D = 300 \text{ }\mu\text{m}$  to achieve a compromise between numerical accuracy and computational cost: decreasing the particle size increases the number of particles thereby the numerical cost. Goel et al. [44] have demonstrated the predictions of slug impact simulations to be reasonably insensitive to the particle size

(or equivalently the number of particles) as along the number of particles across the slug diameter exceeds about 20: with  $D = 300 \mu\text{m}$  this criterion was satisfied.

The contact model of the particle was defined in terms of the four parameters  $K_n$ ,  $e$ ,  $K_s$  and  $\mu$ . Liu et al. [79] demonstrated that these parameters do not affect the interaction response of the granular assembly impacting the beam. However, we shall show via parametric studies that some of these contact properties strongly influence the evolution of the granular slug as it emerges from the launcher. Unless otherwise specified, all calculations presented use the following set of parameters:  $K_n = 1 \text{ MN m}^{-1}$ ,  $K_s/K_n = 2/7$  [4, 112] and  $e = \mu = 0.7$ . Parameter studies to illustrate the sensitivity to these parameter choices are presented in Section 3.4.4.

### 3.4 Evolution of the granular slug during free-flight

It will be shown in Section 3.5 that an accurate prediction of the state of the granular slug just prior to its impact against the beam is critical in capturing the beam's dynamic deflection response. Thus, a key focus of this study is to predict the evolution of the granular slug as it is launched by the impact of the projectile.

Initial calculations suggested that three parameters dominated the evolution of the granular slug; viz. the inter-particle contact stiffness  $K_n$ , the piston velocity  $v_p$  and the ramp time  $T_R$  for the piston to acquire this velocity after impact by the projectile. We first discuss how the values of these parameters were selected, and then show the relatively weak dependence of the granular slug's evolution on the remaining contact parameters.

#### 3.4.1 Estimation of the particle contact stiffness

Uth et al. [126] measured the constrained compression of a WC particle slug in a cylindrical cavity as sketched in Fig. 3.8a. The dimensions and packing of the slug was identical to that used for impact experiments. The measured applied stress  $\sigma_n$  (ratio of the applied compressive force to the cross-sectional area  $A_0$  of the cylindrical cavity) versus nominal strain  $\varepsilon_n$  (ratio the displacement of the piston to the initial height  $h_0$  of the granular assembly within the cylinder) at a strain rate  $\dot{\varepsilon}_n = 10^{-3} \text{ s}^{-1}$  is plotted in Fig. 3.8b. This data was used to estimate the inter-particle stiffness  $K_n$  used in the model.

The WC spherical particles were packed into a rigid cylindrical cavity as sketched in the inset in Fig. 3.8b to create a granular assembly of identical dimensions to that used in the experiment shown in Fig. 3.8a. The spherical particles had an initial volume fraction (prior to the application of the compressive force) of 0.57. Simulations of the compressive response were conducted by compressing the granular assembly via a rigid piston as shown in Fig. 3.8b at a displacement rate  $\dot{\delta} = 200 \text{ mm s}^{-1}$  (corresponding to a nominal strain rate  $\dot{\varepsilon}_n = 10 \text{ s}^{-1}$ ). The predicted nominal stress  $\sigma_n$  versus nominal strain  $\varepsilon_n$

responses are plotted (as three dashed lines) in Fig. 3.8b for three choices of  $K_n$  with the remaining contact parameters kept fixed at their reference values. A contact stiffness  $K_n = 1.0 \text{ MN m}^{-1}$  brought the predictions into closest agreement with the measurements and this normal contact stiffness was then used as the reference case<sup>6</sup>. We emphasise that this calibrated value of  $K_n$  applies to the particle size  $D = 300 \text{ }\mu\text{m}$  employed in the simulations here and we anticipate the calibration to change if another particle size is used.

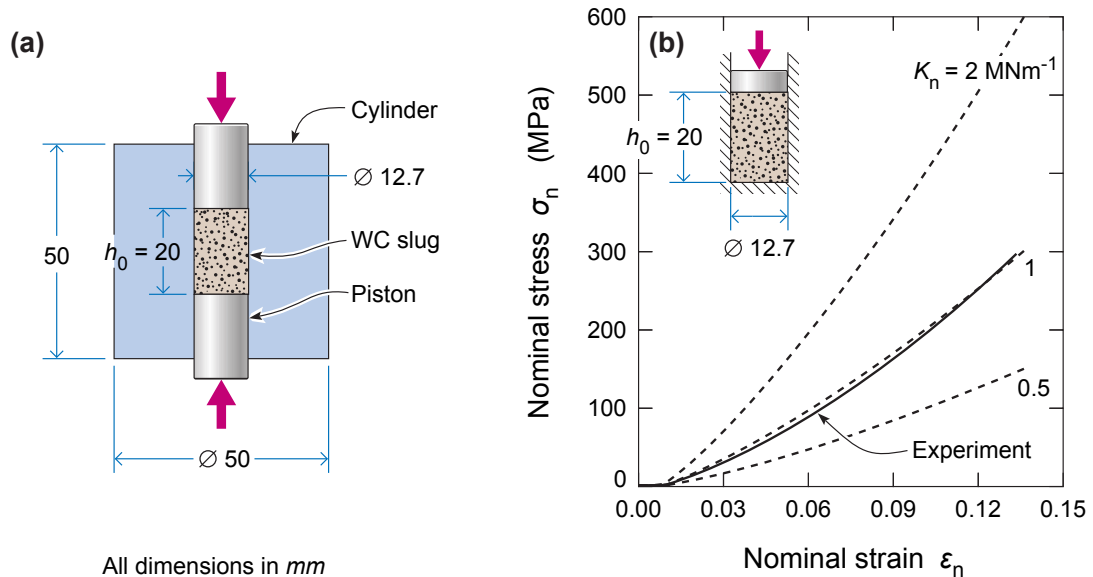


Fig. 3.8 (a) Sketch of the experimental setup employed by Uth et al. [126] to measure the constrained compression response of the granular slug. (b) Comparison between measurements [126] and predictions of the constrained compression response. Predictions are shown for three selected values of the normal inter-particle contact stiffness  $K_n$  and the setup used in the simulations is shown as an inset.

### 3.4.2 The piston velocity

A magnified sketch of the impact of the projectile against the piston that pushes the slug out of the launcher is shown in Fig. 3.9a. Upon impact of the projectile both an elastic and plastic wave emanate from the impacted end and propagate towards the end of the piston in contact with the granular slug. These waves deform the piston and thus the end of the piston in contact with the slug does not attain its final velocity instantaneously. To illustrate this effect, we use the data of Uth et al. [126] to plot the displacement in Fig. 3.9b of the four different markers on the piston shown in Fig. 3.9a for a projectile impact speed  $V = 217 \text{ m s}^{-1}$ . These displacements in Fig. 3.9b are plotted as a function of time  $t_I$ , where  $t_I = 0$  corresponds to the instant of impact of the projectile. The displacement rates of the markers (i.e. the marker velocities) reach the constant and equal value at large  $t_I$  as indicated in Fig. 3.9b. This is consistent with the fact that the deformation of

<sup>6</sup>The friction co-efficient, shear stiffness and damping do not affect the constrained compressive response shown in Fig. 3.8b over an applied strain rate range  $1 \text{ s}^{-1} \leq \dot{\epsilon}_n \leq 100 \text{ s}^{-1}$ .

the piston ceases at some time after impact of the projectile whereupon the piston behaves as a rigid body. This temporally and spatially constant marker velocity is defined as the piston velocity  $v_p$ : for the case of  $V = 217 \text{ m s}^{-1}$ ,  $v_p = 83.5 \text{ m s}^{-1}$ . The piston velocities for all the experiments of Uth et al. [126] are analysed in this manner and the relation between  $V$  and  $v_p$  is shown in Fig. 3.9c. Thus, Fig. 3.9c provides the translation between data in Uth et al. [126] presented in terms of  $V$  and the numerical results presented here in terms of  $v_p$ .

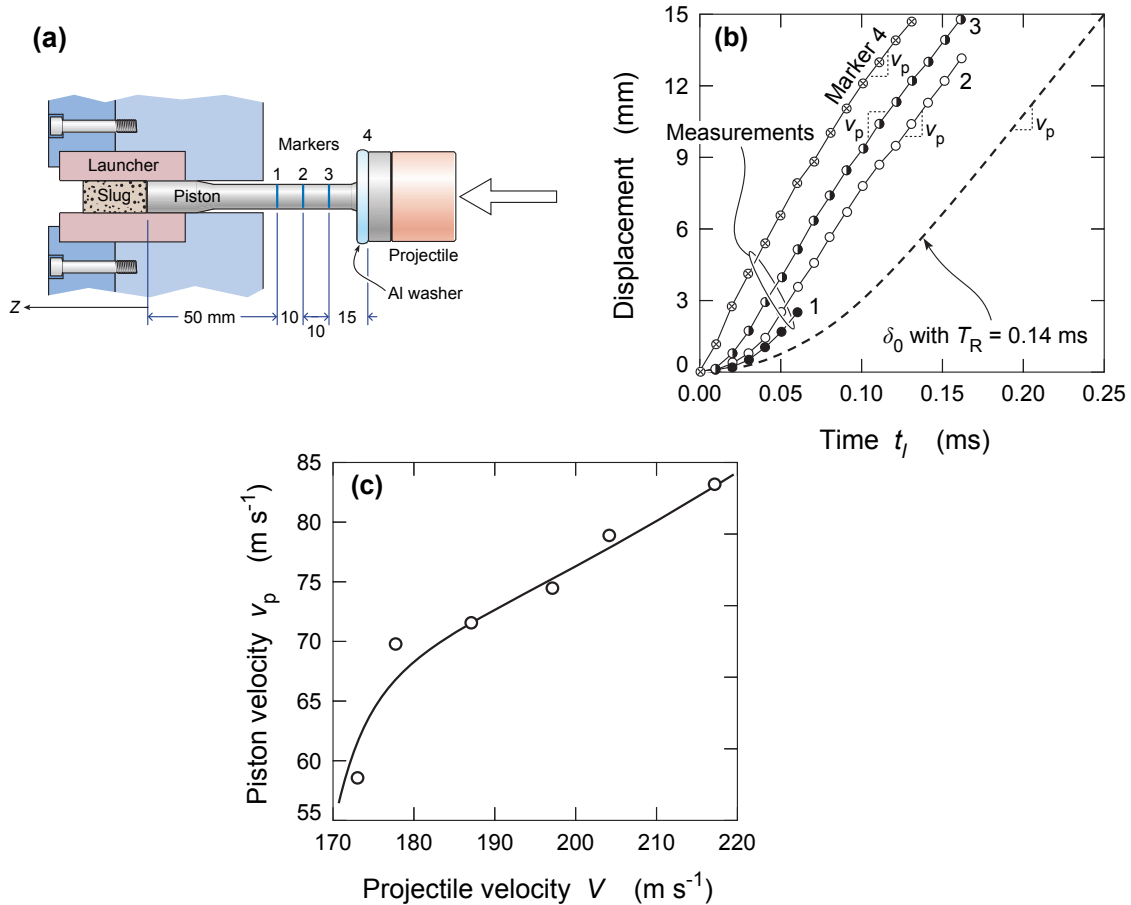


Fig. 3.9 (a) Magnified view of the launcher with the granular slug and the piston that is just impacted by the projectile. The locations of four marker lines on the piston are shown whose displacements are followed from the high-speed photographs of Uth et al. [126]. (b) The temporal evolution of the displacements of the four marker lines in (a) for a projectile impact velocity  $V = 217 \text{ m s}^{-1}$ . Here time  $t_I = 0$  corresponds to the instant of impact of the projectile. (c) The relation between the piston velocity  $v_p$  and projectile velocity  $V$  inferred from the high-speed photographs of the piston motion.

### 3.4.3 The ramp time for piston to acquire its steady-state velocity

In order to simplify the numerical calculations, the piston was modelled as a rigid body, pushing the granular slug out of the launcher (Fig. 3.4). The impact of the projectile with

the piston was not directly modelled, but rather the loading was specified by prescribing the instantaneous velocity relation,  $v_I(t_I)$  of the rigid piston. We thus need to prescribe to the rigid piston a  $v_I(t_I)$  relation measured at the end of the deformable piston that is in contact with the granular slug. However, while this end was not visible in the experiments, the marker displacement data in Fig. 3.9b suggests a piecewise displacement versus time relation for all markers; viz. the displacements first increase approximately quadratically with time for small  $t_I$  and then increase linearly with  $t_I$ . Thus, it is reasonable to approximate  $v_I(t_I)$  as

$$v_I = \begin{cases} \frac{v_p t_I}{T_R} & 0 \leq t_I \leq T_R \\ v_p & t_I > T_R \end{cases} \quad (3.6)$$

where  $T_R$  is the time taken for the piston to ramp up to its final velocity  $v_p$  after which it behaves as a rigid body. For an assumed value of  $T_R = 0.14$  ms, this gives a temporal variation of the displacement  $\delta_0 = \int v_I dt$  of the rigid piston as illustrated in Fig. 3.9b: we expect this displacement to closely resemble the displacement of the end of the piston in contact with the granular slug. While  $T_R = 0.14$  ms seems a reasonable choice given the displacement data in Fig. 3.9b, we emphasise that  $T_R$  cannot be directly inferred from the experimental measurements. We shall thus treat  $T_R$  as a free parameter and estimate it by comparing measurements of metrics of the evolution of the slug with predictions.

Two key metrics of the measured evolution of the slug were used to calibrate  $T_R$  and thereby judge the fidelity of the predictions:

1. The velocity at six markers points along the slug. These markers are diametrical lines fixed at six equally spaced material points along the length of the slug when it first completely emerges from the launcher. This scheme is consistent with that employed by Uth et al. [126] to characterise the particle velocities along the slug. The numbered markers are illustrated in the inset of Fig. 3.10a.
2. The evolution of the length  $L_s$  of the slug with the distance  $s$  travelled by the leading edge of the slug from its resting position as shown in Fig. 3.2c.

Simulations of the ejection of the granular slug from within the launcher were performed as follows. First the spherical WC particles were compacted into a cylindrical cavity of inner diameter  $D_0 = 12.7$  mm capped at one end by a rigid piston as shown in Fig. 3.4a. The compacted slug had a length  $L_0 = 20$  mm and the free end of the slug needed to travel a distance of 10 mm to emerge out of the launcher consistent with the experimental design of Uth et al. [126]. The piston was then imparted a velocity versus time history  $v_I(t_I)$  using Eq. 3.6 so as to push the slug out of the launcher. Unless otherwise stated the results discussed here use the estimate,  $T_R = 0.14$  ms.

Snapshots showing the predicted shape of the slugs at four values of  $s$  for the  $v_p = 83.5$  m s<sup>-1</sup> case are included in Fig. 3.2a along with the corresponding experimental

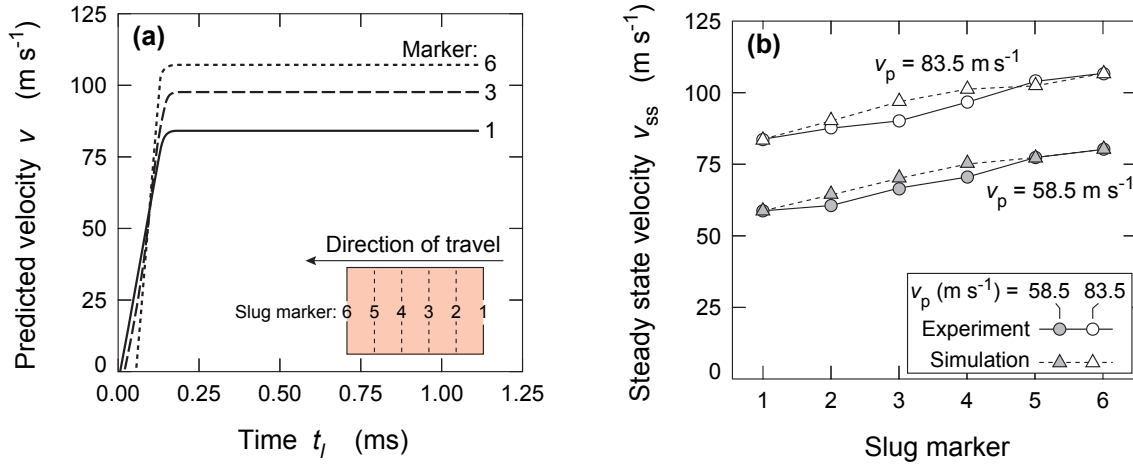


Fig. 3.10 (a) Predictions of the temporal variation of the velocities of material points associated with selected marker lines on the granular slug generated by the piston at a velocity  $v_p = 83.5 \text{ m s}^{-1}$ . The slug is divided into 6 equal segments immediately after it completely emerges from the launcher as indicated in the inset. Time  $t_I = 0$  corresponds to the instant of impact of the projectile. (b) Comparisons between predictions and measurements of the steady-state marker velocities  $v_{ss}$  for two values of the piston velocity  $v_p$ . The simulations are shown with  $T_R = 0.14 \text{ ms}$ .

observations. Consistent with the observations, the simulations predict that the slug elongates with increasing  $s$  while its diameter remains largely unchanged (a slight increase in the diameter of the slug near its trailing end was observed in the experiments and not predicted in the simulations- the reasons for this discrepancy are unclear). To quantify and explain the elongation of the granular slug, we proceed to characterise the velocity distribution along the length of the slug.

Predictions of the velocities of 3 selected markers for  $v_p = 83.5 \text{ m s}^{-1}$  are plotted in Fig. 3.10a as a function of  $t_I$ . Note that the markers were attached to material points after the slug first emerges from the launcher. Thus, these velocities were extracted from the simulations by tracing back the velocities of material points associated with each marker over the entire time history from the instant of the projectile impact. After an initial transient, the material points along the markers acquire a temporally constant velocity. We denote these steady-state marker velocities as  $v_{ss}$  and include predictions of  $v_{ss}$  for the six different markers in Fig. 3.10b for two values of the piston velocity  $v_p$ . In both cases,  $v_{ss}$  increases approximately linearly with marker number, i.e. the slug has a linear spatial velocity gradient with the leading edge moving faster compared to the trailing edge. Measurements of  $v_{ss}$  from Uth et al. [126] are included in Fig. 3.10b and show excellent agreement with the predictions for both the piston velocities. The velocity gradient along the slug implies that the slug elongates as it travels from the launcher towards its target. Predictions of the slug length  $L_s$  as a function of the distance travelled  $s$  are included in Fig. 3.2c for two the values of  $v_p$ : since the simulations capture  $v_{ss}$  with good accuracy it

also follows that predictions of  $L_s$  compare well with measurements over the entire range of measurements.

The velocity gradient along the slug length implies that the packing density of particles evolves with  $s$ . To visualise the evolution of the spatial distribution of the slug density we define  $\bar{n}$  as the number of particles per unit length of the slug in its current configuration. The density  $\bar{n}$  is calculated by first dividing the slug at any instant into  $\Delta L_s = 0.5$  mm long cylindrical discs and then defining  $\bar{n}(z) \equiv N/\Delta L_s$ , where  $N$  is the number of particles within each disc centred at location with axial co-ordinate  $z$ . Predictions of  $\bar{n}$  as function of a spatial co-ordinate  $z$  are included in Fig. 3.11 at three selected times  $t_I$  for  $v_p = 83.5$  m s<sup>-1</sup>. Here,  $z$  is defined in Fig. 3.9a as the spatial co-ordinate along the direction of travel of the slug with  $z = 0$  corresponding to trailing edge of the slug at its resting position within the launcher. A linear spatial velocity gradient along the slug length would have implied a spatially uniform  $\bar{n}$  along the slug with  $\bar{n}$  decreasing with increasing  $t_I$  as the slug elongates. However, the predictions in Fig. 3.11 clearly show a non-uniform spatial distribution of  $\bar{n}$  illustrating that the spatial velocity gradient along the slug length is not completely linear with an accumulation of particles occurring towards the leading edge of the slug.

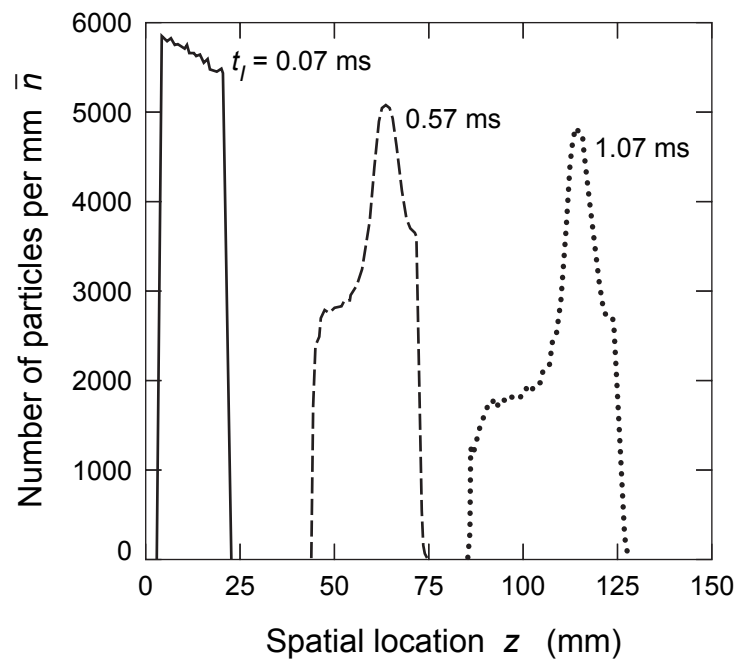


Fig. 3.11 Predictions of the evolution of the number of particles per unit length  $\bar{n}$  in the slug generated by the piston at a velocity  $v_p = 83.5$  m s<sup>-1</sup>. The simulations were performed using  $T_R = 0.14$  ms and the distribution  $\bar{n}(z)$  shown at three selected times  $t_I$ , where  $t_I = 0$  corresponds to the instant of impact of the projectile. The co-ordinate  $z$  is defined in Fig. 3.9a.

The discussion above was restricted to  $T_R = 0.14$  ms with good agreement between predictions and measurements obtained for all the measurements of Uth et al. [126]. To illustrate the sensitivity of the predictions to  $T_R$  we include in Fig. 3.12 predictions of

$v_{ss}$  for the six markers (for  $v_p = 83.5 \text{ m s}^{-1}$ ) for two additional values of  $T_R$ . It is clear that slightly higher or lower values of  $T_R$  give predictions of the spatial velocity gradients that are not in agreement with measurements. Given this agreement with the metrics of slug evolution and the displacement data of Fig. 3.9b, we argue that  $T_R = 0.14 \text{ ms}$  is the appropriate value to use for simulating the experiments of Uth et al. [126].

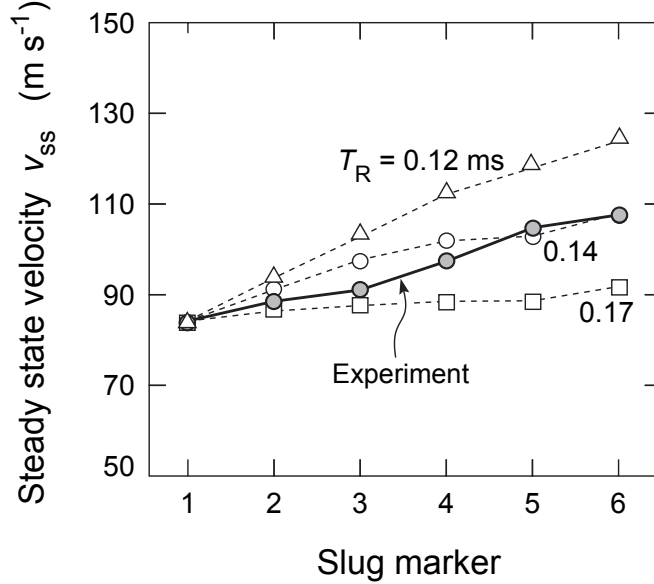


Fig. 3.12 Comparisons between predictions and measurements of the steady-state marker velocities  $v_{ss}$  of the slug for  $v_p = 83.5 \text{ m s}^{-1}$  and three selected values of the ramp time  $T_R$ . All other parameters are kept fixed at their reference values.

### 3.4.4 Sensitivity to contact model parameters

We proceed to illustrate the sensitivity of the predictions of the evolution of the slug to the assumed inter-particle contact parameters with  $T_R = 0.14 \text{ ms}$ . Predictions of the sensitivity of  $v_{ss}$  for the six slug markers (for  $v_p = 83.5 \text{ m s}^{-1}$ ) to  $K_n$ ,  $e$  and  $\mu$  are included in Figs. 3.13a, 3.13b and 3.13c, respectively. In each case, the value of the parameter varied is indicated in the legend with all other contact parameters kept fixed at their reference values. The experimental measurements are included in each case for comparison purposes. It is clear that while the predictions are sensitive to  $K_n$ , the sensitivity to the co-efficient of restitution  $e$  and friction co-efficient  $\mu$  is negligible over a realistic ranges of these parameters. We emphasise that  $K_n$  has been independently estimated using constrained compression test (Section 3.4.1) to justify the choice of  $K_n = 1 \text{ MN m}^{-1}$ . Moreover, particle size also does not directly affect these predictions although changing particle size will affect the calibrated value of  $K_n$  as discussed earlier.

The predictions of Figs. 3.12 and 3.13 illustrate that the spatial velocity gradients increase with decreasing  $T_R$  and  $K_n$ . This observation gives insight into the mechanism

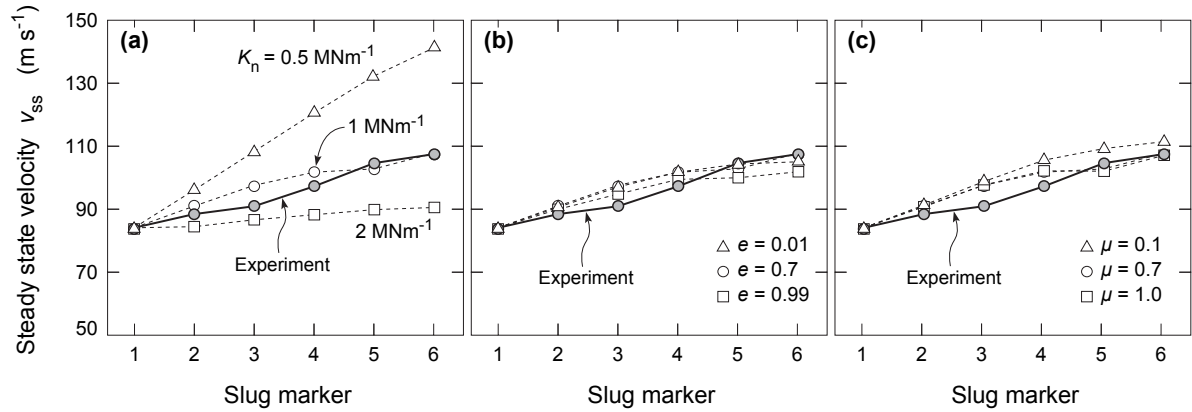


Fig. 3.13 The sensitivity of the predictions of the steady-state marker velocities  $v_{ss}$  of the slug for  $v_p = 83.5 \text{ m s}^{-1}$  to (a) the normal contact stiffness  $K_n$ , (b) co-efficient of restitution  $e$  and (c) friction co-efficient  $\mu$ . In each case, predictions are shown for three values of the respective parameter with all other parameters kept fixed at their reference values. The experimental measurements [126] are included for comparison purposes in each case.

that results in the elongation of the granular slugs. The driving of the piston at  $v_I(t_I)$  results in a compressive elastic wave propagating into the granular slug. When this compressive wave reaches the leading free-edge of the slug at time  $T_L$ , the entire slug starts to move. For times  $t_I < T_L$ , the displacement of the piston is accommodated solely by the compression of the slug. Thus, the compression of the slug is higher if (i) for a given  $v_I(t_I)$ ,  $T_L$  increases as the elastic wave speed is lower and (ii) for a given  $T_L$ ,  $T_R$  is reduced which then increases the piston displacement in time  $T_L$ . The elastic wave speed decreases with decreasing  $K_n$  resulting in a larger compression and stored elastic energy within the slug. Similarly, the stored elastic energy increases with decreasing  $T_R$ . This stored elastic energy is released during the free-flight of the slug and results in a velocity gradient that causes the slug to elongate.

### 3.5 Impact of granular slug against structures

To predict the response of clamped beams impacted normally and centrally by the granular slugs as reported by Uth et al. [126], simulations were conducted as described in Section 3.3.2 with the slug generated for any given piston velocity  $v_p$  using the procedure discussed in Section 3.4. All simulations use the reference beam material and inter-particle contact properties listed in Section 3.3.3 and a ramp time  $T_R = 0.14 \text{ ms}$ . Friction between the particles and beam surface was neglected.

### 3.5.1 Impact against a clamped monolithic beam

In the experiments of Uth et al. [126], measurements are reported by varying two loading parameters; viz. the piston velocity  $v_p$  and the stand-off  $S$  defined as the distance between the leading end of the slug at its resting position within the launcher and the front end of the clamped beam; see Fig. 3.4. Predictions of both the influence of  $v_p$  and  $S$  on the observed response of the beams are therefore investigated.

Comparisons between predictions and observations of the deformation mode of the slug and the beam after impact by the slug are summarised in Fig. 3.3 for the case of  $v_p = 69.5 \text{ m s}^{-1}$  and  $S = 65 \text{ mm}$ . Side view photographs showing the deformations from the experiments along with images of the same view from the simulations are included in Fig. 3.3 for 5 selected values of the time  $t_I$ . Consistent with the observations, the simulations predict that immediately after impact, a plastic wave emanates from the impact site and traverses towards the clamped end of the beam. Such dynamic plastic travelling hinges have been extensively reported; see for example [66]. Simultaneously, the slug compacts and spreads against the beam. After the plastic hinges impinge upon the supports, the slug continues to compact against the beam and the beam deflection continues to increase by a stretching deformation mode. The beam reaches its maximum deflection at  $t_I \approx 1.25 \text{ ms}$ . Some elastic rebound of the beam was observed both in the experiments and simulations after the peak deflection has been attained. This results in reflection of the granular particles in contact with the beam. We emphasise here that there are some minor discrepancies between the predicted slug shapes and observations especially towards the end of the deformation history. For example, at  $t_I = 1.37 \text{ ms}$  the slug has completely densified against the beam in the experiments while the densification process is not yet complete in the simulations. This discrepancy is partly related to the fact that the simulations predict a slightly longer slug (see Fig. 3.2c) and partly to the fact that the simulations do not accurately account for friction between the beam and the particles. This frictional interaction governs the formation of the “friction hill” of particles on the beam as seen in the experiments at  $t_I = 1.37 \text{ ms}$  but is missing in the simulations.

An oblique view of the simulation snapshots shown in Fig. 3.3b is included in Fig. 3.14 with contours of the von Mises equivalent plastic strain now included for the beam. These images more clearly show the spreading of the slug over the surface of the beam along both the width and beam length. Moreover, the contours illustrate that plastic strain (and probability of failure) is maximized at the clamped supports, and although not visible in Fig. 3.14, around the impact site. “Dishing” of the beam at the impact site was observed by Uth et al. [126] and also predicted by the simulations as seen in the cross-sections of mid-span views included in Fig. 3.14.

Comparisons between the predictions and measurements of the variation of the mid-span deflections  $w$  with time  $t_I$  are included in Figs. 3.15a and 3.15b for  $S = 65 \text{ mm}$  and  $110 \text{ mm}$ , respectively. Recall that the impact of the slug results in “dishing-type”

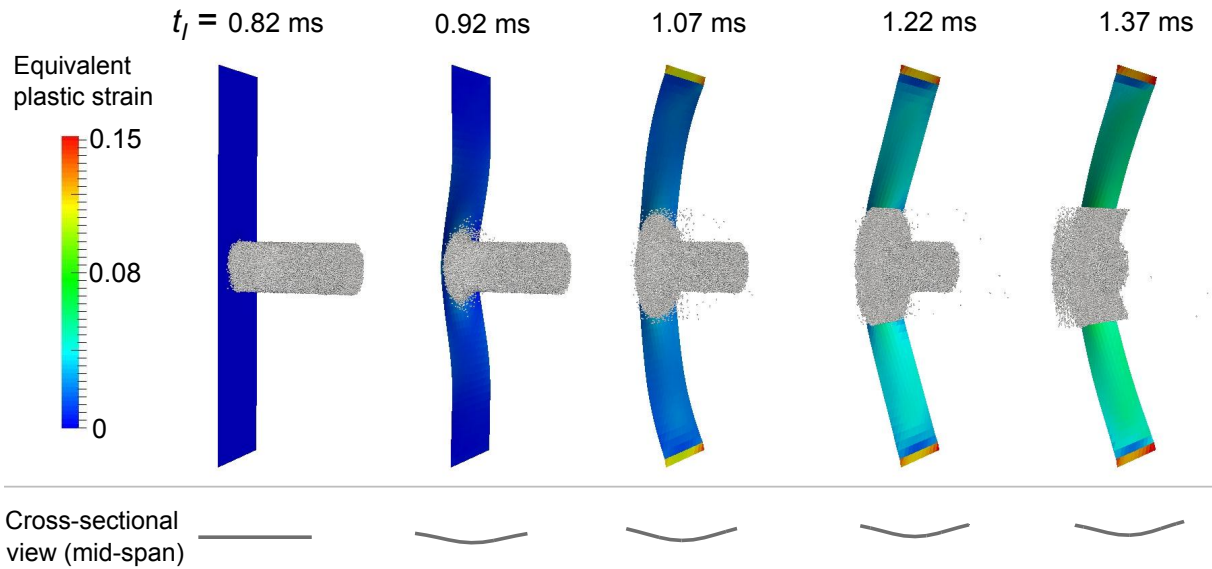


Fig. 3.14 Predictions showing an angled view of the deformation of the beam and granular slug generated by a piston at  $v_p = 69.5 \text{ m s}^{-1}$  impacting the clamped beam at a stand-off  $S = 65 \text{ mm}$ . Contours of von-Mises equivalent plastic strain are included on the beam and the snapshots shown at the 5 selected times  $t_I$  used in Fig. 3.3. Here, time  $t_I = 0$  corresponds to the instant the projectile impacts the piston. Cross sectional views of the mid-span of the beam are also shown for the each  $t_I$ .

deformation under the impact site and thus  $w$  is measured both in the experiments and simulations at the geometric centre of the beam span. Excellent agreement for the temporal variation of  $w$  is observed between the measurements and simulations. While the simulations proceed to long times where a permanent beam deflection is well defined, the temporal measurements of  $w$  reported in Uth et al. [126] do not span the full range of times simulated because spreading of the granular slug obscured the imaging of the beam deflection. However, we have included in Fig. 3.15 measurements of the permanent mid-span deflections  $w_p$  reported in Uth et al. [126] (measured with the beam still in the clamping rig but after all the elastic oscillations have damped out). The measured values of  $w_p$  are in agreement with the steady-state values of the simulated beam deflections  $w$ .

Comparisons between predictions and measurements of  $w_p$  over the range of piston velocities  $v_p$  investigated by Uth et al. [126] for two stand-off  $S$  values are included in Fig. 3.5. The agreement over the entire range of measurements is always within 8% indicating the fidelity of the simulations. The increase in deflection with increasing  $v_p$  is primarily due to the larger momentum of the impacting granular slug (i.e. the larger piston velocities impart a higher velocity to the granular slug). This larger momentum results in larger beam deflections in line with simulations reported in a number of studies of granular impacts against deformable targets; see for example [79, 30, 127]. However, the dependence of  $w_p$  on slug stand-off is less clear since, for a given  $v_p$ , the momentum of the granular slug prior to impact against the beam is independent of  $S$ . We proceed to investigate this dependence by examining the impact of the slug against a rigid stationary target.

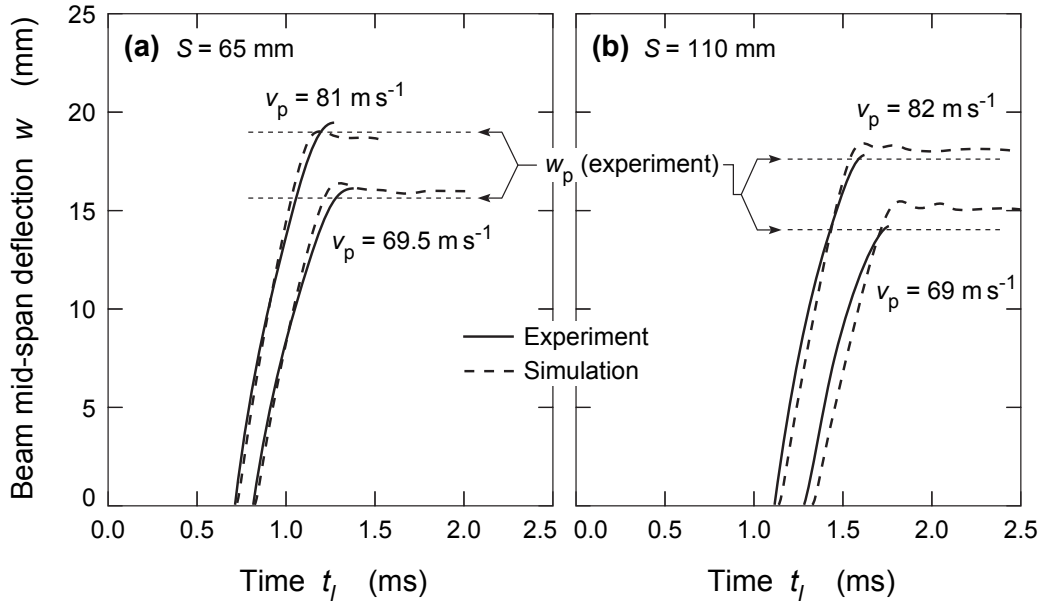


Fig. 3.15 Predictions of the temporal variation of the deflection  $w$  of the geometric centre of the clamped beam with time  $t_I$  for a stand-off (a)  $S = 65$  mm and (b)  $S = 110$  mm. In each case, predictions are shown for two values of the piston velocity  $v_p$  along with the corresponding experimental measurements of Uth et al. [126]. The permanent deflections  $w_p$  reported by Uth et al. [126] are indicated by horizontal dashed lines in each case. Time  $t_I=0$  corresponds to the instant the projectile impacts the piston.

### 3.5.2 Impact against a rigid stationary target

Liu et al. [79] demonstrated that the dynamic response of beams impacted by granular slugs with a spatially uniform density and velocity can be uniquely characterised in terms of two loading parameters: (i) a non-dimensional measure of the momentum of the slug and (ii) the ratio  $\bar{\tau}$  of the loading time to the response time of the beam. A schematic representation of the predictions of Liu et al. [79] are illustrated in Fig. 3.16 where the variation of the  $w_p/L$  is plotted as a function of  $\bar{\tau}$  for fixed values of the non-dimensional momentum  $\bar{I}$ . This sketch captures the salient points: (i)  $w_p/L$  increases with  $\bar{I}$  and (ii) for a given  $\bar{I}$ ,  $w_p/L$  increases with decreasing  $\bar{\tau}$  until it reaches its maximum value corresponding to the impulsive limit for the given  $\bar{I}$ . As  $S$  increases, the slug just prior to impact lengthens, resulting in a longer loading time (i.e. higher  $\bar{\tau}$ ) and therefore smaller beam deflections. It is thus reasonable to conclude that the stand-off dependence seen here is due to slug elongation as it travels towards the beam.

To investigate this further, simulations of the normal impact of the same granular slug against a rigid stationary wall have been conducted. These simulations can be used to determine the loading time and pressure history imparted by the granular slug as a function of the stand-off  $S$  in the absence of any fluid-structure interaction effects that are operative during slug impact with a deformable beam. The setup used for the simulations was similar to that illustrated in Fig. 3.4 with one difference: the monolithic beam target was replaced by a rigid stationary wall. These calculations were conducted with contact

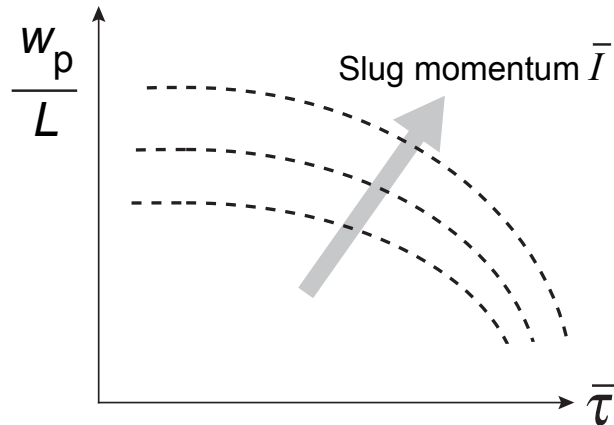


Fig. 3.16 Sketch illustrating the dependence of the normalised beam deflections  $w_p/L$  on the normalised loading time  $\bar{\tau}$ . Curves are shown for selected values of the normalised slug momentum  $\bar{I}$ . This sketch is inferred from the simulations of Liu et al. [79] for slugs with spatially uniform density and velocities impacting clamped beams.

properties between the particles and the wall identical to those between the deformable beam and the particles. Snapshots showing the deformation of the granular slug ( $v_p \approx 69 \text{ m s}^{-1}$ ) at four selected times  $t_I$  are shown in Fig. 3.17 for a rigid wall and a stand-off  $S = 65 \text{ mm}$ . The slug compacts and spreads against the rigid target analogous to the spreading of a water jet during impingement on a rigid wall as previously reported by Pingle et al. [99].

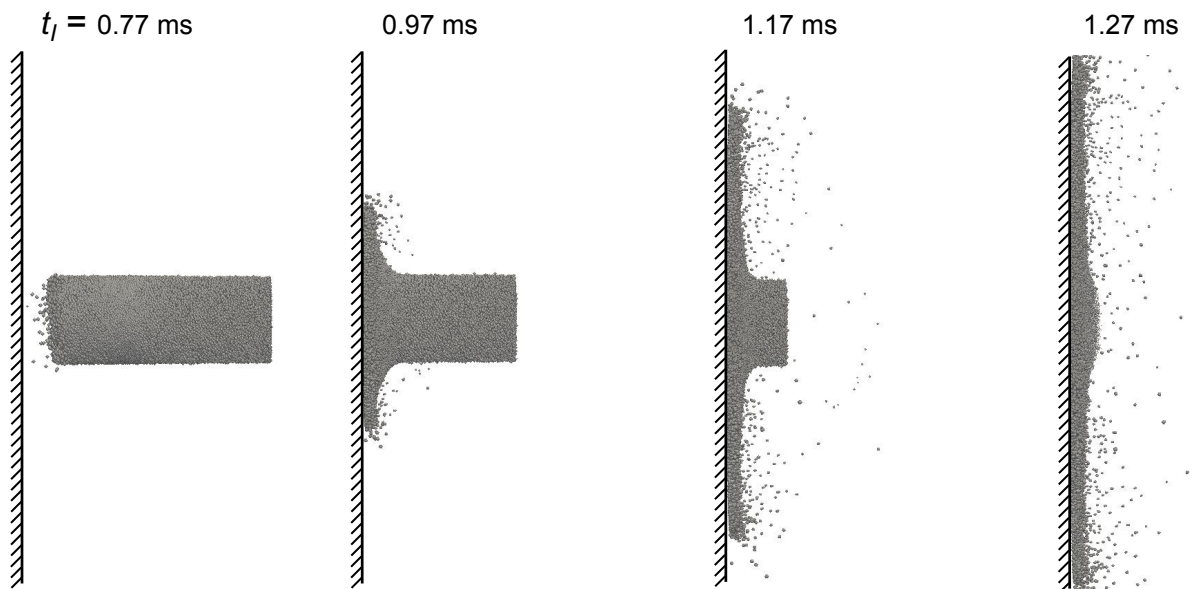


Fig. 3.17 Predictions of the deformation of the slug generated by piston at  $v_p \approx 69 \text{ m s}^{-1}$  impinging the rigid wall at a stand-off  $S = 65 \text{ mm}$ . Snapshots are shown at four selected times  $t_I$ , where  $t_I = 0$  corresponds to the instant the projectile impacts the piston.

We define a nominal pressure  $p_w(t_I)$  exerted by the impinging slug on the wall as the ratio of the total force  $F_w(t_I)$  exerted by the particles on the wall at time  $t_I$  and the

cross-section area  $\pi D_0^2/4$  of the slug within the launcher. Predictions of the variation of  $p_w$  with  $t_I$  are included in Figs. 3.18a and 3.18b for piston velocities  $v_p = 69 \text{ m s}^{-1}$  and  $82 \text{ m s}^{-1}$ , respectively and three values of the stand-off  $S$  in each case. In all the cases, there is a sudden rise in the contact pressure  $p_w$  immediately upon the impact of the slug and subsequently the general trend is for the pressure to decrease. This decrease can be rationalised by noting that we expect the pressure to scale as  $p_w \propto \rho v^2$  [95] where  $\rho$  and  $v$  are the density and velocity of the region of the slug currently in contact with the wall. The decrease in  $p_w$  with increasing time is consistent with the fact that the particle velocity  $v$  decreases from the leading to the trailing edge of the slug; see Fig. 3.10b. Moreover, since slug elongates as it traverses towards the target, the loading time increases with increasing stand-off  $S$ . However, the total slug momentum is independent of  $S$  (as interactions of the slug with air are neglected) and thus the average contact pressure decreases with increasing  $S$ .

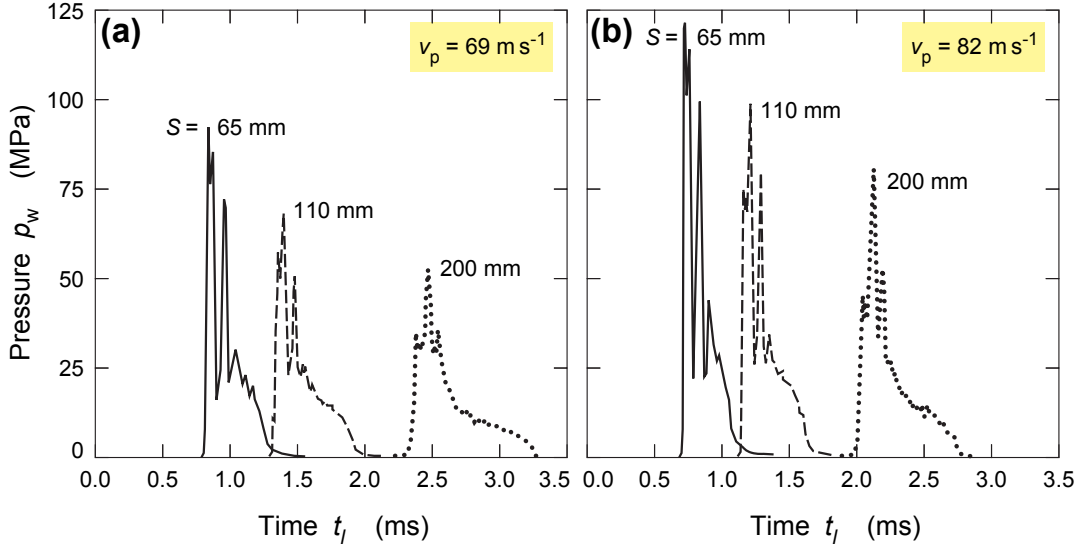


Fig. 3.18 Predictions of the temporal variation of the pressure  $p_w$  exerted by the granular slug impinging normally on a rigid stationary target. The slugs are generated by piston velocities (a)  $v_p = 69 \text{ m s}^{-1}$  and (b)  $v_p = 82 \text{ m s}^{-1}$ . Results are shown in each case for three values of the stand-off  $S$  with time  $t_I = 0$  corresponding to the instant the projectile impacts the piston.

The predictions of the contact pressure exerted by the slug upon normal impact against a rigid stationary target clearly show that the contact pressures decrease with increasing  $S$  and decreasing  $v_p$ . This results in the stand-off and piston velocity dependencies of the beam deflections seen in Fig. 3.5. For the sake of completeness we have included predictions of the permanent deflections of the beam as a function of  $v_p$  in Fig. 3.5 for a stand-off  $S = 200 \text{ mm}$  (Uth et al. [126] did not report measurements for this case). Consistent with expectations, the beam deflections are lower compared to the  $S = 65 \text{ mm}$  and  $110 \text{ mm}$  cases.

In order to illustrate the main features of the sand slug loading predicted in these simulations, we present simple analytical expressions for  $p_w(t_I)$  for the case of a linear velocity distribution within the slug. Such a distribution was experimentally observed by Uth and Deshpande [125]. In this case, the steady-state velocity  $v_{ss}$  of sand particles located at a distance  $X$  ahead of the rear end of the initially stationary slug is given as

$$v_{ss} = \bar{v} + b \left( X - \frac{L_0}{2} \right) \quad (3.7)$$

where  $\bar{v}$  is the mean slug velocity and  $b$  the parameter that sets the gradient of the velocity within the slug of length  $L_0$ . Then, the pressure exerted by the slug on a rigid stationary wall follows from the above-mentioned scaling law as

$$p_w = \rho_0 \left[ \frac{\bar{v} + b \left( X - \frac{L_0}{2} \right)}{\bar{v} + b \left( S + \frac{L_0}{2} \right)} \right] v_{ss}^2 \quad (3.8)$$

where  $\rho_0$  is the initial density of the slug and  $X$  is related to time  $t_I$  via

$$X = \frac{S + L_0 + t_I \left( \frac{bL_0}{2} - \bar{v} \right)}{1 + bt_I} \quad (3.9)$$

These expressions are valid over the time range  $S/(\bar{v} + bL_0/2) \leq t_I \leq (S + L_0)/(\bar{v} - bL_0/2)$  with  $p_w = 0$  outside this time range. Equations 3.8 and 3.9 predict a reducing pressure  $p_w$  with increasing time similar to the numerical results in Fig. 3.18 and also the numerically predicted dependence on the stand-off, i.e. a reduction in the peak pressure and longer time period of loading with increasing  $S$ . However, we do not make detailed numerical comparisons between these analytical predictions and the simulations as the slugs in this study did not have a linear velocity distribution as per Eq. 3.7.

## 3.6 Concluding remarks

Coupled discrete particle/continuum simulations for the normal impact of granular slugs against deformable clamped beams have been reported. The simulations were designed to replicate the experimental setup employed by Uth et al. [126] and detailed comparisons have been made with those observations.

A high velocity granular slug of cylindrical geometry is generated by the ejection of the slug from a launcher by the pushing action of a piston. The pushing action results in storage of elastic strain energy within the slug. The release of this elastic energy during free-flight results in axial stretching due to spatial velocity gradients within the slug. These velocity gradients are a strong function of the inter-particle contact stiffness and the time

required for the piston to reach its final velocity. Other inter-particle contact properties such as damping and friction have a negligible effect on the evolution of the granular slug as it was launched towards its target. Experimental observations were used to estimate both the effective contact stiffness and the piston ramp time. Numerical predictions using these values were in agreement with observations for the evolution of the granular slug in terms of the spatial velocity gradients as well as the overall length of the slug.

Coupled finite element/discrete particle simulations of the impact of these slugs against clamped beams enabled the temporal evolution of the deformations as well as the permanent deflections of the beams to be predicted and compared with measurements. The predictions agreed well with the observations. The increase in the deflections with the slug velocity was a direct consequence of the higher momentum of the slug. The stand-off dependence arose from the lengthening of the slugs as they travel towards the beams. This lengthening resulted in longer loading times and lower contact pressures on the beams which resulted in smaller permanent (plastic) deflections.

The studies of Liu et al. [79] and Pingle et al. [99] demonstrated that for a given sand slug (i.e. given spatial velocity and density distribution), the response of structures is relatively insensitive to the contact properties of the granular particles. However, here we demonstrate that the generation of the slug due to shock loading applied via a piston strongly depends on at-least the time required to accelerate the granular media and the normal contact stiffness between the particles. The ensuing velocity and density distributions within the slug in turn govern the responses of the impacted beams and results in a stand-off effect. There is a wealth of experimental data that suggests a strong dependence of the effect of the type of granular media and stand-off on the response of structures subjected to landmine loading [38, 98, 58, 57]. The simulations reported here have shed light into mechanisms that may help rationalise such observations.

# Chapter 4

## Effect of surface properties on momentum transfer to targets impacted by high-velocity sand slugs

### Abstract

The response of dry and water saturated sand slugs impacting normally oriented and inclined rigid-stationary targets with four different surface coatings is measured with an emphasis on the quantification of the momentum transmitted from the slugs into the targets. The targets were coated with Alumina, PTFE, Aluminium or sand-paper layers in order to investigate the effect of varying surface hardness and surface roughness. In all the cases, the fraction of the slug momentum transferred into the target was equal for dry and water saturated sand slugs and also independent of the slug velocity over the range  $73 \text{ m s}^{-1}$  -  $137 \text{ m s}^{-1}$  that is investigated here. For normal impacts, the surface coatings had no measurable influence on the momentum transfer into the targets and this was attributed to the symmetry of the impact event. However, the break of symmetry in the inclined impact cases resulted in two non-zero components of the net transmitted momentum into the targets and a strong influence of the surface coatings. This is attributed to friction between the sand particles and the target surface with the resultant transmitted momentum increasing in the order Alumina to PTFE to Aluminium to sand-paper surface coatings. In all cases, the transmitted momentum was less than the corresponding value under normal impact. Coupled discrete particle/Lagrangian simulations of these experiments with the sand particles modelled as spheres captured the normal impact measurements with a high degree of fidelity. However, the simulations underestimated the transmitted momentum for the inclined impacts especially for the rough surface coatings such as the sand-paper: increasing the friction coefficient between the particles and the target in the simulations did not improve the predictions. We demonstrate that this discrepancy is due to the spherical particle assumption: in the experiments the sand particles are

sub-spherical and this reduces the tendency of particles to roll on the target surface and thereby increases frictional interactions. Increasing the radius of gyration of particles decreased the discrepancy between the measurements and the predictions but yet could not accurately predict all components of the transmitted momentum. Most numerical calculations tend to use spherical particles to represent the impacting granular media. However, this study demonstrates the need to appropriately parameterise particle shape in such discrete particle calculations to accurately capture the granular media/structure interactions.

## 4.1 Introduction

The design of vehicle underbody structures that can survive the impact of soil ejected by shallow-buried explosives has been a topic of considerable interest for many years. Numerous strategies have been proposed to improve the impulsive load resistance of these underbody structures including (i) replacing the monolithic underbody by sandwich panels [30, 79, 108, 127], (ii) increasing the stand-off distance of the vehicle floor from the ground [30, 11, 56, 98], and (iii) inclining the underbody with respect to the ground by making use of a V-shaped hull design [2, 7, 37, 41] as sketched in Fig. 4.1. In all approaches, understanding the level of momentum transferred from the high-velocity soil ejecta onto the loaded structure (the target) is of primary importance to their successful implementation.

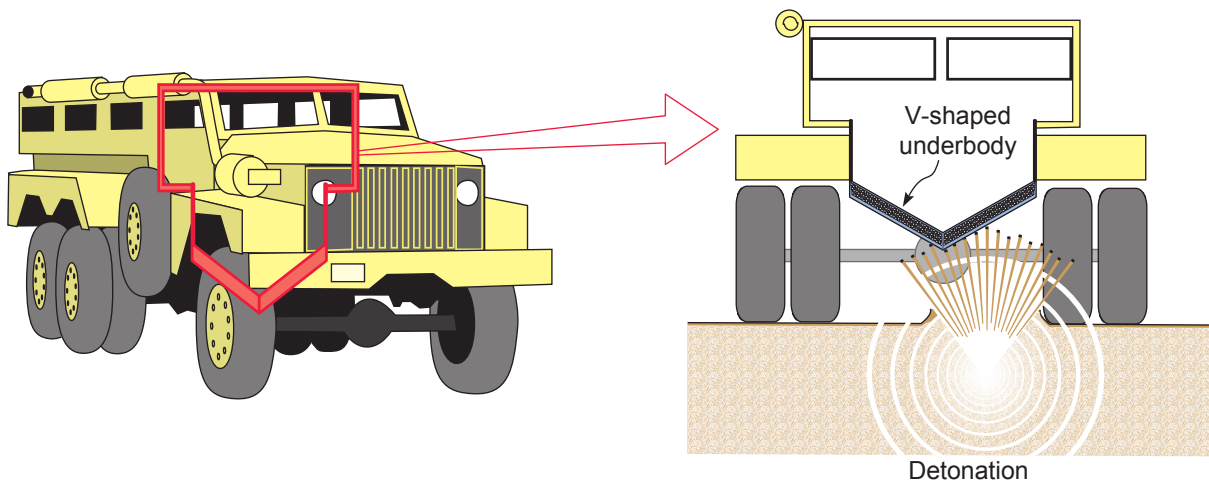


Fig. 4.1 Schematic illustration of a vehicle with V-shaped underbody design to protect against the soil ejecta generated by the detonation of a shallow-buried explosive.

The phenomena that contribute to the dynamic loading of a structure following detonation of shallow-buried explosives are very complex. Empirical models that predict the impulsive loads imposed by soil ejecta [135] as well as structural design codes such as the one proposed by Morris [84] have helped inform more recent experimental characterizations of buried explosive events [8, 88]. Moreover, experimental [7, 106] and recent numerical [11, 33] studies have confirmed that the soil impact is responsible for a substantial fraction

of the blast load applied to a target structure, thus justifying the use of design codes such as those in Westine et al. [135] that neglect loading due to the accompanying air blast.

Experimental studies have shown that increasing the stand-off distance between the target and the explosive/ground also decreases the deflections of monolithic plates [11, 98, 38] and sandwich panels [30]. This decrease has been attributed to a reduction in the momentum transfer from the ejected soil and detonation products to the target due to the spherical expansion of the ejecta; see experiments of Hlady [56] for rigid targets and Pickering et al. [98] for deformable plates. This reaffirms the importance of understanding the momentum transmitted into the targets from the soil ejecta.

Many numerical approaches have been proposed to model the complex dynamic interaction of granular sprays with structures. For example, Rimoli et al. [108] used the soil constitutive model of Deshpande et al. [27] to deduce the impulse applied to structures by explosively driven spherical sand shells, and then simulated the ensuing deformation of Aluminium monolithic and sandwich plates using a finite element method. Grujicic et al. [48, 52, 51] and Wang et al. [130] used coupled Eulerian/Lagrangian simulations of landmine explosions, and compared their predictions with blast impulse and plate deformation measurements from Bergeron and Tremblay [7] and Foedinger [36]. More recently, coupled discrete particle/continuum simulations have been increasingly used to investigate the response of structures impacted by high-velocity granular media. For example, Borvik et al. [11] followed by Dharmasena et al. [30] and Holloman et al. [58, 57] used this approach to simulate the response of a variety of monolithic and sandwich structures loaded by high-velocity sand sprays generated by explosive detonations. The importance of coupling the interaction of the granular medium with the dynamically changing geometry of the impacted surface was demonstrated by Wadley et al. [127] during a reinterpretation of the experiments reported by Rimoli et al. [108]. All these discrete particle approaches typically use spheres to represent the granular particles though some differences exist in individual implementations. For example, Liu et al. [79] and Dharmasena et al. [30] allow for three rotational and three translational degrees of freedom for the particles while the approaches of Borvik et al. [11] and Holloman et al. [58, 57] restrict rotational motion of the spheres even though tangential frictional forces that result in torques on the particles are included in the analyses. It remains as yet unclear whether these differing assumptions affect the predictions.

There is considerable evidence that V-hull construction (Fig. 4.1) significantly enhances the survivability of vehicles subjected to impulsive loading from buried explosions. However, there is a paucity of data in the open literature, with most such studies restricted to rigid targets. If the ejecta launched by a buried explosion is brought to rest by a flat rigid target whose surface is perpendicular to the direction of particle impact, the full normal component of its momentum is transferred to the plate and the plate is subjected to the stagnation pressure associated with bringing a fluid to rest [27, 95]. Experiments [2, 41] suggest that the momentum transferred from the ejecta into an inclined rigid

target is less than that transferred into a normally oriented target while Benedetti [6] and Follett et al. [37] have reported similar findings for V-hulls made from Aluminium sheets and composite materials, respectively. Uth et al. [126] reported detailed laboratory scale measurements of all the components of the momentum transmitted into inclined monolithic and sandwich beams impacted by granular slugs comprising tungsten carbide particles. These detailed measurements indicated that while the resultant momentum transmitted into the inclined targets was indeed less than that for the normally oriented counterparts, it was significantly higher than that anticipated from a “water jet” like impact analysis [18, 64] which neglects friction between the granular particles and the target. We note that the symmetry of the impact situation for normally oriented targets implies that friction does not affect the resultant transmitted momentum. However, friction is expected to influence the momentum transfer when symmetry of the impact geometry is broken.

The symmetric impact of ejecta against a target as analysed in most model situations reported in the literature (see for example [30, 108, 127, 11, 58, 57]) is expected to be a special case rather than the norm for practical situations. Thus, the problem of a granular slug impact against an inclined target, as investigated by Uth et al. [126], serves as a useful prototypical problem to both investigate the response of V-hull type structures and understand the general situation of a non-symmetric granular impact against a target. This is the primary focus of this study where we investigate the influence of surface type and inclination on the momentum transfer into rigid-stationary targets. Coupled discrete particle/Lagrangian numerical simulations that help identify the key physics governing the impact process are also reported to support interpretation of the experimental investigations.

## 4.2 Experimental protocol

Cylindrical slugs comprising silica sand particles were impacted against rigid stationary targets to measure the transmitted momentum. Fig. 4.2a depicts the experimental setup, which comprises four components (from right to left); (i) a gas gun to fire a solid projectile, which then accelerates the piston of (ii) a slug launcher apparatus based upon that developed by Park et al. [95]; (iii) a sand slug that initially rests inside the cylindrical cavity of the launcher; and (iv) the rigid stationary target, mounted on force sensors to measure the transmitted momentum. We proceed to briefly describe the four main components of the experimental setup sketched in Fig. 4.2a.

### 4.2.1 Slug launcher

The launcher was developed by Park et al. [95] and later modified by Uth and Deshpande [125] and Uth et al. [126]. A cross-sectional view of the slug launcher is sketched in Fig. 4.2b and unless otherwise mentioned, all the components were made with low-carbon steel.

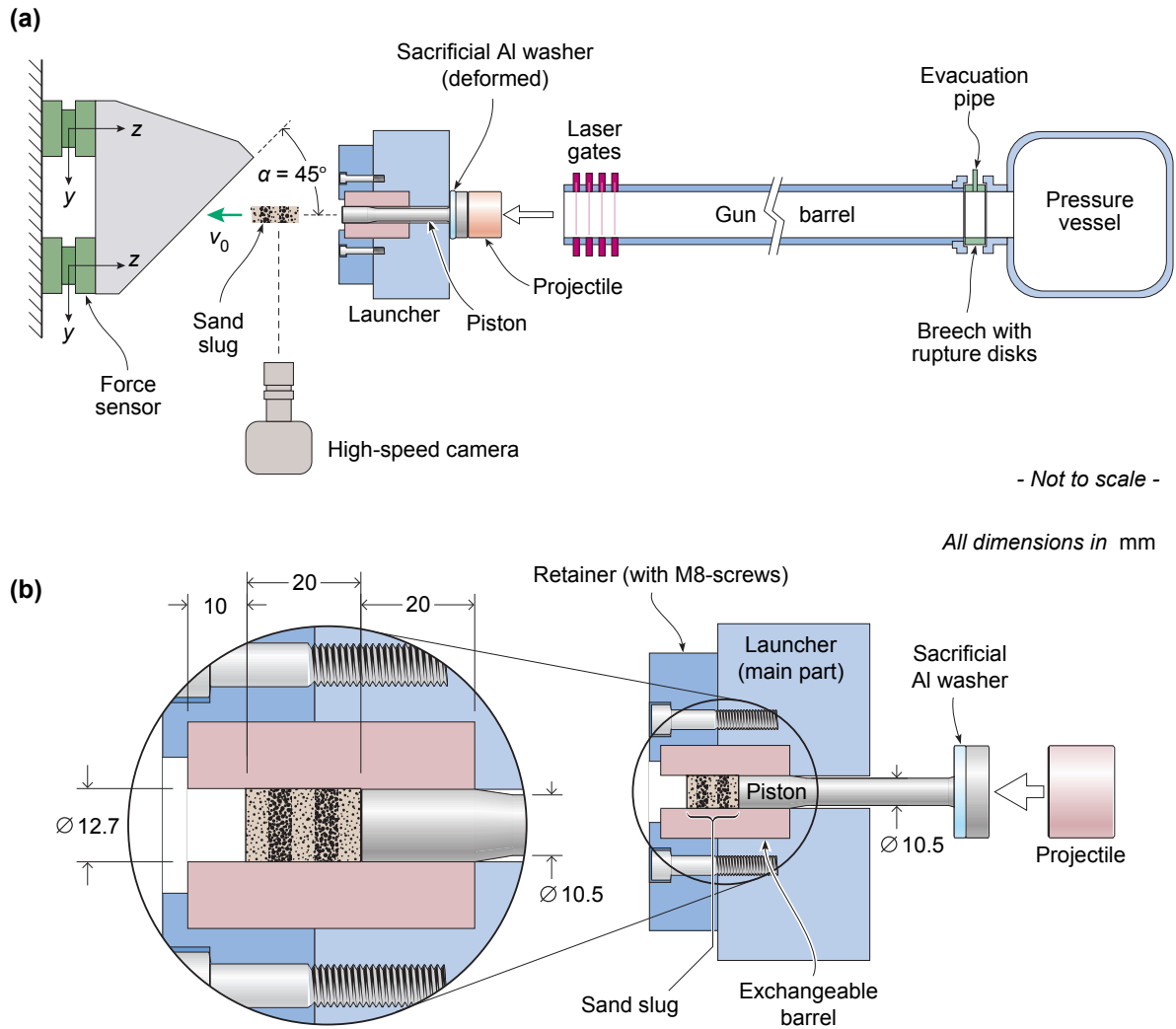


Fig. 4.2 (a) Sketch of the overall setup used to investigate the normal and inclined impact of sand slugs against rigid-stationary targets. The setup includes a gas gun to fire the projectile, a launcher to generate the slug, and a rigid-stationary target. The impact event is imaged using a high-speed camera and the projectile velocity is measured using laser gates. (b) A sketch showing a cross-sectional view of the slug launcher with the inset showing a detailed view of the piston in contact with the slug. All dimensions are in mm.

It comprised a cylindrical cavity for the sand slug and a piston to push the slug out of the cavity when a projectile, fired from a gas gun, impacted the piston head. The launcher was bolted to a rigid support frame so that it remained stationary during the impact event. The launcher consisted of a thick-walled cylinder with an exchangeable barrel of inner diameter 12.7 mm and length 50 mm. The piston had three distinct segments: a front, middle and back with dimensions as sketched in Fig. 4.2b: this segmented geometry was required to allow for both a tight fit of the piston front in contact with the sand and also to allow for “fattening” of the piston near the impacted end without jamming of the piston. The piston head at the back acts as an end-stop to arrest the piston. In addition, a 5 mm thick Aluminium alloy washer of inner diameter 12.7 mm and outer diameter 25 mm (equal to that of the piston head) was slid onto the piston until it was snug against the piston head. This washer cushioned the impact of the piston head against

the launcher. A retainer was bolted to the front of the main part of the launcher to hold the exchangeable barrel in place. Before the launch process, the slug sat inside the exchangeable barrel such that there was a 10 mm gap between the front of the slug and the end of the exchangeable barrel: trial-and-error showed that this extra cavity length helped to maintain the shape of the launched slug. Furthermore, the sand particles abrade the inner wall of the exchangeable inner barrel and hence it was replaced after every three tests to ensure a good sliding fit between the piston and the barrel.

#### 4.2.2 Silica sand slugs

Two types of sand slugs were employed: (i) dry sand slugs of mass  $m_{slug} = 4.2$  g and (ii) water saturated slugs of mass 5.14 g with 4.2 g of sand and 0.94 g of water filling all interstitial spaces between the silica particles. The silica sand<sup>1</sup> particles were sub-spherical with particle sizes in the range 150-300  $\mu\text{m}$ : see micrograph in Fig. 4.3. Before the launch, the cylindrical slugs had a diameter equal to that of the launcher and length  $L = 20$  mm. The slugs were prepared as detailed in Park et al. [95] and comprised 5 equal width alternating layers of coloured and uncoloured particles so as to give the slug a zebra-striped appearance (Fig. 4.2b). This zebra pattern improved the visualisation of the deformation of the slug during free-flight.



Fig. 4.3 Optical micrograph of the sand particles used in both the dry and water saturated sand slugs.

<sup>1</sup>BS 1881-131:1998, fraction D - David Ball Group, Wellington Way, Bourn, CB23 2TQ, UK

### 4.2.3 Gas gun to fire projectile

A steel projectile of 105 g mass and 28.4 mm diameter was accelerated using a gas gun with a barrel length of 4.5 m and inner diameter of 28.5 mm, as shown in Fig. 4.2a. No sabot was employed and the breech mechanism of the gun was formed by bursting copper diaphragms. The impact velocities  $V$  of the projectile against the piston of the launcher ranged from  $V = 126 \text{ m s}^{-1}$  -  $229 \text{ m s}^{-1}$ ; the velocity of the projectile was measured at the exit of the barrel using laser gates. While higher velocities would have been desirable in order to replicate granular media velocities in landmine explosions, impact of the piston at higher velocities irreparably damages the launcher and this limits the maximum projectile velocities employed in this study to about  $230 \text{ m s}^{-1}$ . The impacted end of the piston was placed about 25 mm in front of the end of the gun barrel. The flight of the sand slug and the profile views of the spreading of the sand slug over the target were visualized using a Phantom v1610 digital camera<sup>2</sup> operating at an inter-frame rate of  $47.62 \text{ } \mu\text{s}$  with an exposure time of  $0.45 \text{ } \mu\text{s}$ .

A magnified sketch of the impact of the projectile against the piston that pushes the slug out of the launcher is shown in Fig. 4.4a. Upon impact of the projectile, both elastic and (slower) plastic waves emanate from the impacted end and propagate towards the end of the piston in contact with the granular slug. These waves deform the piston and thus the end of the piston in contact with the slug does not attain its final velocity instantaneously. To illustrate this effect, we plot the displacement in Fig. 4.4b of the four marker lines on the piston shown in Fig. 4.4a for a projectile impact speed  $V = 229 \text{ m s}^{-1}$ . These displacements are plotted as a function of time  $t_I$ , where  $t_I = 0$  corresponds to the instant of impact of the projectile. The displacement rates of the markers (i.e. the marker velocities) all reach a constant and equal value at large  $t_I$  as seen in Fig. 4.4b. This is consistent with the fact that the deformation of the piston ceases sometime after the impact of the projectile, and the piston thereafter behaves as a rigid body. This temporally and spatially constant marker velocity is defined as the piston velocity  $v_p$ . The piston velocities for all the experiments reported here were experimentally obtained in this manner, and the relation between  $V$  and  $v_p$  obtained via this procedure is shown in Fig. 4.4c. We shall refer to experiments via their piston velocity  $v_p$  and this measurement will be directly used as an input to the simulations reported in Section 4.5, thereby avoiding the need to explicitly model the impact of the projectile against the piston.

### 4.2.4 Target design

Experiments were conducted with rigid and stationary targets in one of two orientations as sketched in Fig. 4.5. In the “normal orientation” (Fig. 4.5a), the targets were oriented such that the slugs impacted at an angle  $\alpha = 90^\circ$  to the face of the target while in the

<sup>2</sup>Vision Research, Priory Business Park, Stannard Way, Bedford, MK44 3RZ, UK.

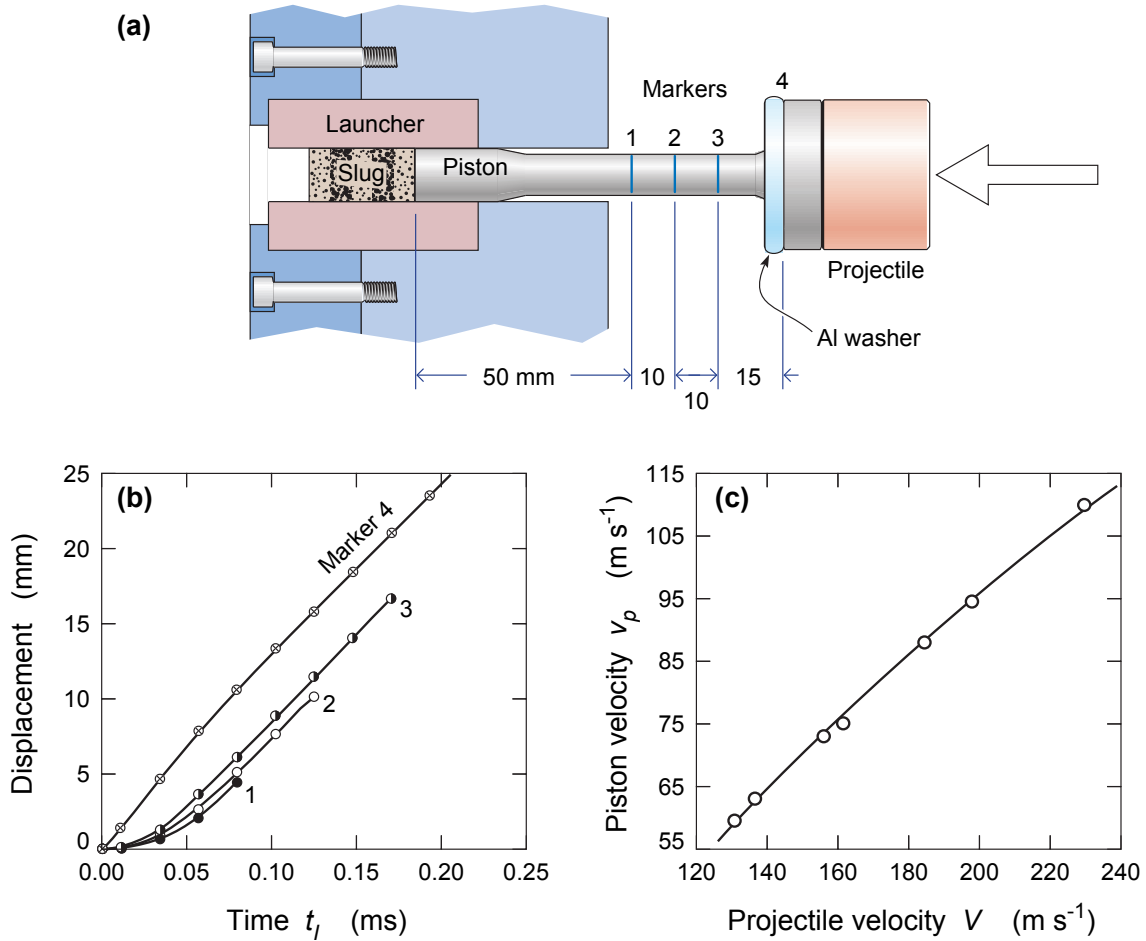


Fig. 4.4 (a) Magnified view of the launcher with the piston that has just been impacted by the projectile. The locations of four marker lines on the piston are shown: the displacements of these markers are followed via the high-speed photography. (b) The temporal evolution of the displacements of the four marker lines in (a) for a projectile impact velocity  $V = 229 \text{ m s}^{-1}$ . Here time  $t_I = 0$  corresponds to the instant of impact of the projectile. (c) The relation between the piston velocity  $v_p$  and projectile velocity  $V$  inferred from the high-speed photographs of the piston motion.

“inclined orientation”, the slugs impacted at  $\alpha = 45^\circ$  (Fig. 4.5b). The targets were 50 mm wide solid blocks of Aluminium with a mass of 1 kg. The length of the target surface facing the slug impact was 50 mm for normal impact (i.e. a square target of dimensions 50 mm  $\times$  50 mm) and 100 mm for inclined impact case, as sketched in Fig. 4.5. This solid Aluminium target can be considered rigid for the levels of slug impact velocities and momenta considered here.

The targets were in turn supported on two 3-component piezoelectric force sensors (Kistler<sup>3</sup>, type 9347C) that were used to measure the momentum transferred by the impacting slug into the target. These sensors measure forces in the three orthogonal directions ( $x, y, z$ ), where the  $z$ -axis was always defined in the direction of the incoming

<sup>3</sup>Kistler Instruments Ltd., Hook, Hampshire RG27 9GR, UK.

slug as shown in Fig. 4.5. The sensors could measure forces of up to 30 kN in the  $z$ -direction and 10 kN in the  $x$ - and  $y$ -directions. The output from the sensors was conditioned using a Kistler 5001 charge amplifier and recorded with a digital oscilloscope (Tektronix<sup>4</sup>, TDS 3014B).

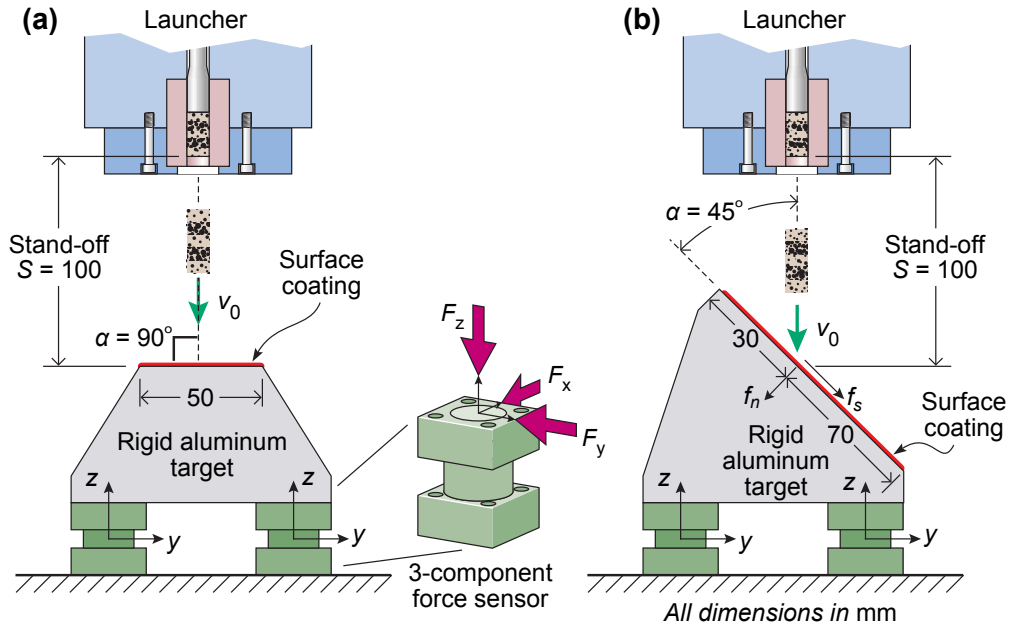


Fig. 4.5 Sketches of the rigid stationary targets in the (a) normal and (b) inclined orientations. The co-ordinate system fixed to the support structure ( $x$ ,  $y$ ,  $z$ ) is sketched along with the piezoelectric force sensors used to measure the momentum transferred into the target. The inset in part (a) shows a detailed view of the force sensors and the three components ( $F_x$ ,  $F_y$ ,  $F_z$ ) of the measured forces. In both (a) and (b) we show a portion of the slug launcher in order to define the stand-off  $S$  and the location of the slug impact on the target. All dimensions are in mm.

A key objective of the experimental program was to determine the effects of the impacted surface properties (hardness and roughness) on the interaction of the sand slug with the target. For this purpose, 4 surface coatings with contrasting surface roughness and hardnesses were adhesively attached the surface of the rigid Aluminium target:

1. 0.6 mm thick plate of solid Alumina (Aluminium Oxide –  $\text{Al}_2\text{O}_3$ );
2. Sand-paper (grade 3M 251D P60-SC1) comprising a so-called “X-weight” cloth which is a heavy duty tear-resistant blend of cotton and polyester coated with Alumina particles having a grit size of P60;
3. 1.5 mm thick plate of the Aluminium alloy (grade EN AW-1050A H14); and
4. 1.5 mm thick plate of PTFE.

The mean roughness  $R_a$  and Vickers hardness of the four coating layers are summarised in Table 4.1. We note that the hardness of the sand-paper is that measured by performing

<sup>4</sup>Tektronix, P.O. Box 500, Beaverton, OR 97077, USA.

a Vickers indentation test on the sand-paper placed on a rigid foundation and represents a combination of the hardness of the backing cloth and the hardness of the Alumina grit (the hardness of the Alumina comprising the grit is  $1600 \text{ kgf mm}^{-2}$ ).

Table 4.1 The mean surface roughness  $R_a$  and Vickers hardness of the four surface coatings employed in this study.

	Mean roughness $R_a$ ( $\mu\text{m}$ )	Vickers Hardness ( $\text{kgf mm}^{-2}$ )
Alumina	0.69	1600
Sand-paper	30.6	27.6
Aluminium	0.15	39.2
PTFE	1.06	3.7

The target was positioned at a stand-off  $S = 100 \text{ mm}$  in all experiments, where  $S$  is defined in Fig. 4.5 as the distance between the front of the stationary sand slug and the front face of the target at the centre of impact location.

#### 4.2.5 Temporal evolution and characterisation of slugs

Sand slugs were generated by firing projectiles against the launcher piston which in turn generated piston velocities in the range  $v_p = 59 \text{ m s}^{-1} - 110 \text{ m s}^{-1}$ . In line with observations made for silica sand slugs [95, 125] and Tungsten Carbide (WC) particle slugs [126], the velocity of the particles within the slugs remained temporally invariant after the slugs fully exit the launcher (i.e. the velocity of the slug was constant over the period during which observations could be made). As in previous studies, the particles within the slug acquired nearly no radial velocity but their axial velocity varied with position along the axis of the slug. To indicate this, Fig. 4.6a shows a montage of high-speed photographs showing the evolution (stretching) of the dry sand slug generated by impact with a piston speed  $v_p = 110 \text{ m s}^{-1}$ . Note the time  $t_I = 0$  corresponds to the instant of the impact of the projectile against the piston. These images clearly show that the slug is elongating, consistent with sand particles having an axial velocity gradient along the slug with those at the front travelling more rapidly than at the tail.

In order to quantify the spatial gradient of the axial velocity, images from the high-speed camera were used to measure the velocities of the boundaries between the coloured and uncoloured sand particle layers. Measurements of the temporally invariant boundary velocities  $v_b^{(i)}$ , where the superscript (i) refers to the boundary number are plotted in Fig. 4.6b for two selected values of  $v_p$  (the boundaries are labelled in the inset of Fig. 4.6b). They clearly show the axial gradient in the particle velocities within the slug with the front of the slug having a higher velocity compared to the rear resulting in elongation of the slug during free-flight. Noting that each of the 5 layers of the slug has equal mass, the free-field momentum of the slug is

$$I_0 = \frac{m_{slug}}{5} \sum_{i=1}^5 \frac{v_b^{(i)} + v_b^{(i+1)}}{2} \quad (4.1)$$

and the average slug velocity is then defined as  $v_0 \equiv I_0/m_{slug}$ . Subsequently, we shall refer to the velocity of slug via this average velocity  $v_0$ .

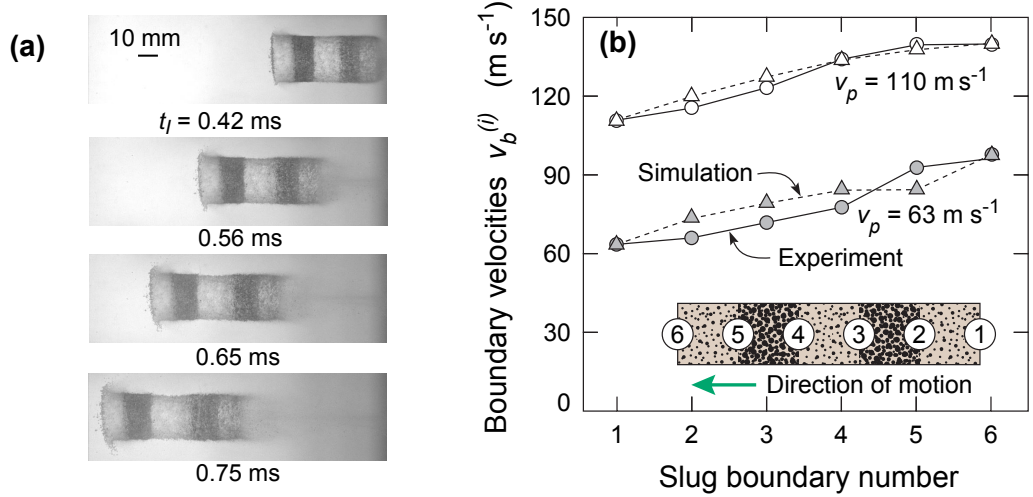


Fig. 4.6 (a) Snapshots showing the evolution of the dry sand slug generated by a piston velocity  $v_p = 110$  m s<sup>-1</sup> at four selected values of time  $t_I$ , where  $t_I = 0$  corresponds to the instant of the impact of projectile against the piston. (b) Measurements and predictions of the steady-state boundary velocities  $v_b^{(i)}$  for two selected values of  $v_p$ . The boundary number indicated by the superscript (i) is illustrated in the inset of (b).

#### 4.2.6 Characterisation of transmitted momentum

The primary goal of this study was to determine the momentum transmitted from the slug into a target whose surface properties were systematically varied. The two force transducers provide measurements of force versus time histories in the  $x$ -,  $y$ - and  $z$ -directions. The transmitted forces depend not only on the actual loads exerted by the slug but also on the location of the force measurements, structural properties of support (e.g. its stiffness and mass) and the clamping setup [77, 120]. However, the integral of force history over time is less dependent on the support structure, which makes it a useful parameter to quantify the effect of impacting slugs. The force component measured by the two transducers (1 and 2) in the  $z$ -direction is identified as  $F_z^1$  and  $F_z^2$ , respectively. Consequently, the momentum  $i_T^z$  transmitted into the support structure in the  $z$ -direction after a time  $t$  (where  $t = 0$  corresponds to the instant that the slug first impacts the target) is given by

$$i_T^z(t) = \int_0^t (F_z^1 + F_z^2) dt \quad (4.2)$$

and  $I_T^z \equiv i_T^z$  (as  $t \rightarrow \infty$ ) is the total momentum transmitted into the target in the  $z$ -direction. Analogous expressions exist for momenta components in the other two directions (viz.  $I_T^y$  and  $i_T^y$  as well as  $I_T^x$  and  $i_T^x$ ). In all experiments,  $i_T^x = 0$  to within the accuracy of the measurements (as dictated by symmetry) and hence the focus here is on the momentum measurements in the  $z$ - and  $y$ -direction and the resultant transmitted momentum given by

$$I_T = \sqrt{(I_T^z)^2 + (I_T^y)^2} \quad (4.3)$$

Consider the case of a dry sand slug impact at  $v_0 \approx 127 \text{ m s}^{-1}$  against the target covered by the Alumina plate. Temporal measurements of  $i_T^z/I_0$  for a normal  $\alpha = 90^\circ$  impact, Fig. 4.5a, (where symmetry dictates  $i_T^y = 0$ ) and both  $i_T^z/I_0$  and  $i_T^y/I_0$  for the inclined impact, Fig. 4.5b, are reported in Fig. 4.7. After a small initial time delay (corresponding to the time taken for the stress waves initiated at the impact location to reach the force transducers), the momentum rises sharply before oscillating about a fixed mean value at a frequency related to natural frequency of the entire setup. It is evident from Fig. 4.7 that  $i_T^y < i_T^z$  for the inclined impact. In order to understand this observation, we note that if  $f_n$  and  $f_s$  are the resultant normal and tangential forces exerted by the sand particles on the target (Fig. 4.5b), momentum balance gives

$$i_T^z(t) = \int_0^t (f_n \sin \alpha + f_s \cos \alpha) dt \quad (4.4)$$

and

$$i_T^y(t) = \int_0^t (f_n \cos \alpha - f_s \sin \alpha) dt \quad (4.5)$$

The tangential force (from friction between the slug particles and the target) has opposite effects on  $i_T^z$  and  $i_T^y$ , and is the source of the separation of the two curves for the inclined impact in Fig. 4.7.

The consequences of Eqs. 4.4 and 4.5 in the limiting case when  $t \rightarrow \infty$  are worth further elaboration as it enables better interpretation of measurements reported subsequently. Symmetry of the normal impact  $\alpha = 90^\circ$  implies  $I_T^z = I_0$  and  $I_T^y = 0$ . By contrast, for the inclined case we cannot independently relate  $I_T^z$  and  $I_T^y$  directly to  $I_0$  without detailed information on  $f_s$  due to the lack of symmetry in the problem. However, in the absence of friction between the particles and the target (i.e. when  $f_s = 0$ ), explicit relations for the transmitted momentum follow

$$I_T^z = I_0 \sin^2 \alpha \quad \text{and} \quad I_T^y = I_0 \sin \alpha \cos \alpha \quad (4.6)$$

For the case of  $\alpha = 45^\circ$  these reduce to  $I_T^z/I_0 = I_T^y/I_0 = 0.5$ . These values are subsequently used as a reference during analysis of the measurements. The measurements

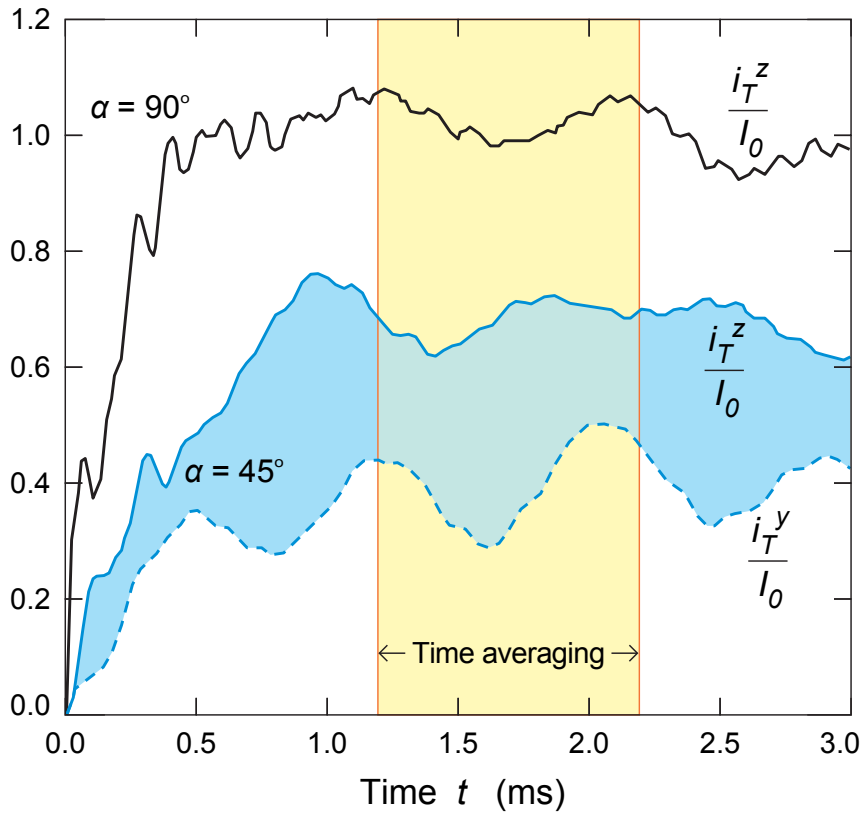


Fig. 4.7 Measurements of the temporal variation of the normalised transmitted momentum  $i_T^z/I_0$  for the normal as well as  $i_T^z/I_0$  and  $i_T^y/I_0$  for the inclined impacts. Time  $t = 0$  corresponds to the instant that the slug impacts the target and results are shown for a dry slug impact at  $v_0 = 127 \text{ m s}^{-1}$  against the Alumina coated target surface.

will invariably have a finite friction between the particles and target and thus the deviations from these estimates serve to quantify the effect of friction between the particles and the target surface.

### 4.3 Measurements for normal impact

A montage of high-speed photographs showing the deformation of dry sand slugs as they impact normally against targets with the Alumina and sand-paper coatings are included in Figs. 4.8a and 4.8b, respectively for a slug velocity  $v_0 = 127 \text{ m s}^{-1}$ . Here, time  $t = 0$  corresponds to the instant the slug impacts the target. The slug is seen to spread laterally against the target in a mode very similar to the spreading of water jet with no visible rebound of the sand particles and no obvious differences between the two surface types. These results are consistent with observations reported by Park et al. [95] and the discrete particle computations of Pingle et al. [99]. We define the transmitted momenta  $I_T^z$  and  $I_T^y$  as the average values of  $i_T^z$  and  $i_T^y$ , respectively over a period of  $1.2 \text{ ms} \leq t \leq 2.2 \text{ ms}$  (Fig. 4.7). The measured normalised transmitted momenta  $I_T^z/I_0$  are included in Fig. 4.9a for slug velocities  $v_0$  in the range  $73 \text{ m s}^{-1} - 127 \text{ m s}^{-1}$ . Over the entire range of velocities,

$I_T^z/I_0 \approx 1$  for both surface types. This measurement is consistent with the observation from the high-speed photographs that indicate (i) negligible rebound of the sand particles from the target and (ii) that the deformation modes of the sand slugs are similar in Figs. 4.8a and 4.8b. We emphasise here that the measured values of  $I_T^z/I_0$  plotted in Fig. 4.9a are slightly greater than 1. This is due to uncertainties in the measurements associated with the vibration of the test setup (see temporal variations plotted in Fig. 4.7) and not due to additional transfer of momentum into the target due to reflection of the sand.

A montage of photographs showing the normal impact of the  $v_0 = 133 \text{ m s}^{-1}$  water saturated sand slug against the Alumina coated target is included in Fig. 4.8c. The overall mode of deformation is similar to those of the dry sand slug in Fig. 4.8a and there is no measurable effect of water on the normalised transmitted momentum with  $I_T^z/I_0 \approx 1$  for the water saturated slugs over the entire velocity range considered here (Fig. 4.9a).

## 4.4 Measurements for inclined impact

We begin by investigating the case of the inclined target with Alumina coating and then use it as the reference case. A montage of high-speed photographs showing the impact of the  $v_0 = 114 \text{ m s}^{-1}$  dry sand slug against the Alumina coated inclined target is included in Fig. 4.10a. The spreading of sand particles against the target is asymmetric with both the mass of the sand particles and spreading velocity in the negative  $y$ -direction being less than the positive  $y$ -direction. This is primarily due to the fact that the momentum of the incoming slug resolves along the target surface in the positive  $y$ -direction. However, the flow of the sand particles along the target surface in the negative  $y$ -direction is caused by the reaction imposed by the target on the sand particles.

Normalised values of the measured transmitted momenta  $I_T^z/I_0$ ,  $I_T^y/I_0$  and resultant transmitted momentum  $I_T/I_0$  are included in Fig. 4.11a over the range of the slug velocities  $v_0$  investigated here. Similar to the normal impact case, the fraction of the transmitted momenta are independent of  $v_0$  over the range of velocities considered here. Moreover, the transmitted resultant momentum,  $I_T/I_0 \approx 0.77$ . This represents approximately a 33% reduction compared to the normal impact case where  $I_T/I_0 \approx 1$ . This is primarily a result of the continued flow of the sand slug along the negative  $z$ -direction (i.e. retention of momentum in the slug) due to the inclination of the target surface.

However, measurements suggest that the transmitted momentum into the inclined target is higher than the predicted value in the absence of friction between the sand particles and the target surface. Recall that in the absence of friction between the sand particles and the target surface we expect that  $I_T^y/I_0 = I_T^z/I_0 = 0.5$ . The measurements in Fig. 4.11a clearly show that  $I_T^y \neq I_T^z$  with  $I_T^y \approx 0.42$  and  $I_T^z \approx 0.64$  which indicates that friction between the sand particles and the target surface substantially affected the transmitted momentum even in this reference case of the Alumina coated target.

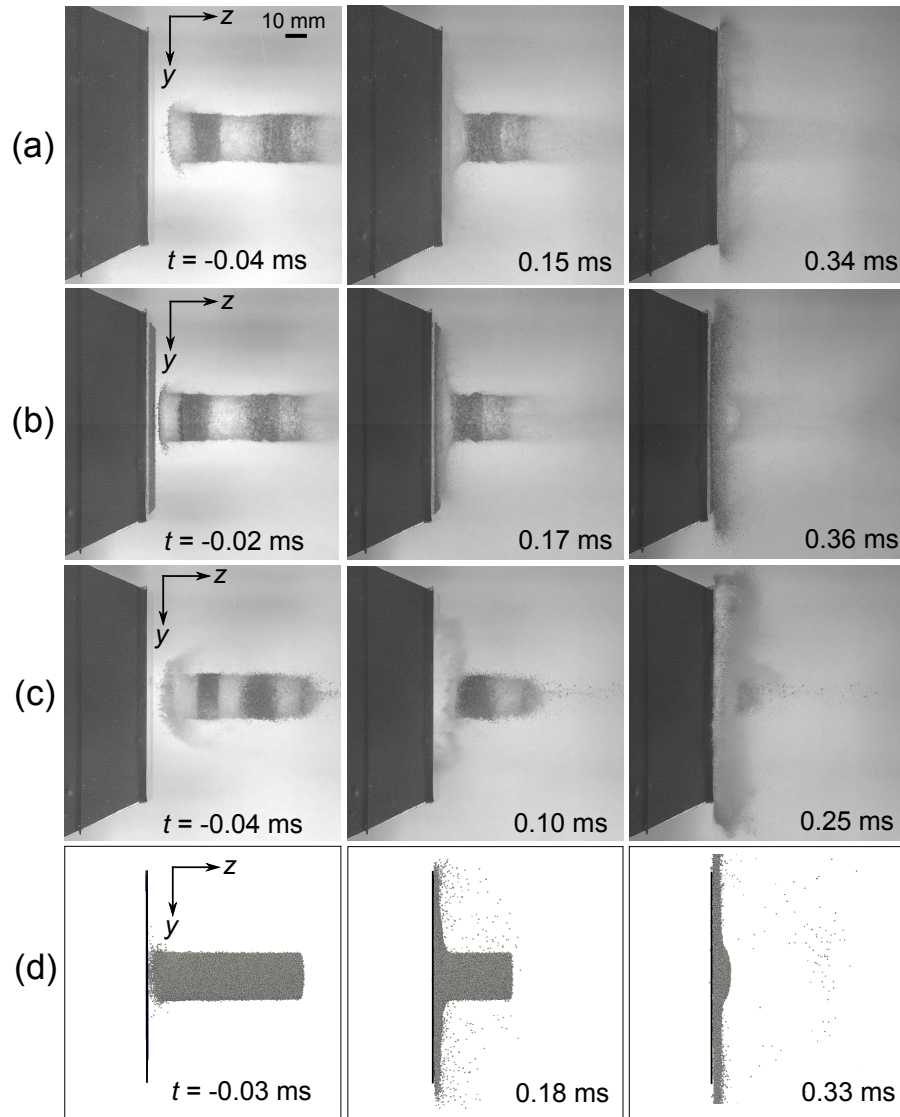


Fig. 4.8 Montage of high-speed photographs showing the deformation of sand slugs impacting the targets in normal orientation: (a) dry sand slug against the Alumina coated target; (b) dry sand slug against the sand-paper coated target and (c) water saturated sand slug against the Alumina coated target. (d) Corresponding predictions of the dry sand slug impacting the Alumina coated target. For (a) and (b), the sand slugs have a velocity  $v_0 = 127 \text{ m s}^{-1}$  while in (c), the slug velocity  $v_0 = 133 \text{ m s}^{-1}$ . Time  $t=0$  corresponds to the instant that the slug impacts the target.

Furthermore, the resultant transmitted momentum  $I_T/I_0 \approx 0.77$ , which represents a 9% increase over the value  $I_T/I_0 = 1/\sqrt{2}$  predicted in the absence of friction between the target surface and the sand particles.

Measurements of transmitted momentum for the impact of the water saturated sand slugs against the inclined target with the Alumina coating are also included in Fig. 4.11a. Again, there is no effect of the slug velocity on the normalised components of all the transmitted momenta and moreover, the measurements of the normalised momenta of the dry and water saturated slugs are identical to within experimental accuracy. We thus

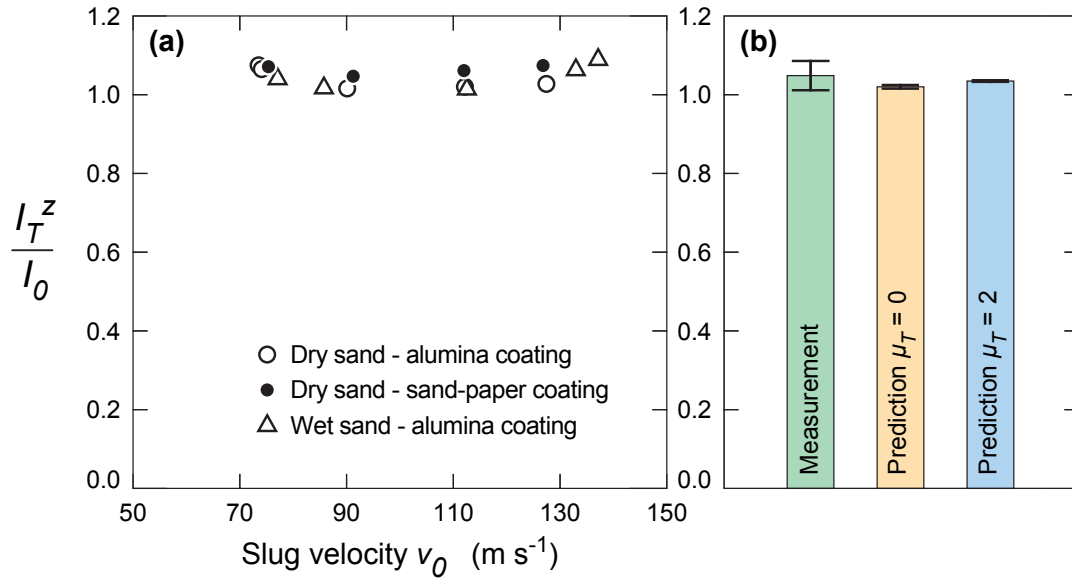


Fig. 4.9 (a) The measured normalised transmitted momentum  $I_T^z/I_0$  as a function of the slug velocity  $v_0$  for normal impact against targets. Measurements are shown for impact of dry sand slug against the Alumina and sand-paper coated targets as well as the water saturated slug against the Alumina coated target. (b) A bar chart showing the measurements and predictions of  $I_T^z/I_0$  for normal impact of the slugs. Predictions for the friction coefficient between the target and the particles  $\mu_T = 0$  and 2.0 are included and the error bars on the bars indicate the variation of the measurements and predictions over the range of slug velocities  $v_0$  investigated here.

conclude that water saturation does not affect the mechanism of momentum transmission to the target and all subsequent results are presented for only the dry sand slugs.

#### 4.4.1 Effect of surface type

Frictional forces between the sand particles and the target surface play an important role in modulating the transmitted momentum for the inclined impact case as shown above. In order to better understand the relation between surface type and the transmitted momentum, the transmitted momentum was investigated for three other surface coatings: (i) PTFE which is known to reduce adhesion but has a low hardness and relatively high surface roughness; (ii) Aluminium which has a low surface roughness but also a relatively low hardness and (iii) sand-paper with a high surface roughness and low hardness. The transmitted momenta for these surfaces is then compared with that of the Alumina surface with relatively low surface roughness and high hardness.

A montage of high-speed photographs showing the deformation of the  $v_0 = 114 \text{ m s}^{-1}$  dry sand slug impacting against the inclined target with PTFE, Aluminium and sand-paper coatings are shown in Figs. 4.10b, 4.10c and 4.10d, respectively. There were no observable differences in the deformation modes of the slugs. By contrast, the transmitted

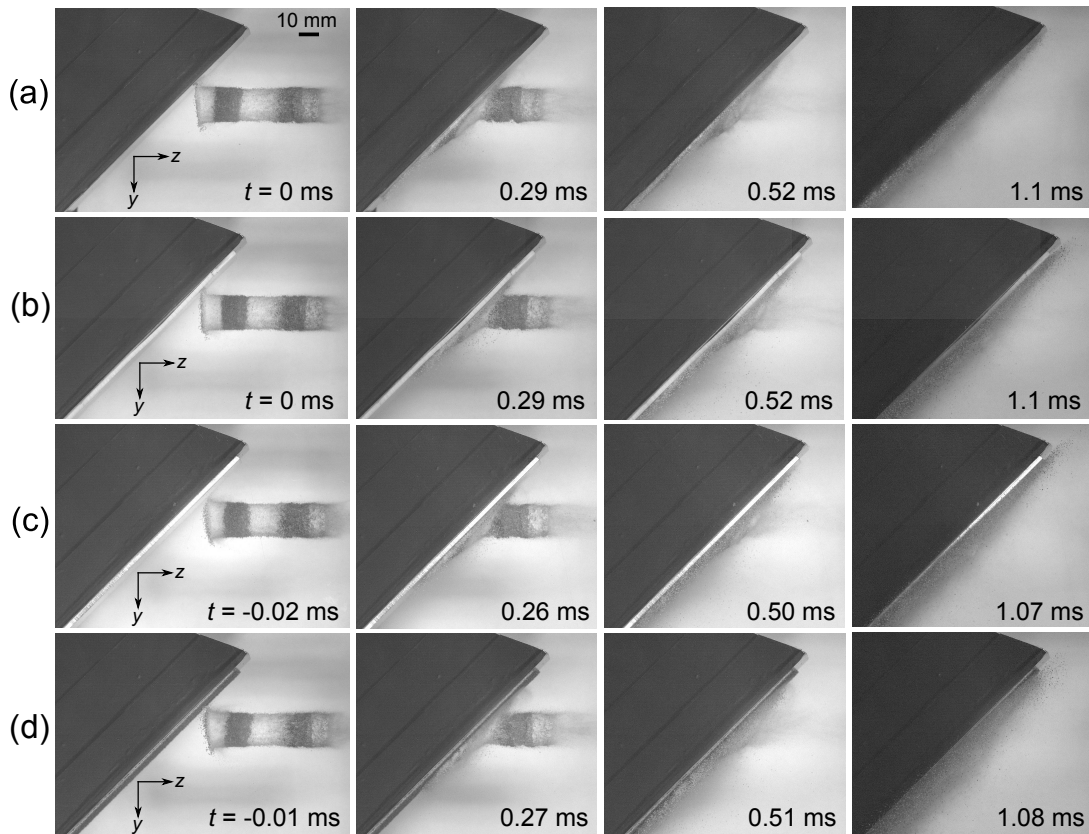


Fig. 4.10 Montage of high-speed photographs showing the deformation of the dry sand slugs for inclined impacts against (a) Alumina, (b) PTFE, (c) Aluminium and (d) sand-paper target surfaces. In all cases, the slugs had a velocity  $v_0 = 114 \text{ m s}^{-1}$  and time  $t = 0$  corresponds to the instant the slug first impacts the target.

momenta were strongly dependent on the surface type as summarised in the bar chart in Fig. 4.12. This figure shows the measured average values of  $I_T^z/I_0$ ,  $I_T^y/I_0$  and  $I_T/I_0$  with the error bars indicating the range of values obtained over the slug velocities  $v_0$  investigated here. We emphasise that no trend with  $v_0$  was observed here similar to the results shown in Figs. 4.9a and 4.11a. Instead, the error bars indicate the variability in the experimental measurements. The resultant transmitted momentum  $I_T/I_0$  for the target surfaces increases in the order Alumina to PTFE to Aluminium to sand-paper though even for the sand-paper case  $I_T/I_0$  is less than the corresponding value for a normal impact. Correspondingly, the transmitted momentum  $I_T^z/I_0$  increases in the same order as  $I_T/I_0$  while  $I_T^y/I_0$  decreases. This is emphasised in Fig. 4.12, where we also include a bar chart summarising the measurements of  $(I_T^z - I_T^y)/I_0$  for the four surface coatings. These measurements clearly show the effect of the surface type on the levels of transmitted momentum. For example,  $I_T^z/I_0$  increased by 25% and  $I_T/I_0$  by 11%, in changing from Alumina to sand-paper coating.

The differences are attributed to frictional interactions between the sand particles and the surface of the target. To provide further insight into these differences Figs. 4.13a, 4.13b and 4.13c show post-test photographs of the PTFE, Aluminium and sand-paper surfaces,

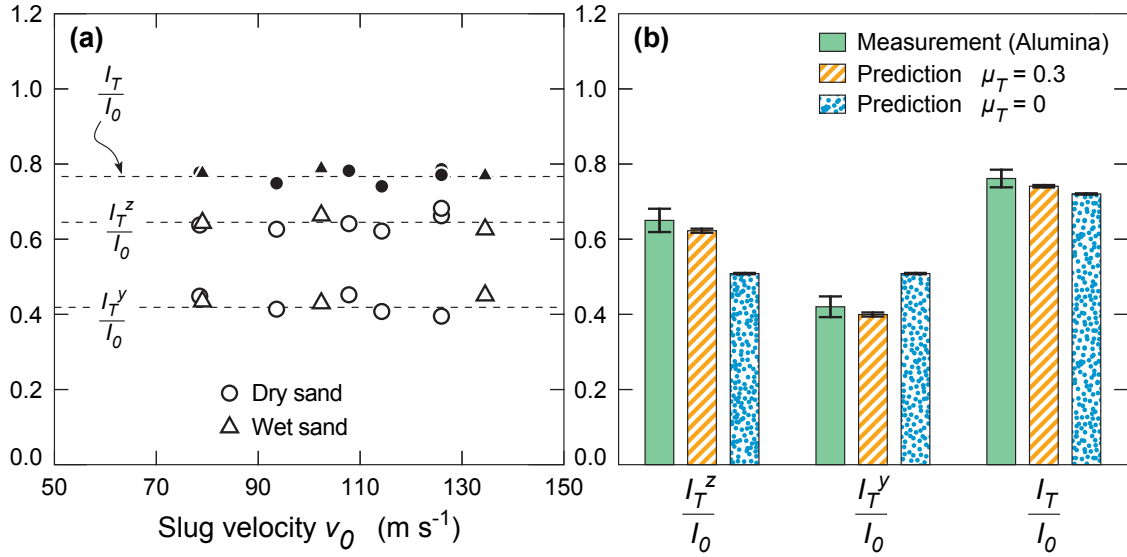


Fig. 4.11 (a) The measured normalised transmitted momenta  $I_T^z/I_0$ ,  $I_T^y/I_0$  and  $I_T/I_0$  as a function of the slug velocity  $v_0$  for inclined impact of dry and water saturated slug against the Alumina coated target. (b) A bar chart showing the measurements and predictions of  $I_T^z/I_0$ ,  $I_T^y/I_0$  and  $I_T/I_0$  for inclined impact of the dry sand slugs against the Alumina coated target. Predictions are shown for the friction coefficient between the target and the sand particles  $\mu_T = 0$  and 0.3. The error bars indicate the variation of the measurements and predictions over the range of slug velocities  $v_0$  investigated here.

respectively after impact by  $v_0 = 114 \text{ m s}^{-1}$  dry sand slugs. The local co-ordinate system  $x_i$  along the surface of the target is defined in Figs. 4.13a and 4.13d, and is oriented such that the primary spreading of the slug occurs along the positive  $x_1$ - direction. Significant embedding of the sand particles into the surface coatings is observed and this embedding increased in the order PTFE to Aluminium to sand-paper. No photograph of the Alumina surface is included as no embedding or any post-test visual indication of the impact of the sand slug was observable for that surface. The measured  $I_T/I_0$  increases with the level of observed embedding of the sand particles. The embedding of the particles is assumed to increase the effective friction between the sand particles and the target surface. Since embedded particles are also fully brought to rest, all their momentum must be transferred to the target.

The measurements reported here demonstrate the importance of the surface properties in governing the transmitted momentum for sand slug impacts with inclined targets. While the level of friction between the particle and the target surface clearly modulates the transmitted momentum, the relationships between surface material properties and the frictional interaction with the granular slug is as yet unclear. The results presented here suggest that the initial surface roughness is not a critical parameter (e.g. the Aluminium surface has a lower  $R_a$  compared to Alumina but results in a higher  $I_T/I_0$ ). Rather, surface properties that govern the embedding of particles into the surface play the crucial role. These properties are hardness and adhesion. For example, the reason the Alumina surface

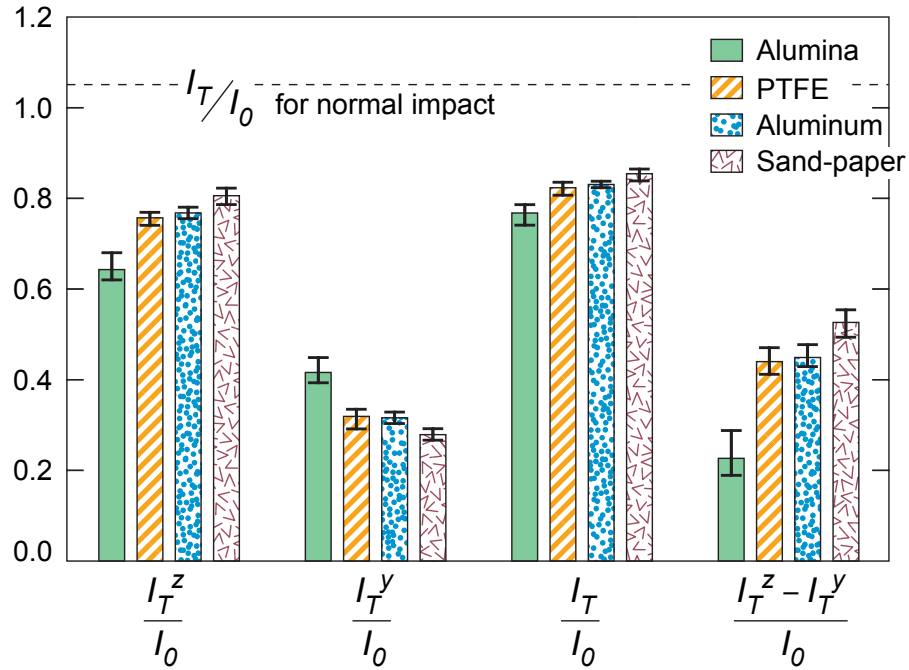


Fig. 4.12 Bar charts summarising the measured values of  $I_T^z/I_0$ ,  $I_T^y/I_0$ ,  $I_T/I_0$  and  $(I_T^z - I_T^y)/I_0$  for inclined impact of the dry sand slugs against targets with the four different surface coatings. The error bars indicate the variation of the measurements over the range of slug velocities  $v_0$  investigated here. For reference we have indicated the normalised resultant momentum  $I_T/I_0$  for normal impact.

seems to minimize friction and thereby  $I_T/I_0$  is that its high hardness implies there is no embedding of sand particles at the impact velocities considered.

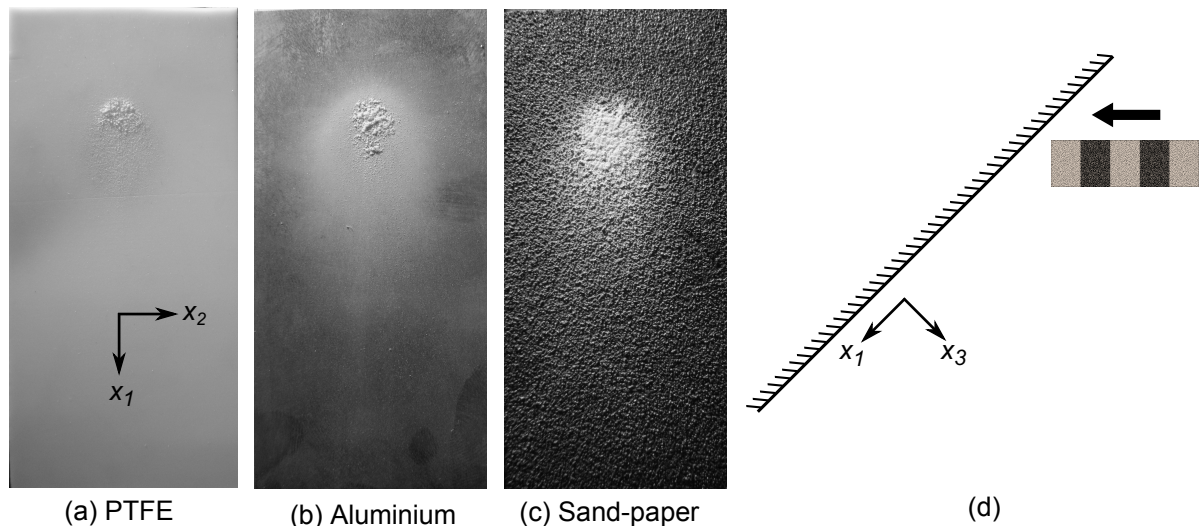


Fig. 4.13 Post-test photographs showing the impacted surfaces of the (a) PTFE, (b) Aluminium and (c) sand-paper coatings subjected to inclined impacts by  $v_0 = 114 \text{ m s}^{-1}$  dry sand slugs. (d) A sketch showing a side view of the impact of the sand slug against the inclined target. The sketch indicates the co-ordinate system  $x_i$  used in (a)-(c) to clarify the direction of the impact and the consequent flow of sand particles.

## 4.5 Discrete particle simulations and comparisons with measurements

The experimental measurements reported above show the effect of surface type on the level of transmitted momentum for both normal and inclined sand slug impacts. Numerical calculations are now utilized to better understand the interactions of sand slugs with the targets. This will enable quantification of the role of friction between the sand particles and the target that was shown experimentally to modulate the transmitted momentum in the inclined impact case.

### 4.5.1 Simulation methodology

The impact of dry sand slug against stationary targets was modelled using a coupled discrete particle/Lagrangian finite element simulation scheme. In this approach, the sand particles were modelled as discrete spherical particles using the GRANULAR package in the multi-purpose molecular dynamics code LAMMPS<sup>5</sup> [100] while the rigid targets were modelled within the Lagrangian commercial finite element package Abaqus<sup>6</sup>. These two modelling schemes were coupled using the MpCCI<sup>7</sup> interface as described below. The modelling scheme therefore consisted of four steps: (i) the discrete particle approach to model the sand particles; (ii) generation of the high-velocity slug due to the pushing of the slug out of the launcher by the piston; (iii) Lagrangian finite element scheme to model the contact between the target and the particles; (iv) an MpCCI interface for coupling between the discrete particle and FE schemes. Effects of gravity and air drag are neglected in the simulations. (At the relatively low velocities considered here, we are in a Stokes drag regime where the reduction in the velocity of the particles over the timescales of the experiments is negligible.)

Three-dimensional simulations are performed using mono-sized spherical particles of diameter  $D$  and mass  $m_p$ . The soft-particle contact model (Fig. 4.14), introduced by Cundall and Strack [24], and extended to large scale simulations by Campbell and Brennen [15] and by Campbell [14], accounted for both inter-particle interactions as well as the interactions of the particles with the target surface. The interparticle contact law comprises:

1. A linear spring with spring constant  $K_n$  and linear dashpot with damping constant  $\gamma_n$  connected in parallel, governing the contact force-displacement relation in the direction connecting the particle centres.
2. A linear spring of constant  $K_s$  and Coulomb friction coefficient  $\mu$  connected in series, governing the tangential contact relationship.

---

<sup>5</sup><http://lammmps.sandia.gov/>

<sup>6</sup><http://www.3ds.com/>

<sup>7</sup><http://www.mpcci.de/>

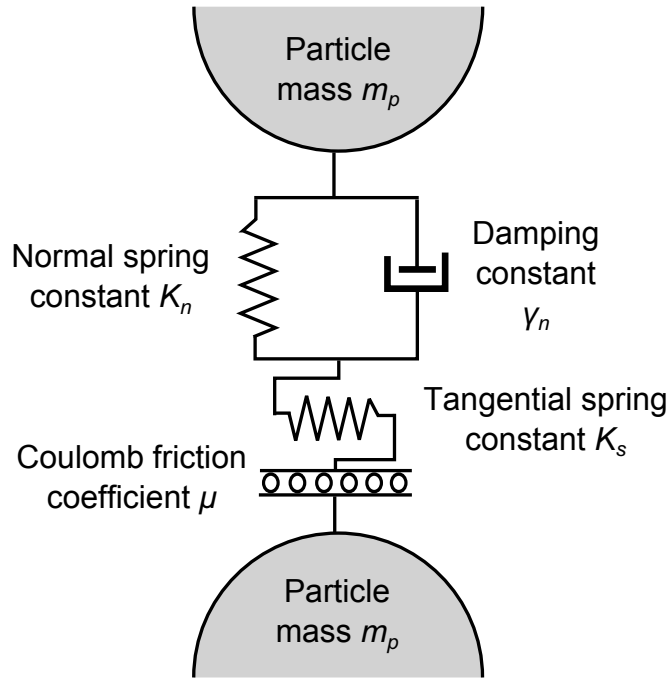


Fig. 4.14 Sketch of the soft inter-particle contact model between spherical particles of diameter  $D$  used to simulate the sand particles.

With  $r$  as the distance of separation of the particle centres, and the particle interpenetration given by  $\delta_n = r - D$ , the normal force during active contact ( $\delta_n < 0$ ) is given by

$$F_n = K_n \delta_n + m_{\text{eff}} \gamma_n \dot{\delta}_n \quad (4.7)$$

where  $m_{\text{eff}}$  is the reduced mass of the two contacting bodies. For impacts between a pair of particles,  $m_{\text{eff}} = m_p/2$  while for impacts between a particle and the target,  $m_{\text{eff}} = m_p$ .

The tangential force  $F_s$  only exists during an active contact, and opposes sliding. It is limited in magnitude to  $|F_s| < \mu |F_n|$ , where  $\mu$  is the friction coefficient as follows. If  $\dot{\delta}_s$  is defined as the tangential displacement rate between the contacting particles,  $F_s$  can be represented by an elastic-plastic relation with stiffness  $K_s$ ,

$$\dot{F}_s = \left\{ \begin{array}{ll} K_s \dot{\delta}_s & \text{if } |F_s| < \mu |F_n| \text{ or } F_s \dot{\delta}_s < 0 \\ 0 & \text{otherwise} \end{array} \right\} \quad (4.8)$$

The critical difference for interactions between particles and between a particle and the target is the coefficient of friction  $\mu$  which will be different for the two cases. Here,  $\mu_p$  and  $\mu_T$  refer to the value of  $\mu$  for inter-particle and particle/target interactions, respectively. The value of damping constant  $\gamma_n$  dictates the loss of particle kinetic energy during normal collision and is directly related to the coefficient of restitution  $e$  according to

$$e = \exp \left[ -\frac{\pi}{\left( \frac{8K_n}{\gamma_n^2 m_p} - 1 \right)^{1/2}} \right] \quad (4.9)$$

The collision time  $t_e$  for individual binary collisions is given as as

$$t_e = -2 \frac{\ln(e)}{\gamma_n} \quad (4.10)$$

and thus in the limit of plastic collisions with  $e \rightarrow 0$ , the contact time  $t_e \rightarrow \infty$ . Newton's equations for both the translational and rotational motions of the particles were integrated using a Verlet time-integration scheme (Newark-Beta with  $\beta = 0.5$ ). The time-step for integration was taken to be less than  $t_e/10$  in order to ensure accurate integration of the equation of motions given by  $\ddot{\delta}_n = F_n/m_p$  and  $\dot{\omega} = F_s D/(2J_s)$ , where  $\dot{\omega}$  is the angular acceleration of the particles with  $J_s$  their second moment of inertia about the diametrical axis.

The rigid targets (dimensions identical to those used in the experiments) were modelled as analytical rigid surfaces in Abaqus finite element analysis code, and all the six degrees of freedom (3 rotational and 3 translational) were constrained to prevent all rigid body motions. The coupling between the LAMMPS discrete particle and the Abaqus finite element calculations was carried out via an MpCCI Code adapter API as follows. At any time  $t$ , suppose that a proportion of the particles are in contact with the target surface. Consider one such particle in contact with the target surface. The interpenetration  $\delta_n$  is defined as  $\delta_n = r - D/2$ , where  $r$  is the distance between particle centre and contact point on the target (note the difference in the definition of  $\delta_n$  for contacts between particles and between the particle and the target). The rate  $\dot{\delta}_n$  is the relative approach velocity of the particle and the point of contact on the target surface, and likewise  $\dot{\delta}_s$  is the tangential velocity. The normal and tangential contact forces are calculated using Eqs. 4.7 and 4.8. These forces were then added as nodal forces to the appropriate surface elements in the Abaqus finite element calculations to complete the coupling between the discrete and finite element calculations. The transmitted momentum was calculated by time integrating the appropriate reaction force on the target; e.g. to calculate  $I_T^z$  we temporally integrate the reaction force in the  $z$ -direction on the target over a sufficiently large time period so as to obtain the steady-state value of  $I_T^z$ .

The following reference properties were assumed in all the calculations. The granular slug was modelled with spherical particles of diameter  $D = 300 \mu\text{m}$  made from a solid of density  $2700 \text{ kg m}^{-3}$  (equal to that of Silica). The particle contact model was defined by four parameters  $K_n$ ,  $e$ ,  $K_s$  and  $\mu_p$ . While Liu et al. [79] demonstrated that these parameters do not affect the interaction response of the granular slug impacting beams, Goel et al. [43] demonstrated that  $K_n$  strongly influence the evolution of the granular slug as it emerges from the launcher. It was therefore necessary to calibrate  $K_n$ , as discussed

below, while maintaining the other parameters fixed at reference values based on previous studies; see for example Refs. [79, 99, 80]. The reference values of the parameters are  $K_n = 0.69 \text{ MN m}^{-1}$ ,  $K_s/K_n = 2/7$  [4, 112],  $e = 0.7$  and  $\mu_p = 0.6$ . The friction coefficient  $\mu_T$  between the sand particles and the target surface depends on the surface type and is unknown. Thus, parametric studies for the sensitivity of the results to this parameter are presented. Frictional interactions between the cylindrical cavity surface of the launcher in contact with the sand particles were neglected.

The sand slug ejected from the launcher had an axial particle velocity gradient as seen in Fig. 4.6b that resulted in the lengthening of the slug during free-flight. Goel et al. [43] demonstrated that this velocity gradient is strongly dependent on  $K_n$  and hence  $K_n$  needed to be calibrated independently. This was performed as follows. Following Uth et al. [126], sand particles in a cylindrical cavity were subjected to constrained compression as sketched in Fig. 4.15a. The measured applied axial stress  $\sigma_n$  (defined as ratio of the applied compressive force to the cross-sectional area  $A_0$  of the cylindrical cavity) versus nominal strain  $\varepsilon_n$  (defined as the ratio of the relative displacements of the two pistons to the initial height  $h_0$  of the granular assembly within the cylinder) is plotted in Fig. 4.15b for an applied strain rate  $\dot{\varepsilon}_n = 10^{-3} \text{ s}^{-1}$ . This data can be used to calibrate the inter-particle stiffness  $K_n$  as follows.

First, the spherical sand particles of the numerical model were packed into a rigid cylindrical cavity as sketched in the inset in Fig. 4.15b to create a granular assembly of dimensions identical to that used in the experiment shown in Fig. 4.15a. The spherical particles had an initial volume fraction (prior to the application of the compressive force) of 0.61. Simulations of the compressive response were conducted by compressing the granular assembly via a rigid piston as shown in Fig. 4.15b at a displacement rate  $\dot{\delta} = 200 \text{ mm s}^{-1}$  (corresponding to a nominal strain rate  $\dot{\varepsilon}_n = 10 \text{ s}^{-1}$ ). The predicted nominal stress  $\sigma_n$  versus nominal strain  $\varepsilon_n$  responses are plotted in Fig. 4.15b for three choices of  $K_n$  with the remaining contact parameters kept fixed at their reference values. A contact stiffness  $K_n = 0.69 \text{ MN m}^{-1}$  brought the predictions in close agreement with the measurements and was therefore used as the reference value for  $K_n$ <sup>8</sup>.

## 4.5.2 Generation of the sand slug

To accurately capture the state of the sand slug during its free-flight and thereby its state just prior to impact, it is necessary to explicitly model the ejection of the sand slug from the launcher as described in Goel et al. [43]. In order to simplify the numerical calculations, the impact of the projectile against the piston and the deformation of the piston were not directly modelled. Rather, the piston was modelled as a rigid body as shown in Fig. 4.16a

<sup>8</sup>The friction coefficient, shear stiffness and damping do not affect the predicted constrained compressive response shown in Fig. 4.15b over an applied strain rate range  $1 \text{ s}^{-1} \leq \dot{\varepsilon}_n \leq 100 \text{ s}^{-1}$ .

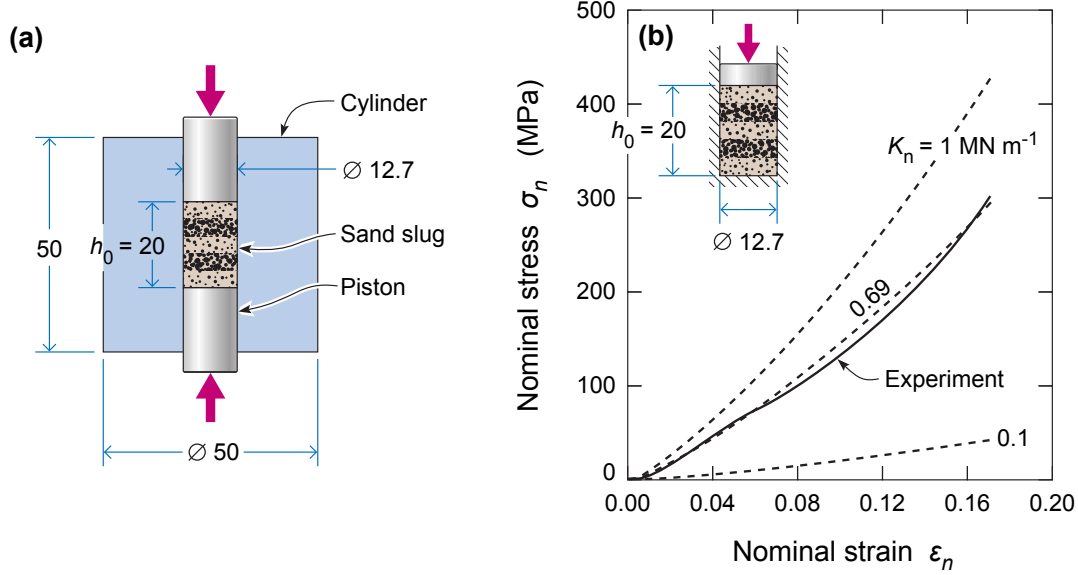


Fig. 4.15 (a) Sketch of the experimental setup used to measure the constrained compression response of the sand slug. (b) Comparison between measurements and predictions of the constrained compression response. Predictions are shown for three selected values of the normal inter-particle contact stiffness  $K_n$ . The setup used in the simulations is shown as an inset. All dimensions are in mm.

and given a velocity  $v_I(t_I)$ , motivated from the data in Fig. 4.4b in a manner similar to that of Goel et al. [43]. Thus, following Goel et al. [43], it suffices to approximate  $v_I(t_I)$  as

$$v_I(t_I) = \left\{ \begin{array}{ll} \frac{v_p t_I}{T_R} & 0 \leq t_I \leq T_R \\ v_p & t_I > T_R \end{array} \right\} \quad (4.11)$$

where  $T_R$  is the time taken for the piston to ramp up to its final velocity  $v_p$ .

Simulations of the ejection of the sand slug from within the launcher were performed as follows. First the spherical sand particles were inserted into a cylindrical cavity of inner diameter  $D = 12.7$  mm capped at one end by a rigid piston as shown in Fig. 4.16a. The compacted slug had a length  $L = 20$  mm and the free end of the slug needed to travel a distance of 10 mm to emerge from the launcher, consistent with the experimental design. The piston was then imparted a velocity versus time history  $v_I(t_I)$  specified by Eq. 4.11 which pushed the slug out of the launcher. The ramp time  $T_R$  was calibrated to ensure agreement between the measured and predicted boundary velocities; see for example Fig. 4.6b. This involved obtaining a value of  $T_R$  for each piston velocity  $v_p$  employed in this study: this calibrated  $v_p - T_R$  relation is plotted in Fig. 4.16b.

The impact of the slugs generated in this manner against the targets is then solved via the coupled discrete particle/Lagrangian method with the target placed at a stand-off  $S = 100$  mm in line with the experimental setup.

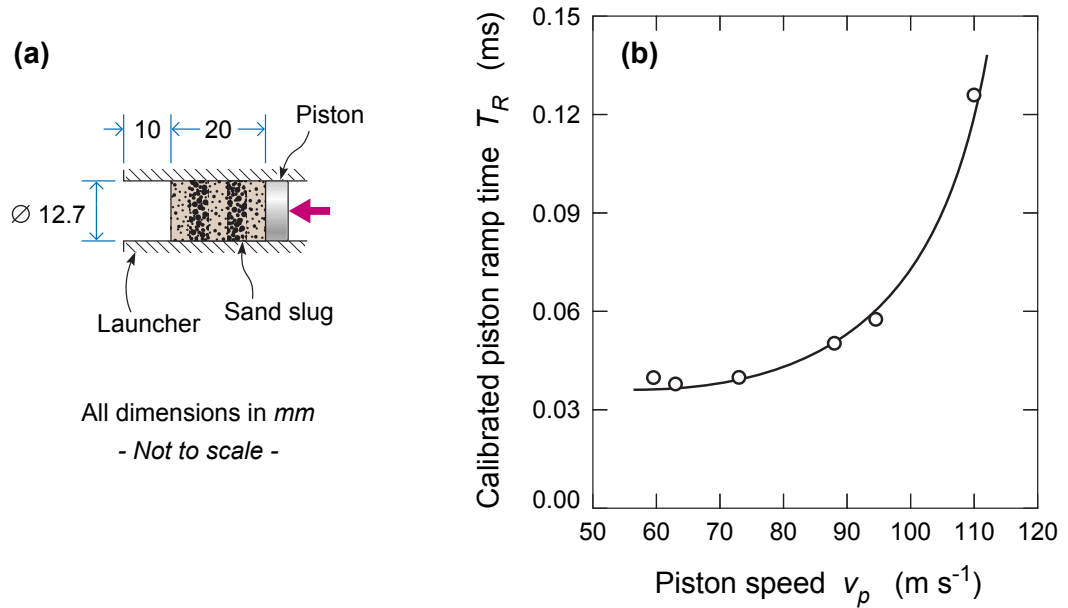


Fig. 4.16 (a) A side view sketch of the launcher/piston setup used in the numerical simulations. (b) The calibrated piston ramp time  $T_R$  versus piston velocity  $v_p$  relation that accurately reproduces the measured spatial distribution of particle velocities in the sand slug during free-flight.

### 4.5.3 Comparison with measurements

Snapshots showing predictions of the spreading of a normally impacted  $v_0 = 127 \text{ m s}^{-1}$  sand slug are included in Fig. 4.8d for three selected times,  $t$ . The friction coefficient between the particles and the target was taken to be  $\mu_T = 0$  in this simulation. Overall, the predicted spreading process appeared consistent with the dry sand impact high-speed photographs for the Alumina and sand-paper coated target surfaces in Figs. 4.8a and 4.8b, respectively. Next, consider the predictions of the transmitted impulse. Similar to the measurements,  $I_T^y = I_T^x = 0$  and  $I_T^z/I_0$  was approximately independent of  $v_0$ . Thus, it suffices to compare the measured and predicted average values of only  $I_T^z/I_0$  over the range of  $v_0$  investigated here. This comparison is shown in the bar chart in Fig. 4.9b for predictions with  $\mu_T = 0$  and a large friction coefficient of  $\mu_T = 2.0$ . In Fig. 4.9b, error bars are used to indicate the variation of the predictions with  $v_0$  - this variation is negligible for the simulations, and hence the error bars are barely discernible. It is evident that: (i) the predictions are in excellent agreement with the measurements, and in all cases  $I_T^z/I_0 \approx 1$  indicating negligible rebound of the sand particles and (ii) the friction coefficient between the particles and target has no discernible effect on the transmitted momentum; consistent with the experimental observation that  $I_T^z/I_0$  values of the Alumina and sand-paper target surfaces were the same (Fig. 4.9a). While  $\mu_T$  does not affect any of the transmitted momentum components ( $I_T^z$ ,  $I_T^y$  or  $I_T^x$ ), the tangential forces between individual particles and the surface in the  $x$  and  $y$ -directions do increase sharply with increasing  $\mu_T$ . However, the symmetry of the impact leads to these forces being cancelled out with the result that

$I_T^y = I_T^x = 0$ . The lack of such symmetry in the inclined impact case examined next is therefore expected to introduce a strong dependence of the transmitted impulse on  $\mu_T$ .

Snapshots from the simulation of the  $v_0 = 114 \text{ m s}^{-1}$  slug impacting the inclined target with  $\mu_T = 0.3$  are shown in Fig. 4.17. Two views are shown in order to better illustrate the spreading of the slug over the target: in Fig. 4.17a, a side view showing the  $y$ - $z$  plane (as observed with the high-speed photographs) is included while in Fig. 4.17b, we show an orthographic view perpendicular to the target surface (i.e. the  $x_1$ - $x_2$  plane as defined in Figs. 4.13a and 4.13d). The sand particles are seen to spread primarily in the positive  $x_1$ -direction consistent with the high-speed photographs in Fig. 4.10 (though a view showing the spreading in the  $x_2$ -direction is not available from the experiments). Again, like the measurements, the normalised transmitted momenta are independent of  $v_0$  and thus comparisons between measurements and predictions of  $I_T^y/I_0$ ,  $I_T^z/I_0$  and  $I_T/I_0$  for impact against the Alumina coated target are shown via a bar chart in Fig. 4.11b similar to Fig. 4.9b. In Fig. 4.11b predictions for  $\mu_T = 0$  and 0.3 are included. The frictionless case overpredicts  $I_T^y/I_0$  and underpredicts  $I_T^z/I_0$  as well as  $I_T/I_0$  but the measurements and predictions are in good agreement using  $\mu_T = 0.3$ . Thus, unlike in the normal impact case the momentum predictions are sensitive to  $\mu_T$  with the simulations suggesting significant frictional forces between the sand particles and the surface even for the Alumina coated case: the surface anticipated to have the lowest frictional effects.

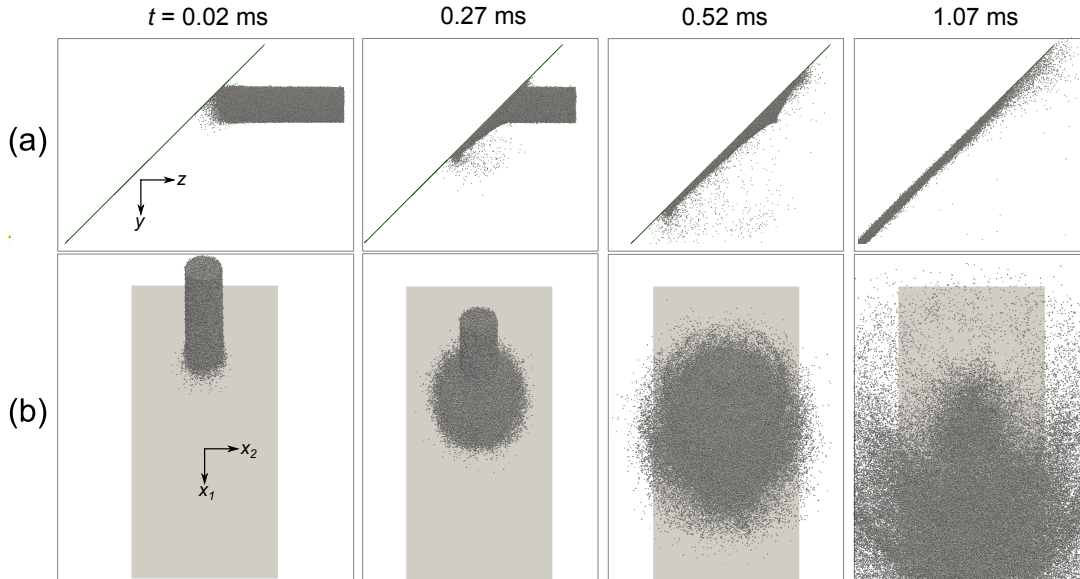


Fig. 4.17 Snapshots from the simulations of the impact of the  $v_0 = 114 \text{ m s}^{-1}$  slug against the inclined target with  $\mu_T = 0.3$ . The snapshots are shown at the same time instants as the high-speed photographs in Fig. 4.10 with time  $t = 0$  corresponding to the instant the slug impacts the target. (a) A side view showing the  $y$ - $z$  plane as seen in the high-speed photographs in Fig. 4.10 and (b) an orthographic view perpendicular to the target surface (i.e. the  $x_1$ - $x_2$  plane as defined in Figs. 4.13a and 4.13d).

Frictional forces between the sand particles and the target increased  $I_T^z/I_0$  and decreased  $I_T^y/I_0$  with  $(I_T^z - I_T^y)/I_0$  increasing as the impact surface was changed from Alumina to

PTFE to Aluminium and finally to sand-paper as seen in Fig. 4.12. It is thus instructive to examine the sensitivity of the predictions of  $(I_T^z - I_T^y)/I_0$  to  $\mu_T$  and these results are presented in Fig. 4.18 where in addition to the reference value of inter-particle friction coefficient ( $\mu_p = 0.6$ ), we show predictions using  $\mu_p = 1.0$  and  $2.0$ . Recall that in the absence of friction between the particles and the target (i.e.  $\mu_T = 0$ ), momentum conservation dictates that  $I_T^z/I_0 = I_T^y/I_0 = 0.5$  and thus  $(I_T^z - I_T^y)/I_0 = 0$  when  $\mu_T = 0$  but  $(I_T^z - I_T^y)/I_0$  increases with  $\mu_T$  before saturating beyond  $\mu_T \approx 1$ . The simulations in Fig. 4.18 indicate that the inter-particle friction has no effect on  $(I_T^z - I_T^y)/I_0$  at low  $\mu_T$  but  $(I_T^z - I_T^y)/I_0$  shows a mild sensitivity to  $\mu_p$  at high values of  $\mu_T$ . For example,  $(I_T^z - I_T^y)/I_0$  increases from approximately 0.3 to about 0.35 as  $\mu_p$  is increased from 0.6 to the unrealistically high value of 2.0. The measured values of  $(I_T^z - I_T^y)/I_0$  for the Alumina and sand-paper coated target surfaces are indicated in Fig. 4.18. We note that while a combination of  $\mu_T$  and  $\mu_p$  could be found to force the simulations to fit the measurements for the Alumina surface, no combination of friction coefficient values were able to bring the predictions into agreement with the measurements for impact with the sand-paper surface. Such a discrepancy also holds for the PTFE and Aluminium surface coatings.

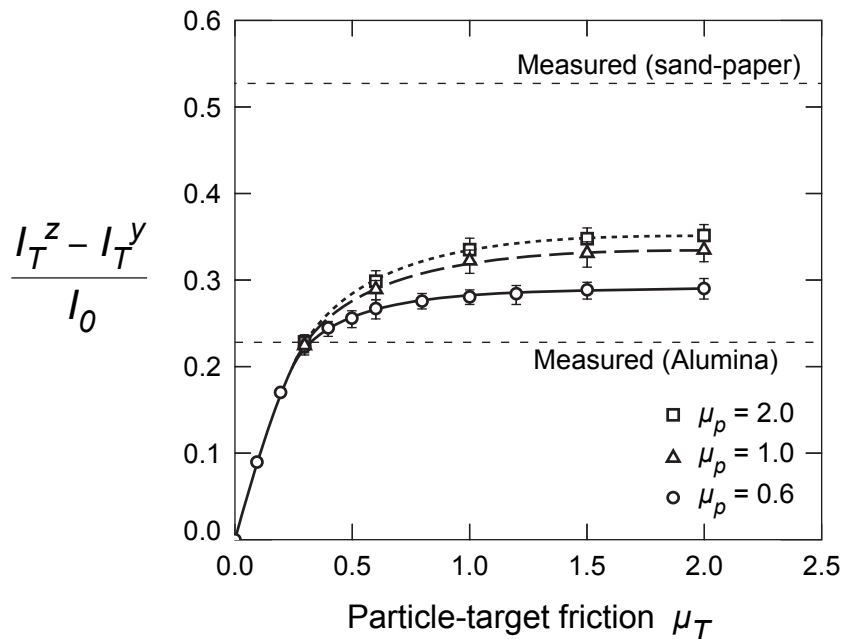


Fig. 4.18 Predictions of the dependence of the transmitted momentum  $(I_T^z - I_T^y)/I_0$  on the friction coefficient  $\mu_T$  between the sand particles and the inclined target surface. Results are shown for three values of the inter-particle friction coefficient  $\mu_p$ . The averaged measured values of  $(I_T^z - I_T^y)/I_0$  for impact of the dry sand slug against the inclined target with the Alumina and sand-paper coatings are also indicated.

The transmitted momentum predicted for the inclined impact is insensitive to any of the other inter-particle contact parameters, consistent with observations for the normal impact case by Pingle et al. [99] and by Liu et al. [79]. Thus, there seems to be a fundamental discrepancy between predictions and measurements. This discrepancy increases when

frictional forces between the particles and the target surface increase, i.e. discrepancies are highest for the sand paper coating which imposes maximum constraint to the flow of the particles.

## 4.6 Sources of the discrepancy between simulations and measurements

The critical conclusion from Fig. 4.18 is that the simulations are unable to capture the interactions between the sand particles and the target accurately when frictional interactions between the particles and the target surface are high. In order to understand this issue, we consider a simpler setting in which the sand slugs have a spatially uniform density characterized by a particle volume fraction  $\bar{\rho}$ . All particles in such slugs now have the same velocity  $v_0$  in the negative  $z$ -direction with the other two translational velocities, and all rotational velocities set equal to zero just prior to impact. Recall that the slug velocity does not affect the normalised transmitted momentum and thus all simulations presented in this section were performed using  $v_0 = 100 \text{ m s}^{-1}$ . Parametric studies of the effect of the inter-particle contact parameters are presented but unless otherwise specified, these values are set equal to the reference values specified in Section 4.5.1 with  $\mu_T = 0.3$ . In addition, the reference particle volume fraction of particles in the slug was  $\bar{\rho} = 0.24$ ; approximately equal to that for the slugs in the experiments just prior to impact.

### 4.6.1 Role of particle and slug properties

The role of particle contact stiffness  $K_n$ , coefficient of restitution  $e$  and particle diameter  $D$  in modulating the momentum transfer for the impact of granular slugs against the inclined targets is first investigated. In each case, while the parameter being investigated was varied, all other parameters were held fixed at their reference values. Calculations were performed for  $0.35 \text{ MN m}^{-1} \leq K_n \leq 2.76 \text{ MN m}^{-1}$ ,  $0.1 \leq e \leq 0.95$  and  $150 \text{ }\mu\text{m} \leq D \leq 600 \text{ }\mu\text{m}$ . These ranges bound the uncertainty in these parameter values for the sand slugs. The components of the transferred momentum were not affected (changes were less than 1%) for simulations using these ranges of the parameters, and was consistent with previous studies. For example, Pingle et al. [99] and Guttenberg [55] demonstrated that  $e$  does not affect the flow of granular jets as increasing  $e$  results in more collisions per unit time so that the total dissipation remains approximately constant. Similarly, while Cheng et al. [18] have shown that as the number of particles across the width of the a granular jet is reduced, the jet stops behaving as an aggregate of particles and more like individual non-interacting particles. However, even with the largest particle diameter of  $600 \text{ }\mu\text{m}$  (for which the slug contained the smallest number of particles) this limit was not approached.

The sand slug in the experiments lengthened in free-flight, and thus the particle volume fraction  $\bar{\rho}$  in the slugs was constantly evolving. While the simulations in Section 4.5 appear to adequately capture the velocity gradients within the slug, there is always some room for uncertainty. In order to investigate whether such uncertainty in  $\bar{\rho}$  could affect the predictions of the transmitted momentum, the role of  $\bar{\rho}$  was investigated by performing impact simulations using sand slugs with  $0.12 \leq \bar{\rho} \leq 0.47$ . All these slugs were of diameter 12.7 mm with reference particle properties and  $\bar{\rho}$  was tuned by changing the length of the slug (the particles were still randomly distributed over the slug volume). Predictions of the variation of  $(I_T^z - I_T^y)/I_0$  and  $I_T/I_0$  with  $\bar{\rho}$  are included in Fig. 4.19 for the reference friction coefficient values  $\mu_T = 0.3$  and  $\mu_p = 0.6$ . An additional set of predictions with very high friction coefficients  $\mu_T = \mu_p = 2.0$  are also included. The increase in the friction coefficients slightly increases both  $(I_T^z - I_T^y)/I_0$  and  $I_T/I_0$ . Further, decreasing  $\bar{\rho}$  also marginally increased the transmitted momenta as the impact changed from the case of an impact of an aggregate of sand particles to individual particle impacts as discussed in Ref. [99]. However, these effects were small and are insufficient to explain the large discrepancies between predictions and measurements for the inclined impact of the sand-paper coated target surfaces reported in Section 4.5.

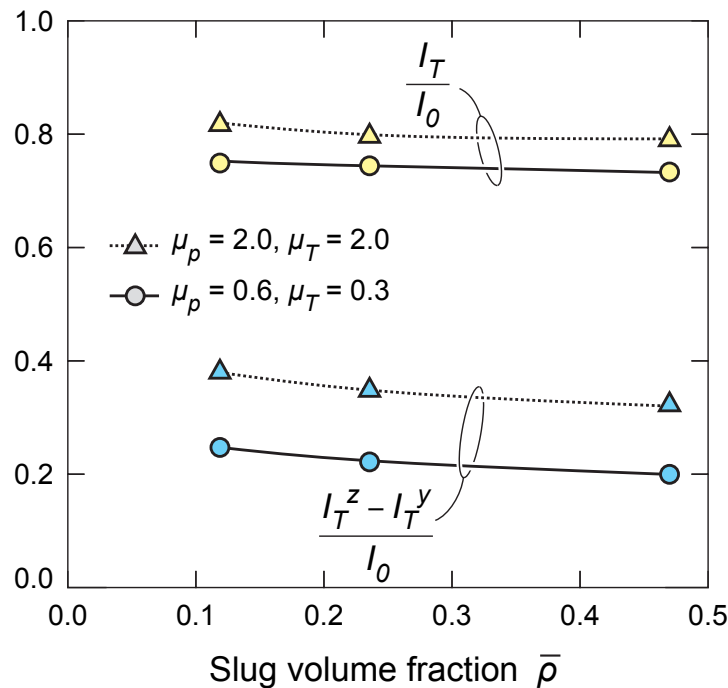


Fig. 4.19 Predictions of the variation of the transmitted momenta  $(I_T^z - I_T^y)/I_0$  and  $I_T/I_0$  with the volume fraction  $\bar{\rho}$  of sand particles within the uniform density slug just prior to impact against the inclined target. Results are shown for the reference inter-particle and particle/target friction coefficients  $\mu_p = 0.6$  and  $\mu_T = 0.3$ , respectively and an additional set of calculations with high values of  $\mu_p$  and  $\mu_T$ .

### 4.6.2 Effect of rotational inertia

The sand particles comprising the slugs are sub-spherical in shape (Fig. 4.3) while in the simulations they are modelled as perfect spheres of diameter  $D$ . The tendency of particles to rotate is expected to decrease with increasing angularity; see for example Refs. [19, 34]. To investigate the role of particle rotation on the transmitted momentum for inclined impact of the slug, it is noted that the rotation of particles is governed by their second moment of inertia,  $J_s$  about their diametrical axis which is given by

$$J_s = \frac{2}{5}m_p \left(\frac{D}{2}\right)^2 \equiv m_p k_s^2 \quad (4.12)$$

where  $k_s \equiv D/\sqrt{10}$  is the radius of gyration of the sphere. In order to explore the role of particle rotation, we maintain the spherical shape of the particles but artificially change the radius of gyration from  $k_s$  to  $k$  and study the sensitivity of the transmitted momentum to the ratio  $k/k_s$ . Such calculations are artificial in the sense that while contact between particles and particles and the target is detected based on spherical particles of diameter  $D = 300\mu\text{m}$ , the rotational motion of the particles is obtained by integrating Newton equations for the individual particles with a second moment of inertia  $J \equiv m_p k^2$  about the diametrical axis.

Predictions of  $(I_T^z - I_T^y)/I_0$  and  $I_T/I_0$  as a function of  $k/k_s$  are included in Figs. 4.20a and 4.20b, respectively for 5 choices of  $\mu_T$  in the range 0.1 to 1.0 with  $\mu_p = 0.6$ . Both  $(I_T^z - I_T^y)/I_0$  and  $I_T/I_0$  increase significantly with increasing  $k/k_s$  for  $\mu_T \geq 0.6$ , i.e. decreasing the tendency of the particles to rotate strongly affects the transmitted momentum when there is a high friction coefficient between the target surface and the particles. In fact for  $k/k_s$  in the range 15 to 50 and  $\mu_T = 1.0$ , the predicted values of  $(I_T^z - I_T^y)/I_0$  and  $I_T/I_0$  seem to lie in the range measured for the sand-paper coated targets.

In order to understand the sensitivity of the transmitted momentum to  $k/k_s$ , we consider the simple situation of the rolling/sliding motion of a single particle along the surface of the target. This particle has a second moment of inertia  $J$  and diameter  $D$  (recall the artificial situation we are considering here where even though the particle shape is fixed as a sphere of diameter  $D$ ,  $J$  is treated as an independent parameter). The particle is given a pure sliding velocity  $v_s$  along the surface of the target at time  $t_s = 0$  and subjected to a constant normal force  $N$ . The frictional force  $F_s = \mu_T N$  acts to reduce the translational velocity  $v$  of the particle while simultaneously increasing its rotational velocity  $\omega$ . With initial conditions  $v = v_s$  and  $\omega = 0$  at time  $t_s = 0$ , the equations of motion of the particle are

$$v = v_s - \frac{F_s}{m_p} t_s \quad (4.13)$$

and

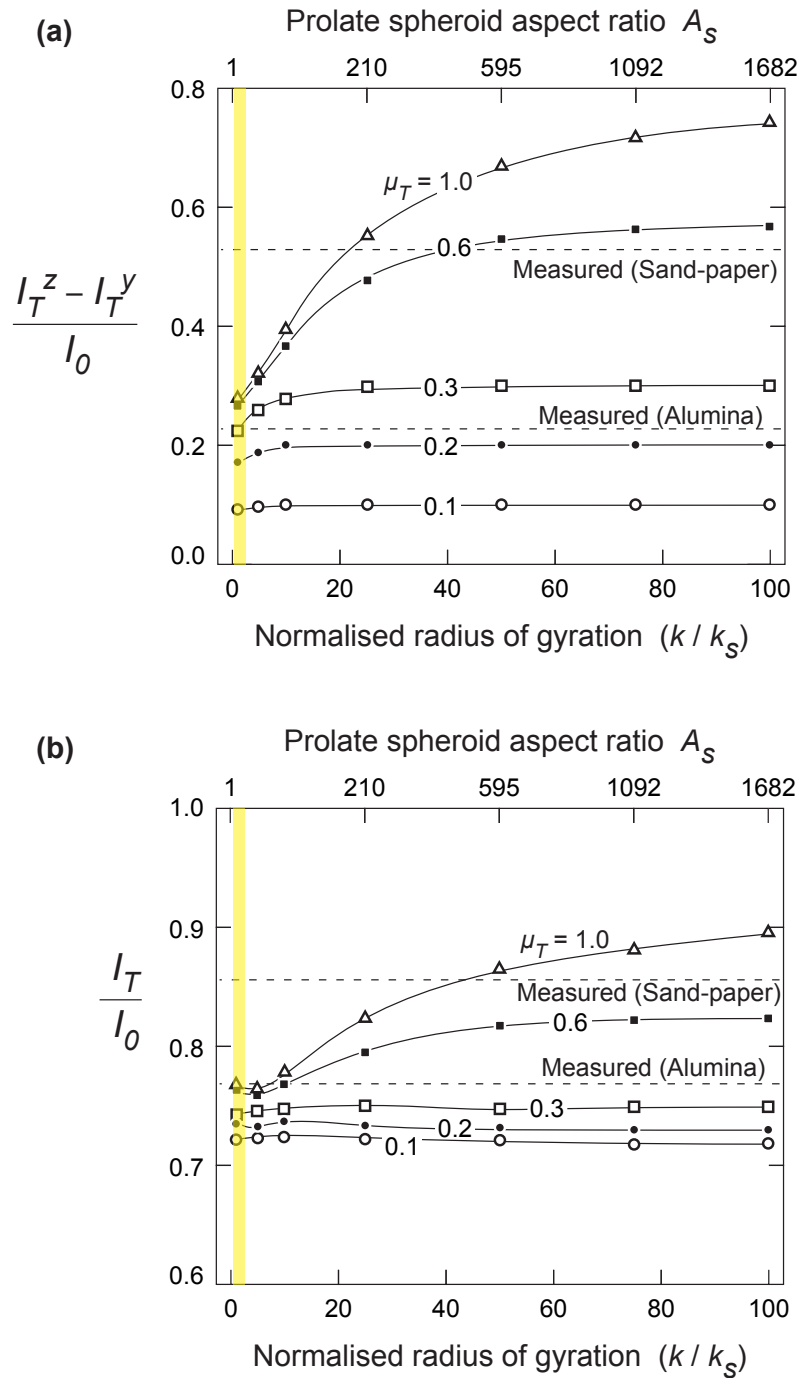


Fig. 4.20 Predictions of the transmitted momenta (a)  $(I_T^z - I_T^y)/I_0$  and (b)  $I_T/I_0$  as a function of the normalised radius of gyration  $k/k_s$  of the particles for impact of the uniform density sand slug against the inclined target. Calculations are shown for 5 selected values of the particle/target surface friction coefficient  $\mu_T$ . The measured values of the transmitted momenta for impact of the dry sand slug against the inclined target with the Alumina and sand-paper coatings are also indicated. The upper  $x$ -axis indicates the aspect ratio  $A_s$  of prolate spheroids with radius of gyration  $k$  about their minor axis and the realistic range of  $A_s$  values for the sand particles used in these experiments is marked by the shaded region.

$$\omega = \frac{F_s D}{2J} t_s \quad (4.14)$$

Sliding terminates with the particle commencing pure rotational motion when  $v = \omega D/2$ . Thereafter, the frictional force reduces to zero as there is no relative sliding between the particle and the target and the particle continues to translate at a steady-state translational velocity  $v^{ss}$  and rotational velocity  $\omega^{ss}$ . These are given from Eqs. 4.13 and 4.14 as

$$v^{ss} = \frac{\omega^{ss} D}{2} = \frac{v_s}{\left[1 + \frac{4J}{m_p D^2}\right]} = \frac{v_s}{\left[1 + \frac{2}{5} \left(\frac{k}{k_s}\right)^2\right]} \quad (4.15)$$

The transmitted momentum  $I_s$  into the target (in a direction parallel to the surface of the target) is  $I_s = m_p(v_s - v^{ss})$  and the normalised transmitted momentum  $I_s/I_0$  (where  $I_0 = m_p v_s$  is the initial momentum of the particle) then follows as

$$\frac{I_s}{I_0} = \frac{\frac{2}{5} \left(\frac{k}{k_s}\right)^2}{\left[1 + \frac{2}{5} \left(\frac{k}{k_s}\right)^2\right]} \quad (4.16)$$

Thus, for a particle with  $k = k_s$ ,  $I_s/I_0 \approx 0.29$  while  $I_s/I_0 \rightarrow 1$  as  $k \rightarrow \infty$  when rotational motion of the particles is inhibited. This simple analysis illustrates the role that the second moment of inertia plays in governing the momentum that is transmitted into the target in a direction parallel to the target surface due to frictional interactions between the target and the particle. Critically, particles with a large radius of gyration will result in larger transmitted momentum  $I_s$ . We thus argue that the discrepancy between the predictions of Section 4.5 and measurements are due to the fact that the particles were modelled as spherical while in the experiments, the particles have a sub-spherical shape (Fig. 4.3) that reduces the tendency of the actual sand particles to rotate.

### 4.6.3 Discussion on effect of particle shape

The measures of transmitted momenta  $(I_T^z - I_T^y)/I_0$  and  $I_T/I_0$  increase with  $k/k_s$  as seen in Fig. 4.20. These calculations were performed using spherical particles in which  $k$  was artificially treated as an independent parameter. In order to gauge the particle shapes corresponding to the range of  $k/k_s$  values covered in Fig. 4.20 we consider particles that are prolate spheroids with aspect ratio  $A_s \geq 1$  and volume equal to that of a sphere of diameter  $D$ . Then the radius of gyration of this prolate spheroid about its minor axis is given by the relation

$$\frac{k}{k_s} = \sqrt{\frac{A_s^{4/3} + A_s^{-2/3}}{2}} \quad (4.17)$$

We include a second  $x$ - axis in Fig. 4.20 (upper scale) to indicate the relation between  $A_s$  and  $k/k_s$  given by Eq. 4.17. The values of  $k/k_s$  that bring the measurements and predictions into agreement for the sand-paper coated targets correspond to large values of  $A_s$ . Prolate spheroids with such large aspect ratios would have a needle-like appearance while the sand particles in the experiments are sub-spherical (Fig. 4.3). Moreover, we note from Figs. 4.20a and 4.20b that there is no single value of  $k/k_s$  that will accurately predict the measured values of both  $(I_T^z - I_T^y)/I_0$  and  $I_T/I_0$ .

The need for these unrealistically large values of  $k/k_s$  (the realistic range is indicated in Fig. 4.20) is due to the artificial assumption used in the calculations wherein the particles retain their spherical geometry but  $k$  is varied independently. For example consider a cubic particle with volume equal to that of a sphere of diameter  $D$ . Then the radius of gyration of this cubic particle about one of its principal axes is

$$\frac{k}{k_s} = \sqrt{\frac{5}{3} \left(\frac{\pi}{6}\right)^{2/3}} \approx 1.04 \quad (4.18)$$

This cubic particle will never attain a state of pure rolling and for the situation discussed in Section 4.6.2, will result in a normalised transmitted momentum  $I_s/I_0 = 1$  in a direction parallel to the target surface even with this relatively low value of  $k/k_s$ . We thus argue that in order to predict the transmitted momentum we need to capture the effect of friction between the particles and the target surface accurately. This will require us to appropriately parameterise shapes of the particles used in the experiments and develop discrete element simulations that explicitly model such particles. Experimental verification of this hypothesis using spherical particles would have been ideal. However, spherical particles (usually made of glass) shatter in impact experiments thus making such studies infeasible. A follow-on numerical study [45] wherein particles of different shapes are explicitly modelled verifies the qualitative arguments on the effect particle shape presented here.

## 4.7 Concluding remarks

The responses of dry and water saturated sand slugs impacting normally oriented and inclined rigid-stationary targets have been measured while simultaneously quantifying the dependence of transmitted momentum on the surface type. Four surface coatings: Alumina, PTFE, Aluminium and sand-paper were employed in this study. Coupled discrete particle/Lagrangian simulations of the experiments are also reported in order to help clarify the physics of the impact process.

The measurements indicate that the slugs deform by spreading along the target surfaces with little rebound of the sand particles. This is reminiscent of the impact of a water jet impacting a rigid target. No measurable differences in the fraction of the transmitted momentum are observed between dry and water saturated sand slugs for both the normal and inclined impact cases. Moreover, over the range of slug velocities investigated here, no effects of slug velocity on the fraction of the transmitted momenta were measured. Symmetry of impact process for the normally oriented target implies that the only non-zero component of the transmitted net momentum is in the direction of the incoming sand slug (i.e.  $I_T^z \neq 0$ , while  $I_T^y = I_T^x = 0$ ) and this also results in no measurable effect of the surface type on the transmitted impulse. By contrast, impact of the sand slug on the target inclined at  $\alpha = 45^\circ$  to the incoming slug results in asymmetric spreading of the sand particles along the surface of the target. This implies that both  $I_T^z \neq 0$  and  $I_T^y \neq 0$  and frictional interactions between the sand particles and the target surface now play a crucial role in modulating the transmitted momentum. In the absence of friction between the sand particles and the target surface we show that  $I_T^z = I_T^y$  for a target inclined at  $\alpha = 45^\circ$ . However, for all surface coatings employed here, we observed  $I_T^z > I_T^y$  with  $I_T^z - I_T^y$  increasing in the order of surface coatings Alumina to PTFE to Aluminium to sand-paper. Correspondingly, the resultant transmitted momentum also increased in the same order.

Coupled discrete particle/Lagrangian simulations of these experiments using spherical particles predicted the measurements for the normal impact accurately and captured the observed insensitivity of the measurements to slug velocity and surface type as parameterised by the particle/target friction coefficient. However for inclined impact, the simulations considerably under-predicted the measured values of  $I_T^z - I_T^y$  especially in the case of the targets with the sand-paper coated surface. No value of the particle/target friction coefficient  $\mu_T$  brought the measurements and predictions into agreement. We have demonstrated that increasing the radius of gyration of the particles and thereby reducing their tendency to rotate and increases the predicted  $I_T^z - I_T^y$ . With the sand particles employed in the experiments having a sub-spherical we argue that this is the main source of the discrepancy between measurements and predictions.

The combined experimental and numerical study presented here has demonstrated the importance of particle shape in governing the momentum transfer to targets for asymmetric sand slug impacts. Such impacts are more likely to occur in practical situations compared to symmetrical impacts. Most numerical calculations tend to use spherical particles to represent the impacting granular media and neither models that permit rotation of the spherical particles [79] or completely restrict their rotation [11] can accurately capture all components of the transmitted momentum. This study has demonstrated the limitation of the widely used spherical particle assumption in granular impact calculations and indicates the need for more accurate representations of actual particle shapes in numerical calculations.

# Chapter 5

## Impact of granular slugs on rigid targets: effect of grain shape and fracture

### Abstract

The effect of grain shape and fracture on the interaction of high velocity granular slugs with rigid stationary targets is analysed for targets in normal and inclined orientations. The granular slugs comprise spherical, rod-shaped or cubic grains and are constructed by connecting together spherical sub-particles with either rigid or beam connectors. The case when grain fracture is suppressed (rigid connectors between sub-particles) is first analysed. With increasing grain aspect ratio, the grains tend to slide rather than roll on the target surface and this increases frictional interactions with the target surface. However, these enhanced frictional forces do not affect the momentum transmitted into normally oriented targets due to the symmetry of the problem. By contrast, the break in the symmetry for inclined targets results in the transmitted momentum increasing with grain aspect ratio. Fracture of the grains (as modelled by the fracture of the beam connectors between sub-particles) is shown to affect the momentum transmitted into the inclined targets. This is a consequence of fracture resulting in a change in grain shape. In this case the simulations show that the transmitted momentum is a function of the initial grain shape, the fracture properties of the grains and the impact velocity. In fact, grain fracture results in an enhanced transmitted momentum for initially cubic grains but fracture of grains with a high initial aspect ratio results in a reduction in transmitted momentum as these grains fragment into more spherically shaped grains.

## 5.1 Introduction

Determining the loads applied to structures by the impact of high velocity granular matter is a problem of significant scientific research and technological interest. For example, the design of ground vehicles subjected to landmine explosions depends upon a detailed understanding of the forces applied during the interaction of the vehicle structure with explosively accelerated soil. The phenomena that contribute to this dynamic loading following detonation of shallow-buried explosives are very complex and current understanding is largely based on empirical models that estimate the impulsive loads imposed by soil ejecta [135]. Such models have helped inform more recent experimental characterizations of buried explosive events [8, 88]. However, there still remains significant uncertainty especially on how properties of the soil affect the loads imposed on structures by the high velocity granular media.

Reduced-scale experiments have been increasingly used for parametric studies to understand phenomena associated with dynamic loading of structures by explosively accelerated granular media. For example, Hlady [56] employed 0.025 kg buried charges in conjunction with a vertical impulse pendulum to investigate the influence of soil properties. Increasing the water saturation was shown to increase the momentum imparted to the target plate, but only if a threshold moisture content was exceeded. In a joint study, Taylor et al. [119] and Fourney et al. [38] considered the scalability of buried charge experiments and demonstrated an influence of plate mass. This dependence on plate mass indicates that fluid-structure interaction (FSI) effects may play a role for granular media impacting structures. Neuberger et al. [88, 87] examined the deformation of clamped plates loaded by spherical charges either flush buried in dry sand (i.e. zero sand overburden) or in air alone and showed that the presence of sand increases the deformation of the target plate.

In the majority of experimental studies, control of the soil conditions is relatively poor and this results in a scatter of  $\pm 15\%$  from nominally identical tests [22]. In fact, such dispersion in observations persists even when soil as specified by the NATO standardisation agreement STANAG 4569 [86] is used and the scatter in observations is commonly attributed to variability in the granular media. For example, Rigby et al. [107] have shown that particle size distributions and soil type (sand versus clay versus gravel) strongly influences the loading imposed on structures. Similarly, Ehrgott et al. [32] conducted a series of experiments with both surface and shallow buried test charges where they carefully varied the soil type and demonstrated a significant variation in impulse loads with soil properties. They attributed the dependence on the soil type to differences in the generated soil ejecta rather than the efficiency of momentum transfer during particle-target impact. An alternative approach to better control the experimental conditions was developed by Dharmasena et al. [30] and involves explosively accelerating silica glass microspheres that encase a spherical explosive charge. This approach has been utilised in a number of studies including by Kyner et al. [74] as it gives repeatable results

and therefore is more suitable for detailed numerical modelling. However, the drawback of this approach is that the influence of soil type, including particle shape, upon the impact loading are neglected.

A number of numerical approaches have been proposed to model the complex dynamic interaction of high velocity granular media with structures. For example, Rimoli et al. [108] used the soil constitutive model of Deshpande et al. [27] to deduce the impulse applied to structures by explosively accelerated spherical sand shells. Grujicic et al. [48, 52, 51] and Wang et al. [130] used coupled Eulerian/Lagrangian simulations of landmine explosions, and attempted to compare their predictions with blast impulse and plate deformation measurements from Bergeron and Tremblay [7] and Foedinger [36]. Recently, coupled discrete particle/continuum simulations have been increasingly used to investigate the response of structures impacted by high velocity granular media. For example, Borvik et al. [11] followed by Dharmasena et al. [30] and Holloman et al. [58, 57] used this approach to simulate the response of a variety of monolithic and sandwich structures loaded by high velocity granular sprays generated by the explosive detonations. These discrete particle approaches typically use spheres to represent the granular particles although some differences exist in individual implementations. For example, Liu et al. [79] and Dharmasena et al. [30] allow for three rotational and three translational degrees of freedom for the spherical particles while the approaches of Borvik et al. [11] and Holloman et al. [58, 57] restrict rotational motion of the spheres, even though tangential frictional forces that impose torques on the particles are included in the analyses. Since all these studies were restricted to spherical particles, they were unable to investigate the effect of particle angularity on the dynamic flow and impact of granular media. However, the static and dynamic flow of granular media is well-known to be strongly influenced by the shape of the granular particles. For example, Cho et al. [19] observed that particle angularity hinders particle rotation, while Farhadi and Behringer [34] showed that particle shape significantly influenced the jamming behaviour of granular media. Most studies on the impact properties of granular media are restricted to spherical particles [46, 68–70, 136] although it has been shown that particle shape strongly influences the interaction of a single particle with a structure [61, 92, 93]. It is worth emphasizing here that particle angularity may not arise only from the initial particle shape; it can also develop by particle fracture during impact events. While some studies [5, 21, 94, 139] have analyzed the fracture of particles, the change in particle shape and its effect on the interaction of granular media with a structure are not well studied or understood.

Loading of targets by high velocity granular media generated by explosive detonations typically results in poorly characterized granular sprays. This is because the explosive gases obscure the view and only the outer surface of granular front is visible; see for example Pickering et al. [98] and Dharmasena et al. [30]. Park et al. [95] developed a technique to generate a high-velocity granular slug within a laboratory setting and without the need for the detonation of an explosive. They thus circumvented the problems

associated with explosive detonations. Uth and Deshpande [125] and Uth et al. [126] employed this setup to investigate the dynamic response of monolithic and sandwich structures impacted by such granular slugs. These measurements indicated that while the momentum transmitted into the inclined targets was less than that for the normally oriented counterparts, it was significantly higher than that anticipated from analyses which neglect frictional interactions between the granular particles and the target; see for example Cheng et al. [18] as well as Johnson and Gray [64]. Goel et al. [44] subsequently showed that frictional interactions between the particles of granular medium and the target surface significantly increase the momentum transfer to the target. Moreover, Goel et al. [44] demonstrated that discrete particle numerical simulations using spherical particles were unable to capture these frictional effects. They argued that modelling the angular particle shapes is critical in order to accurately predict the interaction of high velocity granular media with a target. The primary aim of this study is to begin a fundamental investigation of the effect of particle shape on the momentum transmitted to structures by the impact of a granular media. We numerically analyze the prototypical problem of the impact of granular slugs with rigid stationary targets at normal and inclined angles of incidence as shown in Fig. 5.1, and investigate the effect of particle shape and particle fracture on the momentum transferred from the granular slug into the targets.

## 5.2 Problem description and simulation methodology

Consider the normal and oblique impact of a slug comprising granular particles (referred to subsequently as grains) on rigid stationary targets as shown in Fig. 5.1. The experiments conducted by Goel et al. [44] indicated that friction between the grains and targets strongly influence the momentum transferred during oblique impacts and that coupled discrete particle/Lagrangian finite element (FE) simulations with spherical grains were unable to capture the measurements with sufficient fidelity. Artificially increasing the rotational inertia of the grains, and thereby reducing the rolling of the grains improved the predictions and suggested that grain shape might have a strong influence on momentum transfer. The objective of this numerical study is to investigate the effect of grain shape on the interactions of high velocity granular media with structures. This is accomplished via coupled discrete particle/Lagrangian finite element simulations performed in the commercial package Abaqus.

Simulations of granular slug impact with rigid stationary targets were conducted in two orientations. In the “normal orientation” (Fig. 5.1a), the slugs impacted the target at an angle  $\alpha = 90^\circ$  to the face of the target while in the “inclined orientation”, the slugs impacted the target at  $\alpha = 45^\circ$  (Fig. 5.1b). Prior to impact, the granular slugs were cylindrical with a diameter of 12.7 mm and length  $L = 50$  mm. They comprised a spatially uniform distribution of grains such that the total mass of the slug  $m_{slug} = 4.2$  g and the grains occupied a fraction  $\bar{\rho} \approx 0.25$  of the slug volume. All the grains were given

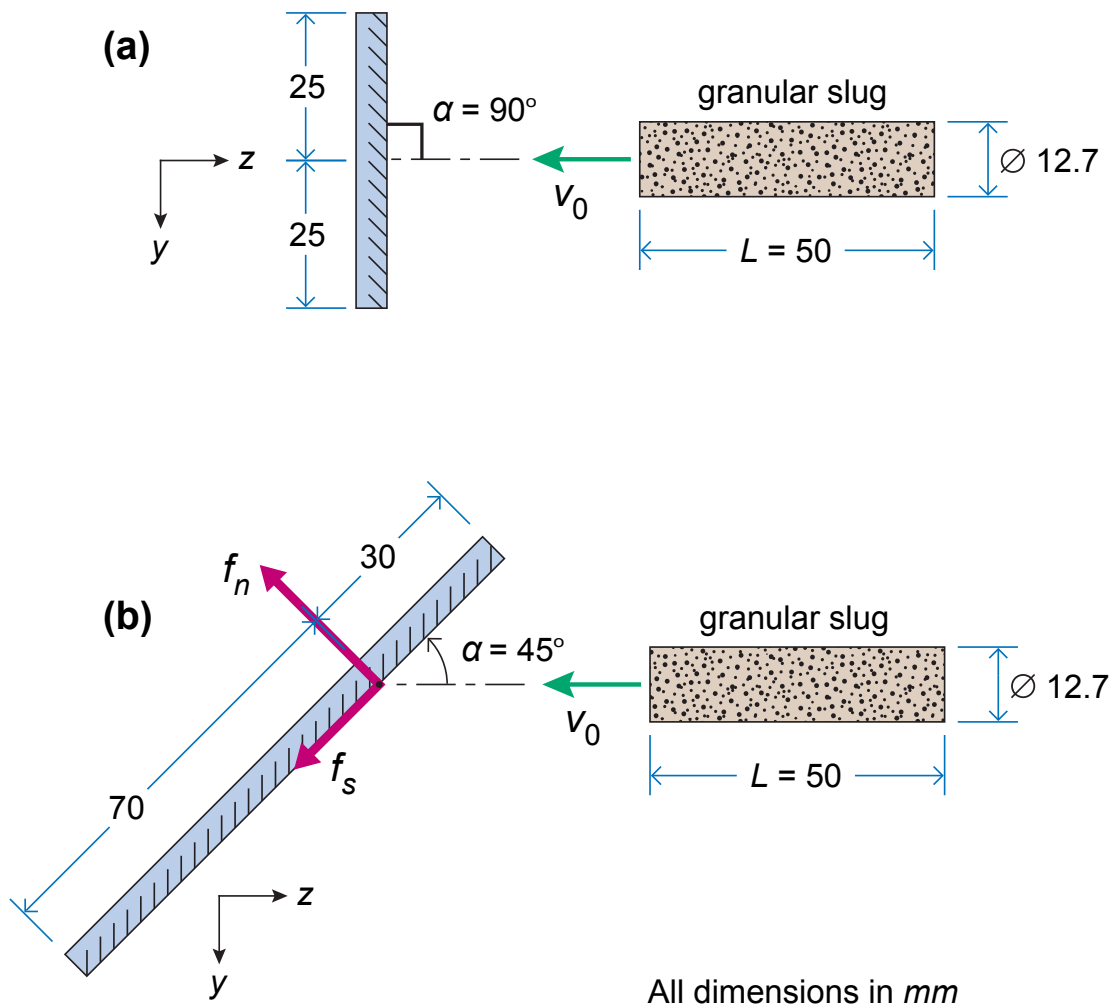


Fig. 5.1 Impact of cylindrical granular slugs with rigid stationary targets in the (a) normal and (b) inclined orientations.

an initial velocity  $v_0$  in the negative  $z$ -direction (Fig. 5.1) with all other components of the translational and all rotational velocity components set to zero. The rigid stationary targets were 50 mm wide in the  $x$ -direction while the length of the target surface facing the slug impact was 50 mm for normal impact (i.e. a square target of dimensions 50 mm  $\times$  50 mm) and 100 mm for inclined impact case, as shown in Fig. 5.1. The slugs were impacted near the target centre: the targets were sufficiently large such that the transmitted momentum was insensitive to the precise location of the impact.

### 5.2.1 Geometry of the grains

Three shapes of grains were used in the calculations presented here: (i) spherical, (ii) rod-shaped and (iii) cubic. We emphasize that the aim here is not to simulate a specific soil type but rather illustrate the effect of grain shape on the interaction of high velocity

granular media with structures. These grains were all constructed by combining together spherical particles. For clarity of terminology, we shall refer to the spherical particles from which the grains were constructed as *sub-particles*. The spherical sub-particles are rigid single node spherical elements (PD3D in the Abaqus notation) of density  $\rho_p$  and diameter  $d_p$  such that they had a mass  $m_p = (4/3)\pi(d_p/2)^3\rho_p$ .

The spherical grains comprised of a single sub-particle of diameter  $D$  as shown in Fig. 5.2a. These spherical grains served as the reference case. The rod-shaped grains comprised a linear array of the sub-particles with centre-to-centre spacing  $d_p$  as shown in Fig. 5.2b. The aspect ratio  $\Phi$  of these rod-shaped grains is defined as the ratio of the grain length to the diameter of the circumscribing cylinder. Thus,  $\Phi = n$  where  $n$  is the number of sub-particles that form the grain. In order to perform a study of the effect of the aspect ratio  $\Phi$ , all grains in the calculations reported here had equal volume. Thus, given the diameter  $D$  of the reference spherical grain, the diameter  $d_p$  of the sub-particles in the rod-shaped grain of aspect ratio  $\Phi$  follows as  $d_p = D/\sqrt[3]{\Phi}$ . The cubic grains consisted of a simple cubic packing of the sub-particles such that a cube of side length  $s \equiv d_p\sqrt[3]{n}$  circumscribes the grain, where  $n$  is the number of sub-particles in the grain; see Fig. 5.2c. Again, the sum of the volume of the sub-particles comprising the cubic grain equals the volume of the reference spherical grain. Thus, the diameter of the sub-particles within cubic grains comprising  $n$  sub-particles is  $d_p = D/\sqrt[3]{n}$ .

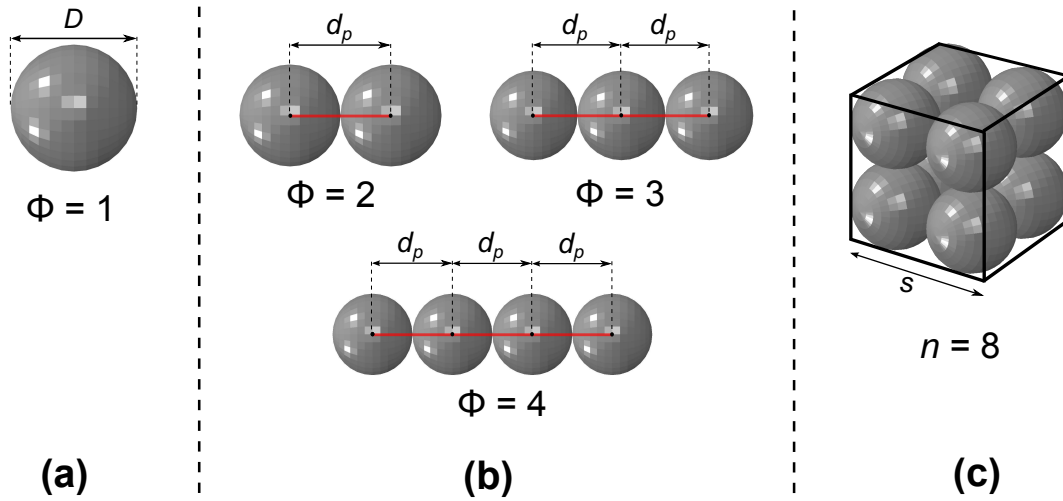


Fig. 5.2 Sketches of the different grain shapes analysed in this study. (a) Spherical grains of diameter  $D$ . (b) Rod-shaped grains with aspect ratios  $2 \leq \Phi \leq 4$  constructed from spherical sub-particles. (c) Cubic grains comprising  $n = 8$  spherical sub-particles.

Two types of connections between the centres of the sub-particles were employed in this study:

1. Rigid connections between the sub-particle centres such that the shape of the grains remained unchanged throughout the impact event. These rigid connections were specified using the multi-point constraint (MPC) functionality in Abaqus.

2. The nearest-neighbour centres of the sub-particles were connected to each other using a single Timoshenko beam element (B31 in the Abaqus notation). The inter sub-particle forces were then equal to the sum of the forces due to these beam connections and inter sub-particle contact law as detailed in Section 5.2.2. These beam elements permitted the grains to deform and fracture (additional details of the beam properties are provided in Section 5.4).

### 5.2.2 The particle contact model and coupling to FE simulations

Since the grains composed of sub-particles in the formulation employed in this study, it is these sub-particles that come into contact with each other as grains collide with each other and/or with the target surface. Thus, it suffices to specify a contact model for sub-particle contact. In line with usual discrete element simulations, the sub-particles were taken to be rigid spheres with contact between the sub-particles and between sub-particles and the target surface modelled using the soft-contact approach (Fig. 5.3) introduced by Cundall and Strack [24]. The inter sub-particle contact law comprises:

1. A linear spring with spring constant  $K_n$  and linear dashpot with damping constant  $\gamma_n$  connected in parallel, governing the radial contact force-displacement relation (in the direction connecting the sub-particle centres).
2. A linear spring of constant  $K_s$  and Coulomb friction coefficient  $\mu$  connected in series, governing the tangential contact relationship.

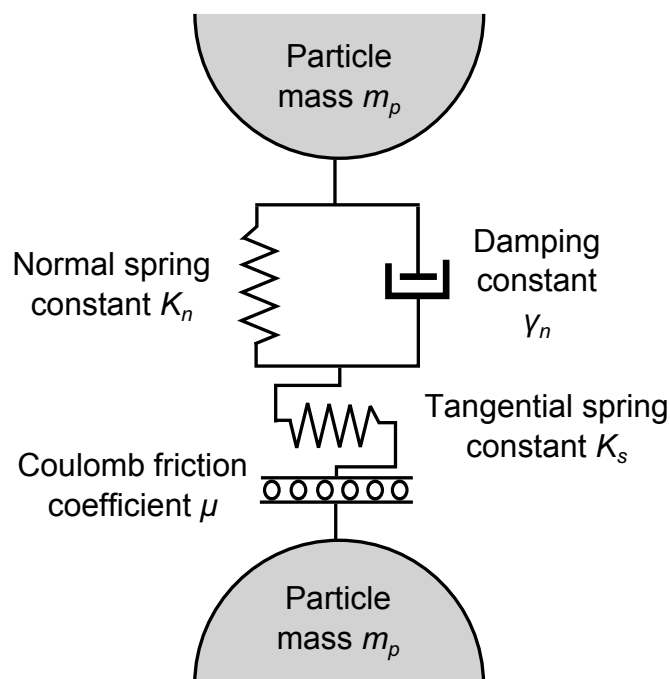


Fig. 5.3 Sketch of the inter sub-particle contact model between spherical sub-particles of diameter.

With  $r$  denoting the distance of separation of the sub-particle centres, and the sub-particle interpenetration given by  $\delta_n = r - d_p$ , the normal force during active contact ( $\delta_n < 0$ ) is given by

$$F_n = K_n \delta_n + m_{\text{eff}} \gamma_n \dot{\delta}_n \quad (5.1)$$

where  $m_{\text{eff}}$  is the reduced mass of the two contacting bodies. For impacts between sub-particles,  $m_{\text{eff}} = m_p/2$  while for impacts between a sub-particle and the target,  $m_{\text{eff}} = m_p$ .

The tangential force  $F_s$  only exists during an active contact, and opposes sliding. It is limited in magnitude to  $|F_s| < \mu|F_n|$ , where  $\mu$  is the friction coefficient and specified as follows. With  $\dot{\delta}_s$  denoting the tangential displacement rate between the contacting sub-particles,  $F_s$  is represented by an elastic-plastic relation with stiffness  $K_s$ , i.e.

$$\dot{F}_s = \left\{ \begin{array}{ll} K_s \dot{\delta}_s & \text{if } |F_s| < \mu|F_n| \text{ or } F_s \dot{\delta}_s < 0 \\ 0 & \text{otherwise} \end{array} \right\} \quad (5.2)$$

The critical difference for interactions between sub-particles and between a sub-particle and the target is the coefficient of friction  $\mu$ : we use  $\mu_p$  and  $\mu_T$  to denote the values of  $\mu$  for inter sub-particle and sub-particle/target interactions, respectively. The value of damping constant  $\gamma_n$  dictates the loss of sub-particle kinetic energy during normal collision and is directly related to the coefficient of restitution  $e$  according to

$$e = \exp \left[ - \frac{\pi}{\left( \frac{8K_n}{\gamma_n^2 m_p} - 1 \right)^{1/2}} \right] \quad (5.3)$$

The collision time  $t_e$  for individual binary collisions is given as as

$$t_e = -2 \frac{\ln(e)}{\gamma_n} \quad (5.4)$$

Thus, in the limit of plastic collisions ( $e \rightarrow 0$ ), the contact time  $t_e \rightarrow \infty$ . The forces (normal and tangential) on each sub-particle are calculated at each time step and the Newton's equations for both the translational and rotational motions of the sub-particles are integrated using an explicit time-integration scheme provided in Abaqus. The time-step for integration was taken to be less than  $t_e/10$  in order to ensure accurate integration of the equations of motion.

The rigid targets were modelled as analytical rigid surfaces and all six degrees of freedom (3 rotational and 3 translational) constrained to prevent all rigid body motions. The coupling between the discrete grains and rigid surfaces was performed as follows. At a given time  $t$ , a proportion of the grains are in contact with the target surface. Consider

one such grain in contact with the target. One or more of the sub-particles of that grain are in contact with the target with an interpenetration  $\delta_n$  defined as  $\delta_n = r - d_p/2$ , where  $r$  is the distance between the sub-particle centre and contact point on the target (note the difference in the definition of  $\delta_n$  for inter sub-particle and sub-particle/target interactions). Denote  $\dot{\delta}_n$  to be the relative approach velocity of the sub-particle and the point of contact on the target surface, and likewise  $\dot{\delta}_s$  is the relative tangential velocity. The normal and tangential contact forces are then calculated using Eqs. 5.1 and 5.2. The targets were modelled using a Lagrangian finite element (FE) framework and these forces were then added as nodal forces in the finite element analysis of the target to complete the coupling between the discrete and finite element calculations.

The primary goal of this study was to determine the momentum transmitted from the impacting slug into the target. Denote the reaction forces in the  $x$ -,  $y$ - and  $z$ -directions on the target as  $F_x$ ,  $F_y$  and  $F_z$ , respectively. Then, the momentum  $i_T^z$  transmitted into the target in the  $z$ -direction after a time  $t$  (where  $t = 0$  corresponds to the instant that the slug first comes into contact with the target) is given by

$$i_T^z(t) = \int_0^t F_z dt \quad (5.5)$$

and  $I_T^z \equiv i_T^z$  (in the limit  $t \rightarrow \infty$ ) is the total momentum transmitted into the target in the  $z$ -direction. Analogous expressions exist for momentum components in the other two orthogonal directions (viz.  $I_T^y$  and  $i_T^y$  as well as  $I_T^x$  and  $i_T^x$ ). For both normal and oblique impacts analysed here, symmetry dictates that  $i_T^x = 0$  and so we focus on the momentum in the  $z$ - and  $y$ -directions and the resultant transmitted momentum given by

$$I_T = \sqrt{(I_T^z)^2 + (I_T^y)^2} \quad (5.6)$$

All results are presented with the transmitted momenta normalised by the initial momentum  $I_0 \equiv m_{slug}v_0$  of the slug in the  $z$ -direction.

### 5.2.3 Construction of granular slugs

Prior to impact, the cylindrical slugs have a spatially uniform distribution of identical grains that occupy a volume fraction  $\bar{\rho}$ . While all grains have the same initial velocity, we desire that the grains are located and oriented randomly within the slug. This was achieved via a four-step process shown schematically in Fig. 5.4 so as to obtain cylindrical slugs with a diameter 12.7 mm and length  $L = 50$  mm.

1. The grains were first randomly located within a cylinder of diameter  $< 12.7$  mm and length  $L > 50$  mm. In this step, while the location of the grains was random, all grains had the same orientation, i.e. the rod-shaped grains were oriented along the axis of the cylinder (Fig. 5.4a) while the cubic grains had two faces parallel to

the flat faces of the cylinder. This process typically resulted in a slug with a grain volume fraction  $\ll \bar{\rho}$ .

2. All grains were then given a velocity  $v = 10 \text{ m s}^{-1}$  in the  $z$ -direction and the end of the cylinder towards which the grains were travelling was capped by a rigid face (Fig. 5.4b). The grains were then allowed to collide with each other, dissipate their kinetic energy via plastic collisions (using contact properties specified in Section 5.2.4) and settle within the cylinder under the influence of gravity that was acting in the positive  $z$ -direction.
3. The grains were then further compacted within the cylinder by the action of a piston as shown in Fig. 5.4c. The collisions and re-arrangements of the grains in steps (ii) and (iii) resulted in a dense random packing of the grains within a cylindrical volume of length  $< 50 \text{ mm}$ .
4. At the end of step (iii), the dense randomly packed grains were within a cylindrical volume with both diameter and length less than the desired values. We then applied a hydrostatic affine transformation (Fig. 5.4d), i.e. the centroid of each grain was displaced by  $u_i = (H/3)\delta_{ij}x_j$ , where  $H$  and  $\delta_{ij}$  are the hydrostatic strain and Kronecker delta, respectively while  $x_j$  is the Cartesian location of the grain centroid. The hydrostatic strain  $H$  was chosen such that the slug attained the desired diameter and length after application of the transformation. We emphasize that iterations were required wherein the initial diameter and length of the slug in step (i) were adjusted such that the final slug had the required overall dimensions.

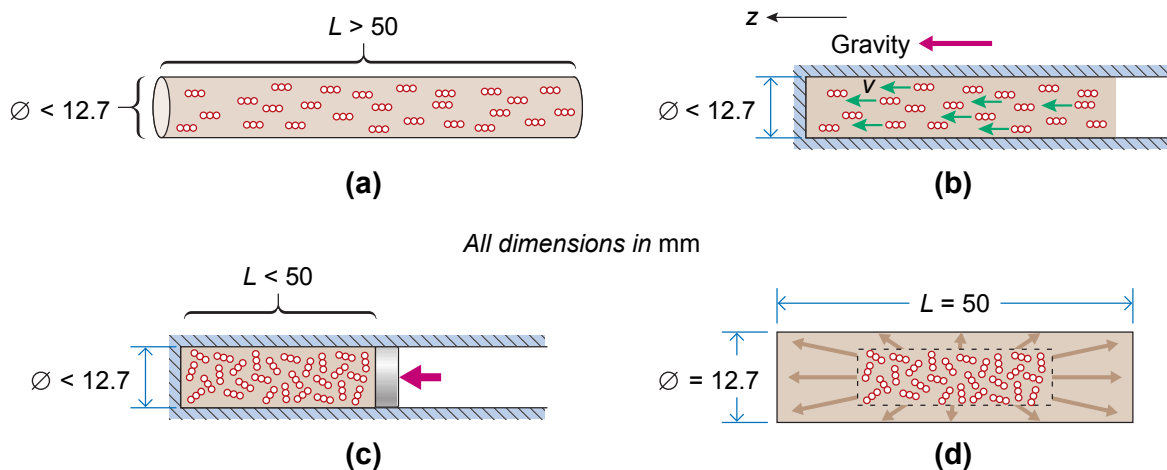


Fig. 5.4 Sketches illustrating the construction of the cylindrical granular slug. (a) Step (i): randomly located but aligned grains. (b) step (ii): settling of the grains under the influence of gravity. (c) step (iii): compaction of the grains in the cylindrical cavity. (d) step (iv): affine expansion to achieve the required size of the slug.

## 5.2.4 Material parameters

All calculations presented here used the following reference properties for the grains and subparticles. The granular slugs had a volume fraction  $\bar{\rho} = 0.25$  of grains and the reference spherical grain had a diameter  $D = 600 \mu\text{m}$ , i.e. the volume of the individual grains was equal to that of a sphere of diameter  $600 \mu\text{m}$ . The sub-particles were assumed to be made from a solid of density  $\rho_p = 2700 \text{ kg m}^{-3}$  (approximately equal to that of the quartz phase of silica) and the sub-particle contact model was defined by four parameters  $K_n$ ,  $e$ ,  $K_s$  and  $\mu_p$ . Liu et al. [79] and Goel et al. [44] demonstrated that these parameters have a negligible effect on the interaction of the granular slug with the targets and thus following these studies we chose them to be  $K_n = 0.69 \text{ MN m}^{-1}$ ,  $K_s/K_n = 2/7$  [4, 112],  $e = 0.7$  and  $\mu_p = 0.6$ . The friction coefficient  $\mu_T$  between the particles and the target surface depends on the target surface and was varied over the range  $0.0 \leq \mu_T \leq 2.0$  in the calculations presented here. The effect of gravity was neglected in all the impact simulations that are discussed subsequently.

The calculations presented in Section 5.3 use rigid non-deformable grains and the properties listed above completely specify the required material properties. The calculations in Section 5.4 allow the grains to deform and fracture by employing sub-particles connected together by deformable beams. The material properties for these beams are presented along with the calculations in Section 5.4.

## 5.3 Effect of particle shape

We proceed to present numerical results for the effect of grain shape on the interaction of high velocity granular slugs with the targets in both the normal and inclined orientations. Since the objective is to investigate only the effect of grain shape, all the simulations were restricted to grains comprising either a single spherical particle or grains constructed by joining together sub-particles via rigid connections. A number of studies [44, 79, 99] have shown that for slugs comprising spherical grains, the transmitted momentum normalised by the initial slug momentum  $I_0$ , is independent of the slug velocity  $v_0$ . Here, we confirmed via spot calculations that this result extrapolates to non-spherical rigid grains that do not fracture. Thus, all numerical simulations presented in this section were conducted with  $v_0 = 100 \text{ m s}^{-1}$  and the calculated transmitted momentum is presented in normalised form, i.e. the momentum transmitted into the structure is normalised by the initial momentum  $I_0$  of the slug.

### 5.3.1 Normal impact on targets

Snapshots showing the flow of the granular slug impacting the normally oriented rigid stationary target are shown in Fig. 5.5 for selected values of the dimensionless time

$\bar{t} \equiv tv_0/L$ , where time  $t = 0$  is defined as the instant the slug begins impact with the target. The grains are coloured by the magnitude of the grain velocity  $v$  normalised by  $v_0$ . First, consider the reference case of spherical grains ( $\Phi = 1$ ) with a friction coefficient  $\mu_T = 1.0$  between the grains and target surface (Fig. 5.5a). The flow is reminiscent of a water jet impinging normally on a rigid stationary surface with the grains flowing along the target surface in the  $y$ -direction. The zone over which the grains change their direction of motion from the negative  $z$ -direction to the  $y$ -direction is negligibly small with no stagnation zone visible in Fig. 5.5a. Next, consider the case of impact by a slug with rod-shaped grains with an aspect ratio  $\Phi = 3$ . The predictions of the flow patterns with  $\mu_T = 1.0$  and no friction ( $\mu_T = 0$ ) between the grains and target surface are included in Figs. 5.5b and 5.5c, respectively. The velocity with which the grains spread along the  $y$ -direction is lower for the case with  $\mu_T = 1.0$ . This is seen in not only the magnitudes of the velocities of the grains (compare Fig. 5.5b with Figs. 5.5a and 5.5c) but also evident in the lower level of spreading seen at  $\bar{t} = 0.8$  in Fig. 5.5b compared to both Figs. 5.5a and 5.5c. This can be understood by recalling that rotation of the rod-shaped grains requires work to be done against the hydrodynamic pressure exerted by the incoming high velocity grains. This impedes the rotation rate of these grains and the grains instead increasingly slide rather than roll along the target surface in the  $y$ -direction. A high friction between the target and the grains then resists this sliding motion and results in the reduction in the velocity with which the grains spread along the target. In contrast, the hydrodynamic pressure exerted by the incoming grains is less effective in impeding the rotation of spherical grains, and thus friction has only a small influence on the flow of these grains along the target surface.

We now proceed to quantify the transmitted momentum. The symmetry of the normal impact implies that  $I_T^y \approx I_T^x \approx 0$  (the approximate signs are used to emphasize that the stochastic nature of the granular slug means that the impact is not perfectly symmetrical in the numerical calculations), and thus the total transmitted momentum  $I_T \approx I_T^z$ . Calculations of the normalised transmitted momentum  $I_T/I_0$  are shown in Fig. 5.6a as a function of grain aspect ratio  $\Phi$  for selected values of  $\mu_T$ . Consistent with conservation of momentum and negligible rebound of the grains (Fig. 5.5),  $I_T/I_0 \approx 1$  in all cases, i.e. the changes in the flow patterns with grain shape seen in Fig. 5.5 do not affect the transmitted momentum for normal impacts. However, as seen in Fig. 5.5, friction between the target surface and grains, and the shape of the grains affects the flow pattern. We thus anticipate these parameters to influence the forces transmitted into the target in the  $y$ -direction. To investigate this, we define a measure  $J_T^y$  of the momentum transmitted into the target in the  $y$ -direction as follows. We divide the target into two halves about the axis of symmetry as shown in the inset of Fig. 5.6b and calculate the total force exerted by the grains on each half of the target in the  $y$ -direction. These forces are labelled  $f_b^y$  and  $f_u^y$  where the subscripts ‘‘b’’ and ‘‘u’’ denote the bottom and upper halves of the target, respectively. Then  $J_T^y$  is calculated as

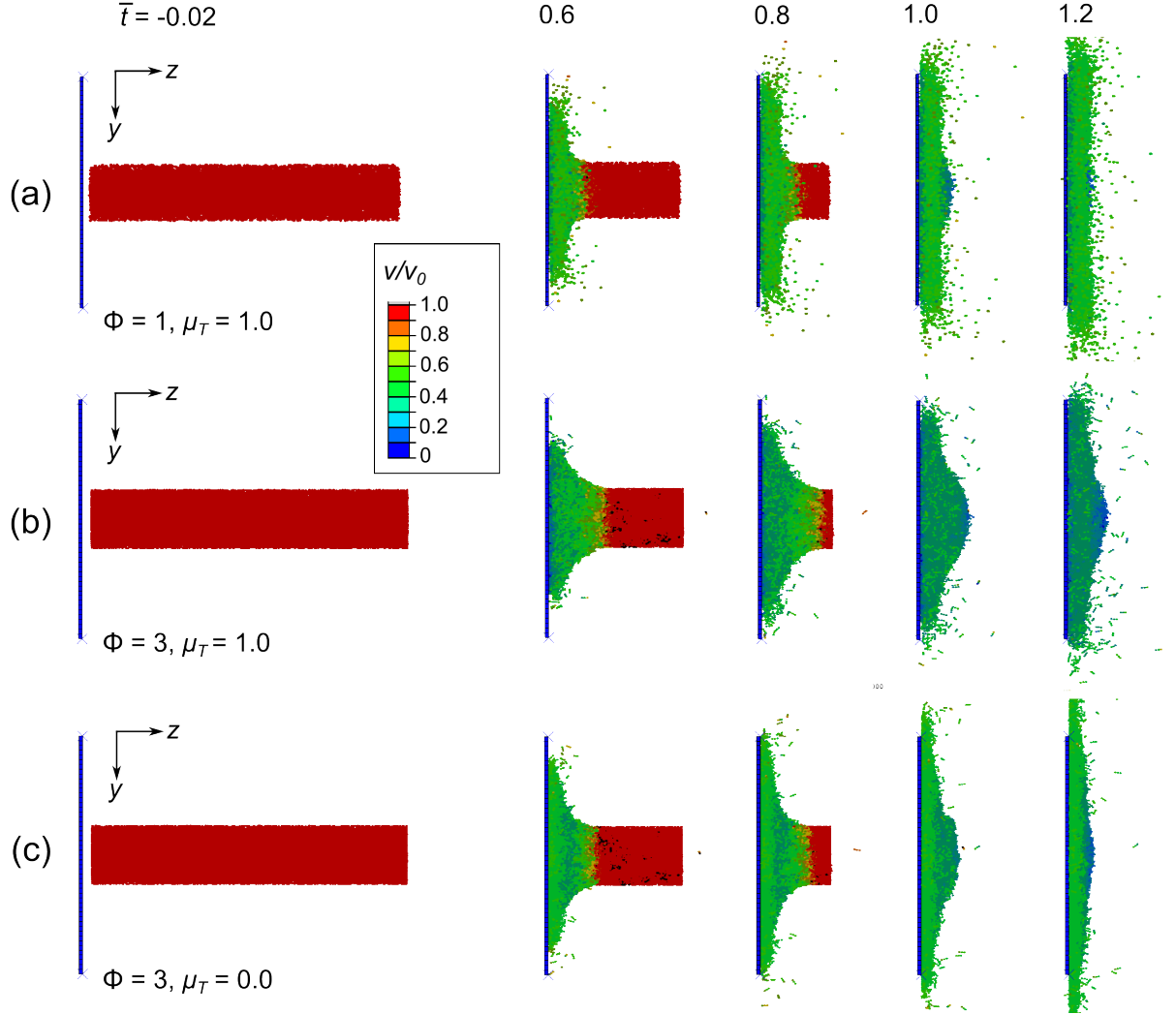


Fig. 5.5 Predictions of the flow of granular slugs impacting normally oriented targets. Results are shown at four selected values of the normalised time  $\bar{t}$  where  $\bar{t} = 0$  is the instant the slug begins impact with the target. (a) Spherical grains with  $\mu_T = 1.0$ , (b)  $\Phi = 3$  rod-shaped grains with  $\mu_T = 1.0$  and (c)  $\Phi = 3$  rod-shaped grains with  $\mu_T = 0$ . In all the cases, the grains are coloured by the magnitudes of their velocity  $v$  normalised by the initial slug velocity  $v_0$ .

$$J_T^y \equiv \lim_{t \rightarrow \infty} \int_0^t (|f_b^y(t')| + |f_u^y(t')|) dt' \quad (5.7)$$

This definition of  $J_T^y$  negates the symmetry of the problem by neglecting the sign of the momentum transferred into the bottom and upper halves of the target and thus unlike  $I_T^y$  does not vanish. Predictions of  $J_T^y/I_0$  are included in Fig. 5.6b for the cases analysed in Fig. 5.6a. When  $\mu_T = 0$ , no momentum can be transferred by the grains into the target in the  $y$ -direction, resulting in  $J_T^y = 0$  for all aspect ratios  $\Phi$ . However,  $J_T^y$  increases with increasing  $\mu_T$  and with grain aspect ratio  $\Phi$ . This increase is mainly over the range  $1 \leq \Phi \leq 2$  with increasing the aspect ratio beyond  $\Phi = 2$  resulting in no further increases in  $J_T^y$ . We rationalise this by noting that the momentum transferred from the grains to

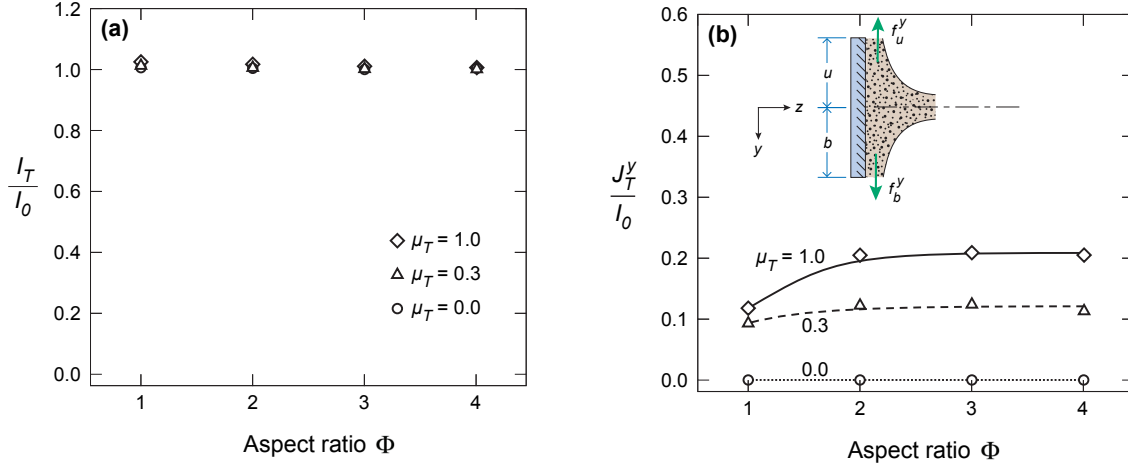


Fig. 5.6 Predictions of the (a) normalised total transmitted momentum  $I_T/I_0$  and (b) the measure  $J_T^y/I_0$  of the normalised momentum transmitted as a function of the aspect ratio  $\Phi$  of the grains. These results are shown for three selected values of  $\mu_T$  for the case of the normally oriented target. The inset in (b) shows the target divided into the upper and bottom halves for the purposes of the calculation of  $J_T^y/I_0$

the target in the  $y$ -direction is a maximum when the grains undergo pure sliding along the target surface while this transfer of momentum vanishes if the grains undergo pure rolling. The results in Fig. 5.6b suggest that while the spherical grains move along the target surface by a combination of rolling and sliding, rolling of the grains is eliminated for  $\Phi \geq 2$ . Thus, increases in  $\Phi$  beyond  $\Phi = 2$  has no influence on  $J_T^y$ .

### 5.3.2 Impact with inclined targets

Before proceeding to present numerical results for granular slugs impacting inclined targets, it is instructive to discuss some of the basic physics of momentum transfer from granular slugs into inclined targets. Let  $f_n$  and  $f_s$  denote the resultant normal and tangential forces exerted by the grains on the target (Fig. 5.1b). Momentum balance then gives

$$i_T^z(t) = \int_0^t (f_n \sin \alpha + f_s \cos \alpha) dt \quad (5.8)$$

and

$$i_T^y(t) = \int_0^t (f_n \cos \alpha - f_s \sin \alpha) dt \quad (5.9)$$

with  $I_T^z \equiv i_T^z(t \rightarrow \infty)$  and  $I_T^y \equiv i_T^y(t \rightarrow \infty)$ . It is evident that the tangential force (resulting from the friction between the grains and the target) has opposite effects on  $i_T^z$  and  $i_T^y$  and for  $\alpha = 45^\circ$  we anticipate that  $i_T^z > i_T^y$ . The consequences of Eqs. 5.8 and 5.9 in the limiting case when  $t \rightarrow \infty$  are also worth further elaboration as it enables better interpretation of numerical predictions reported subsequently. For the case when there are

frictional interactions between the grains and the target surface (i.e.  $\mu_T > 0$ ), we cannot directly relate  $I_T^z$  and  $I_T^y$  to  $I_0$  without detailed information on  $f_s$ . However, in the absence of friction ( $\mu_T = 0$ ),  $f_s = 0$  and explicit relations for the transmitted momentum follow as

$$I_T^z = I_0 \sin^2 \alpha \quad \text{and} \quad I_T^y = I_0 \sin \alpha \cos \alpha \quad (5.10)$$

For the  $\alpha = 45^\circ$  case, these reduce to  $I_T^z/I_0 = I_T^y/I_0 = 0.5$  with  $I_T/I_0 = \sqrt{2}$ . These values will subsequently be used as a reference to aid the quantification of the effect of friction.

Simulations of the flow of granular slugs with spherical or rod-shaped grains ( $\Phi = 3$ ) are shown in Figs. 5.7a and 5.7b, respectively for the case  $\mu_T = 1.0$ . The grains are coloured by the magnitude of the grain velocity  $v$  normalised by  $v_0$ . The grains flow along the inclined surface in both directions although the primary flow is in the positive  $y$ -direction. While differences between the flow patterns in Figs. 5.7a and 5.7b are not immediately evident, a careful comparison of the flow patterns in Figs. 5.7a and 5.7b at  $\bar{t} = 0.9$  indicates that the granular flow is slower for the rod-shaped grains. This is again associated with inhibition of rod-shaped grain rolling which results in higher levels of sliding friction between the grains and the target surface.

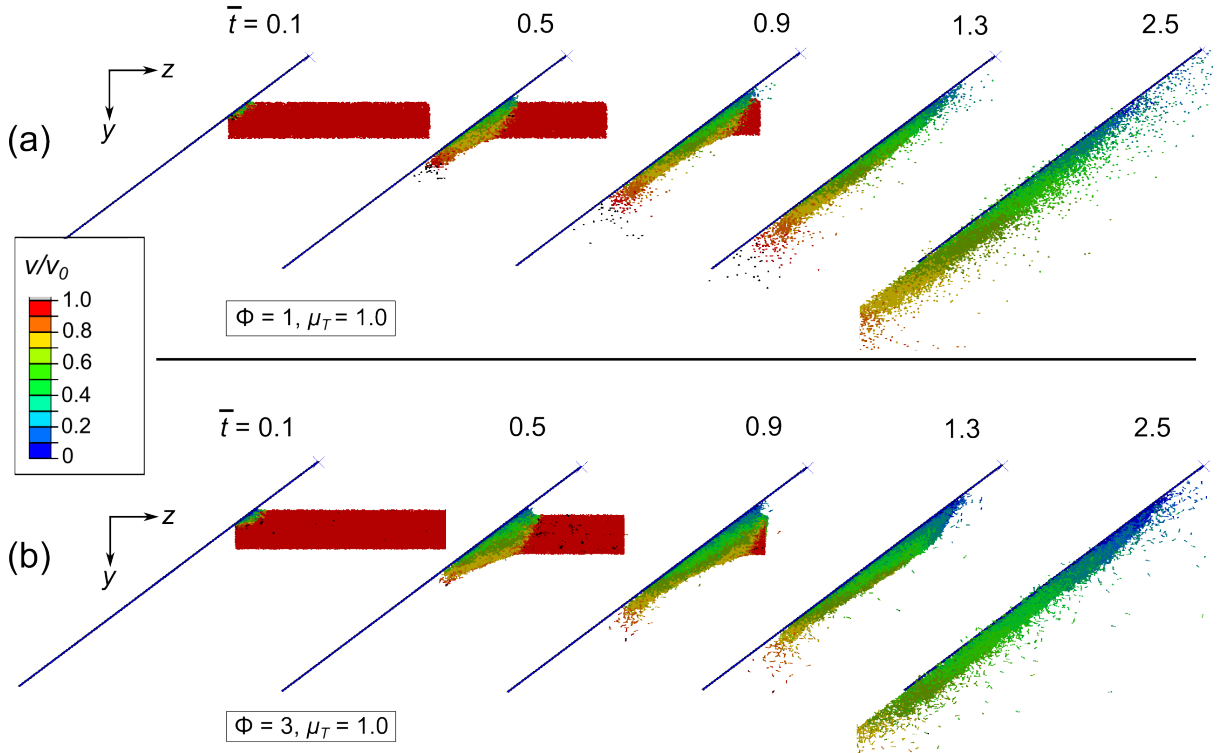


Fig. 5.7 Predictions of the flow of the granular slug impacting the inclined ( $\alpha = 45^\circ$ ) target at selected values of the normalised time  $\bar{t}$  where  $\bar{t} = 0$  is the instant the slug begins impact with the target. Results are shown for slugs comprising (a) spherical grains and (b)  $\Phi = 3$  rod-shaped grains with  $\mu_T = 1.0$  in both cases. In all cases, the grains are coloured by the magnitudes of their velocity  $v$  normalised by the initial slug velocity  $v_0$ .

Unlike for normal impact, the transmitted momentum is also strongly dependent on grain shape for inclined impacts. Predictions of the normalised transmitted momenta  $I_T/I_0$ ,  $I_T^z/I_0$  and  $I_T^y/I_0$  are shown in Fig. 5.8a as a function of  $\Phi$  for the case with  $\mu_T = 1.0$ . As anticipated from Eqs. 5.8 and 5.9,  $I_T^z/I_0 > I_T^y/I_0$  for all  $\Phi$ . Moreover,  $I_T^z/I_0$  increases but  $I_T^y/I_0$  decreases with increasing  $\Phi$ . This can be rationalised as follows. With increasing  $\Phi$ , the grains increasingly slide rather than roll along the target surface thereby increasing frictional interactions with the target. Since, the primary flow of the grains is in the positive  $y$ -direction, increasing frictional interactions reduces  $I_T^y/I_0$  while increasing  $I_T^z/I_0$ . The outcome of these changes in  $I_T^y/I_0$  and  $I_T^z/I_0$  is that the total transmitted momentum  $I_T/I_0$  increases with  $\Phi$  (albeit to a small extent). Recall that in the absence of frictional interactions between the grains and the target surface,  $I_T/I_0 = 1/\sqrt{2} = 0.71$ . Here, we predict for  $\mu_T = 1.0$  that the total transmitted momentum increases from  $I_T/I_0 = 0.76$  for spherical grains to 0.80 for rod-shaped grains with  $\Phi = 4$ . Thus, frictional interactions increase the transmitted momentum into inclined targets for both spherical and rod-shaped grains. These frictional interactions can be parameterised by  $(I_T^z - I_T^y)$ , which from Eq. 5.10, vanishes in the absence of friction between the grains and a target surface inclined at  $\alpha = 45^\circ$ . Predictions of  $(I_T^z - I_T^y)/I_0$  are presented in Fig. 5.8b as a function of  $\Phi$  and selected values of  $\mu_T$ . Clearly,  $(I_T^z - I_T^y)$  not only increases with  $\mu_T$  but also with  $\Phi$  (for non-zero values of  $\mu_T$ ) due to the increasing levels of frictional interaction. However, consistent with the predictions for the normal impact case, the dependence on  $\Phi$  is minimal for  $\Phi > 2$ : these high aspect ratio grains undergo pure sliding along the target surface and thus further increases in  $\Phi$  have a negligible influence on the frictional interactions between the grains and the target surface.

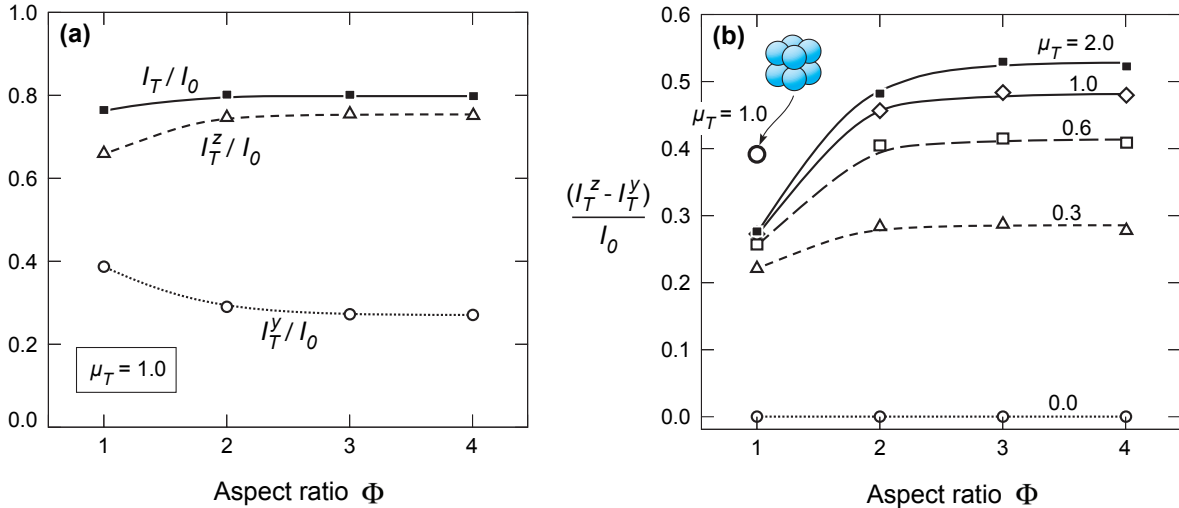


Fig. 5.8 Predictions of the normalised transmitted momenta (a)  $I_T/I_0$ ,  $I_T^z/I_0$  and  $I_T^y/I_0$  and (b)  $(I_T^z - I_T^y)/I_0$  for slugs impacting the inclined ( $\alpha = 45^\circ$ ) target as a function of the grain aspect ratio  $\Phi$ . In (a) results are shown for  $\mu_T = 1.0$  while in (b) we include predictions for selected values of  $\mu_T$ . The prediction of  $(I_T^z - I_T^y)/I_0$  for a slug with cubic grains comprising 8 sub-particles and  $\mu_T = 1.0$  is also included in (b).

All calculations reported up to this point were restricted to spherical and rod-shaped grains whose shape is parameterised by the aspect ratio  $\Phi$ . However, it is worth emphasising that the frictional interactions resulting from the competition between the rolling and sliding of the grains along the target surface depends on the precise shape of the grains with  $\Phi$  insufficient to fully characterise these interactions. To illustrate this, we consider a slug comprising cubic grains constructed with 8 spherical sub-particles (i.e. cubic grains with  $n = 8$ ). The aspect ratio of this grain is defined to be  $\Phi = 1^1$ , i.e. equal to that of a spherical grain. The prediction of  $(I_T^z - I_T^y)/I_0$  for a slug comprising cubic grains with  $\mu_T = 1.0$  included in Fig. 5.8b shows that  $(I_T^z - I_T^y)/I_0$  is 42% above that of the case with spherical grains. This is because the rolling resistance of cubic grains is significantly higher than that of spherical grains resulting in cubic grains having a higher tendency to slide along the target surface. The sliding of the grains increases the frictional interactions between the grains and the target and consequently increases  $(I_T^z - I_T^y)$ . This clearly illustrates that transmitted momenta depend on the precise shape of the grains with a simple parameter like aspect ratio insufficient to characterise the grains for the purposes of determining the transmitted momentum.

## 5.4 Effect of particle fragmentation

The calculations reported so far assume that the grains are rigid and do not fracture upon impact. However, it is well established that high velocity granular impact results in fragmentation of the grains [94, 101, 110, 115] although the effect, if any, on the momentum transfer is not understood. We proceed to investigate the effect of grain fragmentation on the momentum transfer for slugs impacting the  $\alpha = 45^\circ$  inclined targets with a target surface/grain friction coefficient  $\mu_T = 1.0$ . We shall show that effect of grain fragmentation on the momentum transfer emanates from a change in the shape of the grains. Since grain shape does not affect  $I_T/I_0$  for normal impact (Section 5.3.1), attention here is restricted to the inclined impact case.

### 5.4.1 Numerical scheme for particle fragmentation

The breaking/fragmentation of the grains was implemented by connecting the sub-particles to each other via beam elements rather than rigid connections as described in Section 5.2.1. These beams were not designed to model a specific physical fracture process but rather serve as a numerical tool to permit the splitting of grains during the impact event. Thus, the properties of the beams were chosen to permit a parametric study rather than related to fracture properties of a particular granular medium (e.g. silica sand).

---

<sup>1</sup>In general, the aspect ratio of a grain is defined as the ratio of the lengths of the semi-major and smallest semi-minor axes of the best-fit ellipsoid to the grain.

The nearest-neighbour centres of the sub-particles were connected to each other via a single<sup>2</sup> Timoshenko beam element (B31 in the Abaqus notation) with a circular cross-section of diameter  $d_b$ . Built-in connections were specified at the ends of the beam at the sub-particle centres. The beams were assumed to be made from an elastic perfectly plastic material with Young's modulus  $E_b$ , Poisson ratio  $\nu_b$ , yield strength  $Y_b$  and plastic failure strain  $\varepsilon_f$  while the density of the beams was chosen such that the mass of all the beams in a grain was less than 1% of the total grain mass. The Poisson's ratio was set to  $\nu_b = 0.17$  and yield strain  $\varepsilon_y \equiv Y_b/E_b = 0.1\%$  in all the calculations reported here. Since the beams connect the sub-particle centres, the beam length was fixed at  $d_p$  and thus the beams are fully specified through the beam aspect ratio  $d_p/d_b$ ,  $E_b$  and  $\varepsilon_f$ . We report parametric calculations for the effect of  $\varepsilon_f$  with  $d_p/d_b$  and  $E_b$  selected such that in the absence of plasticity and failure, we recover the limiting case of rigid grains. Calibration calculations discussed in the Appendix show that the choice  $d_p/d_b = 1$  and  $\bar{K}_b = 10$  is adequate to recover this rigid limit where

$$\bar{K}_b \equiv \frac{\pi E_b d_b}{4K_n} \left( \frac{d_b}{d_p} \right) \quad (5.11)$$

is the ratio of the axial stiffness of the beam to the normal contact stiffness between the sub-particles. All calculations reported in this section use these properties for the beam connectors between the sub-particles. Moreover, since the level of fragmentation depends on the slug impact velocity  $v_0$ , we shall show that unlike in the case of rigid grains, the transmitted momentum now depends on  $v_0$ . Thus, here we present predictions for a range of normalised impact velocities  $\bar{v}_0 \equiv v_0/\sqrt{Y_b/\rho_p}$ , where  $\rho_p$  is the density of the sub-particle material.

## 5.4.2 Summary of numerical results

It was shown in Section 5.3.2 that increasing the grain aspect ratio increases momentum transfer from a slug into inclined targets due to an increase in the sliding of the grains on the target surface. We therefore anticipate that the primary effect of grain fragmentation is related to the change in the grain shape and with this in mind we consider the following two cases: high aspect ratio grains fragmenting to low aspect ratio grains and vice versa.

### Fragmentation from high to low aspect ratio grains

To investigate the effect of high aspect ratio grains fragmenting to lower aspect ratio grains we restrict attention to the  $\Phi = 3$  rod-shaped grains with all the rigid connections between the sub-particles replaced by the beams described above. Predictions of the total

---

<sup>2</sup>By using a single beam element, we do not capture stress concentrations that develop between the sub-particles. Thus, the calculations can only be used to qualitatively understand the influence of grain fracture with the fracture properties of the beams not related to realistic material parameters.

transmitted momentum  $I_T/I_0$  are included in Fig. 5.9a as a function of the failure strain  $\varepsilon_f$  of the beam connectors. Results are included for three choices of the normalised slug impact velocity  $\bar{v}_0$ . The  $I_T/I_0$  versus  $\varepsilon_f$  relation is reasonably independent of  $\varepsilon_f$  for  $\varepsilon_f < 10\%$  and about 10% lower than that for the rigid grains (this limit is indicated in Fig. 5.9a). At higher failure strains,  $I_T/I_0$  for the two lower impact velocities rises and attains the value for the rigid grains. However, for the highest impact velocity of  $\bar{v}_0 = 0.226$ ,  $I_T/I_0$  rises only by about 1.5% over the entire range of  $\varepsilon_f$  investigated here.

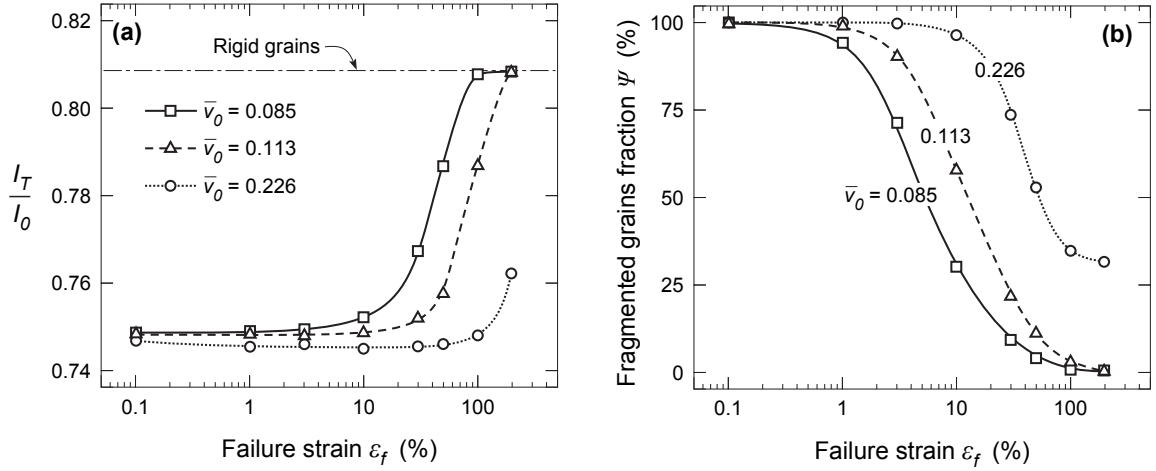


Fig. 5.9 Predictions of (a) the normalised transmitted momentum  $I_T/I_0$  and (b) fraction  $\Psi$  of the fragmented grains as a function of the failure strain  $\varepsilon_f$  for a slug comprising  $\Phi = 3$  rod-shaped grains impacting inclined ( $\alpha = 45^\circ$ ) targets. The predictions are shown for  $\mu_T = 1.0$  and three selected values of the normalised impact velocity  $\bar{v}_0$ .

To understand these dependencies, we include in Fig. 5.9b the corresponding predictions of the fraction  $\Psi$  of fragmented grains after the impact event. Here, we define a grain to be fragmented if at least one of the beam connections present in the original  $\Phi = 3$  rod-shaped grain had failed. The  $\Psi$  versus  $\varepsilon_f$  relation has a sigmoidal shape such that  $\Psi \approx 100\%$  at low  $\varepsilon_f$ , i.e. at low failure strains all the grains in the impacting slug had fractured. This results in the grains converting from  $\Phi = 3$  rod-shaped grains to more spherical grains which have a higher tendency to roll rather than slide along the target surface. As seen in Section 5.3.2, the momentum transfer is lower for more spherical grains and thus an increase in grain fracture reduces momentum transfer from slugs with high aspect ratio grains. With increasing  $\varepsilon_f$  the fraction of grains that fracture decreases with nearly no grain fracturing for the lower two impact velocities when  $\varepsilon_f$  exceeds 100%. Thus, the transmitted momentum increases to attain the value for the rigid  $\Phi = 3$  grains. However, about 30% of the grains continue to fracture even with  $\varepsilon_f = 200\%$  for an impact velocity of  $\bar{v}_0 = 0.226$  and thus the rise in the transmitted momentum with increasing  $\varepsilon_f$  is relatively minor for this high impact velocity case.

### Fragmentation from low to high aspect ratio grains

We now consider the reverse case of low aspect ratio grain fragmentation that results in the grains acquiring a higher aspect ratio after fracture. To achieve this, we consider the case of a slug comprising initially cubic grains with  $n = 8$  sub-particles. These grains have an initial aspect ratio of unity and comprise 12 connectors between sub-particles as shown in Fig. 5.10a. Four of these connectors are modelled as beams such that fracture results in the cubic grain breaking into two flake-like grains (Fig. 5.10b) comprising four sub-particles. The aspect ratio of these flake-shaped grains, as deduced from the best-fit ellipsoid, is 2.41, i.e. the cubic grain with aspect ratio of unity fractures into flake-like grains with a significantly higher aspect ratio.

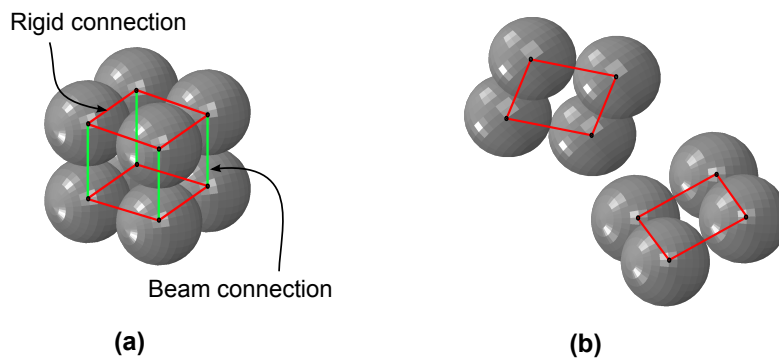


Fig. 5.10 Sketches of the cubic grain comprising 8 sub-particles used to investigate the effect of grain fracture. (a) The cubic grain with 12 connections between sub-particles. The 4 beam connectors are indicated in green while the remainder of the connectors are rigid and marked in red. (b) The flake-like grains resulting from the fracture of the 4 beam connectors.

Predictions of  $I_T/I_0$  and  $\Psi$  versus  $\varepsilon_f$  are shown in Figs. 5.11a and 5.11b, respectively for three normalised impact velocities  $\bar{v}_0$ . A grain is defined to be fragmented if all the four beam connectors have failed such that the cubic grain has split into the two flake-like grains. In this case grain fragmentation results in the conversion of low aspect ratio grains to high aspect ratio grains and thus sliding of the grains along the target surface becomes more prevalent with increasing levels of fragmentation. As a consequence,  $I_T/I_0$  decreases with decreasing levels of fragmentation (or equivalently increasing  $\varepsilon_f$ ). This decrease is relatively minor (Fig. 5.11a) even though the fraction of fractured grains decreases significantly with increasing  $\varepsilon_f$  (Fig. 5.11b). We attribute this to the fact that although the cubic grains have a low aspect ratio, they have a tendency to slide rather than roll and thus transmit a momentum into the inclined target that is comparable to the high aspect ratio rod-shaped grains; see Fig. 5.8b. Therefore, an increase in aspect ratio of cubic grains due to grain fracture has a relatively minor effect. We speculate that the fracture of initially spherical grains will result in a more significant increase in the transmitted momentum. However, such an analysis is computationally beyond the scope of the current method that uses spherical sub-particles to construct the grains.

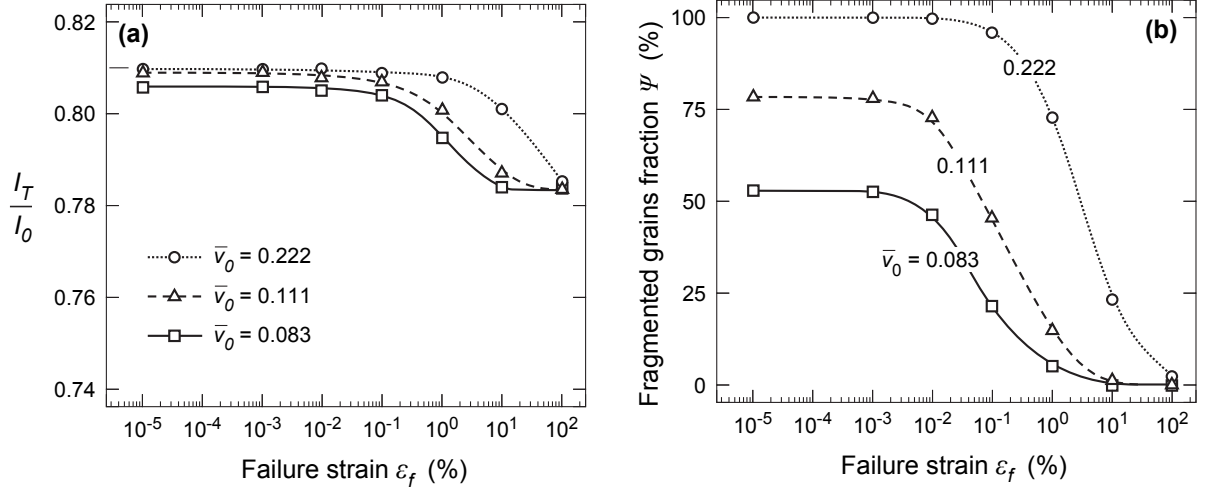


Fig. 5.11 Predictions of (a) the normalised transmitted momentum  $I_T/I_0$  and (b) fraction  $\Psi$  of the fragmented grains as a function of the failure strain  $\epsilon_f$  for slugs comprising cubic ( $n = 8$ ) grains impacting inclined ( $\alpha = 45^\circ$ ) targets. The predictions are shown for  $\mu_T = 1.0$  and three selected values of the normalised impact velocity  $\bar{v}_0$ .

We emphasize that while grain fragmentation can result in relatively small changes to the total transmitted momentum, the individual components of the transmitted momentum are more significantly affected. To illustrate this, we include in Figs. 5.12a and 5.12b predictions of  $(I_T^z - I_T^y)/I_0$  for the cases of fragmentation of high aspect ratio grains to low aspect ratio and vice-versa, respectively, i.e. the cases in Figs. 5.9 and 5.11. As expected, with increasing grain fragmentation (or equivalently decreasing  $\epsilon_f$ ),  $(I_T^z - I_T^y)/I_0$  decreases for the case when grains fragment to lower aspect ratios (Fig. 5.12a) and vice-versa in Fig. 5.12b. More importantly, grain fragmentation affects  $(I_T^z - I_T^y)/I_0$  more substantially as compared to its effect on  $I_T/I_0$ .

Here we have demonstrated that grain fragmentation can influence the momentum transmitted from high velocity granular slugs into targets they impact. While it is attractive to attribute this effect to energy dissipation by the work of fracture associated with grain fracture, there is no direct dependence of the transmitted momentum on energy dissipation. Rather, the grain fracture indirectly affects the transmitted momentum because it changes the shape of the grains which in turn influences the competition between sliding and rolling of the grains on the target surface. This competition affects the transmitted momentum due to frictional interactions between the grains and the target surface. Importantly, in the absence of friction between the grains and the target (i.e.  $\mu_T = 0$ ), grain fracture is predicted to have no influence on the transmitted momentum.

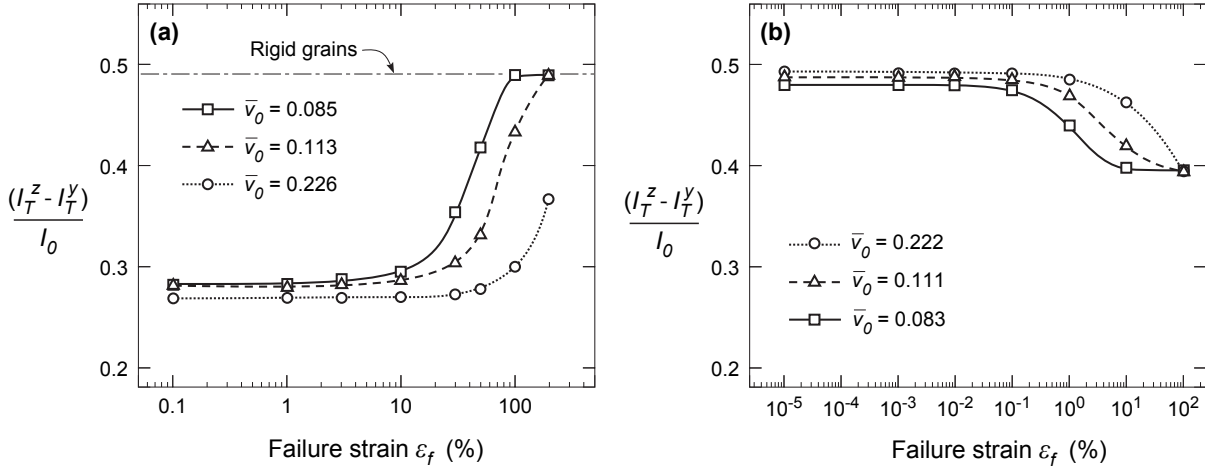


Fig. 5.12 Predictions of  $(I_T^z - I_T^y)/I_0$  as a function of the failure strain  $\varepsilon_f$  for slugs comprising (a)  $\Phi = 3$  rod-shaped and (b) cubic ( $n = 8$ ) grains impacting inclined ( $\alpha = 45^\circ$ ) targets. The predictions are shown for  $\mu_T = 1.0$  and three selected values of the normalised impact velocity  $\bar{v}_0$ .

## 5.5 Concluding remarks

We have reported discrete element calculations to investigate the effect of grain shape and grain fracture on the interaction of high velocity granular media with rigid stationary targets in normal and inclined orientations. The granular media comprised either spherical, rod-shaped or cubic grains constructed by combining spherical sub-particles. These sub-particles were connected to each other with either rigid connectors or beam connectors: the beam connectors can fracture so as to simulate fragmentation of the grains.

When grain fracture was suppressed by employing rigid connectors between the sub-particles, the momentum transmitted from the granular slug into normally oriented targets was independent of grain shape due to the symmetry of the problem. However, with increasing angularity of the grains (i.e. rod-shaped or cubic grains compared to spherical grains), the grains tended to slide rather than roll over the target surface. This increased frictional interactions between the grains and the target and resulted in an increase in the momentum transfer into inclined targets. Moreover, it was shown that a simple parameter such as aspect ratio is unable to fully characterise the interaction of the grains with the target surface as the precise grain shape governs the relative propensity of the grains to slide rather than roll on the target surface.

Fracture of grains during the impact event results in dissipation from the work of fracture. However, this work of fracture has no direct affect upon momentum transfer into the targets. Rather, it is the change in the shape of the grains as a result of fracture that directly influences the momentum transmitted into the inclined targets. The numerical calculations presented here show that fracture of rod-shaped grains results in a reduction in the transmitted momentum as the grains break-up into more spherical grains that have

a higher propensity to roll rather than slide on the target surface. This reduction increases with decreasing fracture strain of the grains and increasing impact velocity. The situation reverses when the initial shape of the grains was more spherical such that upon fracture the grains become more angular. Field experiments that involve the detonation of buried explosive charges show that soil type and impact velocity influence the fraction of the ejecta momentum that is transmitted into targets. The simulations presented here give some insight into reasons for the observed dependencies.

## Appendix: Properties of the beam connectors

The calculations with grain fracture were designed such that they recovered the limit of rigid grains in the absence of beam connector plasticity and failure. To justify the choice of  $d_p/d_b = 1$  and  $\bar{K}_b = 10$  used in Section 5.4, here we consider the case of the  $\Phi = 3$  rod-shaped grains impacting the inclined target at a velocity  $v_0/\sqrt{K_n/(d_p\rho_p)} = 0.13$  with  $\mu_T = 1.0$ . The beams were assumed to be made from an elastic material (i.e. no plasticity or failure) with  $\nu_b = 0.17$ . Predictions of  $(I_T^z - I_T^y)/I_0$  are shown in Fig. 5.13a as a function of  $d_p/d_b$  for three choices of  $\bar{K}_b$ . The measure of transmitted momentum,  $(I_T^z - I_T^y)/I_0$ , increases with increasing  $\bar{K}_b$  and decreasing  $d_p/d_b$ . The asymptote corresponding to rigid grains (marked in Fig. 5.13a) is attained for  $d_p/d_b = 1$  and  $\bar{K}_b = 10$ . The dependency of  $(I_T^z - I_T^y)/I_0$  on  $d_p/d_b$  and  $\bar{K}_b$  is understood by noting that these grains change shape during the impact event due to the bending of the beams that connect the sub-particles. To illustrate this, we consider the case of a slug with  $\Phi = 3$  grains constructed by  $d_p/d_b = 10$  and  $\bar{K}_b = 1$  beam connectors impacting at  $v_0/\sqrt{K_n/(d_p\rho_p)} = 0.13$ . We then isolate three grains from the slug and follow them through their deformation history as shown in Fig. 5.13b. At  $\bar{t} = 0.5$ , the beam connectors bend so significantly that the aspect ratio of the grains reduces. This of course promotes rolling of the grains and reduces  $(I_T^z - I_T^y)/I_0$ . Making the beams stubbier by decreasing  $d_p/d_b$  and increasing their Young's modulus increases the bending stiffness of the beams and makes the grains nearly rigid such that the asymptote corresponding to rigid grains is attained for  $d_p/d_b = 1$  and  $\bar{K}_b = 10$ .

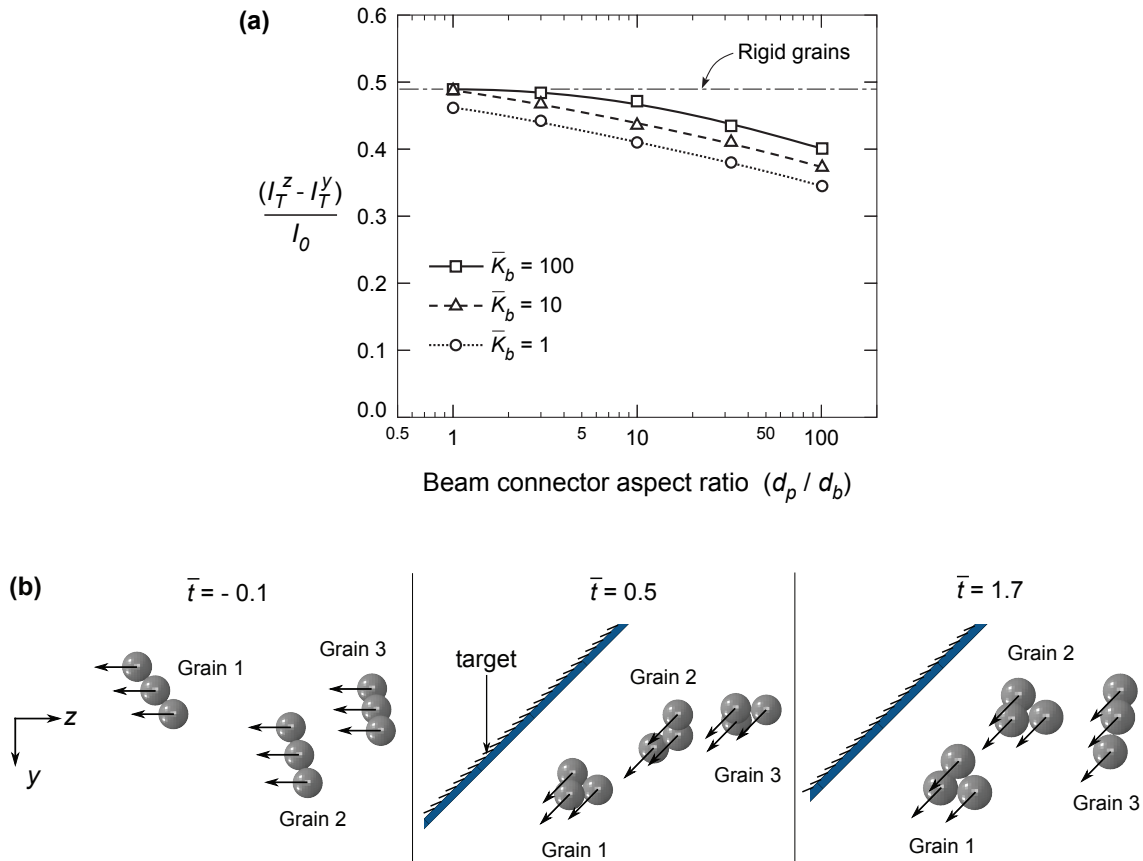


Fig. 5.13 Predictions for slugs comprising  $\Phi = 3$  rod-shaped grains impacting inclined ( $\alpha = 45^\circ$ ) targets at  $v_0/\sqrt{K_n/(d_p\rho_p)} = 0.13$  with  $\mu_T = 1.0$ . The grains were constructed with elastic beams connecting the sub-particles. (a) The normalised measure of transmitted momentum  $(I_T^z - I_T^y)/I_0$  as a function of the beam connector aspect ratio  $d_p/d_b$ . Results are shown for 3 choices of the normalised beam axial stiffness  $\bar{K}_b$  with the asymptote corresponding to rigid grains marked. (b) Snapshots showing the grain shape and velocity directions of three randomly selected grains at three normalised times  $\bar{t}$ . The beam connectors in this case had  $d_p/d_b = 10$  and  $\bar{K}_b = 1$ . The normalised time  $\bar{t} = 0$  corresponds to the instant the slug begins impact with the target.

# Chapter 6

## Effect of sliding coating on the targets impacted by sand slugs

### Abstract

A concept of sliding surface coatings applied on the flat targets impacted by high speed dry sand slugs is analysed as a means to reduce the loading on the target. Experiments and coupled discrete particle/finite element simulations were used in this study. Experiments were conducted using a coating of sand-paper placed on rigid targets with a thin layer of lubricant gel at its interface with the target surface. These targets were inclined at an angle of  $45^\circ$  relative to the incoming slug. The sand-paper coating slides on the target surface during the impact with the slug and we investigate the reduction in transmitted momentum compared to the case where the sand-paper coating is fixed on the target. Simulations were performed using slug made with rod-shaped particles that impact the coating placed on the target surface. The lubricant at the interface between coating and target surface was not explicitly modelled in simulations but the friction coefficient was calibrated. Experiments as well as simulations show that allowing the coating to slide on the target reduces the frictional loading on the inclined target, as compared to the case when the coating is not allowed to slide. This reduces the momentum transmitted to the target and it approaches the case of impact of slugs with non-coated frictionless target surface, which is the theoretical minimum possible transmitted momentum. Simulations were also performed with deformable target plates to analyse the deflection of the target in the presence of a surface coating, for the inclined as well as normally oriented targets. These calculations show that for an inclined target, both the momentum transmitted and target deflection depend on the thickness of target and coating. In contrast, presence of sliding coating for normally oriented deformable target has no effect on the transmitted momentum. The performance of such target is instead degraded because of higher deflection of the target plate when the coating is present.

## 6.1 Introduction

Impact of granular material against structures is of importance for many applications. The current study is motivated by the application of shallow-buried landmine explosions where the vehicle underbody is impacted by high velocity soil (granular media) ejected from ground during explosion. Previous experimental as well as numerical studies have shown that compared to surface laid explosives, shallow-buried explosives result in higher impulse transmission and larger deflections of the afflicted structure [27, 96, 98]. This increased severity of loading has been attributed to the impact of the granular media that is ejected by the expansion of detonation products in shallow-buried explosives [7, 33, 106, 88, 87] compared to explosions in air. The loading on the structure due to this high velocity soil depends on multiple factors and the ways to reduce the damage has been of considerable interest.

A number of strategies have been proposed in the literature to improve the impulsive load resistance of these underbody structures including (i) replacing the monolithic underbody by sandwich panels [30, 79, 108, 127], (ii) increasing the stand-off distance of the vehicle floor from the ground [30, 11, 56, 98], and (iii) inclining the underbody with respect to the ground by making use of a V-shaped hull design [2, 7, 37, 41, 109, 20, 39, 74]. In all these approaches, understanding the level of momentum transferred from the high-velocity soil ejecta onto the loaded structure (the target) has been of primary importance. The phenomena that contribute to the dynamic loading of the target following detonation of shallow-buried explosives are very complex and field testing using explosive charges makes it challenging to capture the details of granular spray generated. To overcome this, Park et al. [95] developed a technique to generate high velocity sand slug within a laboratory setting and without the need for the detonation of explosive. This setup was further used by Uth and Deshpande [125], Uth et al. [126], Goel et al. [44] for the investigation of effect of target stand-off, inclination and surface properties on deformation and impulse transmitted to the targets.

Many numerical approaches have been proposed to model the complex dynamic interaction of granular sprays with structures. For example, Rimoli et al. [108] used the soil constitutive model of Deshpande et al. [27] to deduce the impulse applied to structures by explosively driven spherical sand shells, and then simulated the ensuing deformation of aluminium monolithic and sandwich plates using a finite element method. Grujicic et al. [48, 52, 51] and Wang et al. [130] used coupled Eulerian/Lagrangian simulations of landmine explosions, and attempted to compare their predictions with blast impulse and plate deformation measurements from Bergeron and Tremblay [7] and Foedinger [36]. More recently, coupled discrete particle/continuum simulations have been increasingly used to investigate the response of structures impacted by high velocity granular media. For example, Borvik et al. [11] followed by Dharmasena et al. [30] and Holloman et al.

[58, 57] used this approach to simulate the response of a variety of monolithic and sandwich structures loaded by high velocity sand sprays generated by the explosive detonations.

If the ejecta launched by a buried explosion is brought to rest by a flat rigid target whose surface is perpendicular to the direction of granular impact, the full normal component of its momentum is transferred to the plate [27, 95]. The transmitted momentum reduces if the target is inclined relative to the incident ejecta [2, 41]. Uth et al. [126] reported detailed laboratory scale measurements indicating that while the resultant momentum transmitted into the inclined targets was indeed less than that for the normally oriented counterparts, it was significantly higher than that anticipated from a water jet like impact analysis [18, 64] which neglects friction between the granular particles and the target. Recent study performed by Goel et al. [44] using rigid targets show that the frictional interactions between particles and target surface significantly influences the transmitted momentum, with high friction resulting in high momentum transfer. For an inclination of  $45^\circ$ , frictionless limit for the resultant transmitted momentum is 0.707. Goel et al. [44] observed that even a smooth surface (alumina) had a higher resultant transmitted momentum (by 9 %). The rough surface had much higher (by 21 %) transmitted momentum compared to frictionless limit. This is a result of higher propensity of particles to slide rather than roll on the target surface in case of friction. For perpendicularly oriented target, the frictional properties of the surface was shown to cancel out due to symmetry of the impact.

Hence, a potential approach to significantly reduce the damage to the target is to minimise the frictional interactions between the target and the granular media, in addition to inclining the target against incident slug. However, even an initially smooth surface can undergo indentation and roughening during granular impact. This can result in frictional loading on the surface, thereby increasing the transmitted momentum. To counteract this dynamic roughening of target surface, Kyner et al. [73] used a test facility similar to that utilised by Holloman et al. [58, 57] and implemented additional flat plates on top of rigid target such that the granular ejecta impacted this plate first, rather than the target surface. The interface between this flat plate and target surface was lubricated such that the plate slid off during impact due to frictional loading from granular media and acted as a sacrificial part of the system. Due to low friction between the plate and target, the frictional loading on the target was reduced as compared to the impact of granular media directly on the target. Hence, using sliding plates led to substantial reduction in transmitted impulse. In addition, simulations were performed using spherical particles and particle rotation ignored, concluding that frictional interaction as well as angle of inclination affects the momentum transmitted. The discrete particle approaches typically use spheres to represent the granular particles though some differences exist in individual implementations. For example, Liu et al. [79] and Dharmasena et al. [30] allow for three rotational and three translational degrees of freedom for the particles while the approaches of Borvik et al. [11] and Holloman et al. [58, 57] restrict rotational motion of the spheres

even though tangential frictional forces that result in torques on the particles are included in the analyses. Studies by Cho et al. [19] and Farhadi and Behringer [34] showed that the flow of granular media is strongly influenced by the shape of granular particles and restriction to spherical particles does not capture the effect of angularity in soil grains. Goel et al. [44] demonstrated that simulations using spherical particles were unable to capture the frictional effects with fidelity. Goel et al. [45] investigated the effect of particle shape and particle fragmentation on the momentum transmitted to the target. They showed that modelling the angular particle shapes is critical to accurately predict the interactions. With increasing grain aspect ratio, the grains tend to slide rather than roll on the target surface and this increases frictional interactions with the target surface.

The study presented here uses the sliding plate concept demonstrated by Kyner et al. [73]. Experiments are performed with rigid targets utilising the laboratory setup developed by Park et al. [95]. The target surface had a rough coating, which was allowed to slide during the slug impact. The observations are compared with the case of fixed coating experiments done by Goel et al. [44]. To gain further insight into the physics of this problem, coupled discrete particle/finite element simulations are performed with the slug comprising rod-shaped particles as demonstrated by Goel et al. [45]. Using numerical simulations, the concept of sliding coating is extended to deformable targets in inclined and normal orientations and we show the effect of coating mass on deformation of the target and the transmitted momentum.

## 6.2 Experimental protocol

Cylindrical slugs comprising silica sand particles were impacted against rigid stationary targets to measure the transmitted momentum. Fig. 6.1a depicts the experimental setup, which comprises four components (from right to left); (i) a gas gun to fire a solid projectile, which then accelerates the piston of (ii) a slug launcher apparatus based upon the one developed by Park et al. [95]; (iii) a sand slug that initially rests inside the cylindrical cavity of the launcher; and (iv) the target, mounted on force sensors to measure the transmitted momentum. We proceed to briefly describe the four main components of the experimental set-up sketched in Fig. 6.1a.

### 6.2.1 Slug launcher

The launcher was developed by Park et al. [95] and later modified by Uth and Deshpande [125] and Uth et al. [126]. A cross-sectional view of the slug launcher is sketched in Fig. 6.1b and unless otherwise mentioned, all the components were made with low carbon steel. It comprised a cylindrical cavity for the sand slug and a piston to push the slug out of the cavity when a projectile, fired from a gas gun, impacted the piston head. The launcher was bolted to a rigid support frame so that it remained stationary during the impact event.

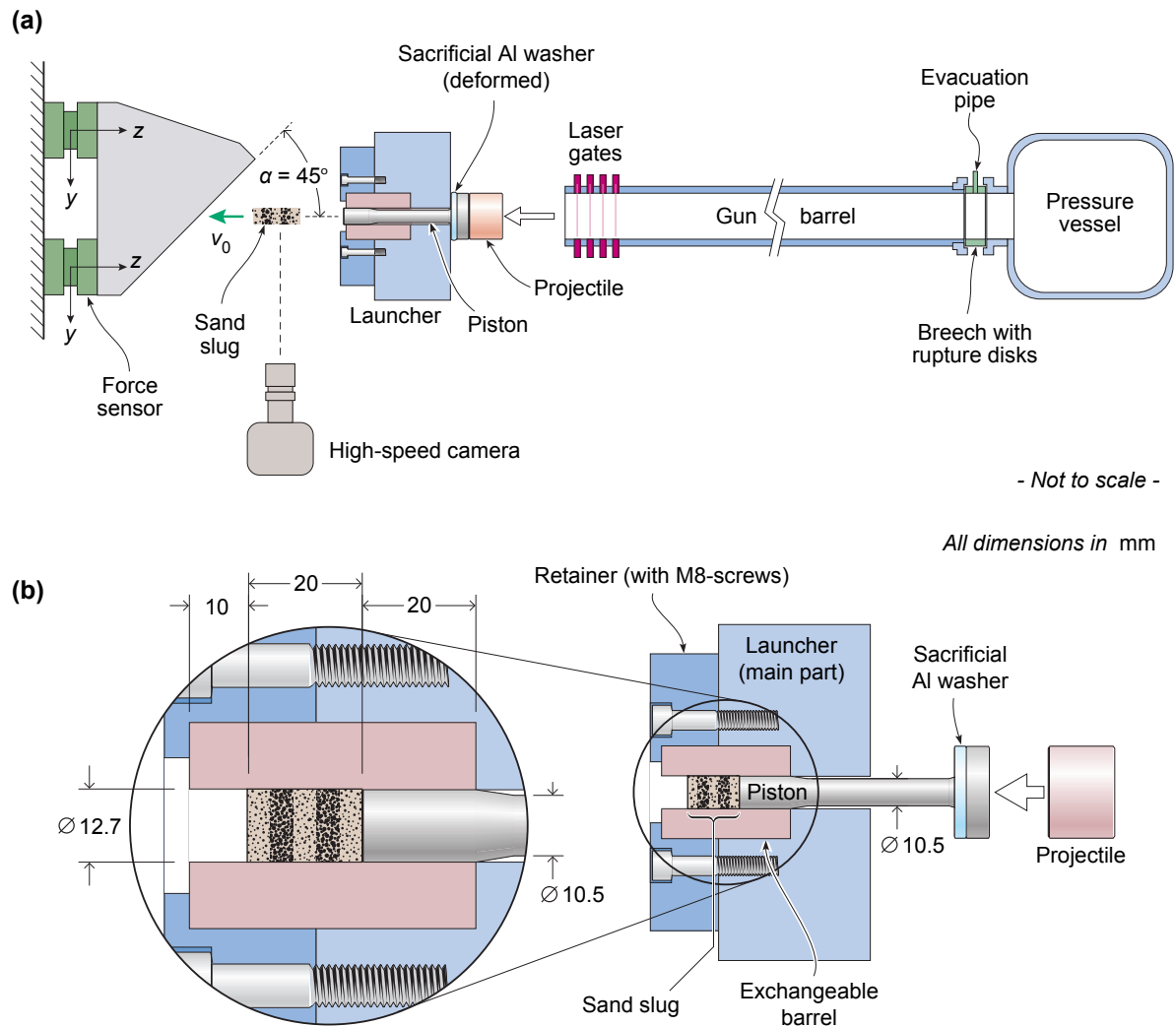


Fig. 6.1 (a) Sketch of the overall set-up used to investigate the impact of sand slugs against rigid-stationary targets. The set-up includes a gas gun to fire the projectile, a launcher to generate the slug, and a rigid-stationary target. The impact event is imaged using a high-speed camera and the projectile velocity is measured using laser gates. (b) A sketch showing a cross-sectional view of the slug launcher with the inset showing a detailed view of the piston in contact with the slug. All dimensions are in mm.

The launcher consisted of a thick-walled cylinder with an exchangeable barrel of inner diameter 12.7 mm and length 50 mm. The piston had three distinct segments: a front, middle and back with dimensions as sketched in Fig. 6.1b: this segmented geometry was required to allow for both a tight fit of the piston front in contact with the sand and also to allow for “fattening” of the piston near the impacted end without jamming of the piston. The piston head at the back acts as an end-stop to arrest the piston. In addition, a 5 mm thick Al alloy washer of inner diameter 12.7 mm and outer diameter 25 mm (equal to that of the piston head) was slid onto the piston until it was snug against the piston head. This washer cushioned the impact of the piston head against the launcher. A retainer was bolted to the front of the main part of the launcher to hold the exchangeable barrel in place. Before the launch process, the slug sat inside the exchangeable barrel such that there was a 10 mm gap between the front of the slug and the end of the exchangeable

barrel: study performed by Park et al. [95] showed that this extra cavity length helped to maintain the shape of the slug after the launch and until the impact with the target. Furthermore, the sand particles abrade the inner wall of the exchangeable inner barrel and hence it was replaced after every three tests to ensure a good sliding fit between the piston and the barrel.

### 6.2.2 Silica sand slugs

Dry sand slugs of mass  $m_{slug} = 4.2$  g were employed where the silica sand<sup>1</sup> particles were subspherical with particle sizes in the range of 150-300  $\mu\text{m}$ : see micrograph in Fig. 6.2. Before the launch, the cylindrical slugs had a diameter (12.7 mm) equal to that of the launcher and length  $L = 20$  mm. The slugs were prepared as detailed in [95] and comprised 5 equal width alternating layers of coloured and uncoloured particles so as to give the slug a zebra-striped appearance (Fig. 6.1b). This zebra pattern improved the visualisation of the deformation of the slug during free-flight and after launch.



Fig. 6.2 Optical micrograph of the sand particles used in slugs.

### 6.2.3 Gas gun to fire projectile

A steel projectile of 105 g mass and 28.4 mm diameter was accelerated using a gas gun with a barrel length of 4.5 m and inner diameter of 28.5 mm, as shown in Fig. 6.1a. No sabot was employed and the breech mechanism of the gun was formed by bursting copper diaphragms. The impact velocities  $V$  of the projectile against the piston of the launcher ranged from  $V = 127$  m s<sup>-1</sup> to 232 m s<sup>-1</sup>; the velocity of the projectile was measured at the exit of the barrel using laser gates. While higher velocities would have been desirable in

<sup>1</sup>BS 1881-131:1998, fraction D - David Ball Group, Wellington Way, Bourn, CB23 2TQ, UK

order to replicate granular media velocities in landmine explosions, impact of the piston at higher velocities irreparably damages the launcher and this limited the maximum projectile velocities employed in this study to about  $232 \text{ m s}^{-1}$ . The impacted end of the piston was placed about 25 mm in front of the end of the gun barrel. The flight of sand slug and the profile views of the spreading of the sand slug over the target were visualized using a Phantom v1610 digital camera<sup>2</sup> operating at an inter-frame rate of  $47.62 \mu\text{s}$  with an exposure time of  $0.45 \mu\text{s}$ .

A magnified sketch of the impact of the projectile against the piston that pushes the slug out of the launcher is shown in Fig. 6.3a. Upon impact of the projectile, both elastic and (slower) plastic waves emanate from the impacted end and propagate towards the end of the piston in contact with the granular slug. These waves deform the piston and thus the end of the piston in contact with the slug does not attain its final velocity instantaneously. To illustrate this effect, we plot the displacement in Fig. 6.3b of the four marker lines on the piston shown in Fig. 6.3a for a projectile impact speed  $V = 232 \text{ m s}^{-1}$ . These displacements are plotted as a function of time  $t_I$ , where  $t_I = 0$  corresponds to the instant of impact of the projectile. The displacement rates of the markers (i.e. the marker velocities) all reach a constant and equal value at large  $t_I$  as seen in Fig. 6.3b. This is consistent with the fact that the deformation of the piston ceases sometime after the impact of the projectile, and the piston thereafter behaves as a rigid body. This temporally and spatially constant marker velocity is defined as the piston velocity  $v_p$ . The piston velocities for all the experiments reported here were experimentally obtained in this manner, and the relation between  $V$  and  $v_p$  obtained via this procedure is shown in Fig. 6.3c. We shall refer to experiments via their piston velocity  $v_p$  and this measurement will be directly used as an input to the simulations, thereby avoiding the need to explicitly model the impact of the projectile against the piston.

#### 6.2.4 Target design

Experiments were conducted with rigid flat targets in an “inclined orientation” as sketched in Fig. 6.4 such that the slugs impacted at an angle  $\alpha = 45^\circ$  to the face of the target. The targets were 50 mm wide solid blocks of aluminium with a mass of 1 kg. The length of the target surface facing the slug impact was 100 mm as sketched in Fig. 6.4. This solid aluminium target can be considered rigid for the range of slug impact velocities and momenta considered here. Goel et al. [44] used these rigid stationary targets with four different surface coatings (Alumina, PTFE, Aluminium and Sand-paper) to study the effect of properties (hardness and roughness) of these coatings on momentum transmitted from impacting sand slug to the target. The surface coating in their study was adhesively attached to the surface of the rigid aluminium target such that it does not move relative to the target surface for the entire duration of the experiment.

---

<sup>2</sup>Vision Research, Priory Business Park, Stannard Way, Bedford, MK44 3RZ, UK.

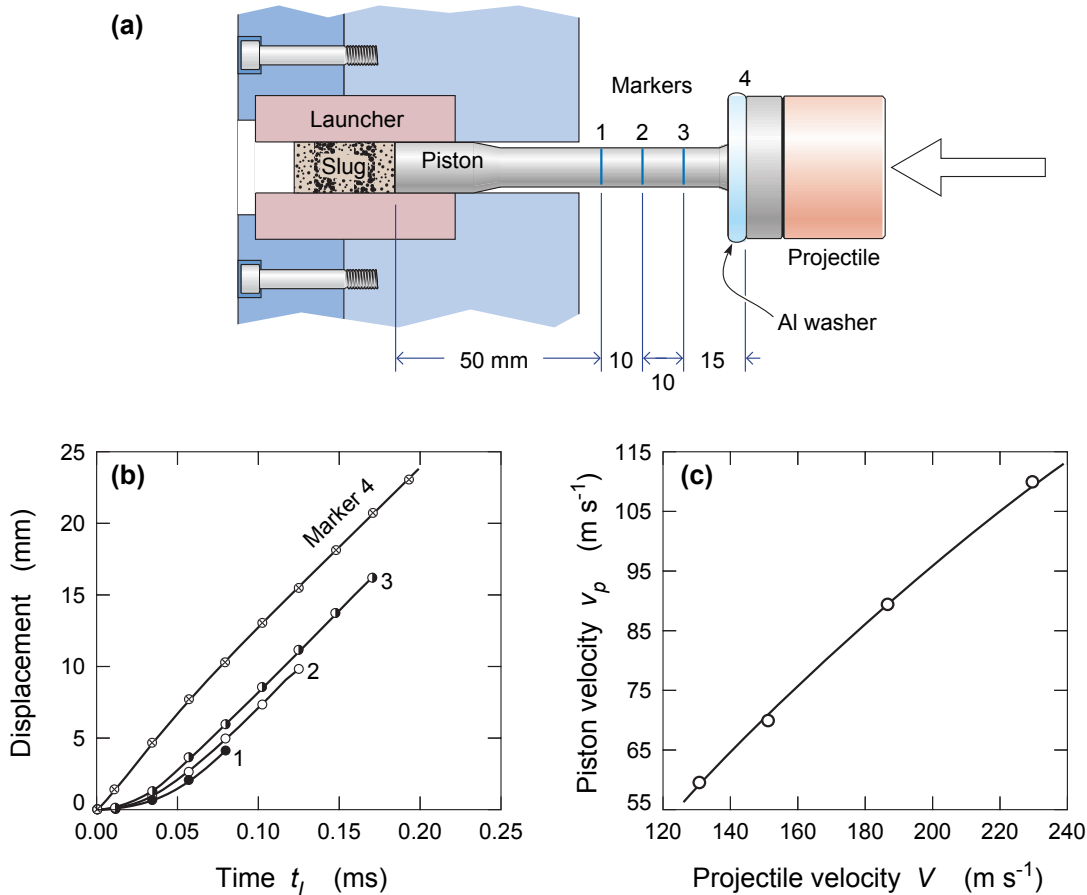


Fig. 6.3 (a) Magnified view of the launcher with the piston that has just been impacted by the projectile. The locations of four marker lines on the piston are shown: the displacements of these markers are followed via the high-speed photography. (b) The temporal evolution of the displacements of the four marker lines in (a) for a projectile impact velocity  $V = 232$  m s<sup>-1</sup>. Here time  $t_I = 0$  corresponds to the instant of impact of the projectile. (c) The relation between the piston velocity  $v_p$  and projectile velocity  $V$  inferred from the high-speed photographs of the piston motion.

In the current study, we use the sand-paper (grade 3M 251D P60-SC1<sup>3</sup>) coating but instead of attaching it adhesively to the surface of the aluminium target, a thin layer of lubricant gel<sup>4</sup> was used at the interface between the coating and the aluminium target surface as shown in Fig. 6.4. When the sand slug impacts the sand-paper coating, there are normal and tangential loads on the target surface for which we define the resultants as  $f_n$  and  $f_s$ , respectively indicated in Fig. 6.4. Due to the tangential load  $f_s$ , there would be a tendency for the coating to slide on the target surface. Having a lubricant between the coating and the target surface allows the sliding of this coating, while the normal force  $f_n$  prevents separation between the coating and the target surface. The sand-paper coating had a mean surface roughness  $R_a$  of 30.6  $\mu\text{m}$  and Vickers hardness of 27.6 kgf

<sup>3</sup>Comprising “X-weight” cloth which is a heavy duty tear resistant blend of cotton and polyester coated with Alumina particles having a grit size P60.

<sup>4</sup>Alberto Balsam ultra strong styling gel - [www.albertobalsam.com](http://www.albertobalsam.com)

$\text{mm}^{-2}$ . We note that the hardness of the sand-paper is that measured by performing a Vickers indentation test on the sand-paper placed on a rigid foundation and represents a combination of the hardness of the backing cloth and the hardness of the Alumina grit (the hardness of the Alumina comprising the grit is  $1600 \text{ kgf mm}^{-2}$ ).

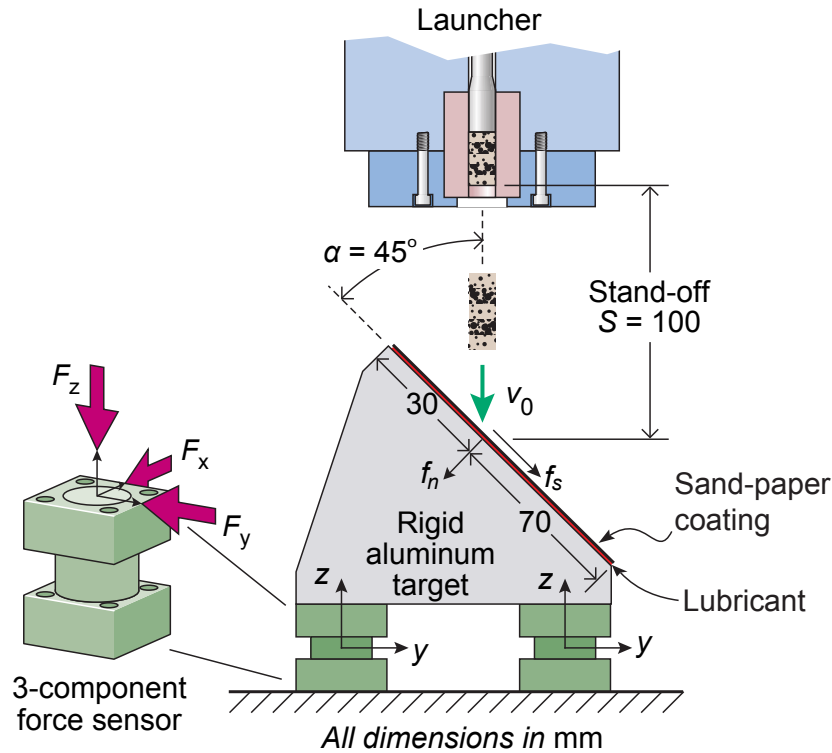


Fig. 6.4 Sketch of the rigid target in the inclined orientation. The coordinate system fixed to the support structure  $(x, y, z)$  is sketched along with the piezoelectric force sensors used to measure the momentum transferred into the target. A detailed view of the force sensor and the three components  $(F_x, F_y, F_z)$  of the measured forces is sketched. A portion of the slug launcher is shown in order to define the stand-off  $S$  and the location of the slug impact on the target. All dimensions are in mm.

The targets were positioned at a stand-off  $S = 100$  mm in all experiments, where  $S$  is defined in Fig. 6.4 as the distance between the front of the stationary sand slug and the front face of the target at the centre of impact location. The targets were in turn supported on two 3-component piezoelectric force sensors (Kistler<sup>5</sup>, type 9347C) that were used to measure the momentum transferred by the impacting slug into the target. These sensors measure forces in the three orthogonal directions  $(x, y, z)$ , where the  $z$ -axis was always defined in the direction of the incoming slug as shown in Fig. 6.4. The sensors could measure forces of up to 30 kN in the  $z$ -direction and 10 kN in the  $x$ - and  $y$ -directions. The output from the sensors was conditioned using a Kistler 5001 charge amplifier and recorded with a digital oscilloscope (Tektronix<sup>6</sup>, TDS 3014B).

<sup>5</sup>Kistler Instruments Ltd., Hook, Hampshire RG27 9GR, UK.

<sup>6</sup>Tektronix, P.O. Box 500, Beaverton, OR 97077, USA.

### 6.2.5 Temporal evolution and characterisation of slugs

Sand slugs were generated by firing projectiles against the launcher piston which in turn generated piston velocities in the range  $v_p = 60 \text{ m s}^{-1} - 112 \text{ m s}^{-1}$ . In line with the observations made for silica sand slugs [95, 125, 44], and Tungsten Carbide (WC) particle slugs [126, 43], the velocity of the particles within the slugs remained temporally invariant after the slugs fully exit the launcher (i.e. the velocity of the slug was constant over the period during which observations could be made). As in previous studies, the particles within the slug acquired nearly no radial velocity but their axial velocity varied with position along the axis of the slug. The slug elongates, consistent with sand particles having an axial velocity gradient along the slug with those at the front travelling more rapidly than at the tail.

In order to quantify the spatial gradient of the axial velocity, images from the high-speed camera were used to measure the velocities of the boundaries between the coloured and uncoloured sand particle layers. Measurements of the temporally invariant boundary velocities  $v_b^{(i)}$ , where the superscript  $(i)$  refers to the boundary number are plotted in Fig. 6.5 (the boundaries are labelled in the inset of Fig. 6.5) for two selected values of  $v_p$ . They clearly show the axial gradient in the particle velocities within the slug with the front of the slug having a higher velocity compared to the rear resulting in elongation of the slug during free flight. Noting that each of the 5 layers of the slug has equal mass, the free-field momentum of the slug is

$$I_0 = \frac{m_{slug}}{5} \sum_{i=1}^5 \frac{v_b^{(i)} + v_b^{(i+1)}}{2} \quad (6.1)$$

and the average slug velocity is then defined as  $v_0 \equiv I_0/m_{slug}$ . Subsequently, we shall refer to the velocity of slug via this average velocity  $v_0$ .

### 6.2.6 Characterisation of transmitted momentum

As in the previous study by Goel et al. [44], the primary aim of the experiments here was to determine the momentum transmitted from the slug into the target. The two force transducers provide measurements of force versus time histories in the  $x$ -,  $y$ - and  $z$ -directions. The transmitted forces depend not only on the actual loads exerted by the slug but also on the location of the force measurements, structural properties of support (e.g. its stiffness and mass) and the clamping set-up [77, 120]. However, the integral of force history over time is less dependent on the support structure, which makes it a useful parameter to quantify the effect of impacting slugs. The force component measured by the two transducers (1 and 2) in the  $z$ -direction is identified as  $F_z^1$  and  $F_z^2$ , respectively. Consequently, the momentum  $i_T^z$  transmitted into the support structure in the  $z$ -direction

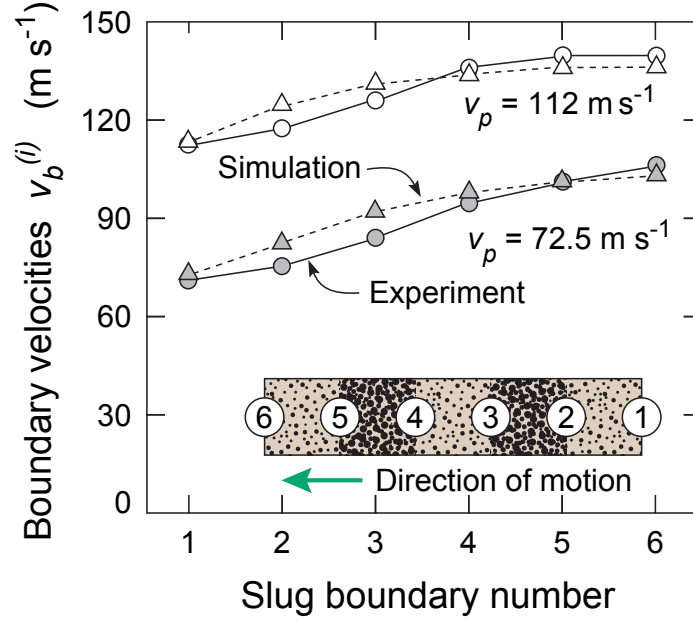


Fig. 6.5 Measurements and predictions of the steady-state boundary velocities  $v_b^{(i)}$  for two selected values of  $v_p$ . The boundary number indicated by the superscript ( $i$ ) is illustrated in the inset.

after a time  $t$  (where  $t = 0$  corresponds to the instant that the slug first impacts the target) is given by

$$i_T^z(t) = \int_0^t (F_z^1 + F_z^2) dt \quad (6.2)$$

and  $I_T^z \equiv i_T^z(\text{as } t \rightarrow \infty)$  is the total momentum transmitted into the target in the  $z$ -direction. Analogous expressions exist for momenta components in the other two directions (viz.  $I_T^y$  and  $i_T^y$  as well as  $I_T^x$  and  $i_T^x$ ). In all experiments  $i_T^x = 0$  to within the accuracy of the measurements (as dictated by symmetry) and hence the focus here is on the momentum measurements in the  $z$ - and  $y$ -direction and the resultant transmitted momentum given by

$$I_T = \sqrt{(I_T^z)^2 + (I_T^y)^2} \quad (6.3)$$

As defined previously,  $f_n$  and  $f_s$  are the resultant normal and tangential forces exerted by the sand particles on the target (Fig. 6.4). The momentum balance gives

$$\begin{aligned} i_T^z(t) &= \int_0^t (f_n \sin \alpha + f_s \cos \alpha) dt & \text{and} \\ i_T^y(t) &= \int_0^t (f_n \cos \alpha - f_s \sin \alpha) dt \end{aligned} \quad (6.4)$$

The tangential force  $f_s$  has opposite effects on  $i_T^z$  and  $i_T^y$  and hence we observe  $I_T^y < I_T^z$ . After the slug finishes impacting (and spreading) against the target, the sand particles have a negligible velocity perpendicular to the target surface. This implies,

$$\lim_{t \rightarrow \infty} \int_0^t f_n dt = I_0 \sin \alpha \quad (6.5)$$

If the target is oriented normal ( $\alpha = 90^\circ$ ) to the incident slug,  $f_s = 0$  by symmetry giving  $I_T^z = I_0$  and  $I_T^y = 0$ . By contrast, for the inclined case presented here, we cannot independently relate  $I_T^z$  and  $I_T^y$  directly to  $I_0$  without detailed information on  $f_s$ . However, for the special case of  $\alpha = 45^\circ$ , Eq. 6.4 and Eq. 6.5 gives the equality  $I_0 = I_T^z + I_T^y$  as discussed by Uth et al. [126]. Moreover, in the absence of friction between the particles and the target (i.e. when  $f_s = 0$ ), explicit relations for the transmitted momentum follow from Eq. 6.4 as

$$I_T^z = I_0 \sin^2 \alpha \quad \text{and} \quad I_T^y = I_0 \sin \alpha \cos \alpha \quad (6.6)$$

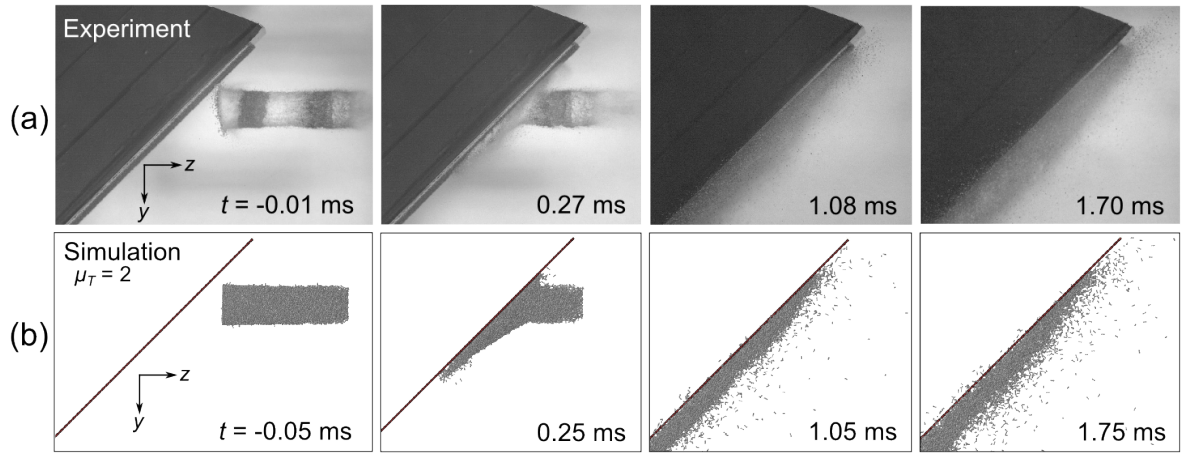
For the case of  $\alpha = 45^\circ$  these reduce to  $I_T^z/I_0 = I_T^y/I_0 = 0.5$ . These values are subsequently used as a reference during analysis of the measurements.

### 6.3 Experimental results

We proceed to report the measurements of sand slug impacting the inclined target having sand-paper coating which is allowed to slide on the target surface. These observations are compared with the experiments performed by Goel et al. [44] where the sand-paper coating was adhesively attached to the target. For the sake of clarity, we denote the experiments having fixed coating as ‘no-slip’ condition and those with sliding coating as ‘slip’ condition. Two sets of high speed photographs showing impact of dry sand slug with  $v_0 = 112 \text{ m s}^{-1}$  on inclined target are presented in Fig. 6.6a and Fig. 6.6c. Fig. 6.6a is for fixed sand-paper coating (no-slip condition) as observed by Goel et al. [44] whereas the observation for sliding sand-paper coating (slip condition) is shown in Fig. 6.6c. Here, time  $t = 0$  corresponds to the instant the slug impacts the target. In both the ‘slip’ and ‘no-slip’ cases, the spreading of sand particles against the target is asymmetric with both the mass of the sand particles and spreading velocity in the negative  $y$ -direction being less than their corresponding quantities in the positive  $y$ -direction. This is primarily due to the fact that the momentum of the incoming slug resolves along the target surface in the positive  $y$ -direction. However, the flow of the sand particles along the target surface in the negative  $y$ -direction is caused by the reaction imposed by the target on the sand particles. In Fig. 6.6c, the initial location of the top edge of the coating is indicated by a horizontal dashed line and its location at any time instant  $t$  is indicated by a circular marker. It was observed that the coating slides on the target surface after the impact from sand slug.

This is due to the fact that the slug applies a tangential load ( $f_s$ : see Fig. 6.4) along the target face. Symmetry across the  $y$ - $z$  plane dictates that there is no movement of coating in  $x$ -direction. Also, the normal load ( $f_n$ : see Fig. 6.4) applied by the slug ensures no separation between the coating and target surface during the impact process.

### No-slip



### Slip

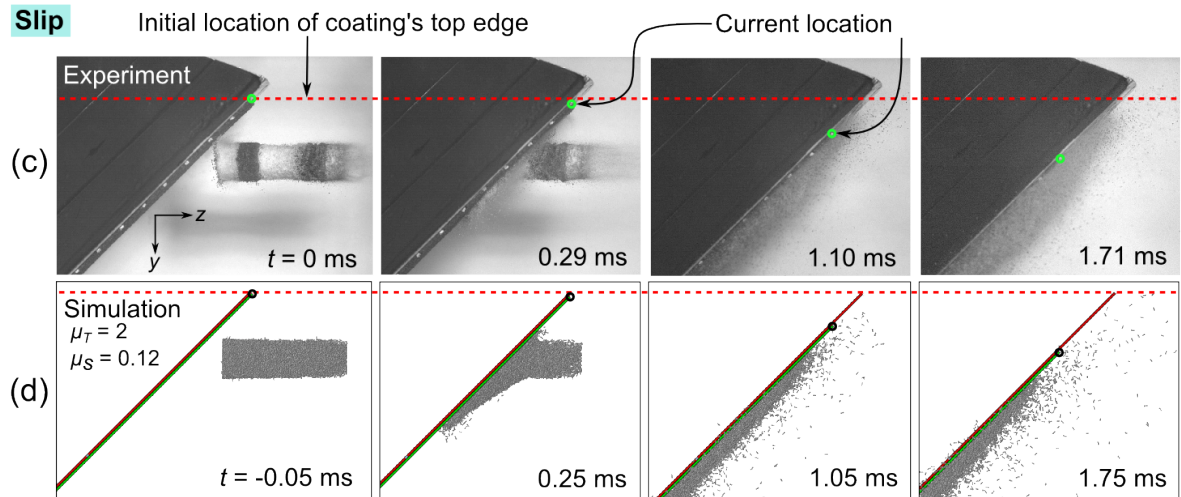


Fig. 6.6 Montage of high-speed photographs showing deformation of sand slugs impacting the inclined targets having: (a) fixed sand-paper coating - ‘no-slip’ case [44] and (c) sliding sand-paper coating - ‘slip’ case where a lubricant was used at the interface between the coating and target surface. The slugs have a velocity  $v_0 = 112 \text{ m s}^{-1}$  and time  $t = 0$  corresponds to the instant that the slug impacts the target. In (c), the dashed horizontal line indicates the initial location of the top edge of the coating and the circular marker shows the location at the time  $t$  indicated in the photo. (b) and (d) are the corresponding predictions for no-slip and slip conditions shown in (a) and (c), respectively.

The measured normalised transmitted momenta  $I_T^z/I_0$  and  $I_T^y/I_0$  are included in Fig. 6.7a for the slug velocities  $v_0$  in the range  $76$ – $128 \text{ m s}^{-1}$ . The results are shown for no-slip condition [44] as well as slip condition. Similar to the measurements of no-slip condition [44], the fraction of the transmitted momenta are independent of  $v_0$  for slip condition as well over the range of velocities considered here. As anticipated from Eq. 6.4,  $I_T^z/I_0 > I_T^y/I_0$ . Goel et al. [44] have demonstrated that the transmitted momentum for

impacts with inclined surfaces is strongly influenced by surface properties of the target. Measurements presented in Fig. 6.7a show that by allowing the sand-paper coating to slide on the target surface, the value of  $I_T^z/I_0$  decreases and  $I_T^y/I_0$  increases for a given slug velocity. This observation can be explained using Eq. 6.4 by considering a reduction in the resultant tangential force  $f_s$  on the target, i.e. if the coating is allowed to slide,  $f_s$  reduces resulting in decreasing  $I_T^z$  and increasing  $I_T^y$ . The values of  $I_T^z/I_0$ ,  $I_T^y/I_0$  and  $I_T/I_0$  averaged across the slug velocities  $v_0$  are shown in Fig. 6.7b with the error bars indicating the variation of values over the velocity range  $v_0$ . Goel et al. [44] performed experiments with four different surface coatings: Alumina, PTFE, Aluminium and sand-paper showing the effect of the surface type on the levels of transmitted momentum. They demonstrated that the surface property that govern the embedding of particles into the surface play a crucial role in modulating the transmitted momentum. Amongst all the surface coatings tested by Goel et al. [44], Alumina resulted in least transmitted momentum  $I_T/I_0$  and sand-paper in highest  $I_T/I_0$  (due to a decrease in  $I_T^y/I_0$  and increase in  $I_T^z/I_0$ ) with 11% increase compared to those for Alumina coatings. When the same sand-paper coating was allowed to slide in the experiments presented here, the normalised transmitted momenta  $I_T^z/I_0$ ,  $I_T^y/I_0$  and  $I_T/I_0$  are closer to those obtained from no-slip Alumina coating (see Fig. 6.7b), i.e.  $\sim 11\%$  decrease as compared to fixed sand-paper coating.

We note here that for the Alumina coating itself, Goel et al. [44] showed that the transmitted momentum into the inclined target was higher than the predicted value in the absence of friction between the sand particles and the target surface. Recall that in the absence of friction between the sand particles and the target surface we expect that  $I_T^z/I_0 = I_T^z/I_0 = 0.5$  and  $I_T/I_0 = 1/\sqrt{2}$ . The measurements in Fig. 6.7b show resultant transmitted momentum  $I_T/I_0 \approx 0.77$  for Alumina coating, which represents a 9% increase over the value expected in absence of friction.

The observations presented in this section show that the frictional loading on the target can be reduced by allowing the coating to slide on the existing target. We emphasise that if the existing target surface facing impact is already smooth (e.g. frictionless or alumina coating as discussed above), adding a sliding coating may not provide additional benefit. However, if the target is rough and if this rough layer is allowed to slide, it reduces the frictional loading, and hence the overall transmitted momentum. There are several other aspects that may influence the transmitted momentum in this slip condition. These may be: properties of the lubricant used at the interface, properties of contact between coating and the target surface, mass of the coating, friction between the coating and particles, etc. In the following sections, we perform simulations to examine some of these aspects to get a better understanding of the physics in this problem.

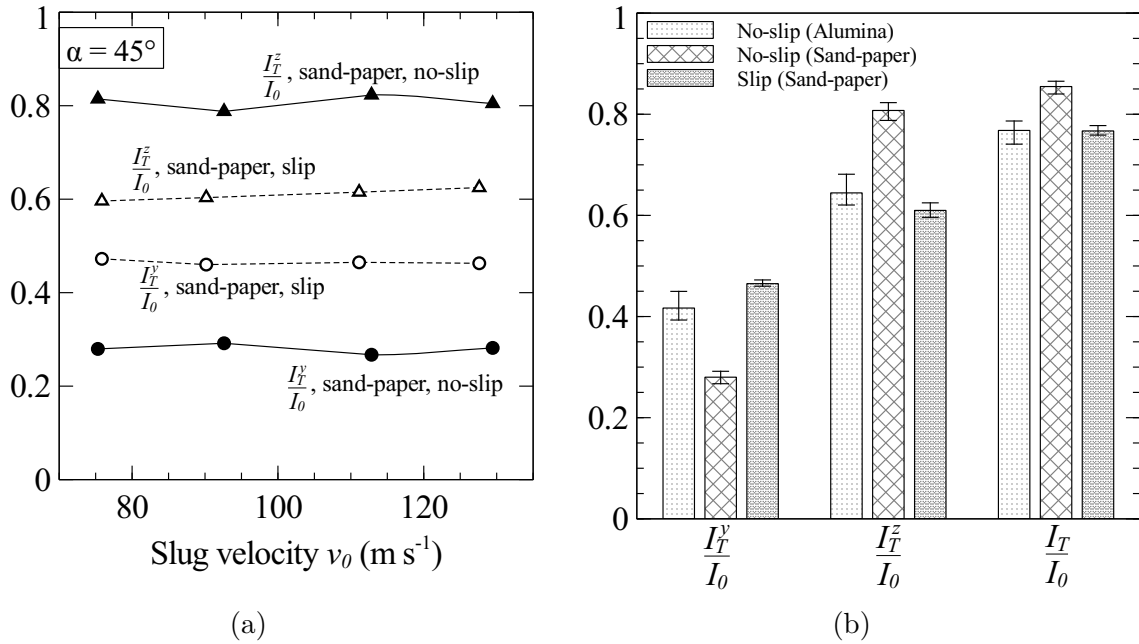


Fig. 6.7 (a) Measured normalised transmitted momentum  $I_T^z/I_0$  and  $I_T^y/I_0$  as a function of slug velocity  $v_0$  for impacts against inclined targets. Measurements are shown for impact of dry sand slug against target with fixed sand-paper coating (no-slip condition) and sliding sand-paper coating (slip condition). (b) A bar chart showing the measurements of no-slip condition with alumina and sand-paper coating, along with the slip condition using sand-paper coating. Additional data set is shown for the measurements of resultant transmitted momentum  $I_T/I_0$ . The error bars indicate the variation of the measurements over the range of slug velocities  $v_0$  investigated here. All the no-slip condition measurements are from Goel et al. [44].

## 6.4 Simulation methodology

The experimental measurements reported above show the effect of allowing the coating to slide on the rigid target surface. It was observed that the ‘slip’ condition has reduced amount of transmitted momentum compared to the ‘no-slip’ condition. Numerical calculations are now utilized to better understand these interactions and extend the understanding to also see the effect on deformable targets. The coupled discrete particle/Lagrangian finite element simulations were performed using the commercial package Abaqus.

### 6.4.1 Geometry of the granular particles

Recent experiments by Goel et al. [44] demonstrated that friction between the particles and targets strongly influences the transmitted momentum for the case of impacts on inclined targets. However, coupled discrete particle/Lagrangian finite element (FE) simulations performed by Goel et al. [44] with spherical particles were unable to predict the measured response with sufficient accuracy. They also demonstrated that artificially increasing the rotational inertia of the particles and thereby reducing the rolling of the particles brought the predictions closer to observed results and this suggested that particle shape has a

strong influence on momentum transfer. The reason for this is that in reality, sand particles are sub-spherical in shape, which have reduced tendency of rotation when interacting with the target, as compared to spherical particles in such impact scenarios. This changed rotational tendency changes the frictional loading and hence the momentum transmitted to the target. More recently, Goel et al. [45] have reported discrete element calculations to investigate the effect of particle shape on the interaction of high velocity granular media with rigid stationary targets in normal and inclined orientations. They show that with increasing annularity, the particles tended to slide over the target surface rather than roll. This increases frictional interactions between the particles and the target, implying that for the case of impact against an inclined target, the transmitted momentum increased with increasing particle angularity.

For the current study, we use the particle slug with rod shaped angular particles as utilised by Goel et al. [45]. These rod-shaped particles were all constructed by combining together spherical particles and hence for the sake of clarity of terminology, we shall refer to the granular particles as *grains* and the spherical particles from which they are constructed as *sub-particles*. The spherical sub-particles are rigid single node spherical elements (PD3D in the Abaqus notation) of density  $\rho_p$  and diameter  $d_p$  such that they have a mass  $m_p \equiv (4/3)\pi d_p^3 \rho_p$ .

The spherical grains (serving as a reference) comprise a single sub-particle of diameter  $D = d_p$  as shown in Fig. 6.8a. The rod-shaped grains comprise a linear array of the sub-particles with centre-to-centre spacing  $d_p$  as shown in Fig. 6.8b. The rod aspect ratio  $\Phi$  is defined as the ratio of the grain length to circumscribing cylinder diameter and thus  $\Phi = n$ , where  $n$  is the number of sub-particles that form the grain. Given the diameter  $D$  of the reference spherical grain, the diameter  $d_p$  of the sub-particle in the rod-shaped grain of aspect ratio  $\Phi$  follows as  $d_p = D/\sqrt[3]{\Phi}$ . Rigid connections were enforced between the sub-particle centres such that the shape of the grains remain unchanged throughout the impact event. These rigid connections were specified using the multi-point constraint (MPC) functionality in Abaqus. Goel et al. [45] showed that the momentum transmitted from slug to inclined target was insensitive to increase in the aspect ratio over  $\Phi = 3$ . Hence, for the current study, we use  $\Phi = 3$  for rod-shaped grains to construct granular slug. We emphasise that modelling of rod-shaped grains as shown by Goel et al. [45] is not an accurate representation of the real sub-spherical shape of the particles. Nevertheless, such a representation simulates the reduction of rotation of particles during the impact with the target.

### 6.4.2 The particle contact model and coupling to FE simulations

Since the grains comprise sub-particles, it is these sub-particles that come into contact with each other as grains collide with each other and with the coating. Thus, it suffices to specify contact model for sub-particle contact. In line with usual discrete element simulations

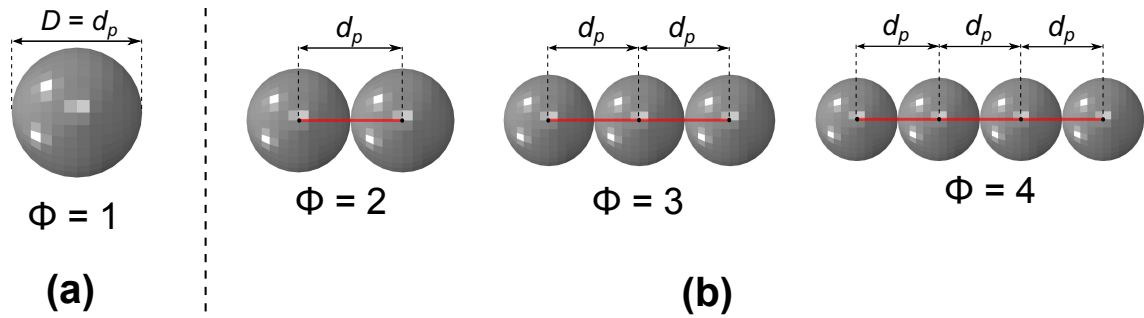


Fig. 6.8 Sketches of the different rod-shaped grains used by Goel et al. [45]. (a) Spherical grains of diameter  $D = d_p$   $\mu\text{m}$ . (b) Rod-shaped grains with aspect ratios  $2 \leq \Phi \leq 4$  constructed from spherical sub-particles.

while the sub-particles are rigid spheres, contact between the grains as well as the grains and the coating is modelled using the soft-contact approach (Fig. 6.9) introduced by Cundall and Strack [24] and extended to large scale simulations by Campbell and Brennen [15] and Campbell [14]. The inter sub-particle contact law comprises:

1. A linear spring with spring constant  $K_n$  and linear dashpot with damping constant  $\gamma_n$  connected in parallel, governing the contact in the direction connecting the sub-particle centres.
2. Linear spring of constant  $K_s$  and Coulomb friction coefficient  $\mu$  connected in series, governing the tangential contact.

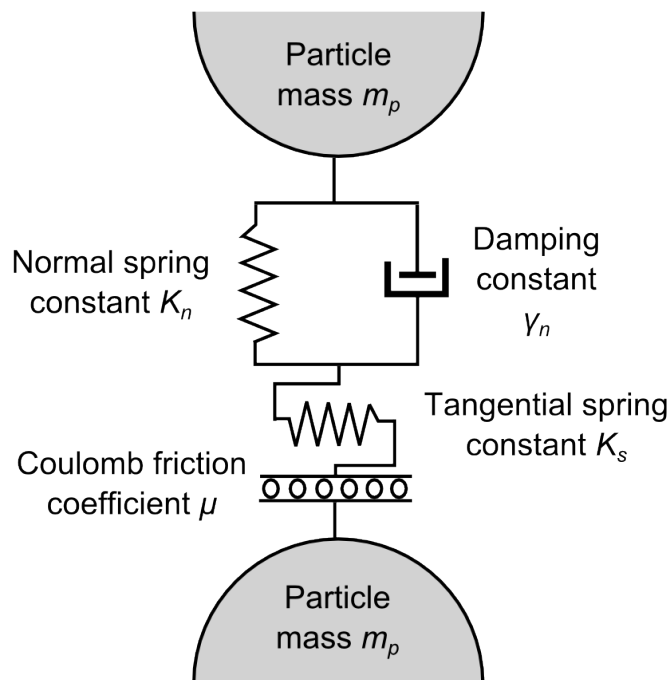


Fig. 6.9 Sketch of the inter-particle contact model between sub-particles used to simulate grains in the granular slug.

With  $r$  as the separation of the sub-particle centres, and the interpenetration given by  $\delta_n = r - d_p$ , the normal force during active contact ( $\delta_n < 0$ ) is given by

$$F_n = K_n \delta_n + m_{\text{eff}} \gamma_n \dot{\delta}_n \quad (6.7)$$

where  $m_{\text{eff}}$  is the effective or reduced mass of the two contacting bodies. We take  $m_{\text{eff}} = m_p/2$  for impacts between sub-particles, and  $m_{\text{eff}} = m_p$  for impacts between a sub-particle and the coating.

The tangential force  $F_s$  only exists during active contact, and opposes sliding. It is limited in magnitude to  $|F_s| < \mu |F_n|$  as follows. With  $\dot{\delta}_s$  defined as the tangential displacement rate between the contacting sub-particles,  $F_s$  can be represented by an elastic-plastic relation of Coulomb type with stiffness  $K_s$ , i.e.

$$\dot{F}_s = \begin{cases} K_s \dot{\delta}_s & \text{if } |F_s| < \mu |F_n| \text{ or } F_s \dot{\delta}_s < 0 \\ 0 & \text{otherwise} \end{cases} \quad (6.8)$$

The critical difference for interactions between sub-particles and between sub-particles and other surfaces is the co-efficient of friction  $\mu$ : we shall use  $\mu_p$  and  $\mu_T$  to refer to the value of for inter sub-particle and sub-particle/structural interactions, respectively. The value of damping constant  $\gamma_n$  dictates the loss of sub-particle kinetic energy during normal collision and is directly related to the coefficient of restitution  $e$  according to

$$e = \exp \left[ -\pi \left( \frac{8K_n}{\gamma_n^2 m_p} - 1 \right)^{-1/2} \right] \quad (6.9)$$

The collision time  $t_e$  for individual binary collisions follows from Eq. 6.7 as

$$t_e = -2 \frac{\ln(e)}{\gamma_n} \quad (6.10)$$

and thus, in the limit of plastic collisions with  $e \rightarrow 0$ , the contact time  $t_e \rightarrow \infty$ . The forces (normal and tangential) on each sub-particle are calculated and the Newton's equations for both the translational and rotational motions of the sub-particles were integrated using an explicit time-integration scheme within Abaqus. The time-step for integration was taken to be less than  $t_e/10$  in order to ensure accurate integration of the equations of motion.

The target surface and coating were modelled via a Lagrangian FE framework using reduced integration 4 noded shell elements (S4R in Abaqus notation). To model rigid targets, all the nodes in the mesh had six degrees of freedom (3 rotational and 3 translational) constrained. The coupling between the discrete grains and FE parts made of shell elements was performed as follows. At any time  $t$ , a proportion of the grains are in contact with the FE part. Consider one such grain. One or more of the sub-particles of this grain

are in contact with the FE part with an interpenetration  $\delta_n$  defined as  $\delta_n = r - d_p/2$ , where  $r$  is the distance between the sub-particle centre and contact point on the FE part (note the difference in the definition of  $\delta_n$  for inter sub-particle and sub-particle/FE part interactions). The rate  $\dot{\delta}_n$  is the relative approach velocity of the sub-particle and the point of contact on the FE part, and likewise  $\dot{\delta}_s$  is the relative tangential velocity. The normal and tangential contact forces are calculated using Eqs. 6.7 and 6.8. These forces are then added as nodal forces to the appropriate elements in FE calculations to complete the coupling between the discrete and FE calculations.

### 6.4.3 Construction of initial granular slugs

The cylindrical slugs have an initial diameter of 12.7 mm and length  $L = 20$  mm as shown in Fig. 6.14a. All the grains in the slug are rod shaped with an aspect ratio  $\Phi = 3$  and they occupy a volume fraction  $\bar{\rho} = 0.55$  in the slug. We desire that the grains are located and oriented randomly within the slug which is achieved via a process similar to used by Goel et al. [45] and is detailed below:

1. The grains were first randomly located within a cylinder of diameter  $< 12.7$  mm and length  $> 20$  mm. In this step, while the location of grains was random, all the grains had same orientation, i.e. the rod-shaped grains were oriented along the axis of the cylinder. This process typically resulted in a slug with a volume fraction  $\ll \bar{\rho}$ .
2. All grains were then given a velocity  $v = 10 \text{ m s}^{-1}$  in the axial direction, with the end of the cylinder towards which the grains are travelling capped by a rigid face. The grains were then allowed to collide with each other and settle within the cylinder under the influence of gravity.
3. The grains were then further compacted within the cylinder by the action of a piston. The collisions and re-arrangements of the grains in steps 2 and 3 resulted in dense randomly packed grains ( $\bar{\rho} \approx 0.55$ ) within a cylindrical volume of length  $L = 20$  mm.

This slug is then used as the initial slug impacted by piston. In these calculations, the grains were always constructed using rigid connections between the sub-particles and the sub-particle properties were taken to be the same as those in the remainder of the calculations as detailed in Section 6.4.6.

### 6.4.4 Generation of granular slug

To accurately capture the state of the granular slug during its free-flight and thereby its state just prior to impact, it is necessary to explicitly model the ejection of the slug from the launcher as described in Goel et al. [43] and later used by Goel et al. [44]. In order to simplify the numerical calculations, the impact of the projectile against the piston and the

deformation of the piston were not directly modelled. Rather, the piston was modelled as a rigid body as shown in Fig. 6.14a and given a velocity  $v_I(t_I)$ , motivated from the data in Fig. 6.3b in a manner similar to that of Goel et al. [43, 44]. Thus, following Goel et al. [43, 44], it suffices to approximate  $v_I(t_I)$  as

$$v_I = \left\{ \begin{array}{ll} \frac{v_p t_I}{T_R} & 0 \leq t_I \leq T_R \\ v_p & t_I > T_R \end{array} \right\} \quad (6.11)$$

where  $T_R$  is the time taken for the piston to ramp up to its final velocity  $v_p$ .

Simulations of the ejection of the granular slug from within the launcher were performed as follows. The slug was constructed as described in Section 6.4.3, placed into a cylindrical cavity of inner diameter  $D = 12.7$  mm capped at one end by a rigid piston as shown in Fig. 6.14a. The compacted slug had a length  $L = 20$  mm and the free end of the slug needed to travel a distance of 10 mm to emerge from the launcher, consistent with the experimental design. The piston was then imparted a velocity versus time history  $v_I(t_I)$  specified by Eq. 6.11 which pushed the slug out of the launcher. In line with the procedure followed by Goel et al. [44], the ramp time  $T_R$  was calibrated to ensure agreement between the measured and predicted boundary velocities. This involved obtaining a value of  $T_R$  for each piston velocity  $v_p$  employed in this study. The impact of the slugs generated in this manner against the FE part is then solved via the coupled discrete particle/Lagrangian method with the target placed at a stand-off  $S = 100$  mm, same as that used in the experimental setup.

### 6.4.5 Calculation of transmitted momentum

For rigid targets, the transmitted momentum was calculated by integrating the reaction forces, similar to the procedure used in experiments (see Section 6.2.6). For instance, to calculate  $I_T^z$  we temporally integrate the reaction force in the  $z$ -direction on the target over a sufficiently large time period so as to obtain the steady-state value of  $I_T^z$ . Similar procedure was used for  $I_T^y$  and  $I_T^x$ .

If the target structure is deformable, it oscillates after the impact from the slug, as shown by Goel et al. [43]. This results in an oscillating reaction load on the supports and an oscillating calculated transmitted momentum by integration of loads. These target oscillations die down eventually but it may take a long time, implying a higher computational cost. To eliminate any ambiguity from the calculations for a deformable target due to these oscillations, we use conservation of momentum by accounting for the momentum of slug to calculate the momentum transmitted to the target. To do this, momentum of all the grains are determined before and after the impact in each direction. The momentum transmitted to the target in any particular direction can be calculated as the difference between total initial and final momentum of all the grains in that direction.

When the simulation includes sliding coating, its momentum is also accounted for in momentum conservation calculations to obtain the momentum transmitted just to the target.

All results are presented with the transmitted momenta normalised by the initial momentum  $I_0 \equiv m_{slug}v_0$  of the slug in the  $z$ -direction.

### 6.4.6 Material parameters

All calculations presented here use the following reference properties for the grains and sub-particles. The granular slugs comprise rod-shaped grains of aspect ratio  $\Phi = 3$  constructed corresponding to the reference spherical grain of diameter  $D = 600 \mu\text{m}$ . Goel et al. [44] have shown that the momentum transmitted to a rigid inclined target is insensitive to the particle size range  $150 \mu\text{m} \leq D \leq 600 \mu\text{m}$ . While Cheng et al. [18] have shown that as the number of particles across the width of the a granular jet is reduced, the jet stops behaving as an aggregate of particles and more like individual non-interacting particles. However, even with the largest particle diameter of 600  $\mu\text{m}$ (for which the slug contained the smallest number of particles) this limit was not approached in the simulations by Goel et al. [44].

The total weight of the slug was  $\sim 4.2 \text{ g}$  where the sub-particles were assumed to be made from a solid of density  $2700 \text{ kg m}^{-3}$  (equal to that of Silica). The sub-particle contact model was defined by four parameters  $K_n$ ,  $e$ ,  $K_s$  and  $\mu_p$ . While Liu et al. [79] demonstrated that these parameters do not affect the interaction response of the granular slug impacting targets, Goel et al. [43] demonstrated that  $K_n$  strongly influence the evolution of the granular slugs as it emerges from the launcher. Here, a calibrated value  $K_n = 0.69 \text{ MN m}^{-1}$  (as estimated by Goel et al. [44]) was used. For other parameters, the reference values are:  $K_s/K_n = 2/7$  [4, 112],  $e = 0.7$  and  $\mu_p = 0.6$ . Frictional interactions between the cylindrical cavity surface of the launcher in contact with the sand particles were neglected. In all the impact simulations presented here, the effect of gravity was neglected. As mentioned previously, the friction coefficient between grains and FE parts (target surface, coating) is defined by  $\mu_T$ . No-slip condition can be thought of as either having a fixed coating with grain/coating friction coefficient  $\mu_T$  or equivalently as having no coating with grain/target surface friction coefficient  $\mu_T$ . For the case of sliding coating, the lubricant at target/coating interface was not explicitly modelled in simulations. Rather, the frictional effect at this interface was captured using the friction coefficient  $\mu_s$ . The effect of changing  $\mu_T$  and  $\mu_s$  is presented in this study.

For simulations having rigid targets, the coating was modelled as rigid with a thickness of 1 mm and material density of  $1200 \text{ kg/m}^3$  so that its weight is equal to that of sand-paper used in experiments discussed in preceding sections. For the analysis presented in Section 6.7 using deformable targets, a rate-insensitive elastic-perfectly plastic material was used

for the target plate as well as the coating with the following properties: Young's modulus = 69 GPa; Poisson's ratio = 0.3; Yield stress = 50 MPa and density = 2700 kg/m<sup>3</sup>.

## 6.5 Simulation - fixed coating, rigid target

Before we attempt to predict the response with sliding coating ('slip' condition), it is vital for the numerical model to be able to predict experimental results for case of rigid target with fixed coating ('no-slip' condition); see Goel et al. [44] for the details of experiments. To do this, we use two approaches that better represent experimental observations: (i) increasing the angularity of the grains in the slug - using  $\Phi = 3$  (Section 6.4.1), and (ii) calibrating the friction coefficient  $\mu_T$  between the grains and the coating. Both these strategies are expected to increase the frictional loading on the target, increasing the transmitted momentum to the level observed in experiments by Goel et al. [44].

Snapshots showing the predictions of sand slug at  $v_0 = 112 \text{ m s}^{-1}$  impact on inclined rigid target are included in Fig. 6.6b. The shown slug has particles with aspect ratio  $\Phi = 3$  and the calibrated friction coefficient between grains and coating  $\mu_T = 2.0$ . The flow of grains is along the surface of the target with minimal reflection, as also observed in experiments (Fig. 6.6a). The averaged values of  $I_T^y/I_0$ ,  $I_T^z/I_0$  and  $I_T/I_0$  are included in Fig. 6.10 for experiments with fixed Alumina and sand-paper coating [44] along with those from simulations performed for the current study and presented in Fig. 6.6b. The difference between observations for fixed alumina and sand-paper coating was attributed to frictional loading and embedding of grains (See [44] for details). As can be seen from Fig. 6.10,  $\Phi = 3$  and  $\mu_T = 2.0$  results in good agreement of transmitted momentum with that observed in experiments by Goel et al. [44].

## 6.6 Simulation - sliding coating, rigid target

We proceed to numerically analyse the case of allowing the coating to slide on the rigid target surface. The simulations presented in this section were performed using  $\mu_T = 2.0$  as this was shown to be an appropriate quantification of friction coefficient between grains and sand-paper coating (see Section 6.5). The coating/target friction coefficient  $\mu_s$  is a variable and its effect has been analysed. In experiments, this friction would be provided by the lubricant used and the interaction between the back surface of sand-paper coating and front of the target surface. In Fig. 6.6d, a series of snapshots are included for numerical predictions having a sliding coating with particle/coating friction  $\mu_T = 2.0$  and a calibrated coating/target friction  $\mu_s = 0.12$ . As observed in experiments (Fig. 6.6c), the particles flow along the plate after impact and the front plate starts sliding after the impact. To understand the effect of coating-target friction coefficient  $\mu_s$ , we first analyse

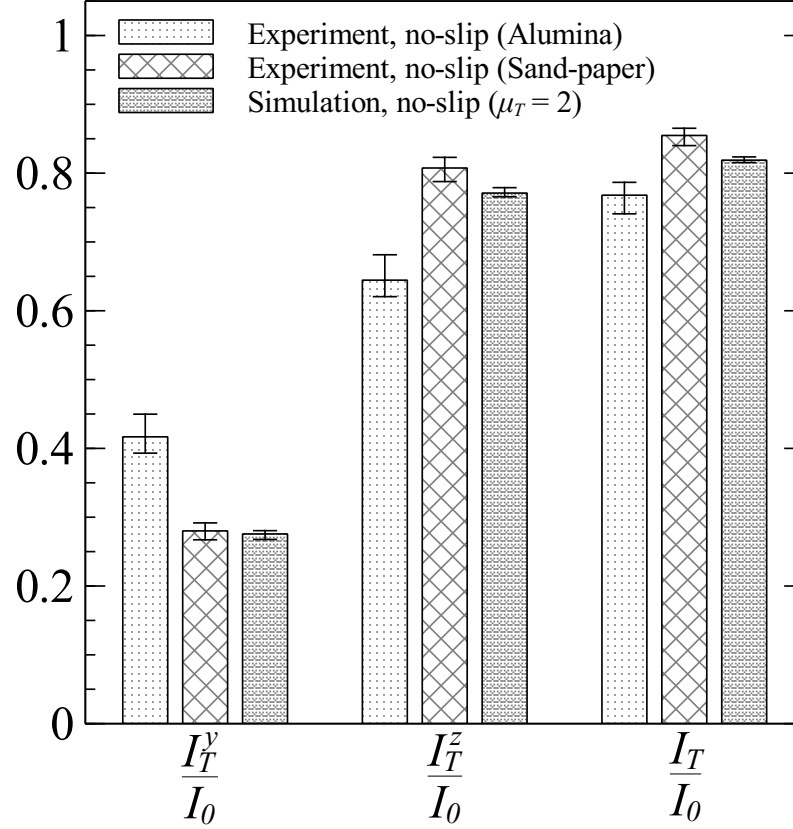


Fig. 6.10 A bar chart showing the measurements and predictions of  $I_T^y/I_0$ ,  $I_T^z/I_0$  and  $I_T/I_0$  for the impact of the dry sand slugs against inclined rigid target. Experimental results are shown for fixed Alumina and sand-paper coated target as observed by Goel et al. [44]. Predictions are shown for the friction coefficient  $\mu_T = 2.0$  between the grains and the coating. The error bars indicate the variation of the measurements and predictions over the range of slug velocities  $v_0$  investigated here.

the case when there is no friction between sliding coating and target (i.e.  $\mu_s = 0$ ) and then proceed to discuss the results for  $\mu_s > 0$ .

### 6.6.1 Sliding coating - no interface friction ( $\mu_s = 0$ )

As discussed in Section 6.3, having a sliding coating reduces the frictional loading on the target surface and brings the transmitted momentum closer to what is observed from a target with relatively smooth surface. In simulations, this frictional loading would now depend upon the friction coefficient  $\mu_s$  used between the sliding coating and target. For this reason, we first compare the case of sliding coating having  $\mu_s = 0$  and  $\mu_T = 2.0$  to the case of fixed coating having  $\mu_T = 0$ .

We quantify the results using the total momentum of grains and sliding coating in different directions. The momentum of all the grains in  $y$  and  $z$ -directions is denoted by  $I_p^y$  and  $I_p^z$ , respectively. Similarly, the momentum of sliding coating is denoted by  $I_s^y$  and  $I_s^z$ . The prediction for normalized momentum of grains and sliding coating in  $z$  and

$y$ -directions against time  $t$  is shown in Fig. 6.11a and 6.11b, respectively for slug velocity  $v_0 = 128 \text{ m s}^{-1}$ . Here, time  $t = 0$  corresponds to the instant that slug impacts the coating. In this figure, the solid curve is normalised momentum of the grains for the case of fixed coating (no-slip condition) having  $\mu_T = 0$ . Other curves (dashed and dotted) are for the case of sliding coating (slip condition) having  $\mu_T = 2.0$  and  $\mu_s = 0$ . For the slip condition, the three curves shown are: momentum of all the grains ( $I_p$ ), momentum of the sliding coating ( $I_s$ ), and a summation ( $I_p + I_s$ ) of momentum of grains and sliding coating. For both slip and no-slip conditions,  $I_p^z/I_0 = -1$  and  $I_p^y/I_0 = 0$  at  $t = 0$  because all the grains in the slug are moving in  $-z$  direction and have total momentum of  $I_0$ . During the impact, the grains flow along the coating surface, such that their momentum decreases in  $-z$  direction ( $I_p^z/I_0$  increases: Fig. 6.11a) and increases in  $y$ -direction ( $I_p^y/I_0$  increases: Fig. 6.11b). For the sliding coating,  $I_s^z/I_0 = I_s^y/I_0 = 0$  at  $t = 0$  because it is at rest before the start of impact. During the impact, it gains momentum in  $-z$  and  $+y$  direction: See Fig. 6.6d for pictures. Hence,  $I_s^z/I_0$  decreases (Fig. 6.11a) and  $I_s^y/I_0$  increases (Fig. 6.11b). From Fig. 6.11a and Fig. 6.11b, it is clear that the total momentum of grains and coating in  $z$ -direction ( $I_p^z + I_s^z)/I_0$  and  $y$ -direction ( $I_p^y + I_s^y)/I_0$  for slip condition with  $\mu_T = 2.0$  and  $\mu_s = 0$  is similar to the momentum of grains  $I_p^z/I_0$  and  $I_p^y/I_0$  for no-slip condition with  $\mu_T = 0$ . This shows that even if the grain/coating coefficient of friction is high ( $\mu_T = 2.0$ ), having a zero friction ( $\mu_s = 0$ ) at the interface of coating and target surface makes the system equivalent to the case of fixed coating with zero grain/target friction (i.e. the momentum of grains in no-slip condition  $\approx$  momentum of grains + coating in the slip condition). Using conservation of momentum, this implies that the momentum transmitted to the target would be the similar in the two cases.

Bar chart showing averaged predictions of  $I_T^y/I_0$ ,  $I_T^z/I_0$  and  $I_T/I_0$  are presented in Fig. 6.12 for the two cases discussed above: no-slip condition with  $\mu_T = 0$  and slip condition with  $\mu_T = 2.0$ ,  $\mu_s = 0$ . In addition, we have included the predictions for no-slip condition with  $\mu_T = 2.0$ . As discussed earlier, it is clear that having a sliding coating with  $\mu_T = 2.0$  and  $\mu_s = 0$  transmits similar momentum to the target as in no-slip condition with  $\mu_T = 0$ . It can also be seen that the transmitted momentum for no-slip condition with  $\mu_T = 2.0$  has significantly higher transmitted momentum  $I_T/I_0$  than the two cases discussed here. In conclusion, the analysis presented in this section shows that (i) If a sliding coating is used on the inclined rigid target surface for impact with granular slugs, the initial momentum  $I_0$  of the grains in the slug is distributed into 3 parts: momentum transmitted to the target, momentum gained by the coating and final momentum of the grains. (ii) Having a sliding coating can potentially reduce the momentum transmitted to the inclined rigid target even if the friction  $\mu_T$  between the grains and the coating is high. The only requirement is to have a low friction  $\mu_s$  between the coating and the target. (iii) To minimise the transmitted momentum to an inclined rigid target, the best scenario is to have no-slip condition and a frictionless contact between the grains and coating ( $\mu_T = 0$ ).

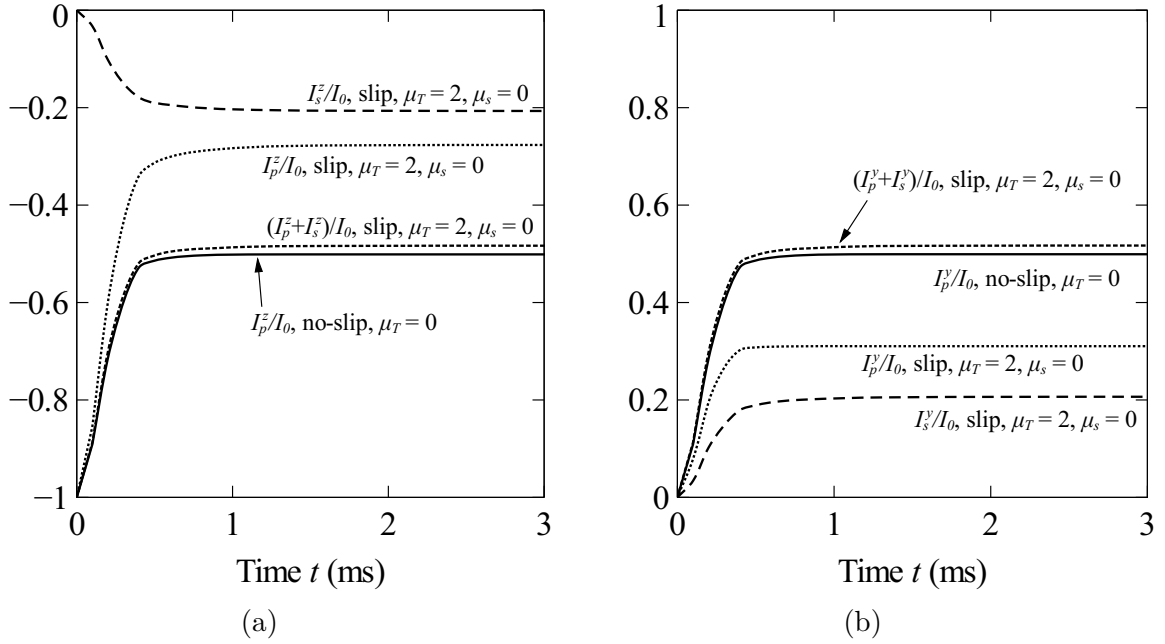


Fig. 6.11 Normalized momentum in (a)  $z$ -direction and (b)  $y$ -direction against time  $t$  for the case with sliding coating (slip condition) where grain/coating friction  $\mu_T = 2.0$  and coating-target friction  $\mu_s = 0$ . These are the momenta for the grains and coating rather than the momentum transmitted to the target. Solid curve shows the momentum of grains for the case of fixed coating (no-slip condition) and grain/coating friction  $\mu_T = 0.0$ . The slugs have a velocity  $v_0 = 128 \text{ m s}^{-1}$  and  $t = 0$  corresponds to the instant that slug first impacts the coating.

### 6.6.2 Sliding coating - with interface friction ( $\mu_s \neq 0$ )

In the previous section, we discussed the predictions using sliding coating and no friction at the interface between the coating and target, i.e.  $\mu_s = 0$ . For the experiments presented earlier using sliding coating, we used a lubricant between the coating and target (see Section 6.2.4) which reduces the friction at their interface. In this section, we present simulations in order to predict the experimental results for sliding coating by increasing the value of  $\mu_s$ . The model set-up for these simulations was the same as used previously and  $\mu_s$  was gradually increased. It was found that for  $\mu_s = 0.12$ , the predictions of  $I_T^y/I_0$ ,  $I_T^z/I_0$  and  $I_T/I_0$  match closely with experimental measurements as shown in bar charts in Fig. 6.12: see the cases ‘slip  $\mu_T = 2.0$ ,  $\mu_s = 0.12$ ’ and ‘Experiment (slip)’. If  $\mu_s > 0.12$  (not analysed here), the frictional loading on the target is expected to further increase and the momenta to approach that for the case of fixed sand-paper coating. In Fig. 6.6d, predictions are shown for sliding coating with  $\mu_T = 2.0$  and  $\mu_s = 0.12$ , which can be compared with Fig. 6.6c where experimental observations are shown for sliding coating having a lubricant at the interface with target surface. The dashed horizontal line in Fig. 6.6c and Fig. 6.6d indicate the initial location of the top edge of sliding coating. At different times  $t$  after impact, the position of the top edge of the coating is indicated by circular marker. It is clear that the movement of coating matches closely between predictions and measurements.

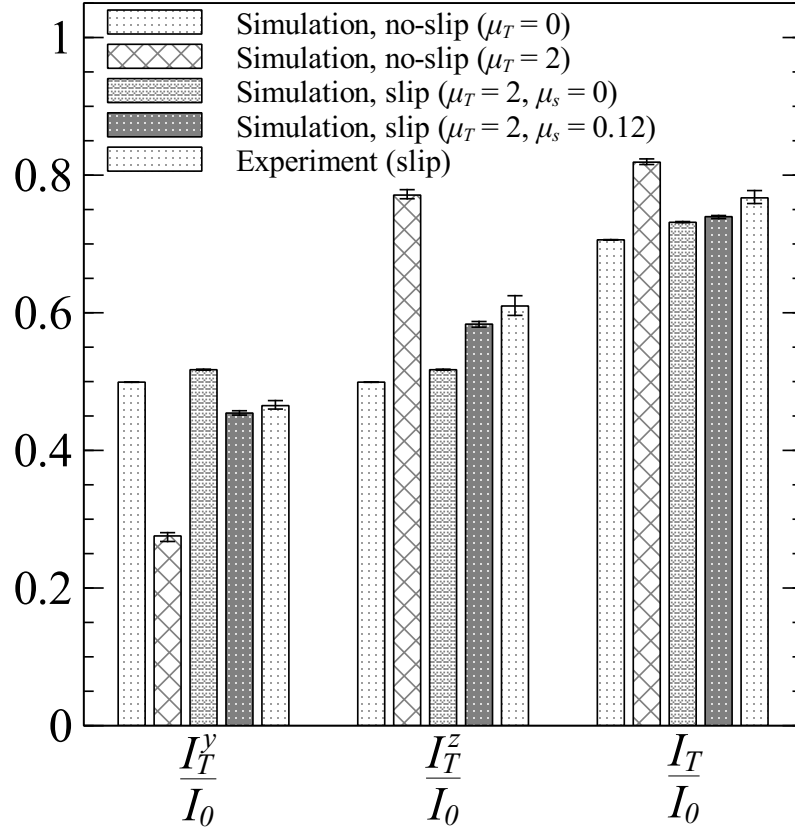


Fig. 6.12 A bar chart showing predictions and measurements of  $I_T^y/I_0$ ,  $I_T^z/I_0$  and  $I_T/I_0$  for the impact of the dry sand slugs against inclined rigid target. Predictions are shown for two scenarios ( $\mu_T = 0.0$ ,  $\mu_T = 2.0$ ) of no-slip condition, two scenarios ( $\mu_s = 0.0$ ,  $\mu_s = 0.12$ ) for the slip condition with  $\mu_T = 2.0$ . Measurements are shown for the experiments with slip condition. The error bars indicate the variation of the measurements and predictions over the range of slug velocities  $v_0$  investigated here.

Because of the symmetry of granular flow in  $x$ -direction the overall force on the sliding coating in  $x$ -direction is zero and hence it does not move in the  $x$ -direction. We define the velocity  $v_s$  of the sliding coating on the target surface as the resultant velocity given by  $v_s = \sqrt{v_y^2 + v_z^2}$  where  $v_y$  and  $v_z$  are the velocities of coating in  $y$  and  $z$ -directions, respectively. A comparison of  $v_s$  between experiment and simulation is shown in Fig. 6.13a for the slug speed  $v_0 = 111 \text{ m s}^{-1}$ . The data is plotted against time  $t$  where  $t = 0$  indicates the moment when the slug first impacts the coating. It is evident that during the impact process, the velocity  $v_s$  rises sharply and reaches a steady value for  $t > 0$ . The experimental measurement in Fig. 6.13a was generated by using the snapshots from the high speed camera to obtain the position of the sliding coating at each time frame, which was then used to derive its velocity. The frame rate of the high-speed camera limits the refinement of data with respect to time, which results in the sudden variation of  $v_s$  as seen in the figure. As long as the coating is in contact with the target, there would be frictional forces which would decelerate the coating. Since the size of coating is approximately the same as the target surface, the coating starts losing contact area with the target surface as soon as the sliding starts. Before the deceleration of the coating is observed, it loses

contact with the target surface, which is when it reaches a steady velocity, indicating there are no additional forces on the coating from the target or grains. We denote this steady velocity of the coating by  $V_s$  and present a comparison of  $V_s$  between experiment and simulation in Fig. 6.13b for the four different slug speeds used. As expected,  $V_s$  increases with  $v_0$  because the force exerted by slug on the coating would be larger for larger  $v_0$ . The predicted speeds  $V_s$  for simulations match closely with those observed in experiments.

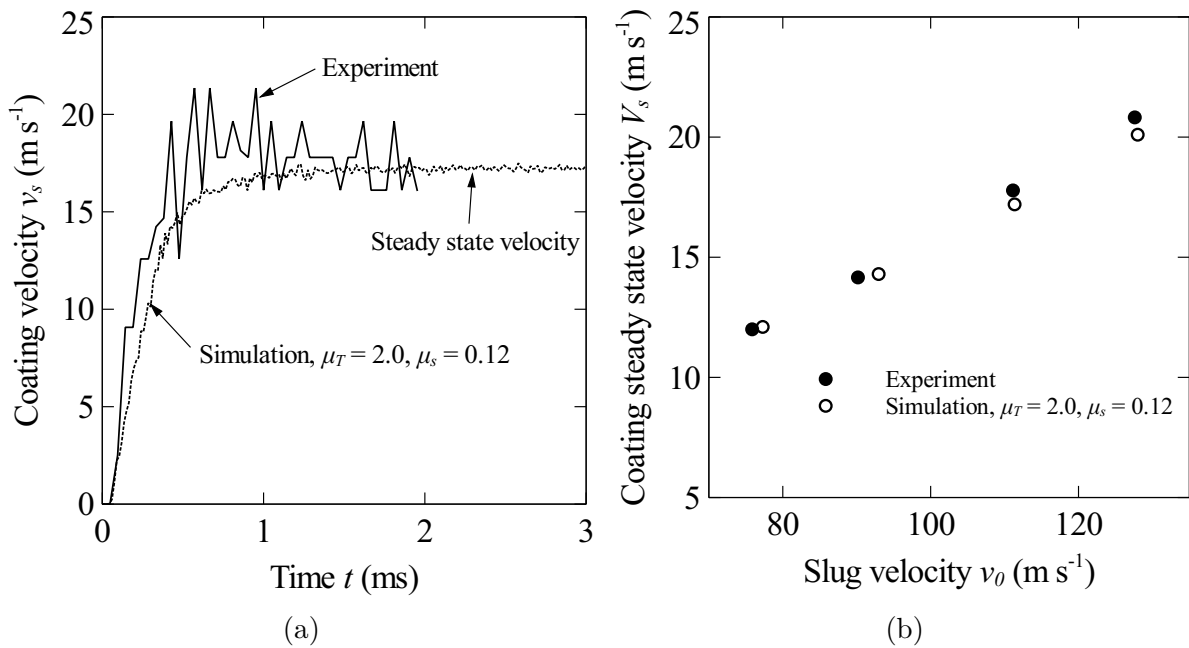


Fig. 6.13 (a) Resultant instantaneous velocity  $v_s$  of the sliding coating against time  $t$  for slug average speed  $v_0 = 111 \text{ m s}^{-1}$ . The plot shows data from the experiment and the corresponding numerical prediction with  $\mu_T = 2.0$  and  $\mu_s = 0.12$ . (b) The resultant steady state velocity  $V_s$  of the sliding coating against the average speed  $v_0$  of slug used. Here, time  $t = 0$  corresponds to the instant the slug first impacts the coating. The plot shows the experimental as well as simulation data.

The analysis in this section shows that the calibrated friction coefficient  $\mu_s = 0.12$  between sliding coating and target surface was found to be sufficient for predicting the results obtained by experiments for sliding coating done by using a lubricant between the coating and the target. If this friction is increased, the tangential loading on the target would increase, resulting in increased  $I_T^z/I_0$ , decreased  $I_T^y/I_0$  (see Eq. 6.4) and a higher overall transmitted momentum  $I_T/I_0$ .

## 6.7 Simulation - sliding coating, deformable target

In the previous sections with the help experiments and simulations, we have shown that the momentum transmitted to a rigid inclined target can be reduced by introducing a coating on the impact face which slides on the target surface during the slug impact. To

get further insight, we proceed to analyse deformable targets impacted by granular slugs with the help of simulation techniques used previously.

For the experiments performed using rigid target, the slug impacted at a distance of 30 mm from the top edge of the target: see Fig. 6.4. For the corresponding simulations using rigid target, we used the same point of impact on the target. If the point of slug impact was taken as the geometric centre of the target surface (50 mm from the top edge), we would still expect the benefit of using a sliding coating, with little difference in actual values of the transmitted momentum. For the simulations of impact with deformable target presented in this section, the location of impact was changed to the geometric centre of the target surface as shown in Fig. 6.14. This is because we also analyse slug impact with a deformable target normal ( $\alpha = 90^\circ$ ) to the incident slug, which is compared with the results using deformable inclined target ( $\alpha = 45^\circ$ ). For the target with normal orientation, if the impact happens at the centre of target surface, the impact would be symmetric in  $x$  as well as  $y$ -direction. Additionally, the deformation of the normal target would be higher if the impact force is applied at the centre as compared to the force applied closer to one of the supports, providing better opportunity to analyse impacts at lower speeds.

For the deformable inclined target (Fig. 6.14a), the target face was the same dimension 100 mm x 50 mm as used for rigid target and had a thickness of 2.0 mm. This thickness included the thickness of the sliding coating such that if the sliding coating was not used, the thickness of the target plate was 2.0 mm and if the sliding coating was used, the total thickness of target plate and the coating was 2.0 mm. The target plate and coating had the same material properties as detailed in Section 6.4.6. This was done in order to conserve the total mass of the system. The top and bottom edges ( $+z$  and  $-z$  edges) of the target were fully constrained in all the degrees of freedom. The sliding coating was not constrained and was in contact with the target surface initially. The particle/coating friction  $\mu_T = 2.0$  and coating/target friction  $\mu_s = 0$ . We define two parameters  $M$  and  $M_s$  as the combine mass (of target plate and coating) and the mass of coating, respectively. Since, the material properties and areal dimensions were same for the sliding coating and target plate, the normalised values of  $M_s$ , defined as  $M_s/M$  would directly be the ratio of thickness of coating and combined thickness (2 mm as mentioned previously). A zero value of  $M_s/M$  means that there is no sliding coating which is also equivalent to having fixed coating. The highest value of  $M_s/M$  used was 0.5, which means that the coating and the target plate have the same thickness of 1.0 mm. Hence, the thickness of target plate is highest for  $M_s/M = 0$  and decreases to its minimum value of 1.0 mm when  $M_s/M = 0.5$ . As discussed in Section 6.4.5, a momentum conservation is used to estimate the momentum transmitted to deformable target by calculating the total momentum of grains and sliding coating in different directions before and after the impact. We also analyse the deflection of the target using  $w_p$  which is the permanent maximum deflection of the target. This is the deflection at the geometric centre of the target plate after the impact event completes and oscillation of the target dies down.

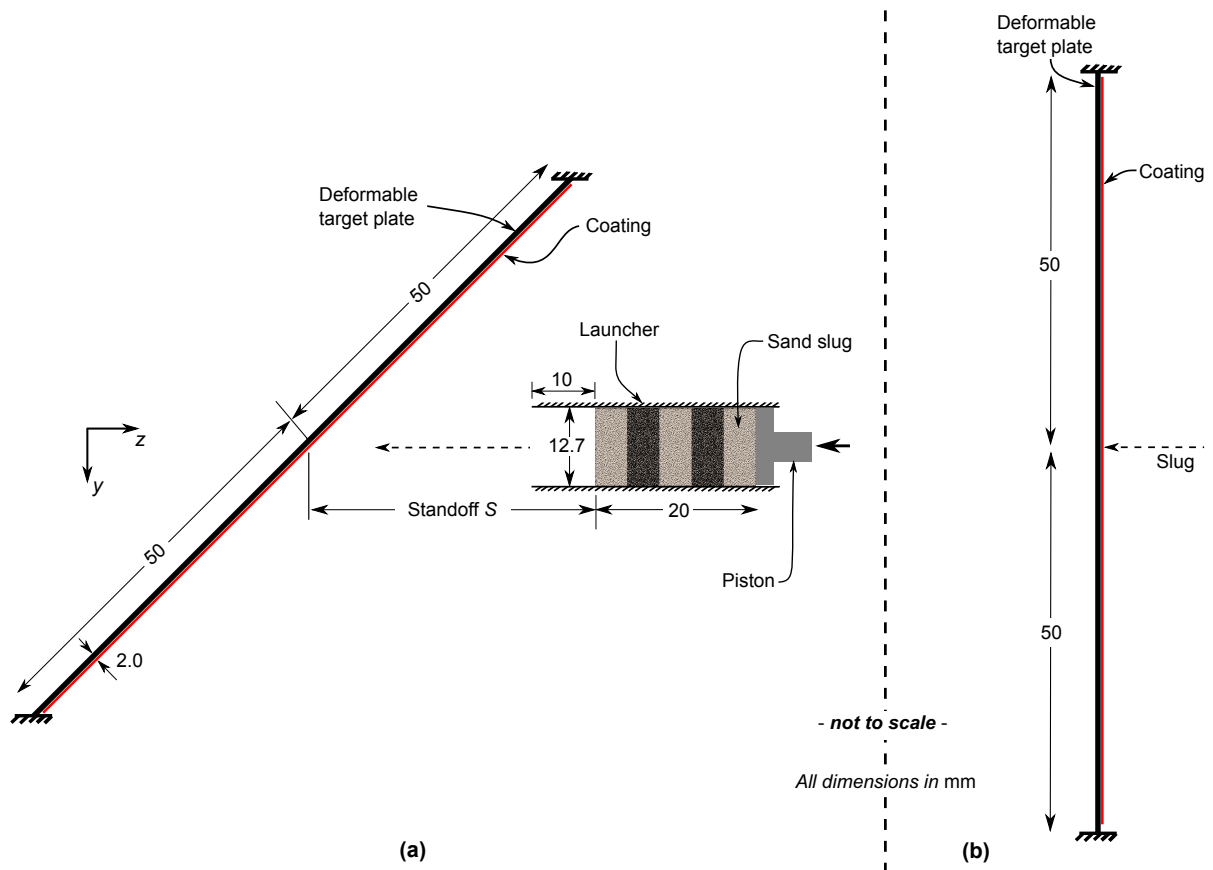


Fig. 6.14 A side view sketch showing the setup used in the numerical simulations with (a) inclined ( $\alpha = 45^\circ$ ) deformable target plate with a sliding coating and (b) normally oriented ( $\alpha = 90^\circ$ ) deformable target plate with a sliding coating. All critical dimensions of the launcher, sand slug and target are marked in (a) along with the definition of stand-off  $S$ . The length of target plate and coating is 100 mm as shown. The width (in  $x$ -direction) is 50 mm. The sketch is not shown to scale.

### 6.7.1 Inclined impact

Snapshots of simulations for impact of sand slug on a deformable inclined target are shown in Fig. 6.15. In Fig. 6.15a, there is no coating (equivalent to no-slip condition) with  $\mu_T = 2.0$  as the friction between grains and target plate. Fig. 6.15b and Fig. 6.15c shows the cases with sliding coating having  $M_s/M = 0.1$  and  $M_s/M = 0.5$ , respectively where the grain/coating friction  $\mu_T = 2.0$  and coating/target interface friction  $\mu_s = 0$ . The snapshots are shown for different time instants  $t$  where  $t = 0$  is the instant when the slug impacts the target plate or coating. At each time  $t$ , the deformation profile of the target plate is qualitatively similar for all the cases, irrespective of the presence of sliding coating. In each case, the grains flow along the downward slope of the target. When the coating is present, it also deforms with the target plate and moves along the surface of the target plate. The thinner sliding coating (Fig. 6.15b) has higher deformation and moves faster than the heavier coating (Fig. 6.15c): see for example  $t = 1.45$  ms. Again, because of symmetry of impact about the  $y$ - $z$  plane, the displacement of the coating is vanishingly small in the  $x$ -direction.

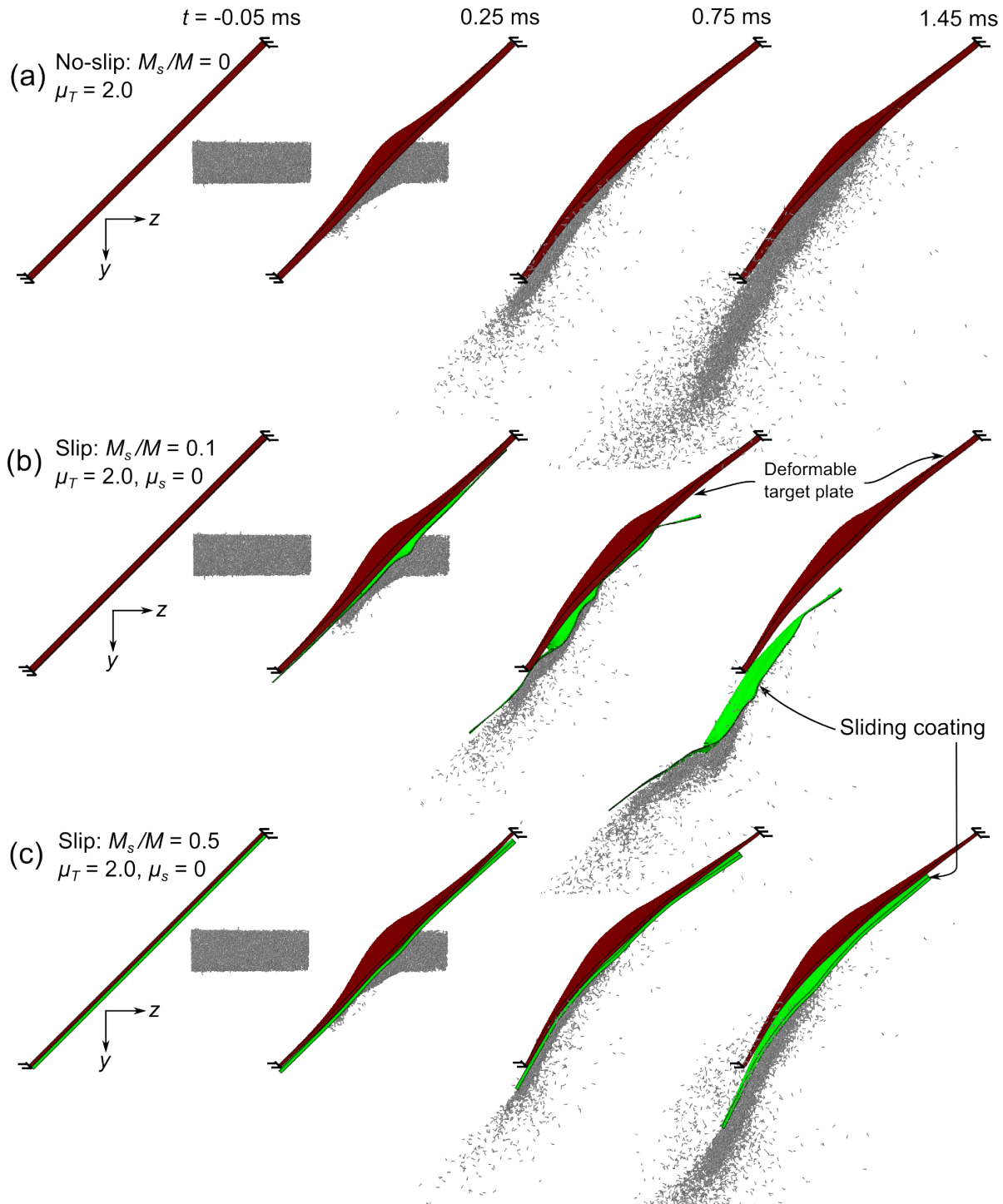


Fig. 6.15 Predictions showing the impact of sand slug at  $v_0 = 128 \text{ m s}^{-1}$  against inclined deformable target plate (a) is case without coating ( $M_s/M = 0$ ) and grain/target plate friction  $\mu_T = 2.0$ . (b) and (c) shows impact in the presence of sliding coating ( $M_s/M = 0.1$  and  $0.5$ , respectively) in front of the target plate having grain/coating friction  $\mu_T = 2.0$  and coating/target interface friction  $\mu_s = 0$ . Here,  $t = 0$  corresponds to the instant that slug first impacts the target surface (for the case of no coating) or sliding coating (when sliding coating is present).

The predictions of permanent deflection  $w_p$  of the target plate and normalised total transmitted momentum  $I_T/I_0$  are shown in Fig. 6.16a and 6.16b, respectively against a

range of  $M_s/M$  for selected slip and no-slip conditions. The predictions are shown for two values of slug velocity  $v_0 = 77 \text{ m s}^{-1}$  and  $v_0 = 128 \text{ m s}^{-1}$ . A higher  $v_0$  results in higher values of  $w_p$  and  $I_T/I_0$  due to the larger momentum of the impacting granular slug, as reported in a number of studies of granular impacts against deformable targets: See for example [43, 79, 30, 127]. In Fig. 6.16a and 6.16b, the predictions for the case with no sliding coating, i.e.  $M_s/M = 0$  (equivalent to no-slip condition) and grain/target friction  $\mu_T = 2.0$  are also included (using solid markers).

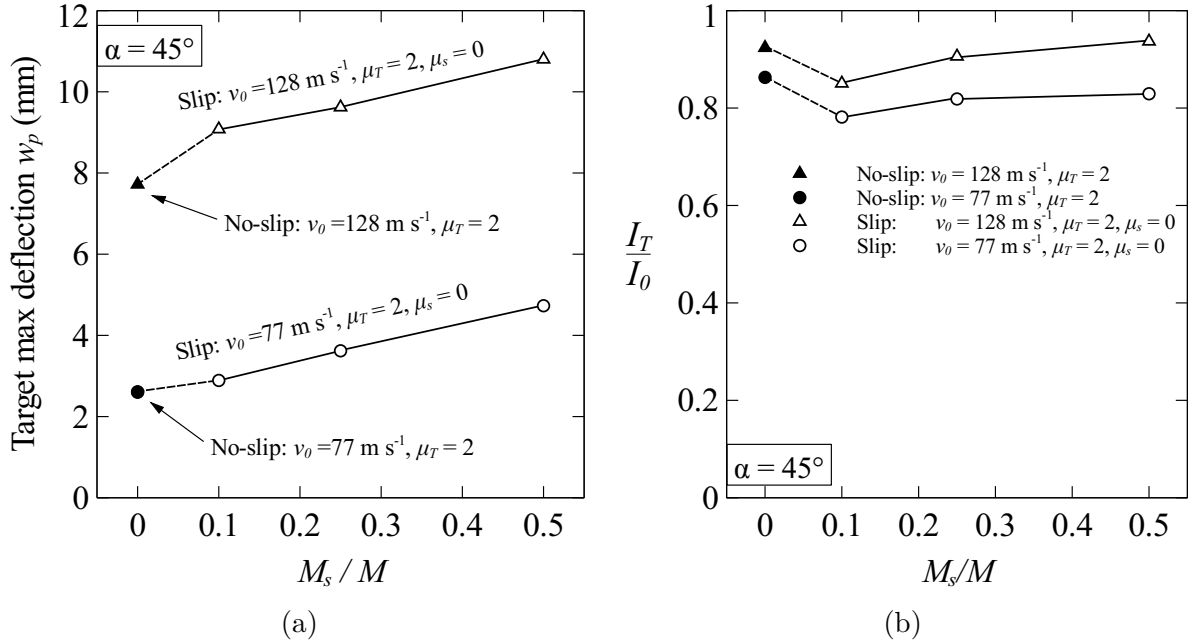


Fig. 6.16 (a) Prediction of permanent deflection  $w_p$  of the centre of the target plate and (b) normalised transmitted momentum  $I_T/I_0$  against the ratio  $M_s/M$  of sliding coating mass to total mass of the target.  $M_s/M = 0$  (shown by solid markers) is the case with no coating and grain/target friction  $\mu_T = 2.0$ .  $M_s/M > 0$  (shown by hollow markers) are the cases having sliding coating with grain/coating friction  $\mu_T = 2.0$  and coating/target interface friction  $\mu_s = 0$ . The predictions are shown for the two slug speeds  $v_0 = 77 \text{ m s}^{-1}$  and  $128 \text{ m s}^{-1}$ .

For any given  $v_0$ , the deflection  $w_p$  increases with increasing  $M_s/M$  because a higher the value of  $M_s/M$  results in a thinner target plate: recall that  $M_s$  is the mass of coating and  $M$  is the combined mass of target plate and coating, where  $M$  is kept constant.  $I_T/I_0$  also increases with increase in  $M_s/M$  when the coating is present (i.e. when  $M_s/M > 0$ ), as shown by hollow markers. This increase in transmitted momentum can be explained by two phenomena:

1. A thinner coating (low  $M_s/M$ ) attains the momentum quicker, starts sliding on the target surface and takes the grains ‘away’ from the target before much of the momentum is transmitted to the target. Hence, less momentum is transmitted to the target if thinner plate is used.
2. For a thick coating (high  $M_s/M$ ), a higher deformation of the target plate (because it is thin) would result in increased momentum of the grains in  $y$ -direction and

reduced flow in  $z$ -direction after the impact, resulting in increased momenta  $I_T^y$  and  $I_T^z$  transmitted to the target.

When the sliding coating is not present (no-slip condition, i.e.  $M_s/M = 0$  indicated by solid markers in Fig. 6.16b), the transmitted momentum  $I_T/I_0$  is high because of high frictional forces ( $\mu_T = 2.0$ ) from the slug to the target. The analysis in this section shows that for a granular slug impacting deformable inclined target, the deflection of the target is least when there is no sliding coating. However, the momentum transmitted is high if the grain/target friction is high. The transmitted momentum can be reduced by either having frictionless contact with grains or implementing a sliding coating with low interface friction and minimising the coating mass.

### 6.7.2 Normal impact

We proceed to analyse the response of a deformable target plate oriented normal ( $\alpha = 90^\circ$ ) to the impacting slug, as shown in Fig. 6.17. Snapshots are shown at time instants  $t$  for (a) no coating, (b) coating with  $M_s/M = 0.1$  and (c) coating with  $M_s/M = 0.5$ . The frictional conditions are the same used in the preceding section. The symmetry of impact dictates that frictional loading on the coating and target would cancel out in  $x$  and  $y$ -directions. As a consequence, the coating does not slide relative to the target plate. The coating deforms under the loading and contacts with the target around the location of slug impact. Since there is no sliding of the coating and normal orientation of target, the initial momentum  $I_0$  of the slug would be completely transmitted to the target, i.e.  $I_T^z \approx I_0$ ,  $I_T^x = I_T^y = 0$ . The predictions of permanent deflection  $w_p$  of the centre of the target plate and normalised transmitted momentum  $I_T^z/I_0$  are presented in Fig. 6.18a and 6.18b, respectively. As expected, the permanent deflection  $w_p$  increase with increase in  $M_s/M$  because of the reduced target thickness. Also, there is no effect of having a sliding coating on  $I_T^z/I_0$ , i.e.  $I_T^z/I_0$  does not change with a change in  $M_s/M$ . We conclude from the above analysis that for the case of a normal impact, the presence of a sliding coating does not influence the transmitted momentum, and it only degrades the performance because of higher target plate deformation.

## 6.8 Conclusion

The presented study explores the potential of a sliding coating over the target in mitigating the damage to the target resulting from the impact of a high speed granular media. The extent of damage is gauged by momentum transmitted to the target and its deflection. Experiments and numerical simulations were conducted to analyse the slugs of sand particles fired at high speed on to flat targets with inclined ( $\alpha = 45^\circ$ ) and normal ( $\alpha = 90^\circ$ ) orientations relative to the oncoming slug. The surface of the target had a coating

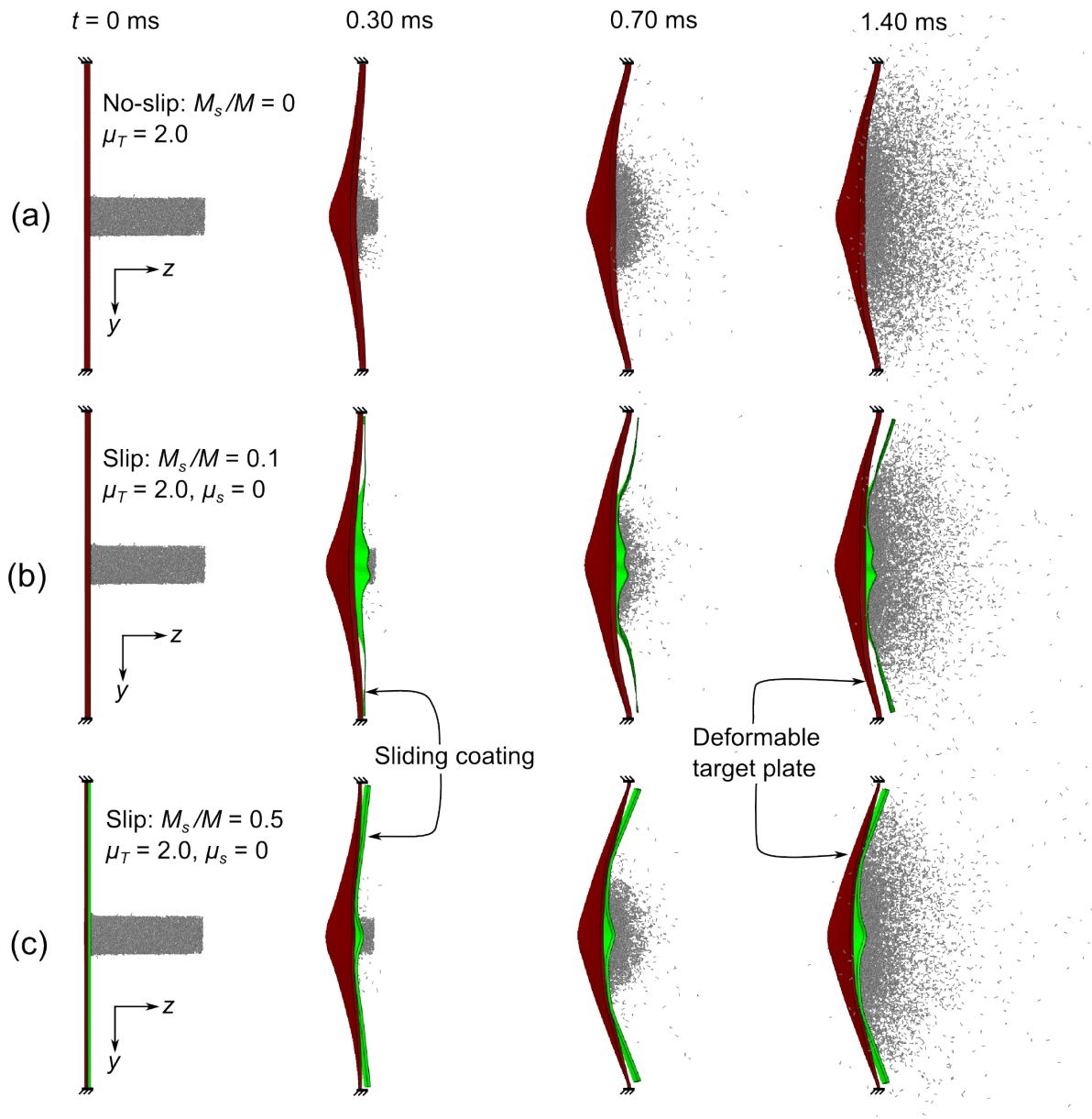


Fig. 6.17 Predictions showing the impact of sand slug at  $v_0 = 128 \text{ m s}^{-1}$  against normally oriented deformable target plate (a) is case without coating ( $M_s/M = 0$ ) and grain/target plate friction  $\mu_T = 2.0$ . (b) and (c) shows impact in the presence of sliding coating ( $M_s/M = 0.1$  and  $0.5$ , respectively) in front of the target plate having grain/coating friction  $\mu_T = 2.0$  and coating/target interface friction  $\mu_s = 0$ . Here,  $t = 0$  corresponds to the instant that slug first impacts the target surface (for the case of no coating) or sliding coating (when sliding coating is present)

which faces the slug and slides on the target surface during impact. High speed imaging was used to study the impact phenomenon and the sliding of the coating. As for the numerical simulations, a coupled discrete particle/Lagrangian finite element method was used. Following are the main conclusions as drawn from this study:

1. For a rigid inclined ( $\alpha = 45^\circ$ ) target with a rough surface facing the slug impact, the damage to the target can be reduced by including the sliding coating having

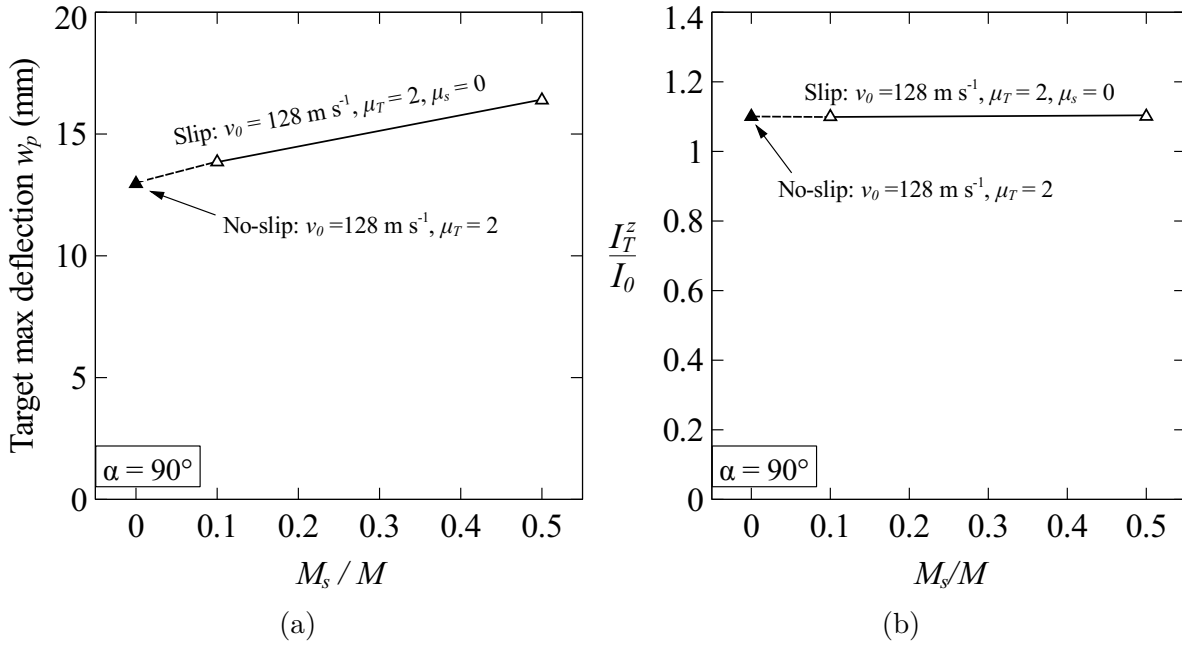


Fig. 6.18 For normal impact: (a) Prediction of permanent deflection  $w_p$  of the centre of the target plate and (b) normalised transmitted momentum  $I_T^z/I_0$  against the ratio  $M_s/M$  of sliding coating mass to total mass of the target.  $M_s/M = 0$  (shown by solid markers) is the case with no coating and grain/target friction  $\mu_T = 2.0$ .  $M_s/M > 0$  (shown by hollow markers) are the cases having sliding coating with grain/coating friction  $\mu_T = 2.0$  and coating/target interface friction  $\mu_s = 0$ . The predictions are shown for the slug speed  $v_0 = 128 \text{ m s}^{-1}$ .

reduced friction at its interface with the target surface. When the slug impacts the coating, the coating undergoes rapid acceleration while the frictional loading on the target is reduced due to low friction at the interface with the coating. This results in reduction of the momentum transmitted to the target as observed in the experiments and validated through numerical simulations. The reduced transmitted momentum when using the sliding coating approached the least possible theoretical value, which happens when there is no coating and target is frictionless.

2. For deformable targets with inclined orientation, having a sliding coating reduces the transmitted momentum as seen in the case of rigid targets. However, when the total areal mass of the system (target plate + coating) is kept constant, having a sliding coating reduces the thickness of the target plate, diminishing its stiffness and resulting in larger deformation than for the case without a sliding coating. So, for a deformable inclined target, the best strategy towards reducing the damage is to have a sliding coating with minimum possible thickness and minimum possible friction at its interface with the target surface.
3. For deformable targets with normal ( $\alpha = 90^\circ$ ) orientation, there is no benefit of having a sliding coating in terms of transmitted momentum. Moreover, due to the reduced thickness and stiffness of the target plate, the damage is increased as it undergoes higher deflection.

It was found that the best strategy towards reducing the damage to the target (for both rigid and deformable targets, and for both normal and oblique impacts) is to eliminate the friction between the grains of the slug and the target. This, however, is not possible to achieve in practice. A practical strategy then is to implement a sliding coating over a deformable target, as discussed in this study.



# Chapter 7

## Conclusions and future work

This chapter draws conclusions for the thesis using the work presented in Chapter 3 to Chapter 6. The conclusions are structured according to the objectives defined in Section 1.2 while introducing this thesis.

### 7.1 Conclusions

This thesis examines the fundamental problem of flat targets impacted by granular aggregates. Laboratory scale experiments were conducted using cylindrical shaped granular slugs, initially contained at rest in a launcher and ejected due to impact by a high speed piston. The pushing action of the piston generates a spatial velocity gradient along the slug, resulting in its axial stretching. The slug generated typically kept their cylindrical shape, with constant diameter. This, in combination of high speed camera for imaging enabled the characterisation of the evolution of granular flow and the loading on the target. On rigid targets, the slugs deform by spreading along the target surface, with little rebound of the particles. Simulations were performed by primarily utilising discrete particle methodology for modelling the particles in the slug. This was combined with finite element method to simulate the fully coupled interaction of the slug with the target. To quantify the effect on the targets, the two measures used were its deflection and the momentum transmitted by the slug. The fraction of incident slug momentum transmitted to the target is indicated by  $I_T/I_0$ , where  $I_T$  is the momentum transmitted to the target and  $I_0$  is the initial momentum of the slug.

### 7.1.1 Factors affecting the loading of structure from high speed granular aggregate

#### Target properties: Stand-off, inclination, surface type

Stand-off, which is the initial distance between the slug and the target, has been shown to influence the deformation of the target. This analysis was performed numerically and the results were compared with the experimental observations of Uth et al. [126] for slug impact on deformable monolithic beams. A higher stand-off meant further lengthening of slugs due to the axial velocity gradient, resulting in longer duration of loading and lower contact pressures on the target, as revealed by simulations of slug impact on rigid target. Hence, for a given incoming slug, even though the momentum of the slug is the same, the deformation of the target is lower for a higher stand-off distance. This shows that velocity and density distribution within the slug governs the deformation of the target and results in a stand-off effect.

The effect of target inclination has been shown using rigid targets by measuring the transmitted momentum. Two inclinations of the target were studied: (i) Normal orientation, when the face of the target is perpendicular to the incoming slug and (ii) Inclined orientation, when the face of the target is inclined at an angle  $45^\circ$  to the incoming slug. For normally oriented targets, symmetry of the impact governs that the net momentum transmitted to the target is in the direction of the incoming slug and amount transmitted is approximately equal to incident momentum, i.e.  $I_T/I_0 \approx 1$ . For inclined targets, the spreading of granular particles is asymmetrical, and for the target inclination of  $45^\circ$ , the theoretical minimum  $I_T/I_0 \approx 0.71$  in absence of friction between the target surface and particles in the slug. In reality, zero friction is difficult to achieve, which increases  $I_T/I_0$ . However, it is still significantly lower than in the  $I_T/I_0$  in case of a normal target.

The properties of the target surface is shown to have a significant effect on the loading from the granular aggregates. This was analysed using four surface coatings: Alumina, PTFE, Aluminium and sand-paper. When the surface coating changes, the frictional interactions and hence the loading on the targets change. For normally oriented targets, this change in frictional interactions cancels out due to symmetry of the granular flow, resulting in no effect of the surface type. For inclined targets, the normalised resultant transmitted momentum  $I_T/I_0$  increases in the order of surface coatings Alumina to PTFE to Aluminium to sand-paper. The lowest transmitted momentum was with alumina coating having  $I_T/I_0 \approx 0.77$ , which is higher than the theoretical minimum possible value of 0.71. By changing from Alumina to sand-paper coating,  $I_T/I_0$  increases by 11%. Irrespective of the surface coating used, the value of  $I_T/I_0$  was still substantially lower compared to the normal impact case where  $I_T/I_0 \approx 1$ .

### Granular properties: Slug velocity, particle shape, particle fracture

Since the slug is ejected from the launcher due to the impact from piston, a higher piston speed results in a faster slug. A faster slug imposes larger deflections of the target and transmits more momentum  $I_T$  to the target. However, the fraction of the incident slug momentum transmitted into the target  $I_T/I_0$  was found to be independent of the slug velocity.

The effect of shape of particles in the slug was studied using simulations, where the surface type was parametrised using particle/target friction coefficient. The numerical predictions were compared with experimental observations where the particles employed had a sub-spherical shape. When spherical particles were used in simulations, they predicted the measurements for the normal impact accurately and also replicated the observed insensitivity of the measurements to slug velocity and surface type. However for inclined impact cases, there were discrepancies in the results for the transmitted momentum and the simulations under-predicted the momentum transmitted to the target, regardless of how high the particle/target friction coefficient was used. Increasing the radius of gyration of the particles and thereby reducing their tendency to rotate improved the predictions, demonstrating the need to accurately model the particle shapes in the simulations.

To analyse this, simulations were performed using either spherical, rod-shaped or cubic particles in the slug. These particles were constructed by combining spherical sub-particles, connected to each other using rigid connectors. If the angularity of the particles is increased, they tend to slide rather than roll on the target surface, resulting in an increase in friction loading to the target and higher transmitted momentum. The particle shape was shown to have no effect for the normal impacts due to symmetry. However, for the targets in inclined orientation the angularity of the particles have significant influence, with increasing transmitted momentum as the particle angularity increases.

In addition, the effect of particle fragmentation during the impact with the target is shown here. To simulate this, the sub-particles were connected using beam connectors, which were allowed to fail at a specified strain level. As a result of fracture, the particle shape changes, which changes in momentum transferred to the inclined targets. When the rod-shaped particles are allowed to break up into more spherical particles, it results in more rolling of particles on the surface, compared to sliding. This reduces the transmitted momentum. The transmitted momentum is further reduced if more particles break during impact, which was tested by reducing the fracture strain of the beam connectors and increasing the impact speed of the slug. A reverse scenario was modelled by using cube shape particles (consisting of 8 spherical sub-particles), which were allowed to break into flake like particles having higher angularity. An increase in transmitted momentum was predicted due to increase in angularity, confirming the hypothesis that particle angularity directly influences the transmitted momentum for granular slug impacting the targets.

### 7.1.2 Numerical parameters

After the impact loading from piston, the slug attains a spatial velocity gradient along its length, which results in its stretching before the impact with the target. This velocity gradient depends strongly on the normal contact stiffness between the particles in the discrete particle simulations and the time required by piston to accelerate the slug. Other inter-particle contact parameters such as damping and friction have negligible effect on the velocity gradient. This was confirmed using simulations and calibration with the experimental observations. By contrast, for a given granular slug (i.e. given spatial velocity and density distribution), none of the parameters of the inter-particle contact model are shown to have any effect on the target response.

A numerical methodology was used to analyse the effect of particle shape in the slug, as discussed in the previous section. A simple approach of combining spherical sub-particles was used to create non-spherical particles. The connection between spherical sub-particles was made by either rigid connectors or breakable beam connectors. The beam connectors were allowed to break during impact, representing fragmentation of particles. The basic particle shapes generated using this method did not represent the actual shape of the sub-spherical particles used in the experiments, but served as a method to change the behaviour of their interaction with the target and study the effect of particle fragmentation. A spherical shape is the most widely used assumption to model the particles in granular media. Calculations presented in this thesis demonstrate the limitation of this spherical shape assumption and show the importance of implementing more realistic particle shapes.

The discrete particle approach adopted here may not be applicable to general soils with a number of constituents, different particle sizes, plastic deformation and cohesion between the particles. However, using this simple model, it is possible to obtain a better insight into the physics of soil-structure interaction.

### 7.1.3 Sliding plate concept for load reduction

In the Chapter 6 of the thesis, experiments and simulations were performed for a sliding plate concept introduced by Kyner et al. [73]. This method can be used to reduce the loading on the target impacted by high speed granular material. Slugs were impacted on flat targets in the same laboratory setting as discussed previously. A sand-paper coating was placed in front of the target surface using a lubricant at the interface, allowing it to slide-off during the impact with the slug. Rigid as well as deformable targets were used for this analysis. For deformable targets, the total areal mass of the target (target plate + coating) was kept constant by reducing the target plate thickness when the coating was implemented.

For normally oriented rigid targets, the coating does not slide because of the frictional loads cancelling out due to symmetry. Hence, there is no effect on the transmitted

momentum. However, for the normally oriented deformable targets, using a coating reduced the thickness and stiffness of the target plate, resulting in higher deflections.

For 45° inclined rigid targets, the coating slides on the target surface during the slug impact, resulting in reduced frictional loading on the target. Hence, the momentum transmitted to the target is reduced, approaching towards the minimum possible theoretical  $I_T/I_0 = 0.71$  for a frictionless target at 45° inclination. For inclined deformable targets as well, the sliding coating is shown to reduce the transmitted momentum. However, due to a reduced thickness of the target plate, the deflection increases. It was shown that for a deformable inclined target, the best scenario to minimise the momentum transfer and deflections is include sliding coating with minimum possible thickness while also minimising the friction between the coating and target surface.

The best theoretical case for all types of target would be to have a zero friction between target and particles, without including sliding coating. In practice however, a sliding coating can be potentially used to reduce the loading on the target.

## 7.2 Future work

Based on the research presented in this thesis, the following topics are recommended for future work:

**Slug speeds:** Granular speeds considered in this thesis were lower than those observed in field experiments. This is a limitation of the available equipment and it is not known if the results can be directly scaled. The basic conclusions made regarding physical phenomenon would be applicable at higher speeds. However, a study using higher speed of granular aggregates is needed to confirm this and produce better quantification of the effects.

**Effect of air and gravity:** For the simulations presented in this thesis, the influence of air and gravity are ignored. At relatively low velocities and millisecond time frames considered in this thesis, the effect of air drag and gravitational forces would be negligible. The change in momentum of the particles is considered to be purely due to collisions with other particles and the target. At high speeds and stand-off however, air drag to the particles due to infiltration into the slug and the gravitational forces may influence the flow of particles and consequently the loading on the target.

**V shaped targets:** In Chapters 4 through 6, the effect of target orientation is studied. However, the targets used were always flat and the slugs impacted around the centre of the target. In reality, the hull of armoured vehicles are V-shaped, which is a combination of two inclined surface. The shape of V targets would mean a different deformation behaviour and hence different blast momentum deflection characteristics.

**Target damage:** In this thesis, deflection and transmitted momentum are the two factors considered to quantify the effect on target. This helps understand the basic physics of the interaction. A natural extension would be to allow the target to fail/fracture due to impact. For instance, the targets can be penetrated by the high speed particles, changing the overall flow of the granular aggregates and influencing the loading and further damage.

**Particle shape variation:** The simulations to study the effect of particle shape in this thesis utilised different particle shapes/angularities. However for a given slug, all the particles had the same shape and size, enabling a clear comparison with the slug consisting particles of a different shape and size. In reality, the granular slugs would have a multiple shape and size distribution of the particles, and the result of this randomness is not known.

**Simulation of explosion:** The granular slugs used in this thesis gained momentum due to impact from a piston. This can be extended by replacing the piston with a shock loading by air, as demonstrated using shock tube experiments by Kandan et al. [67].

# References

- [1] Alghamdi, A. A. A. (2001). Collapsible impact energy absorbers: An overview. *Thin-Walled Structures*, 39(2):189–213.
- [2] Anderson, C. E., Behner, T., and Weiss, C. E. (2011). Mine blast loading experiments. *International Journal of Impact Engineering*, 38(8-9):697–706.
- [3] Bagnold, R. (1954). Experiments on a gravity-free dispersion of large solid particles in a Newtonian fluid under shear. *Proceedings of the Royal Society, London*, A225:49e63.
- [4] Bathurst, R. and Rothenburg, L. (1988). Micromechanical aspects of isotropic granular assemblies with linear contact interactions. *Journal of Applied Mechanics*, 55(1):17–23.
- [5] Behera, B., Kun, F., McNamara, S., and Herrmann, H. J. (2005). Fragmentation of a circular disc by impact on a frictionless plate. *Journal of Physics: Condensed Matter*, 17(24):S2439–S2456.
- [6] Benedetti, R. E. (2008). Mitigation of explosive blast effects on vehicle floorboard. *Master thesis, University of Maryland, College Park, MD, USA*.
- [7] Bergeron, D. and Tremblay, J. (2000). Canadian research to characterize mine blast output. *Proceedings of the 16th International MABS Symposium, Oxford, UK*.
- [8] Bergeron, D., Walker, R., and Coffey, C. (1998). Detonation of 100-gram anti-personnel mine surrogate charges in sand-A test case for computer code validation. *Suffield Report No. 668, Defence Research Establishment Suffield, Ralston, Alberta, Canada*.
- [9] Borvik, T., Dey, S., and Olovsson, L. (2015). Penetration of granular materials by small-arms bullets. *International Journal of Impact Engineering*, 75:123–139.
- [10] Borvik, T., Hanssen, A., Langseth, M., and Olovsson, L. (2009). Response of structures to planar blast loads – A finite element engineering approach. *Computers & Structures*, 87(9-10):507–520.
- [11] Borvik, T., Olovsson, L., Hanssen, A., Dharmasena, K., Hansson, H., and Wadley, H. (2011). A discrete particle approach to simulate the combined effect of blast and sand impact loading of steel plates. *Journal of the Mechanics and Physics of Solids*, 59(5):940–958.
- [12] Brach, R. M. (1988). Impact dynamics with applications to solid particle erosion. *International Journal of Impact Engineering*, 7(1):37–53.
- [13] Braid, M. (2001). Experimental investigation and analysis of the effects of anti-personnel landmine blasts. *Canada: Defence Research Establishment Suffield, (Special Publication, DRES SSSP)*.
- [14] Campbell, C. (2002). Granular shear flows at the elastic limit. *Journal of Fluid Mechanics*, 465:261–291.

- [15] Campbell, C. and Brennen, C. (1985). Chute flows of granular material: Some computer simulations. *Journal of Applied Mechanics*, 52:172–178.
- [16] Cendón, D. A., Gálvez, F., Enfedaque, A., and Sánchez-Gálvez, V. (2007). Analysis of armoured vehicles blast protection by using finite element codes. *23rd International Symposium on Ballistics*, (April):843–852.
- [17] Chen, X. and Hutchinson, J. W. (2002). Particle impact on metal substrates with application to foreign object damage to aircraft engines. *Journal of the Mechanics and Physics of Solids*, 50(12):2669–2690.
- [18] Cheng, X., Varas, G., Citron, D., Jaeger, H., and Nagel, S. (2007). Collective Behavior in a Granular Jet: Emergence of a Liquid with Zero Surface Tension. *Physical Review Letters*, 99(18):188001.
- [19] Cho, G. C., Dodds, J., and Santamarina, J. C. (2006). Particle Shape Effects on Packing Density, Stiffness, and Strength: Natural and Crushed Sands. *Journal of Geotechnical and Geoenvironmental Engineering*, (May):591–602.
- [20] Chung Kim Yuen, S., Langdon, G., Nurick, G., Pickering, E., and Balden, V. (2012). Response of V-shape plates to localised blast load: Experiments and numerical simulation. *International Journal of Impact Engineering*, 46:97–109.
- [21] Cil, M. B. and Alshibli, K. A. (2012). 3D assessment of fracture of sand particles using discrete element method. *Geotechnique Letters*, (2):161–166.
- [22] Clarke, S. D., Fay, S. D., Tyas, A., Warren, J., Rigby, S. E., Elgy, I., and Livesey, R. (2014). Repeatability of buried charge testing. In: *Proceedings of the 23rd International Symposium on Military Aspects of Blast and Shock. International Symposium on Military Aspects of Blast and Shock, 7-12 September 2014, Oxford, UK*.
- [23] Coetzee, C. (2016). Calibration of the discrete element Method and the effect of particle shape. *Powder Technology*, Submitted:50–70.
- [24] Cundall, P. A. and Strack, O. D. L. (1979). A discrete numerical model for granular assemblies. *Géotechnique*, 29(1):47–65.
- [25] Deshpande, V. and Fleck, N. (2005). One-dimensional response of sandwich plates to underwater shock loading. *Journal of the Mechanics and Physics of Solids*, 53(11):2347–2383.
- [26] Deshpande, V., Heaver, A., and Fleck, N. (2006). An underwater shock simulator. *Proceedings of the Royal Society A: Mathematical, Physical and Engineering Sciences*, 462(2067):1021–1041.
- [27] Deshpande, V., McMeeking, R., Wadley, H., and Evans, A. (2009). Constitutive model for predicting dynamic interactions between soil ejecta and structural panels. *Journal of the Mechanics and Physics of Solids*, 57(8):1139–1164.
- [28] Dhar, S., Krajac, T., Ciampini, D., and Papini, M. (2005). Erosion mechanisms due to impact of single angular particles. *Wear*, 258(1-4):567–579.
- [29] Dharmasena, K. P., Queheillalt, D. T., Wadley, H. N. G., Dudt, P., Chen, Y., Knight, D., Evans, a. G., and Deshpande, V. S. (2010). Dynamic compression of metallic sandwich structures during planar impulsive loading in water. *European Journal of Mechanics, A/Solids*, 29(1):56–67.

- [30] Dharmasena, K. P., Wadley, H. N., Liu, T., and Deshpande, V. S. (2013). The dynamic response of edge clamped plates loaded by spherically expanding sand shells. *International Journal of Impact Engineering*, 62:182–195.
- [31] Drucker, D. and Prager, W. (1952). Soil mechanics and plastic analysis or limit design. *Quarterly of Applied Mathematics*, 10:157–165.
- [32] Ehrgott, J. Q., Akers, S. a., Windham, J. E., Rickman, D. D., and Danielson, K. T. (2011). The influence of soil parameters on the impulse and airblast overpressure loading above surface-laid and shallow-buried explosives. *Shock and Vibration*, 18(6):857–874.
- [33] Fairlie, G. and Bergeron, D. (2002). Numerical Simulation of Mine Blast Loading on Structures. *17th Military Aspects of Blast Symposium, Las Vegas, Nevada*, (June):2–9.
- [34] Farhadi, S. and Behringer, R. P. (2014). Dynamics of Sheared Ellipses and Circular Disks: Effects of Particle Shape. *Physical Review Letters*, 112(14):148301.
- [35] Fleck, N. A. and Deshpande, V. S. (2004). The Resistance of Clamped Sandwich Beams to Shock Loading. *Journal of Applied Mechanics*, 71(3):386.
- [36] Foedinger, J. (2005). Methodology for improved characterization of landmine explosions, SBIR Phase-II plus program. 2005. *Proceedings of the Technical Interchange Meeting, Material Science Corporation*.
- [37] Follett, S., Analysis, L., Composite, O. F., Hulls, S., Experimental, N., and Approach, N. (2011). Blast analysis of composite V shaped hulls: An experimental and numerical approach. *PhD thesis, Cranfield University, UK*, (July).
- [38] Fourney, W., Leiste, U., Bonenberger, R., and Goodings, D. (2005). Explosive impulse on plates. *Fragblast*, 9(1):1–17.
- [39] Fourney, W. L., Leiste, H. U., Hauch, A., and Jung, D. (2010). Distribution of Specific Impulse on Vehicles Subjected to IED's. *Proceedings of the IMPLAST 2010 Conference*.
- [40] Fox, D. and Lee, J. (2014). The influence of water, dry sand, and unsaturated sand constitutive behavior on the blast response of a rigid target. *International Journal of Impact Engineering*, 65:163–173.
- [41] Fox, D. M., Huang, X., Jung, D., Fourney, W. L., Leiste, U., and Lee, J. S. (2011). The response of small scale rigid targets to shallow buried explosive detonations. *International Journal of Impact Engineering*, 38(September):882–891.
- [42] Genson, K. (2006). Vehicle shaping for mine blast damage reduction. *Dissertation, University of Maryland, College Park, USA*.
- [43] Goel, A., Uth, T., Liu, T., Wadley, H. N., and Deshpande, V. S. (2018a). Coupled discrete/continuum simulations of the impact of granular slugs with clamped beams: Stand-off effects. *Mechanics of Materials*, 116:90–103.
- [44] Goel, A., Uth, T., Wadley, H. N., and Deshpande, V. S. (2017). Effect of surface properties on momentum transfer to targets impacted by high-velocity sand slugs. *International Journal of Impact Engineering*, 103:90–106.
- [45] Goel, A., Wadley, H. N., and Deshpande, V. S. (2018b). Impact of granular slugs on rigid targets: effect of grain shape and fracture. *Accepted for publication, European Journal of Mechanics/A Solids*.
- [46] Gorham, D. A. and Kharaz, A. H. (2000). The measurement of particle rebound characteristics. *Powder Technology*, (112):193–202.

- [47] Grujicic, M., Pandurangan, B., and Cheeseman, B. a. (2006a). A computational analysis of detonation of buried mines. *Multidiscipline Modeling in Mat. and Str.*, 2(4):363–388.
- [48] Grujicic, M., Pandurangan, B., and Cheeseman, B. A. (2006b). The effect of degree of saturation of sand on detonation phenomena associated with shallow-buried and ground-laid mines. *Shock and Vibration*, 13(1):41–61.
- [49] Grujicic, M., Pandurangan, B., Haque, I., Cheeseman, B., Roy, W., and Skaggs, R. (2007a). Computational analysis of mine blast on a commercial vehicle structure. *Multidiscipline Modeling in Mat. and Str.*, 3(4):431–460.
- [50] Grujicic, M., Pandurangan, B., Huang, Y., Cheeseman, B., Roy, W., and Skaggs, R. (2007b). Impulse loading resulting from shallow buried explosives in water-saturated sand. *Proceedings of the Institution of Mechanical Engineers, Part L: Journal of Materials: Design and Applications*, 221(1):21–35.
- [51] Grujicic, M., Pandurangan, B., Mocko, G. M., Hung, S. T., Cheeseman, B. A., Roy, W. N., and Skaggs, R. R. (2008a). A Combined Multi-Material Euler/Lagrange Computational Analysis of Blast Loading Resulting from Detonation of Buried Landmines. *Multidiscipline Modeling in Materials and Structures*, 4(2):105–124.
- [52] Grujicic, M., Pandurangan, B., Qiao, R., Cheeseman, B., Roy, W., Skaggs, R., and Gupta, R. (2008b). Parameterization of the porous-material model for sand with different levels of water saturation. *Soil Dynamics and Earthquake Engineering*, 28(1):20–35.
- [53] Grujicic, M., Yavari, R., Snipes, J. S., and Ramaswami, S. (2012). Extension of a Current Continuum-Level Material Model for Soil into the Low-Density Discrete-Particle Regime. *Journal of Materials Engineering and Performance*, 22(5):1268–1283.
- [54] Gurumurthy, G. (2008). Blast mitigation strategies for vehicles using shape optimization methods. *Master's Thesis, Massachusetts Institute of Technology*.
- [55] Guttenberg, N. (2012). Microscopic dissipation in a cohesionless granular jet impact. *Physical Review E*, 85(5):051303.
- [56] Hlady, S. (2004). Effect of soil parameters on landmine blast. *18th Military Aspects of Blast and Shock (MABS) Conference, Bad Reichenhall, Germany*.
- [57] Holloman, R. L., Deshpande, V., and Wadley, H. N. (2015a). Impulse transfer during sand impact with a cellular structure. *International Journal of Impact Engineering*.
- [58] Holloman, R. L., Deshpande, V., and Wadley, H. N. (2015b). Impulse transfer during sand impact with a solid block. *International Journal of Impact Engineering*, 76:98–117.
- [59] Hopkins, M. A. (2014). Polyhedra faster than spheres? *Engineering Computations*, 31(3):567–583.
- [60] Huang, Y. J., Chan, C. K., and Zamankhan, P. (2010). Granular jet impingement on a fixed target. *Physical Review E*, 82:031307.
- [61] Hutchings, I. M. (1977). Deformation of metal surfaces by the oblique impact of square plates. *International Journal of Mechanical Sciences*, 19:45–52.
- [62] Hutchings, I. M., Macmillan, N. H., and Rickerby, D. G. (1981). Further studies of the oblique impact of a hard sphere against a ductile solid. *International Journal of Mechanical Sciences*, 25(I):639–646.

- [63] Ji, S., Shen, H. H., and Asce, M. (2006). Effect of Contact Force Models on Granular Flow Dynamics. *Journal of Engineering Mechanics, ASCE*, (November):1252–1259.
- [64] Johnson, C. G. and Gray, J. M. N. T. (2011). Granular jets and hydraulic jumps on an inclined plane. *Journal of Fluid Mechanics*, 675:87–116.
- [65] Johnson, T. E. and Basudhar, A. (2015). A metamodel-based shape optimization approach for shallow-buried blast-loaded flexible underbody targets. *International Journal of Impact Engineering*, 75:229–240.
- [66] Jones, N. (1989). Structural impact. *Cambridge University Press, Cambridge, UK*.
- [67] Kandan, K., Khaderi, S., Wadley, H., and Deshpande, V. (2017). Surface instabilities in shock loaded granular media. *Journal of the Mechanics and Physics of Solids*, 109:217–240.
- [68] Kharaz, A. H. and Gorham, D. A. (2000). A study of the restitution coefficient in elastic-plastic impact. *Philosophical Magazine Letters*, 80(8):549–559.
- [69] Kharaz, A. H., Gorham, D. A., and Salman, A. D. (2001). An experimental study of the elastic rebound of spheres. *Powder Technology*, 120(3):281–291.
- [70] Kleis, I. and Hussainova, I. (1999). Investigation of particle - wall impact process. *Wear*, pages 168–173.
- [71] Kondic, L. (1999). Dynamics of spherical particles on a surface: collision-induced sliding and other effects. *Physical review. E, Statistical physics, plasmas, fluids, and related interdisciplinary topics*, 60(1):751–70.
- [72] Kuwabara, G. and Kono, K. (1987). Restitution Coefficient in a Collision between Two Spheres. *Japanese Journal of Applied Mechanics*, 26(8):1230–1233.
- [73] Kyner, A., Deshpande, V., and Wadley, H. N. (2017a). Momentum transfer during the impact of granular matter with inclined sliding surfaces. *Journal of the Mechanics and Physics of Solids*, 106:283–312.
- [74] Kyner, A., Dharmasena, K., Williams, K., Deshpande, V., and Wadley, H. (2017b). High intensity impulsive loading by explosively accelerated granular matter. *International Journal of Impact Engineering*, 108:229–251.
- [75] Laine, L., Ranestad, O., Sadnvik, A., and Snekkevik, A. (2002). Numerical simulations of anti- tank mine detonations. *Shock Compression of Condensed Matter Melville, NY: American Institute of Physics*, pages 431–4.
- [76] Laine, L. and Sandvik, A. (2001). Derivation of mechanical properties for sand. *Proceedings of the 4th Asia-Pacific Conference on Shock and Impact Loads on Structures, CI-Premier PTE LTD, Singapore*, (November):361–368.
- [77] Liang, Y., Spuskanyuk, A., Flores, S., Hayhurst, D., Hutchinson, J., McMeeking, R., and Evans, A. (2007). The Response of Metallic Sandwich Panels to Water Blast. *Journal of Applied Mechanics*, 74(1):81.
- [78] Lichtenfeld, J. A., Mataya, M. C., and Tyne, C. J. V. (2006). Effect of strain rate on stress-strain behavior of alloy 309 and 304L austenitic stainless steel. *Metallurgical and Materials Transactions A*, 37(January):147–161.
- [79] Liu, T., Fleck, N., Wadley, H., and Deshpande, V. (2013). The impact of sand slugs against beams and plates: Coupled discrete particle/finite element simulations. *Journal of the Mechanics and Physics of Solids*, 61(8):1798–1821.

- [80] Liu, T., Wadley, H., and Deshpande, V. (2014). Dynamic compression of foam supported plates impacted by high velocity soil. *International Journal of Impact Engineering*, 63:88–105.
- [81] McGeary, R. (1961). Mechanical packing of spherical particles. *Journal of The American Ceramic Society*, 44(10).
- [82] McShane, G., Deshpande, V., and Fleck, N. (2013). A laboratory-scale buried charge simulator. *International Journal of Impact Engineering*, 62:210–218.
- [83] McShane, G. J., Deshpande, V. S., and Fleck, N. A. (2007). The underwater blast resistance of metallic sandwich beams with prismatic lattice cores. *Transactions of the ASME. Journal of Applied Mechanics*, 74(2):352–364.
- [84] Morris, B. (1993). Analysis of improved crew survivability in light vehicles subjected to mine blast. *Final report for contract no. DAAK70-92-C-0058 for the U.S. Army Belvoir RDEC, Ft. Belvoir, VA.*
- [85] NATO (2007). Test methodology for protection of vehicle occupants against anti-vehicular landmine effects. *RTO Technical Report*, 323(April).
- [86] Nato (2009). Stanag 4569. 4569(Edition 3):3–6.
- [87] Neuberger, A., Peles, S., and Rittel, D. (2007a). Scaling the response of circular plates subjected to large and close-range spherical explosions. Part I: Air-blast loading. *International Journal of Impact Engineering*, 34(5):859–873.
- [88] Neuberger, A., Peles, S., and Rittel, D. (2007b). Scaling the response of circular plates subjected to large and close-range spherical explosions. Part II: Buried charges. *International Journal of Impact Engineering*, 34(5):874–882.
- [89] Norouzi, H., Zarghami, R., and Mostoufi, N. (2015). Insights into the granular flow in rotating drums. *Chemical Engineering Research and Design*, 102:12–25.
- [90] Olovsson, L., Hanssen, A. G., Borvik, T., and Langseth, M. (2010). A particle-based approach to close-range blast loading. *European Journal of Mechanics - A/Solids*, 29(1):1–6.
- [91] Papini, M. and Dhar, S. (2006). Experimental verification of a model of erosion due to the impact of rigid single angular particles on fully plastic targets. *International Journal of Mechanical Sciences*, 48(5):469–482.
- [92] Papini, M. and Spelt, J. K. (2000a). Impact of rigid angular particles with fully-plastic targets Part I : Analysis. *International Journal of Mechanical Sciences*, 42:991–1006.
- [93] Papini, M. and Spelt, J. K. (2000b). Impact of rigid angular particles with fully-plastic targets Part II : Parametric study of erosion phenomena. *International Journal of Mechanical Sciences*, 42:1007–1025.
- [94] Parab, N. D., Claus, B., Hudspeth, M. C., Black, J. T., Mondal, A., Sun, J., Fezzaa, K., Xiao, X., Luo, S., and Chen, W. (2014). Experimental assessment of fracture of individual sand particles at different loading rates. *International Journal of Impact Engineering*, 68:8–14.
- [95] Park, S., Uth, T., Fleck, N., Wadley, H., and Deshpande, V. (2013). Sand column impact onto a Kolsky pressure bar. *International Journal of Impact Engineering*, 62:229–242.

- [96] Peles, S., Touati, D., Azulay, I., and Neuberger, A. (2008). Numerical simulation of mine detonation beneath a generalized add-on armor structure. *Proc. 24th Int. Symp. Ballistics, 1. Lancaster, PA: DEStech Publications, Inc.*, pages 439–47.
- [97] Pickering, E., Chung Kim Yuen, S., and Nurick, G. (2013). The influence of the height of burial of buried charges - Some experimental observations. *International Journal of Impact Engineering*, 58:76–83.
- [98] Pickering, E., Chung Kim Yuen, S., Nurick, G., and Haw, P. (2012). The response of quadrangular plates to buried charges. *International Journal of Impact Engineering*, 49:103–114.
- [99] Pingle, S., Fleck, N., Wadley, H., and Deshpande, V. (2012). Discrete element calculations of the impact of a sand column against rigid structures. *International Journal of Impact Engineering*, 45:74–89.
- [100] Plimpton, S. (1995). Fast parallel algorithms for short range molecular dynamics. *Journal of Computational Physics*, 117(1):1–19.
- [101] Potapov, A. V. and Campbell, C. S. (1997). The two mechanisms of particle impact breakage and the velocity effect. *Powder Technology*, 93:13–21.
- [102] Ramasamy, A., Hill, A. M., Hepper, A. E., Bull, A. M. J., and Clasper, J. C. (2009). Blast Mines: Physics, Injury Mechanisms And Vehicle Protection. *J R Army Med Corps*, 155(4):258–264.
- [103] Ramasamy, A., Hill, A. M., Masouros, S. D., Gordon, F., Clasper, J. C., and Bull, A. M. J. (2011a). Evaluating the effect of vehicle modification in reducing injuries from landmine blasts. An analysis of 2212 incidents and its application for humanitarian purposes. *Accident; analysis and prevention*, 43(5):1878–86.
- [104] Ramasamy, A., Masouros, S. D., Newell, N., Hill, A. M., Proud, W. G., Brown, K. a., Bull, A. M. J., and Clasper, J. C. (2011b). In-vehicle extremity injuries from improvised explosive devices: current and future foci. *Philosophical transactions of the Royal Society of London. Series B, Biological sciences*, 366:160–170.
- [105] Ramirez, R., Poschel, T., Brilliantov, N. V., and Schwager, T. (1999). Coefficient of restitution of colliding viscoelastic spheres. *Physical Review E*, 60(4):24–26.
- [106] Reichenbach, H., Behrens, K., and Kuhl, A. L. (1991). Exploratory depth-of-burst experiments. *Interim report, CONTRACT No. DNA 001-91-C-0039, Prepared for: Defense Nuclear Agency, Washington, DC, USA.*
- [107] Rigby, S. E., Fay, S. D., Tyas, a., Clarke, S. D., Reay, J. J., Warren, J. a., Gant, M., and Elgy, I. (2017). Influence of particle size distribution on the blast pressure profile from explosives buried in saturated soils. *Shock Waves*.
- [108] Rimoli, J., Talamini, B., Wetzel, J., Dharmasena, K., Radovitzky, R., and Wadley, H. (2011). Wet-sand impulse loading of metallic plates and corrugated core sandwich panels. *International Journal of Impact Engineering*, 38(10):837–848.
- [109] Saeimi-Sadigh, M.-A., Paykani, A., Afkar, A., and Aminollah, D. (2014). Design and energy absorption enhancement of vehicle hull under high dynamic loads. *Journal of Central South University*, 21(4):1307–1312.
- [110] Samimi, A., Moreno, R., and Ghadiri, M. (2004). Analysis of impact damage of agglomerates: Effect of impact angle. *Powder Technology*, 143-144:97–109.

- [111] Shi, Y. and Zhang, Y. (2008). Simulation of random packing of spherical particles with different size distributions. *Applied Physics A*, 92(3):621–626.
- [112] Silbert, L., Ertas, D., Grest, G., Halsey, T., Levine, D., and Plimpton, S. (2001). Granular flow down an inclined plane: Bagnold scaling and rheology. *Physical Review E*, 64(5):051302.
- [113] Snyman, I., Reinecke, D., Ahmed, R., and Ramaloko, P. (2007). SIIMA landmine comparative tests after upgrade. *Technical Report GLBL-AG500-07-0002*, (1).
- [114] Snyman, I. M. (2013). Mitigation of Mine Blast Loading by Collapsible Structures. *Defense Science Journal*, 63(3):262–270.
- [115] Subero, J. and Ghadiri, M. (2001). Breakage patterns of agglomerates. *Powder Technology*, 120(3):232–243.
- [116] Taylor, G. (1963). The pressure and impulse of submarine explosion waves on plates. The Scientific Papers of Sir Geoffrey Ingram Taylor. *Aerodynamics and the Mechanics of Projectiles and Explosions*, G. Batchelor, Cambridge University Press, Cambridge, UK, Vol. III:287–303.
- [117] Taylor, L., Fournery, W., Leiste, U., and Cheeseman, B. (2008). Loading mechanism on a target from detonation of a buried charge. *Proc. 24th Int. Symp. Ballistics*, 2. Lancaster, PA: DEStech Publications, Inc., pages 975–83.
- [118] Taylor, L., Fournery, W. L., and Leiste, H. U. (2010). Pressures on Targets From Buried Explosions. *Proceedings of the IMPLAST 2010 Conference, Providence, Rhode Island USA*, pages 3–10.
- [119] Taylor, L., Skaggs, R., and Gault, W. (2005). Vertical impulse measurements of mines buried in saturated sand. *Fragblast*, 9(1).
- [120] Tilbrook, M. T., Deshpande, V. S., and Fleck, N. a. (2006). The impulsive response of sandwich beams: Analytical and numerical investigation of regimes of behaviour. *Journal of the Mechanics and Physics of Solids*, 54(11):2242–2280.
- [121] Torquato, S., Truskett, T., and Debenedetti, P. (2000). Is random close packing of spheres well defined? *Physical review letters*, 84(10):2064–7.
- [122] Toussaint, G. and Durocher, R. (2010). Finite Element Simulation using SPH Particles as Loading on typical Light Armoured Vehicles. *10th International LS-DYNA® Users Conference*, pages 11–18.
- [123] Tremblay, J. E. (1998). Impulse on blast deflectors from a landmine explosion. *Technical Report DREV-TM-9814*, Defence Research Establishment, Valcartier, Quebec.
- [124] Tremblay, J. E., Bergeron, D. M., and Gonzalez, R. (1998). Protection of soft-skinned vehicle occupants from landmine effectsTitle. *The Technical Cooperation Program, Subcommittee on Conventional Weapons Technology, Technical Panel W-1, USA*, pages 1–29.
- [125] Uth, T. and Deshpande, V. (2014). Response of clamped sandwich beams subjected to high-velocity impact by sand slugs. *International Journal of Impact Engineering*, 69:165–181.
- [126] Uth, T., Wadley, H. N. G., and Deshpande, V. S. (2015). The effect of inclination and stand-off on the dynamic response of beams impacted by slugs of a granular material. *International Journal of Solids and Structures*, 56-57:154–174.

- [127] Wadley, H., Børvik, T., Olovsson, L., Wetzel, J., Dharmasena, K., Hopperstad, O., Deshpande, V., and Hutchinson, J. (2013). Deformation and fracture of impulsively loaded sandwich panels. *Journal of the Mechanics and Physics of Solids*, 61(2):674–699.
- [128] Wadley, H., Dharmasena, K., Chen, Y., Dudt, P., Knight, D., Charette, R., and Kiddy, K. (2008). Compressive response of multilayered pyramidal lattices during underwater shock loading. *International Journal of Impact Engineering*, 35(9):1102–1114.
- [129] Wang, J. (2001). Simulation of a landmine explosion using LS-DYNA3D software. *Australia: Department of Defence*, DSTO-TR116.
- [130] Wang, Z., Hao, H., and Lu, Y. (2004). A three-phase soil model for simulating stress wave propagation due to blast loading. *International Journal for Numerical and Analytical Methods in Geomechanics*, 28(1):33–56.
- [131] Wang, Z. and Lu, Y. (2003). Numerical analysis on dynamic deformation mechanism of soils under blast loading. *Soil Dynamics and Earthquake Engineering*, 23(8):705–714.
- [132] Weckert, S. and Anderson, C. (2006). A Preliminary Comparison Between TNT and PE4 Landmines. *Report no. DSTO-TN-0723*. Edinburgh, South Australia: Defence Science and Technology Organization.
- [133] Wei, Z., Deshpande, V., Evans, A., Dharmasena, K., Queheillalt, D., Wadley, H., Murty, Y., Elzey, R., Dudt, P., Chen, Y., Knight, D., and Kiddy, K. (2008). The resistance of metallic plates to localized impulse. *Journal of the Mechanics and Physics of Solids*, 56(5):2074–2091.
- [134] Wei, Z., Dharmasena, K. P., Wadley, H. N. G., and Evans, a. G. (2007). Analysis and interpretation of a test for characterizing the response of sandwich panels to water blast. *International Journal of Impact Engineering*, 34(10):1602–1618.
- [135] Westine, P., Morris, B., Cox, P., and Polch, E. (1985). Development of computer program for floor plate response from land mine explosions. *Contract Report No. 1345 for U.S. Army TACOM Research and Development Centre*.
- [136] Wu, C.-y., Li, L.-y., and Thornton, C. (2003). Rebound behaviour of spheres for plastic impacts. *International Journal of Impact Engineering*, 28:929–946.
- [137] Xue, Z. and Hutchinson, J. (2004). A comparative study of impulse-resistant metal sandwich plates. *International Journal of Impact Engineering*, 30(10):1283–1305.
- [138] Zakrisson, B., Wikman, B., and Johansson, B. (2008). Half scale experiments with rig for measuring structural deformation and impulse transfer from land mines. *24th international symposium on ballistics*. DEStech Publications, Inc., pages 497–504.
- [139] Zheng, K., Du, C., Li, J., Qiu, B., Fu, L., and Dong, J. (2015). Numerical simulation of the impact-breakage behavior of non-spherical agglomerates. *Powder Technology*, 286:582–591.